ISSN number 0971 - 9709

IGU
Promoting Earth System Sciences

The Journal of Indian Geophysical Union

A SCI Journal

Impact Factor (2026) 0.3



AN OPEN ACCESS BIMONTHLY JOURNAL OF IGU

VOLUME 30, ISSUE 6, NOVEMBER, 2026

The Journal of Indian Geophysical Union (JIGU)
Editorial Board

Chief Editor
O.P. Pandey (Geosciences), Hyderabad

Associate Editors
N. V. Chalapathi Rao (Geological Sciences), Thiruvananthapuram
D. Srinivasa Sarma (Geology, Geochemistry), Hyderabad
D. Shashidhar (Seismology), Hyderabad
S. P. Sharma (Exploration Geophysics), Kharagpur
P.S. Sunil (Seismology, Marine sciences), Kochi
Anand K. Pandey (Himalayan geology, Geodynamics) , Hyderabad

Editorial Board
Solid Earth Geosciences:
Zhigang Peng (Seismology, Remote sensing), Atlanta, USA
Maurizio Fedi (Geodesy, Geophysics), Naples, Italy
Jiancang Zhuan (Statistical modelling, Seismicity), Tokyo, Japan
Ravi P. Srivastava (Exploratioin Geophysics), Bergen, Norway
Kalachand Sain (Seismic, Seismology, Gas hydrate), Hyderabad
Muppidi. Ravi Kumar (Potential field), Hyderabad
Priyeshu Srivastava (Magnetism, Geochemistry), Mumbai
Bhaskar Kundu (Tectonic geodesy), Rourkela
Satish Maurya (Seismology), Mumbai
K. Madhusudhana Rao (Seismology), Gandhinagar
Praful K. Singh (Hydrogeology, Geospatial technology), Gaya
Priyadarshi Chinmoy Kumar (Machine Learning, Hydrocarbon), Dehradun
S. Lasitha (Seismotectonics, Geology), Pondicherry
Bikram Bali (Tectonics, Geology), Srinagar
Dhruv Sen Singh (Sedimentology, Quat. Geology), Lucknow
Himanshu Mittal (Seismology), New Delhi
P.V. Nagmani (Ocean sciences), Hyderabad
Abhishek Saha (Geology, Oceanography), Goa
Abhishek Kumar Rai (Hydrogeology, Geothermal), Kharagpur
Labani Ray (Geothermal), Hyderabad
Saurabh Dutta Gupta (Seismic, Hydrocarbon), Dhanbad

Marine Geosciences and Atmospheric and Space Sciences:
Jayashree Bulusu (Space sciences), Mumbai
B. V. Laxmi (Paleomagnetism), Mumbai
R. Bhatla (Meteorology), Varanasi
Monika J. Kulshrestha (Atmospheric Sciences), New Delhi
Firoz Kadar Badesab (Marine Geophysics), Goa
P. Mahesh (Seismology, Ocean Science), Goa
Rahul Mohan (Ocean science), Goa
R. S. Mahendra (Geoinformatics, Oceanography), Hyderabad
D. Rajan (Atmospheric Science, Monsoon), Coimbatore

Managing Editor:
ASSSRS Prasad (Exploration Geophysics), Hyderabad

Indian Geophysical Union (IGU)
Executive Council

President
Dr.M. Ravichandran, Secretary,
Ministry of Earth Sciences, New Delhi

Vice Presidents
Dr.Prakash Kumar, Director, CSIR-NGRI, Hyderabad
Dr.A.P. Dimri, Director, IIG, Mumbai
Ms. Sushma Rawat, Director (Exploration)-(Retd), ONGC, New Delhi
Dr. T. Srinivas Kumar, Hyderabad

Honorary Secretary
Dr. Abhey Ram Bansal, CSIR-NGRI, Hyderabad

Joint Secretary
Prof. M Radhakrishna, IITM, Mumbai

Org. Secretary
Dr. ASSSRS Prasad, CSIR-NGRI(Retd.), Hyderabad

Treasurer
Mr. Md. Rafique Attar, CSIR-NGRI, Hyderabad

Executive Members
Prof. P.Rajendra Prasad, Andhra University, Vishakhapatnam
Prof. Devesh Walia, NIHU, Shillong
Prof. Rajiv Bhatla, BHU, Varanasi
Dr. Naresh Kumar, WIHG, Dehradun
Dr. A. Vasanthi, CSIR-NGRI, Hyderabad
Dr. P. S. Sunil, CUSAT, Kochi
Dr. Manisha Sandhu, Kurukshetra University, Kurukshetra
Dr. Uday Laxmi, Osmania University, Hyderabad
Prof. Y. Srinivas, MS University, Tirunelveli
Dr. Sumer Chopra, ISR, Gandhinagar
Prof. Bikram Bali, Srinagar University, Srinagar
Prof. Sanjit Kumar Pal, IIT (ISM), Dhanbad

PUBLISHED BY
Indian Geophysical Union, NGRI Campus, Uppal Road, Hyderabad- 500 007
Telephone: 91-4027012739, 27012332; Telefax:+91-04-27171564
Email: jigu1963@gmail.com, website: http://iguonline.in/journal/

The Journal with six issues in a year publishes articles covering
Solid Earth Geosciences; Marine Geosciences; and Atmospheric, Space and Planetary Sciences.

The Journal is supported by CSIR-NGRI & MoES, Govt. of India

Annual Subscription
Individual Rs -1000/- per issue and Institutional Rs- 5000/- for six issues
Payments should be sent by DD drawn in favour of "The Treasurer, Indian Geophysical Union", payable at Hyderabad,
Money Transfer/NEFT/RTGS (Inter-Bank Transfer), Treasurer, Indian Geophysical Union, State Bank of India, Habsiguda Branch,
Habsiguda, Uppal Road, Hyderabad- 500 007
A/C: 52191021424, IFSC Code: SBIN0020087, MICR Code: 500002318, SWIFT Code: SBININBBHO9.
For correspondence, please contact, Hon. Secretary, Indian Geophysical Union, NGRI Campus, Uppal Road,
Hyderabad - 500 007, India; Email: igu123@gmail.com; Ph: 040 27012332

ISSN: 0257-7968 (Clarivate Analytics)
ISSN: 0971-9709 (NISCAIR)
Approved as bimonthly ESCI journal by Clarivate Analytics
Cited in Indian Citation Index (ICI), New Delhi
Evaluated by NISCAIR, New Delhi
UGC Approved Journal

CONTENTS

Research Articles

INVITED ARTICLE

2026 Nepal Floods caused by bedrock failure north of Langtang Lirung peak

R. K. Chadha **441**

Identification of fracture-related discontinuities using integrated seismic attribute analysis in the Krishna-Godavari Basin, India

Pelluri Latha Sri* and Nittala Satyavani **451**

Integrated well-log analysis and 3D transient modeling for optimizing reservoir flow in CO_2 storage settings

Tanmoy Chetia, Pallavi Banerjee Chattopadhyay*, Aakash Jaiswal, Nimisha Vedanti, Ravi Shankar Dubey, and A. D. Sarath **462**

Magnetic methods in delineation and depth assessment of Banded Iron Formation: A case study from Sonbhadra District (Uttar Pradesh), India

Gautam Kumar*, C. B. Tiwari, S. P. Chaubey and Tashmeet Kaur **474**

Assessing the impact of saline water intrusion, aquaculture practices and oil–gas operations on groundwater in the Godavari Delta, Andhra Pradesh, India

B. Naga Jyothi*, GunnamVenkataRatnalu, K. BhimaRaju, P.V. Nagamani, G. Udaya laxmi **489**

District level long range forecast of rainfall during Monsoon

Onkari Prasad*, K. Prasad and O. P. Singh **503**

Rare Earth Element (REE) geochemistry of placer ilmenites from the east coast of India: Implications for provenance and genetic parentage

Mokka Jagannadha Rao*, G. Sandeep and J. Venkataramana **520**

Performance of CMIP6 climate models for temperature and precipitation over the Northwest Himalaya

Vartika Sharma*, Veluswamy Venkatramanan, Peeyush Gupta, M. S. Shekhar, R. Bhatla and Jashandeep Singh **528**

J. Ind. Geophys. Union, 30(6) (2026), 441-450
http://doi.org/10.71122/JIGU.30(6)2026.0044

INVITED ARTICLE

2026 Nepal Floods caused by bedrock failure north of Langtang Lirung peak

R. K. Chadha
Former Raja Ramanna Fellow, CSIR-National Geophysical Research Institute, Hyderabad-500007, India
Corresponding author: rajen0555@gmail.com

ABSTRACT

On 26 August 2026, a catastrophic flash flood tore through the Himalayan border region of Nepal and Tibet, unleashing a devastating wall of water and rock debris that swept away entire villages along the narrow Bhotekoshi and Trishuli river corridors downstream beyond 125 km. The flood destroyed several hydropower projects, bridges, houses, and roads, leaving over 1,300 dead and 5,000 missing. Since the region had experienced a similar flood in July 2025, triggered by the breaching of a glacial lake upstream of the Lhende Khola in Tibet, this event was initially assumed to be another Glacial Lake Outburst Flood (GLOF). However, satellite imagery of the region revealed a substantial bedrock failure with an overriding glacier in the hanging valley north of Langtang Lirung peak in central Himalaya. The bedrock failed at a height of 5,200 m and fell violently 1,200 m down into another glacier on the valley floor. The event was unprecedented in scale, speed, and mechanism, releasing energy so immense that it was recorded on global seismic stations and classified by the U.S. Geological Survey as a M 5.2 landslide rather than a tectonic earthquake. The mass of rock and ice that fell into the valley transformed into a rock-ice avalanche that surged into the Lhende Khola, 6 km downstream. As the ice melted due to friction with the rolling rock and sediments, and additional water entrained, the flow evolved into a debris flow, racing down the narrow canyon to the Gyirong Port (Nepal–Tibet check post) at Rasuwagadhi, located 22 km from the bedrock collapse. This distance was covered in about 7 minutes, at an ultra-fast speed exceeding 170 km/h. The high velocity and height of the debris flow toppled and destroyed the Gyirong Port complex completely. This paper presents an in-depth analysis of the disaster, examining the role of tectonics, geological structures, rock types, and geomorphology in triggering the catastrophic debris flow Disaster in Nepal. The study traces the debris flow from its source area to over 250 km downstream in Uttar Pradesh and Bihar in India, where a lot of mud and human remains were recovered in the Gandak River.

Keywords: 2026 Nepal floods, Nepal-Tibet border, Rasuwagadhi, Himalaya, Langtang glacier, debris flow, bedrock failure, ultra-fast speed

INTRODUCTION

The Nepal-Tibet border check post at Rasuwagadhi was struck without warning by a catastrophic flash flood on 26 August 2026 at 8:44 a.m. Nepal Standard Time (NST). The debris flow toppled and destroyed the Gyirong Port building and the entire complex, sweeping away people, electric vehicles awaiting export from China to Nepal, trucks and buses transporting goods and pilgrims to China and Mount Kailash. The event was unprecedented in its geographic scale, structural mechanism, and destructive velocity. It was triggered by the failure of highly fractured bedrock beneath an overriding glacier in a hanging valley north of Langtang Lirung peak in the central Himalaya. The bedrock failed at an elevation of about 5,200 m and plunged 1,200 m into the valley below, colliding with another glacier on the floor and generating a violent rock-ice avalanche that surged toward the Lhende Khola valley.

As the ice melted through gravitational potential energy conversion to motion, frictional heating and water entrained from valley sediments and existing moraine deposits, the avalanche evolved into a super mobile debris flow. It raced through the narrow Lhende Khola, Bhotekoshi, and Trishuli river corridors, destroying settlements and infrastructure along its path. The debris flow traveled 22 km to Gyirong Port at the confluence of the Lhende Khola and Bhotekoshi River in about 7 minutes, corresponding to an average speed of more than 170 km/h. The combined death toll exceeded 1,300, with the vast majority of fatalities occurring in Nepal, while more than 5,000 people remained missing. The extreme hydromorphological dynamics of the flow transported human remains more than 150 km downstream, demonstrating its extraordinary sediment-transport capacity and extensive spatial footprint. The principal impact zone extended from Gyirong Port to Devighat along the Bhotekoshi and Trishuli river corridrs, where much of the debris was deposited or temporarily confined (Figure 1).

The high-energy flood, laden with sediment and debris, continued downstream for more than eight hours and traveled over 125 km, altering river channels and burying villages beneath mud, slurry, and rock. At several locations, water levels in the Bhotekoshi and Trishuli valleys rose by 7 to 9 m, washing away houses, people, bridges, infrastructure, and hydropower facilities. The flood also inundated tunnels and damaged roads and settlements as far downstream as Devghat Dham and beyond, where the energy of the primary surge gradually dissipated. More than 700 human remains were recovered from Chitwan and Nawalparasi along Gandaki, also known as the Narayani River, downstream of the Trishuli. About 17 bodies were reportedly recovered from the Gandak River in Uttar Pradesh and Bihar, India, more than 250 km from the source area.

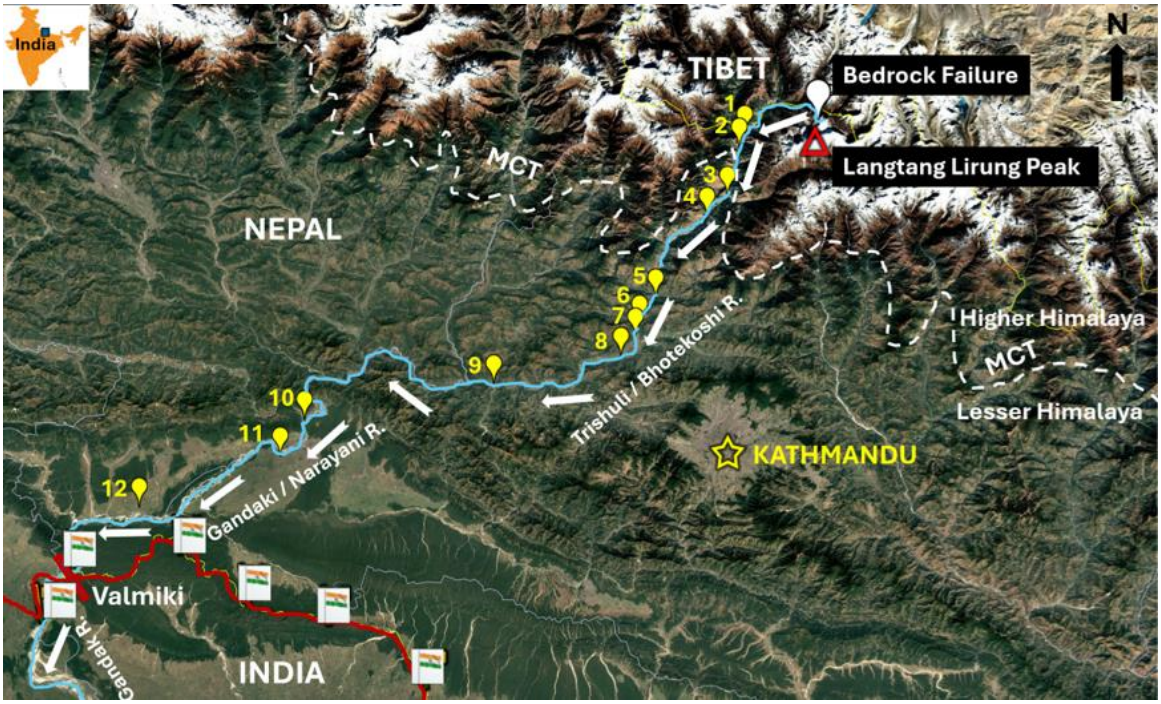


Figure 1. Shows the route of the debris flow from source of bedrock failure downstream. Blue line is Trishuli River which is known as Bhotekoshi in upstream Tibet. White balloon is bedrock failure site in the hanging valley glacier. Red triangle is Langtang Lirung peak. Yellow balloons are locations severely affected during the floods. 1: Gyirong Port (Nepal-Tibet border, Rasuwagadhi), 2: Timure, 3: Syapru Besi, 4: Dhunche, 5: Betrawoti, 6: Nuwakot, 7: Trishuli Bazaar, 8: Devighat, 9: Malekhu, 10: Devghat Dham, 11: Chitwan, 12: Nawalparasi. MCT (Main Central Thrust), separating Lesser and Higher Himalaya is shown as broken white line.

The bedrock and glacier collapse coincided with a seismic event that U.S. Geological Survey (USGS) catalogued as a M 4.4 earthquake at 8:37 a.m. NST on the same day. The event was located at a depth of 0.0 km, 55 km northwest of Kodārī, Nepal (28.271°N, 85.515°E), near the Nepal–Tibet border (https://earthquake.usgs.gov/earthquakes/). However, after further analysis of data from nearby seismic stations, long-period seismic waves, and satellite imagery, the event was reclassified as a M 5.2 landslide. The GFZ Helmholtz Centre for Geosciences in Potsdam, independently reported the event as a M 5.7 landslide. The seismic energy was therefore attributed to the impact of the collapsing bedrock and overlying ice on the valley floor, followed by a rock-ice avalanche, rather than to a tectonic earthquake.

This paper analyses the roles of regional tectonics, geological structures, lithology, and geomorphology in the bedrock failure that initiated the rock-ice avalanche. It further examines how the avalanche transformed into a catastrophic debris flow, ultimately producing unprecedented flooding and widespread destruction in Nepal.

BEDROCK FAILURE

The Langtang Lirung region, situated north of the Main Central Thrust (MCT), comprises high-grade metamorphic and intrusive rocks belonging to the Higher Himalayan Crystalline Sequence (HHCS). The MCT separates the Higher Himalaya from the Lesser Himalaya (Reddy et al., 1992). In this region, the dominant foliation of the HHCS changes orientation from WNW–ESE to N–S or NNE–SSW (Takagi et al., 2003). The main rock type is the gneiss, a coarse-grained metamorphic rock, characterized by distinct alternating light and dark-coloured mineral bands, including Augen granite gneiss exposed in the upper reaches of the valley. High Himalayan leucogranites and younger tourmaline-bearing granite intrusions, are also widespread. The coarse-grained leucogranites that occurs as sills and dykes are particularly susceptible to weathering along joints and fractures, thereby contributing to rock-mass weakening and slope instability (Searle et al., 1997).

Figure 2 shows the fault scarp of the bedrock failure, exposing a sharply layered sequence of pink, black, and white gneissic bands dipping more than 45° to the southwest. The pink layers are felsic bands composed primarily of quartz–feldspathic segregations. Their distinctive colour reflects a high concentration of potassium-rich feldspar (K-feldspar), such as microcline or orthoclase, intergrown with quartz. By contrast, the dark layers are mafic bands enriched in iron and magnesium-bearing minerals that remained relatively refractory during migmatization.

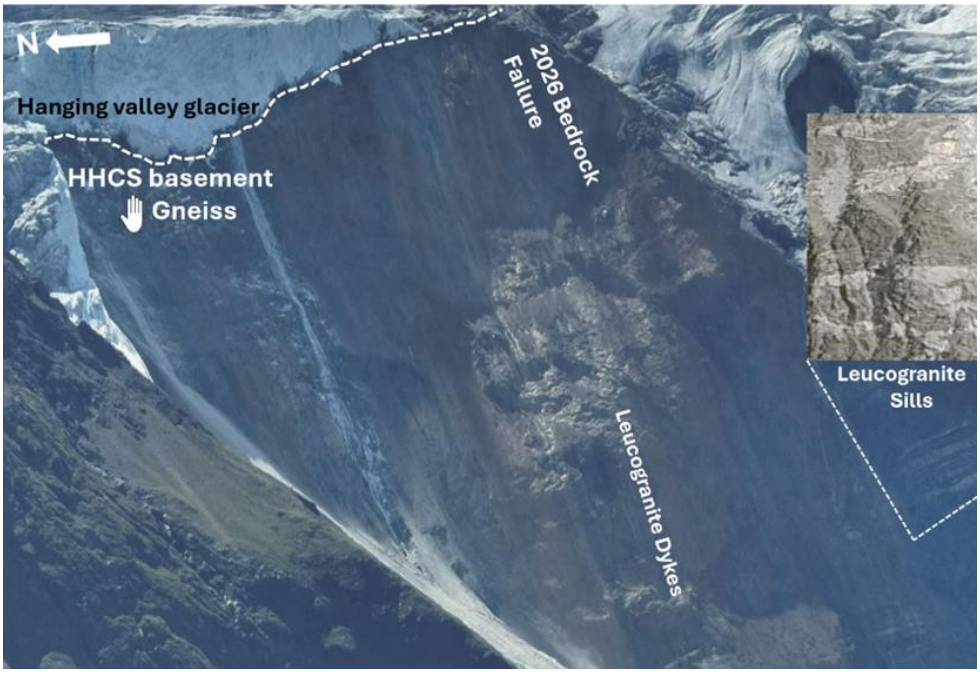


Figure 2. Fault scarp of the bedrock failure with overriding glacier in the Higher Himalayan Crystalline Sequence (HHCS). The felsic and mafic bands in gneisses are pink and black or greenish black in colour, which dip >45^0 SW. The leucogranites occur both as dykes and sills. Inset shows an enlarged portion of leucogranite sills cross-cutting the general foliation of gneiss in NNE-SSW direction.

These dark layers are dominated by biotite, together with other high-grade metamorphic minerals characteristic of the Langtang gneisses, including garnet, sillimanite, and tourmaline (Jain et al., 2018).

White intrusive bands of leucogranites occurring as sills and dykes either cut across or running parallel to the regional fabric. These bands contain mostly tourmaline-muscovite and associated quartz-feldspar veins. They were formed when highly fluid, silica-rich melts were injected into fractures and foliation planes within the older gneissic host rock (Searle et al., 1997; Enos, 2017). The sharp lithological contrasts, pervasive foliation, intersecting fractures, and brittle leucogranitic intrusions, especially into the biotite rich layers, likely contributed to the structural weakening of the slope and influenced the initiation and propagation of the bedrock failure.

Figure 3a shows a highly brecciated zone within the mafic gneiss layer exposed along the fault scarp along which the basement rock failed. Figures 3b and 3c**,** provide close-up views of the pumice-like microbreccia and slickenside surfaces preserved within this intensely deformed mafic band. Similar structures have been documented by Schramm et al. (1998) in the Tsergo Ri slope failure, 10 km southeast of Langtang Peak. Masch and Preuss (1977) and Heuberger et al. (1984), attributed the formation of such microbreccias and slickensides to frictional fusion during rapid fault movement. Weidinger et al. (1996) proposed that pre-existing lithotectonic fault planes, slickenside surfaces, and discordant leucogranite intrusions within the mafic gneiss bands, played an important preparatory role in weakening of the basement rock and promoting slope failure in the Langtang region.

DEBRIS FLOW

Figure 4 illustrates the debris-flow pathway from its source in the Langtang Valley, through the Lhende Khola, to the Gyirong Port check post at Rasuwagadhi on the Nepal-Tibet border, and onward into the Bhotekoshi and Trishuli river systems. The mass of bedrock and ice that collapsed 1,200 m into the Langtang Valley, traveled approximately 22 km to the Gyirong check post in just 7 minutes, corresponding to an average speed of more than 170 km/h. The exceptional velocity and mobility of the debris flow, suggest that substantial melting

and water entrainment occurred before it reached the confluence with the Lhende Khola, transforming the initial rock-ice avalanche into a super mobile fluid debris flow. At the confluence, the impact was sufficiently powerful to drive the flow up to 400 m up the opposite valley slope before it was redirected downstream. This interpretation is supported by post-impact erosion and depositional features, preserved on the opposing hillslope at the junction of the flow from the Langtang Valley glacier and the Lhende Khola.

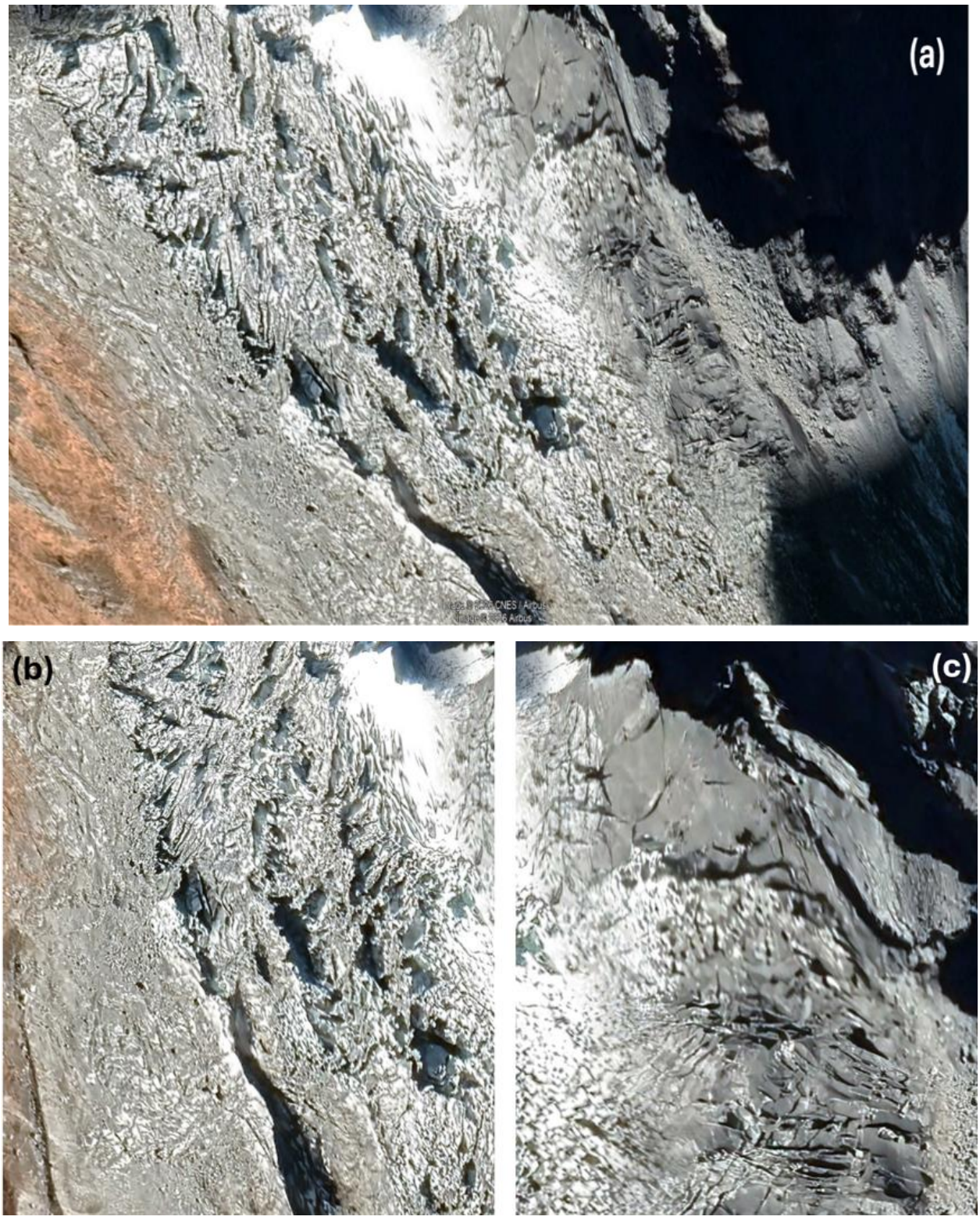


Figure 3. **(a)** A horizon showing pumice like microbreccia and slickensides surfaces in the highly deformed migmatites and leucogranites in mafic band in gneiss. **(b)** A closeup of pumice microbreccia and **(c)** Pre-existing lithotectonic fault planes and slickensides surfaces in biotite rich dark bands in gneiss. These structures functioned as preparatory causal factors for the sliding planes.

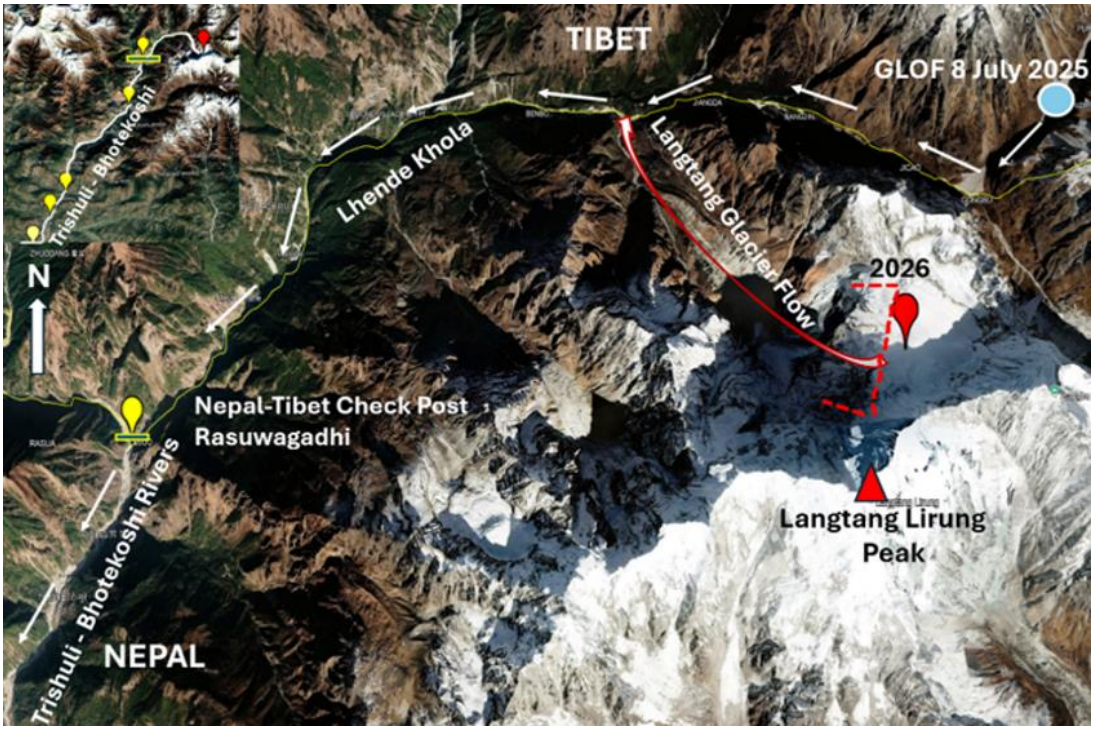


Figure 4. The route of debris flow from the source (Red balloon) to Nepal-Tibet Gyirong Port check post (Yellow balloon) in 7 minutes and further downstream Bhotekoshi and Trishuli rivers. Red arrow shows flow direction in the Langtang valley and white in Lhende Khola and further downstream. Red broken line indicates the glacier collapse boundary. The location of a GLOF in Tibet that affected the same rivers valleys in 2025 is shown as blue circle.

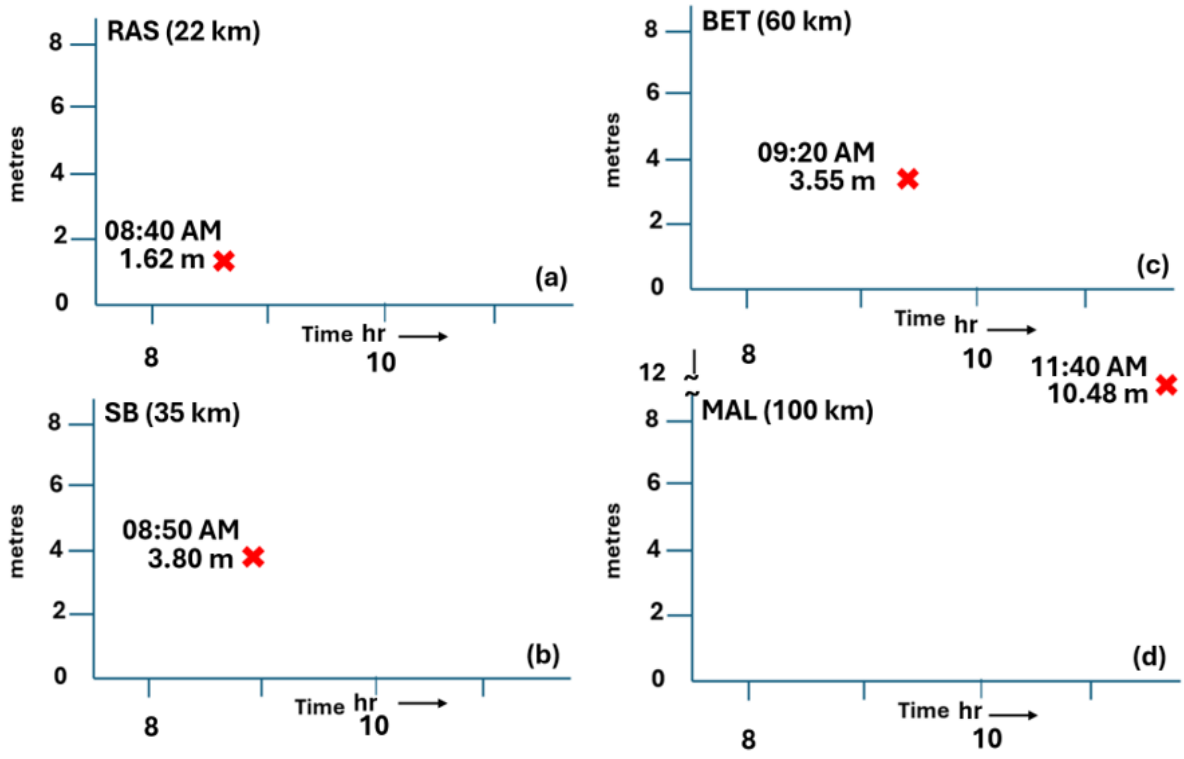


Figure 5. Last recorded readings at four river gauge stations from Nepal-Tibet Gyirong Port border check post at Rasuwagadhi. RAS: Rasuwagadhi, SB: Syapru Besi, BET: Betrawoti, and MAL: Malekhu (See Figure 1 for locations). Distances are from source of bedrock collapse in Langtang valley. Red cross symbol is the last river gauge reading before destruction.

Downstream of the Lhende Khola confluence, the debris flow accelerated through a confined canyon. The narrow valley walls restricted lateral spreading, causing the flow depth to increase substantially, reaching locally estimated heights of up to 100 m, at places, before the surge reached the Gyirong Port check post. This vertical confinement may have reduced relative basal drag and helped maintain the flow's extreme mobility, allowing the flood wave to attain a terminal velocity exceeding 170 km/h. The surge overtopped and destroyed the 60 to 80 ft high Gyirong Port main building and the entire complex, sweeping away people and infrastructure, including the Friendship Bridge, which had been reconstructed after a similar GLOF related flood from Tibet last year in July 2025. The last river gauge reading recorded at Rasuwagadhi before the flash flood struck was 1.62 m at 8:40 a.m. Four minutes later, the gauge was destroyed and washed away by the surge (Figure 5).

MECHANISM AND DOWNSTREAM IMPACT

The glacier ice overlying the failed bedrock likely played a central role in transforming the initial rock-ice avalanche into a fast-moving debris flow down the Lhende Khola valley. As the glacier and its underlying bedrock slipped downslope, gravitational potential energy was rapidly converted into kinetic energy, fragmenting and pulverizing the rock-ice mass. This fragmentation increased the contact area between rock and ice, enhancing frictional heating and promoting rapid melting. The highly fractured bedrock, probably intensified this process by facilitating the entrainment of meltwater and the fluidization of the debris, thereby increasing its mobility. In addition, abundant ice preserved in the lower glacier on the valley floor and within morainic deposits left by earlier glacier retreat, would have supplied further meltwater and contributed to the rapid mobilization of the debris flow.

After destroying Gyirong Port, the debris flow surged downstream through the Bhotekoshi and Trishuli river systems (Figure 1). The first severely affected settlement was Timure, a border town approximately 3 km from the Nepal-Tibet border, along with nearby settlements on both sides of the river. The 111-MW Rasuwagadhi Hydropower Project and the Timure dry port, where transboundary cargo was stored, were completely washed away. In Timure Bazaar, located along Nepal's busiest trans-Himalayan trade route, hundreds of local residents and workers were reported missing.

Approximately 12 km further downstream, the market town of Syapru Besi, located near the confluence of the Bhotekoshi and Langtang rivers, was similarly devastated. The flow swirled through the confined valley, eroding sections of the mountainside and inundating settlements on both banks. The old town on the eastern bank and the newer main street on the western bank with dozens of local businesses and hotels serving tourists were swept away. The last river-gauge reading at Syapru Besi was 3.80 m at 8:50 a.m., after which the gauge was destroyed. The flood then entered Nuwakot District after sweeping away dams, bridges, and a hydropower project. Residents were stranded, while workers at the upstream power plant were trapped inside tunnels. At Betrawoti, the last river-gauge reading showed 3.55 m at 9:20 a.m.; the gauge was subsequently destroyed. Between Betrawoti and Trishuli Bazaar, enormous boulders carried within the debris flow struck and demolished multistorey buildings and foundations of the bridges on an unprecedented scale. The corridor extending downstream to Devighat experienced some of the most severe impacts, with river levels rising by 7 to 9 m in places and extensively scouring the valley slopes. The affected corridor had also suffered substantial damage during 2015 M 7.8 Gorkha earthquake in Nepal. The earthquake triggered an ice avalanche on the southern slope of the Langtang Lirung peak and buried people in the Trishuli River corridor and caused extensive damage to structures. Figure 5 presents the last recorded river-gauge readings at few sites to 100 km distance in Bhotekoshi and Trishuli rivers before the observation stations were flooded.

As the river gradient decreased and the flow entered broader valleys, the flood velocity gradually declined. Nevertheless, the debris current retained sufficient energy and carrying capacity to transport human remains to over 150 km downstream. More than 700 remains were recovered from muddy debris deposits in Chitwan and Nawalparasi along the Gandaki River, also known as the Narayani River, downstream of Devghat Dham (Figure 1). After approximately eight hours of extreme devastation, the primary flood surge finally dissipated at around 4:30 p.m.

DISCUSSION

The 2026 Nepal floods were initially assumed to have been caused by another Glacial Lake Outburst Flood (GLOF), as the region had experienced a similar avalanche-driven flood along the Lhende Khola, Bhotekoshi, and Trishuli rivers in July 2025, following the breach of a glacial lake upstream in Tibet (Alexander Klaus et al., 2026). However, the first evidence of a different mechanism emerged from satellite imagery, which revealed the rapid failure of a glacier-bearing slope in a hanging valley on the northern flank of Langtang Lirung peak in the central Himalaya, 60 km north of Kathmandu. This event is similar to the 2021 disaster in

Chamoli district, where a massive rockslide of ~ 23 million cubic meter volume containing base rock, ice and snow broke off the northern slopes of the Trishul mountain range and flowed into the Ronti Gad valley located 1.5 km downstream of Ronti Glacier snout (Chadha, 2023). Nepal disaster looks to be at least 5 to 6 times bigger than Chamoli involving roughly 150 million cubic metres of rock and ice glacier.

The U.S. Geological Survey (USGS) initially catalogued the event as a M 4.4 earthquake at 8:37 a.m. NST, near the location of the bedrock collapse. Following analysis of long-period seismic waves, data from regional seismic stations, and satellite imagery, the event was reclassified as a M 5.2 landslide, rather than a tectonic earthquake. The GFZ German Research Centre for Geosciences in Potsdam, independently reported it as a M 5.7 landslide. The detection of the signal at distant seismic stations, indicates that the impact of the collapsing bedrock and overlying ice on the valley floor released substantial seismic energy, equivalent to that generated by an earthquake of M > 5. Subsequent analysis indicated that the glacier-bearing bedrock, descended approximately 1,200 m into the valley, generating an ice-rock avalanche that transformed into a highly mobile debris flow. According to CCTV footage, the flow reached the Gyirong Port complex at the Nepal–Tibet border at 8:44 a.m.

This observation raises two important questions. First, how could the debris flow travel 22 km in just 7 minutes, corresponding to an average speed exceeding 170 km/h? Second, what was the source of the large volume of water required to generate a debris flow that reportedly reached heights of up to 100 m in the Lhende Khola valley at a few places before overtopping and destroying the Gyirong Port complex? The exceptionally short travel time and extreme speed challenge the initial hypothesis that the rock-ice avalanche temporarily blocked Lhende Khola at the junction with Langtang valley, followed by a sudden breach of the impounded body of water.

Based on the evidence and data currently available from open sources, a possible interpretation is proposed for the sequence of processes that began with bedrock failure, progressed through a solid rock–ice avalanche, and ultimately transformed into an ultrafast, highly bulked, and hypermobile debris flow. Figure 6 presents a Google Earth image of the area acquired on 2 January 2026, in which possible precursory signs of bedrock instability are clearly visible on the creeping glacier surface in the Langtang Valley. Although these features may represent the preparatory phase of the failure, the underlying deformation and associated precursory processes are likely to have begun much earlier. A second Google Earth image, acquired on 6 January 2026, shows a prominent glacier occupying the valley floor, with apparent meltwater drainage extending downstream into a broader valley. The valley also contains morainic deposits that record earlier glacial retreat (Figure 7). So, as of 15 January 2026, there was enormous amount of water available in the Langtang glacier (Upper Glacier) as well in the Lower Glacier (LG) at the bottom of the valley (Figure 8).

Proposed failure and flow-transformation sequence

The gradual melting of glaciers in the hanging valley and the northern face of the Langtang Lirung mountain slope, resulted in persistent ice accumulation that infiltrated fractures and fissures within the gneissic bedrock. Over time, this infiltration increased the pore-fluid pressure along pre-existing shear zones. Castle et al. (1980) have demonstrated that the elevated pore-fluid pressure can promote slip on faults that are already close to failure under the prevailing tectonic stress conditions. Although monsoon rainfall in the region was reportedly normal, precipitation between June and August 2026, contributed additional infiltration leading to thawing of ice in the fractures and fissures, especially in the biotite rich shear zones in gneiss. This process reduced effective normal stress and shear resistance along steeply southwest-dipping planes inclined at more than 45° within the mafic gneissic bands. On 26 August 2026, the highly fractured bedrock and overlying glacier, ultimately failed along a southwest dipping fault plane in the shear zone. The fractured mass then plunged into the valley below crushing the lower glacier in the valley. The impact of the falling rock and ice on the lower glacier likely promoted rapid ice melting through the conversion of gravitational potential energy into kinetic energy, frictional heat, and mechanical crushing. The resulting thermal heat and mechanical processes, flash-melted a substantial proportion of the ice into liquid water, accelerating the rock–ice avalanche and enabling it to entrain additional water and sediment from morainic deposits on the valley floor.

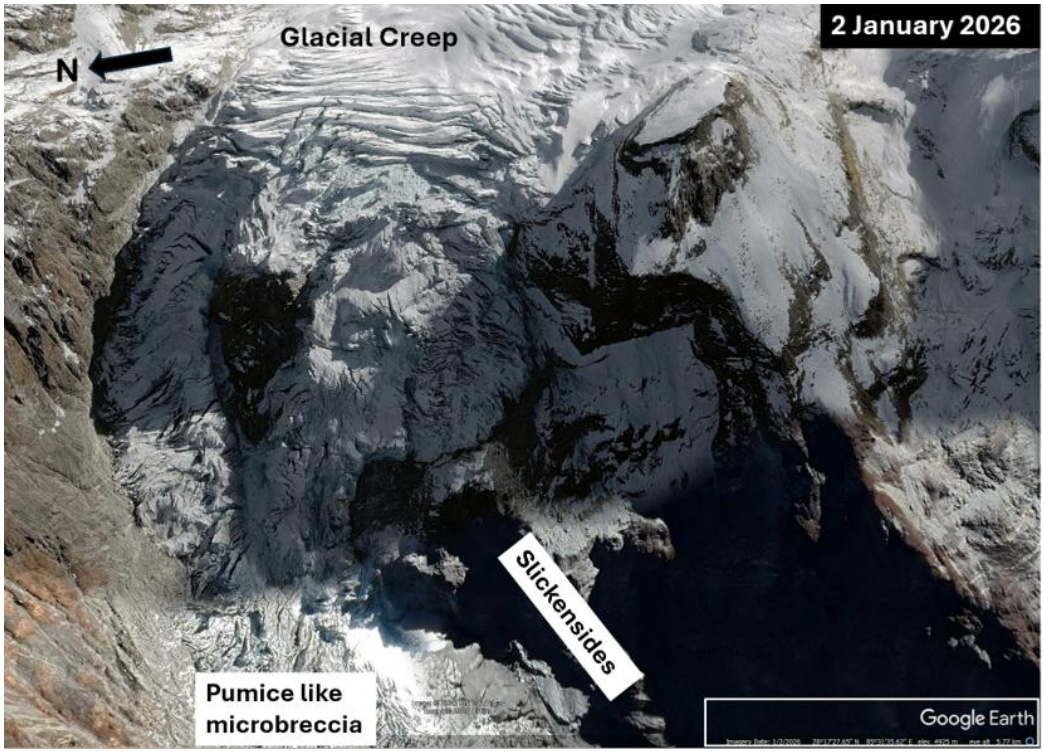


Figure 6. Google Earth image on 2 January 2026. Clear signs of glacier creep are visible in the Langtang hanging valley six months prior to the bedrock failure. A shear zone in the biotite rich mafic bands in gneisses, shows presence of pumice like microbreccia with adjacent slickensides surfaces. Clear evidence of possible shear planes along which the bedrock failed.

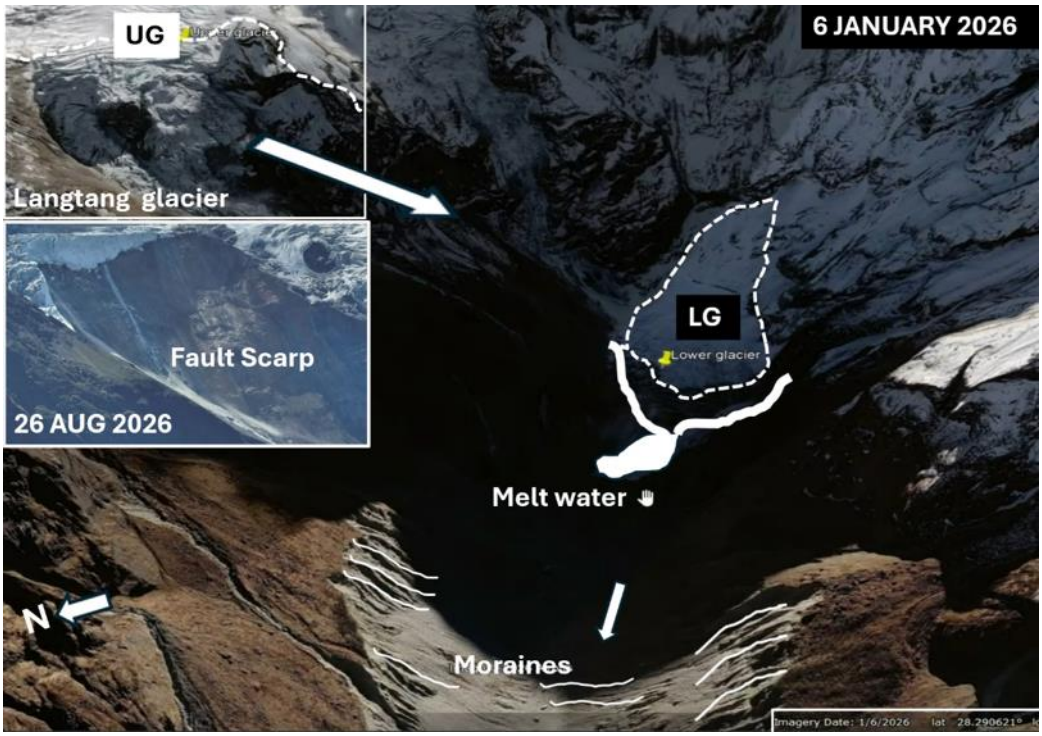


Figure 7. Google Earth image on 6 January 2026. Two hanging glaciers, one in the upper valley that failed with underlying bedrock and a lower glacier in the valley bottom with some pockets of melted water. UG: Upper Glacier and LG: Lower glacier. Moraine deposits in the valley indicate the glaciers in the past.

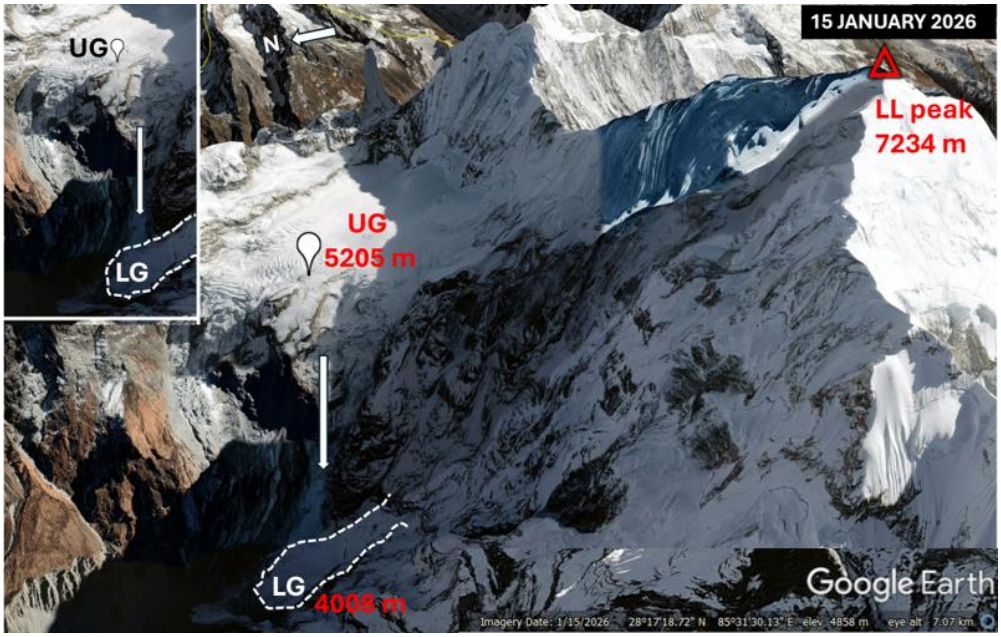


Figure 8. A close up of Google Earth image on 15 January 2026 viewing from west. Glacial creeps on the UG (Upper Glacier) and ice melting on the northern face of Langtang Lirung Peak and a growing LG (Lower Glacier) are clearly seen.

As the avalanche continued grinding and deforming during its descent through the Langtang Valley, further water was generated and entrained. The initially solid rock-ice avalanche therefore progressively transformed into a super mobile debris flow before reaching the Lhende Khola. The approximately 6-km distance between the bedrock-collapse site and the Lhende Khola junction was traversed in about 2 minutes, indicating exceptionally high super mobility due to almost complete melting of ice into liquid water. At the confluence, the flow retained sufficient momentum to run about 400 m up the opposite valley slope before being redirected downstream which already had some water flowing in the river due to monsoon. A freshly eroded trimline and associated impact marks at the junction, provide field evidence of this extreme run-up.

Downstream of the Lhende Khola confluence, the debris flow entered a confined canyon and continued to accelerate while entraining material and water from the valley sides. The narrow valley walls restricted lateral spreading and promoted vertical bulking, with flow heights locally reported to have reached up to 100 m at some locations before the surge arrived at the Gyirong Port check post. This confinement may have reduced relative basal drag and helped the flow retain its exceptional high mobility, ultimately reaching an estimated velocity of more than 170 km/h. The surge overtopped and destroyed the 60-80 ft high main building of Gyirong Port and other structures in the complex. It swept away people and infrastructure, including the Friendship Bridge, which had been reconstructed following a GLOF related disaster last year in July 2025. The super mobile debris flow continued for more than 125 km downstream and took eight hours till the primary surge dissipated as the gradient decreased. The proposed sequence remains provisional and should be tested against detailed field evidence, including rupture-surface mapping, sedimentological analysis, rock-ice volume estimates, flood-stage reconstruction, and numerical debris-flow modelling.

CONCLUSIONS

The 2026 Nepal floods were initiated by bedrock failure in a hanging valley north of Langtang Lirung peak. The collapse generated a rock-ice avalanche that rapidly transformed into a highly mobile debris flow travelling at exceptionally high velocity. The principal scientific uncertainty concerns the relative contributions of frictional melting, direct displacement of river water, entrainment of valley-floor ice and sediment, and any pre-existing or temporarily stored water. Resolving these questions will require detailed field mapping, high-resolution satellite analysis, digital elevation-model differencing, sedimentological investigations, hydrological reconstruction, and numerical modelling of flow initiation and downstream propagation.

The disaster demonstrates that Himalayan hazards must be understood as interconnected processes rather than isolated phenomena, especially amidst growing climate change evidence. Effective protection of downstream communities will require integrated multi-hazard mapping, risk-sensitive land-use planning, resilient infrastructure, transboundary

data sharing, continuous monitoring of glaciers and unstable slopes, automated warning dissemination, and regular evacuation exercises. These measures are particularly important for high-magnitude events, that may provide communities with only a few minutes of warning. An integrated, basin-wide, and transboundary risk-management framework is therefore essential for reducing future human and economic losses across the Himalayan region.

Acknowledgements

The information and data used in the preparation of this manuscript is mostly from the open source available on different internet and social media platforms. Google Earth images are extensively used to analyse the available data. Prof. Shawn Willsey inputs were helpful and gratefully acknowledged. The picture of the fault scarp is by Prof. Guoxiong Zheng and is gratefully acknowledged. The Author thanks the Editor for fine tuning the manuscript.

Author credit statement

The research work is conceived, analyzed, interpreted and the manuscript is prepared by the author.

Data availability

The paper is based on data that is available in the open source on various platforms including media and Google Earth. Earthquake data used in the study is from the open source of the USGS website (www.usgs.gov) and is available at https://earthquake.usgs.gov/earthquakes.

Compliance with ethical standards

The author declares that he has no conflict of interest and adheres to copyright norms.

References

Alexander Klaus, Schmidt, S., Florchinger, V., Lama, T. and Nüsser, M., 2026. Before and after the 2015 disaster: Development trajectories in the Himalayan riskscape of Langtang from 1949 to 2025. Progress in Disaster Science (Elsevier), 30, 100585, https://doi.org/10.1016/j.pdisas.2026.100585.

Castle, R.O., Clark, M.M., Grantz, A. and Savage, J.C., 1980. Tectonic state: its significance and characterization in the assessment of seismic effects associated with reservoir impounding. Eng. Geol., 15, 53–103.

Chadha, R.K., 2023. 2022. Joshimath Subsidence. J. Geol. Soc. Ind., 99, 289, https://doi.org/10.1007/s12594-023-2298-9

Enos, P., 2017. Sedimentary Structures Preserved in Greater Himalayan Gneiss: Phenomenon or Fantasy? J. Geology, 125 (2), 125–139, https://doi.org/10.1086/690211.

Heuberger, H., Masch, L., Preuss, E. and Schro¨cker, A., 1984. Quaternary landslides and rock fusion in Central Nepal and in the Tyrolean Alps. Mountain Res. Dev., 4, 345–362.

https://earthquake.usgs.gov/earthquakes/map/?extent=7.10089, 150.73242&extent=60.37043,-39.19922

Jain, A.K., Sushmita, Singh, S. and Mukherjee, P.K., 2018. Migmatization, Granite Generation and Melt Accumulation in the Himalayan Orogenic Channel, Central and Eastern Bhutan. Curr. Sci., 114 (09), 1903, DOI: 10.18520/cs/v114/i09/1903-1912.

Masch, L. and Preuss, E., 1977. Das Vorkommen des Hyalomylonits von Langtang, Himalaya, Nepal. N. Jahrb. Min. Abh. 129, 292–311.

Reddy, S.M., Searle, M.P. and Massey, J.A., 1992. Structural evolution of the high Himalayan Gneiss sequence, Langtang Valley, Nepal. In: Treloar, P.J., Searle, M.P. (Eds), Himalayan Tectonics. Geol. Soc. Special Publ., no. 74, pp. 375–389.

Schramm, J.M., Weidinger, J.T. and Ibetsberger, H.J., 1998. Petrologic and structural controls on geomorphology of prehistoric Tsergo Ri slope failure, Langtang Himal, Nepal. Geomorphology, 26, 107–121.

Searle, M.P., Parrish, R.R., Hodges, K.V., Hurford, A., Ayres, M.V. and Whitehouse, M.J., 1997. Shisha Pangma Leucogranite, South Tibetan Himalaya: Field Relations, Geochemistry, Age, Origin, and Emplacement. J. Geology, 105, 295–317.

Takagi, H., Kazunori, A., Sawaguchi, T., Kobayashi, K. and Awaji, D., 2003. Kinematic history of the Main Central Thrust zone in the Langtang area, Nepal. Tectonophysics, 366 (3), 151-163, DOI: 10.1016/S0040-1951(03)00052-0.

Weidinger, J.T., Schramm, J.-M. and Surenian, R., 1996. On preparatory causal factors, initiating the prehistoric Tsergo Ri landslide Langtang Himal, Nepal. Tectonophysics, 260, 95–107.

Received on: 14-09-2026; Revised on: 18-09-2026; Accepted on: 23-09-2026

J. Ind. Geophys. Union, 30(6) (2026), 451-461
http://doi.org/10.71122/JIGU.30(6)2026.0045

Identification of fracture-related discontinuities using integrated seismic attribute analysis in the Krishna-Godavari Basin, India

Pelluri Latha Sri[1,2*] and Nittala Satyavani[1,2]
[1]CSIR- National Geophysical Research Institute, Uppal Road, Hyderabad, 500007, India.
[2]Academy of Scientific and Innovative Research (AcSIR), Ghaziabad-201002, India.
*Corresponding author: lathasrilathapelluri@gmail.com

ABSTRACT

Accurate identification of fracture networks is essential for reservoir characterization and structural interpretation. However, subtle fractures are often difficult to detect on conventional seismic sections because of feeble discontinuity signatures and the presence of residual seismic noise. This study presents an integrated workflow for fracture detection, using a 3D seismic dataset from the Krishna-Godavari (KG) Basin, India. The workflow combines median-filter-based seismic conditioning, variance attribute analysis, and ant-tracking enhancement. A median filter was first applied to reduce random noise while preserving structural discontinuities. The conditioned seismic volume was then used to generate a variance attribute, which highlights the lateral changes associated with the faults and fractures. Thereafter, ant tracking was applied to the variance volume to enhance discontinuity connectivity and improve the delineation of fracture networks. The ant-tracking results reveal a vertically continuous seismic discontinuity, interpreted as a potential fracture-related feature. By examining the selected inline together with multiple crossline sections and time slices, the fracture feature has been traced from 1500 to 2200 ms, demonstrating strong structural continuity and connectivity showing from 1800 to 2100 ms. The results reveal multiple interconnected and laterally continuous fracture-related discontinuities within the seismic volume. Compared with conventional seismic interpretation, the proposed workflow provides improved visualization of subtle discontinuities and enhances the delineation of fracture corridors, conduit pathways, and structurally connected fracture networks.

Keywords: Ant-tracking; Median filter; Variance attribute; Fractures; Attribute analysis; Krishna-Godavari basin

INTRODUCTION

Fractures and faults beneath the surface, play a key role in controlling how fluids move through rock formations. In conventional oil and gas reservoirs, these structural features act as pathways along which hydrocarbons travel from source rocks into traps, and they also determine reservoir connectivity (Sibson, 1996; Aydin, 2000; Chopra and Marfurt, 2007a; Jibrin et al., 2009; Ngeri et al., 2015). In tight and shale gas reservoirs, where the rock itself has almost no ability to transmit fluid, natural fractures become the main flow pathways. Without a good understanding of the location and extent of fractures, it is very difficult to predict well performance or plan an effective development strategy (Xie et al., 2022; Zhao et al. 2023). Therefore, the accurate mapping of fracture networks assumes high priority at every stage of reservoir investigation.

Seismic attributes are quantitative measures derived from seismic data, and they enhance the interpretation of subsurface geological features. The variety of available attributes has increased significantly over the past five decades (Sheriff, 2002; Chopra and Marfurt, 2005), making them indispensable in structural interpretation from seismic data. Early seismic attributes primarily focused on amplitude and travel time measurements. With advances in seismic interpretation, a wide range of geometric attributes has been developed, including coherence, curvature, variance, and chaos. These attributes enhance variations in reflector geometry and continuity, making them particularly useful for identifying faults, fractures, and other structural discontinuities (Chopra and Marfurt, 2007b; Jaglan et al., 2015).

Seismic discontinuity attributes such as coherence, similarity, semblance, and variance are widely used for fault and fracture mapping because they highlight abrupt lateral changes in seismic reflections (Chopra and Marfurt, 2007a; Jaglan et al., 2015). Among these, variance is one of the most commonly used attributes as it measures the degree of dissimilarity between neighbouring seismic traces. High variance values typically correspond to faults, fractures, and other structural discontinuities, making the attribute particularly effective for identifying fault and fracture boundaries (Ngeri et al., 2015; Zhang et al., 2020). The characterization of fracture networks becomes particularly challenging in geologically complex settings, where fractures occur at multiple scales and orientations, and where residual seismic noise may reduce the visibility of discontinuity signatures (Nelson, 2001; Jaglan et al., 2015; Xie et al., 2022). The Ant tracking algorithm can be effectively used in such situations which aims at automated fracture deformation.

This method is based on ant colony optimization theory, originally proposed by Dorigo et al. (1996), which mimics the way real ants find food by laying chemical trails. In the seismic application, large numbers of virtual ants are placed inside a discontinuity attribute volume and guided to move along surfaces where the seismic signal is disrupted. As the ants repeatedly follow similar pathways, structurally connected features are progressively enhanced. This process improves the continuity and visibility of faults and fractures, enabling the extraction of sharper and more connected fracture networks than those obtained from conventional discontinuity attributes alone (Randen et al., 2001; Pedersen et al., 2002; Fehmers and Hocker, 2003). Previous studies

have also shown that ant tracking produces more reliable results when applied to pre-processed discontinuity attributes, such as variance, rather than directly to raw seismic amplitude data (Ngeri et al., 2015; Zhang et al., 2020). Nevertheless, the effectiveness of any ant-tracking workflow remains strongly dependent on the quality of the seismic data and the conditioning applied prior to attribute computation (Fehmers and Hocker, 2003; Ngeri et al., 2015). In the present study, we have used the ant-tracking algorithm on a variance attribute volume derived from median-filter-conditioned seismic data to delineate fracture corridors and structurally connected conduit pathways. Therefore, this study demonstrates an integrated workflow combining median-filter-based seismic conditioning, variance attribute generation, and ant-tracking for fracture characterization in the Krishna Godavari (KG) Basin.

The KG Basin is a major hydrocarbon-bearing basin along the eastern continental margin of India. Multiple tectonic events have generated complex fault and fracture networks that play a key role in fluid migration and reservoir connectivity. Although several studies have focused on structural interpretation, seismic attribute analysis, and reservoir characterization within the basin, the application of ant-tracking techniques for fracture characterization remains limited. Although median filtering, variance attributes, and ant tracking have individually been applied in previous seismic interpretation studies (Lavendra Kumar et al., 2015; Satheesh et al., 2025), their systematic application for fracture-related discontinuity characterization in the offshore KG Basin is not attempted. The present study applies median-filter-based seismic conditioning followed by variance attribute analysis and ant tracking to enhance and delineate subtle fracture-related discontinuities within the 3D seismic volume. The main contribution of this work is the demonstration of the workflow's applicability for mapping the spatial distribution and continuity of interpreted fracture corridors in the structurally complex KG Basin. An attempt is also made to (i) improve discontinuity detection through median-filter conditioning, (ii) delineate interpreted fracture-related discontinuities and evaluate their spatial continuity, and (iii) evaluate the effectiveness of the workflow for fracture characterization using conventional 3D seismic data.

STUDY AREA

The KG Basin (Figure 1) is a major peri-cratonic sedimentary basin located along the eastern continental margin of India (Rao, 2001). Covering both onshore and offshore regions, the basin forms one of India's most important hydrocarbon-producing provinces, containing thick sedimentary sequences ranging in age from Permian to Recent. Significant oil and gas discoveries within the basin have attracted considerable exploration interest, particularly in the offshore sector. The basin was formed during the Early Cretaceous breakup of India and East Antarctica and subsequently evolved through phases of rifting, thermal subsidence, and deltaic sedimentation (Rao, 2001; Subrahmanyam and Chand, 2006). As a result of this complex tectonic history, the KG Basin contains a wide variety of structural features, including horsts, grabens, growth faults, normal faults, shale diapirs, and associated fracture systems. The structural framework of the basin is predominantly controlled by NE-SW trending fault systems, which influence sediment deposition, reservoir architecture, and hydrocarbon migration (Sastri et al., 1974; Ramana et al., 2007). Previous studies have shown that fracture networks and fault-bounded conduits, provide important pathways for fluid migration and hydrocarbon accumulation in the offshore KG Basin (Collett et al., 2019, Latha Sri and Satyavani 2026). Seismic attribute studies have also demonstrated the presence of complex fault and fracture systems within the basin, highlighting the importance of detailed fracture characterization for understanding reservoir behaviour and fluid-flow pathways. Large growth faults developed within the Paleogene-Neogene succession, act as major structural elements, while associated secondary fractures and fault-related damage zones, enhance subsurface connectivity.

METHODOLOGY

Seismic data processing

Marine seismic data from KG basin is used in this study. The 3D volume covers an area of 147 sq.km acquired using four streamers with a streamer separation of 400 m and a shot interval of 25 m. Each streamer contained 204 receiver channels with a channel spacing of 25 m, resulting in a total of 816 receiver groups per shot. After acquisition, the seismic data were integrated with navigation information and processed to generate a 3D seismic volume. The final volume was binned with an inline spacing of 50 m and a crossline spacing of 12.5 m, comprising 160 inlines and 1450 crosslines. The data were processed using a conventional post-stack processing workflow to generate a high-quality stacked seismic volume suitable for attribute analysis. The processing sequence commenced with the loading of field seismic records and their integration with navigation information to establish accurate spatial positioning of the seismic traces. Data muting was performed to remove noisy traces and suppress unwanted arrivals occurring above the seafloor, thereby improving data quality prior to further processing. A band-pass filter with corner frequencies of 5-10-80-120 Hz was applied to attenuate low- and high-frequency noise and enhance the signal-to-noise ratio of the seismic data.

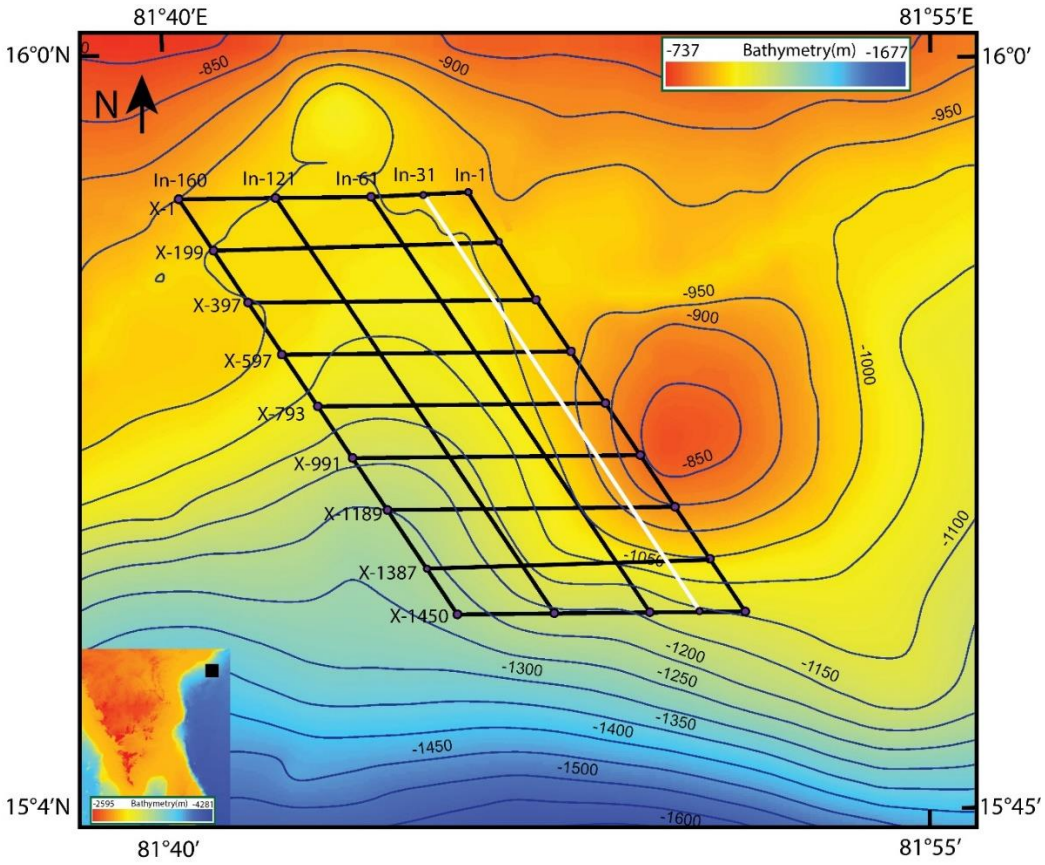


Figure 1. Study area showing the 3D seismic acquisition grid covering approximately 147 sq. km. Black lines represent the seismic survey layout, with inlines (1-160) at 50 m spacing and crosslines (1-1450) at 12.5 m spacing. The white color line is inline 31 considered for the ant-tracking analysis.

Velocity analysis was carried out on super gathers generated at 1 km × 1 km grid intervals throughout the survey area to estimate stacking velocities and characterize subsurface velocity variations. The derived velocity information was used to perform normal moveout (NMO) correction, ensuring proper alignment of reflection events across seismic gathers. Following NMO correction, common midpoint (CMP) traces were stacked to improve reflection continuity and further enhance the signal-to-noise ratio. The post-stack time migration was also carried out to move the dipping reflectors to their true locations. The resulting migrated stacked seismic volume served as the input dataset for subsequent seismic conditioning, interpretation and fracture characterization workflows.

Seismic data conditioning

Prior to attribute generation, seismic conditioning was performed to improve the quality of the stacked seismic volume and enhance the reliability of fracture detection (Fehmers and Hocker, 2003; Basir et al., 2013; Ngeri et al., 2015). A median filter was applied to the complete 3D seismic volume using an inline radius of 3 samples, crossline radius of 3 samples, and depth of 3 samples. The median filter is a non-linear filter that works by sorting the values within a defined window around each data point and replacing the central value with the median of that sorted list. This approach removes noise effectively without averaging nearby values together, which means it does not blur the sharp edges associated with faults and fractures, a known limitation of conventional smoothing filters such as Gaussian or mean filters (Sheriff, 2002; Jaglan et al., 2015). This characteristic makes it particularly suitable for fracture characterization, where preserving subtle discontinuity signatures is essential. The conditioned seismic volume was subsequently used as the input for variance attribute computation and ant-tracking analysis. By reducing noise while maintaining structural edges, the median-filtered data provided a more reliable basis for discontinuity enhancement and fracture-network delineation.

Variance attribute analysis

Variance is a geometric seismic attribute that quantifies the degree of dissimilarity between neighbouring seismic traces within a predefined analysis window (Chopra and Marfurt,

2007a; Zhang et al., 2020). Areas exhibiting high variance values correspond to abrupt lateral changes in seismic reflections and are commonly associated with faults and fracture-related discontinuities. Consequently, variance is widely used for structural interpretation and fracture characterization because of its ability to highlight discontinuity features that may not be visible on conventional seismic amplitude data. In this study, the variance attribute was computed from the median-filtered seismic volume using an inline range of 5 samples, crossline range of 5 samples, and vertical smoothing of 10 samples to enhance discontinuity signatures while minimizing the influence of random noise. The resulting variance volume provided a clear representation of fault- and fracture-related features by emphasizing reflector discontinuities and reducing reflector continuity. This enhanced discontinuity volume served as the primary input for the subsequent ant-tracking analysis, facilitating improved detection and delineation of fracture networks (Ngeri et al., 2015; Xie et al., 2022).

Ant tracking analysis

Ant tracking was applied to the variance attribute volume to enhance and extract seismic discontinuities associated with potential fault and fracture networks. Since variance highlights abrupt lateral changes in seismic reflections, areas with elevated variance values are interpreted as potential fault and fracture zones that serve as preferred pathways for ant propagation (Randen et al., 2001; Pedersen et al., 2002; Fehmers and Hocker, 2003). The ant-tracking algorithm is controlled by several parameters, including the initial ant distribution area, maximum deviation angle, step length, permitted off-track steps, required on-track steps, and stopping criteria (Xie et al., 2022). The parameters were selected through iterative testing of different parameter combinations, and the resulting volumes were evaluated for improvement in the continuity of subtle features by minimizing the spurious/ noise-related features. The final parameter configuration used in this study was: initial ant boundary 5, ant-tracking deviation 3, ant step size 3, illegal steps allowed 1, legal steps required 3, and stop criteria (5%). A custom ant-tracking configuration was employed to optimize the detection of subtle fracture-related discontinuities within the study interval. The tracking parameters were adjusted iteratively to improve discontinuity connectivity while minimizing the extraction of noise-related features. Essential work flow is as shown in (Figure 2).

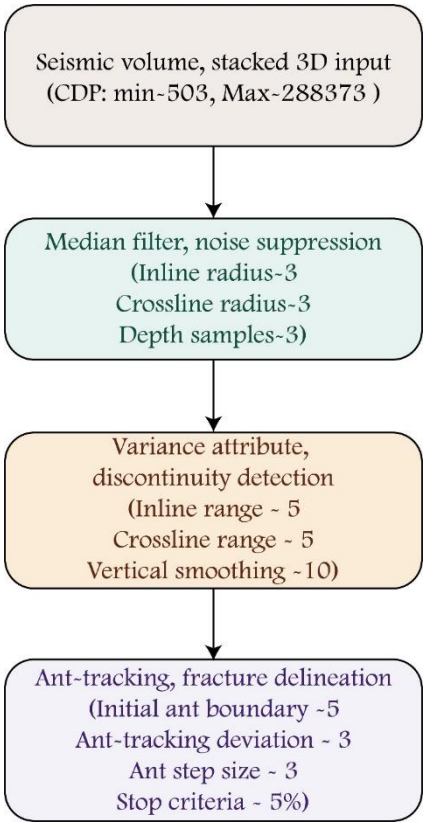


Figure 2. Schematic workflow for fracture detection from 3D seismic data

RESULTS

The workflow explained in the earlier sections was applied to the entire 3D time-migrated seismic volume. For detailed interpretation, Inline 31 was selected as a representative seismic section to illustrate the effect of each processing stage on fracture detection. The original seismic section (Figure 3) contains reflector discontinuities associated with structural features, but the presence of random noise reduces the visibility of subtle fracture-related signatures. Following median-filter-based conditioning (Figure 4), random noise is significantly reduced while reflector continuity and discontinuity boundaries are preserved, resulting in an improved seismic image for subsequent attribute analysis.

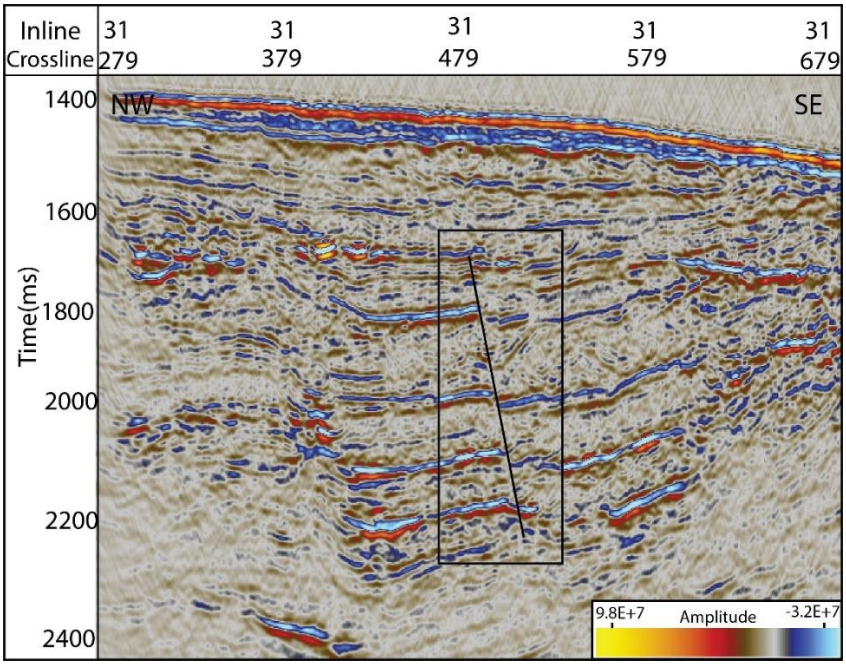


Figure 3. Processed seismic section along Inline 31 from the 3D seismic volume.

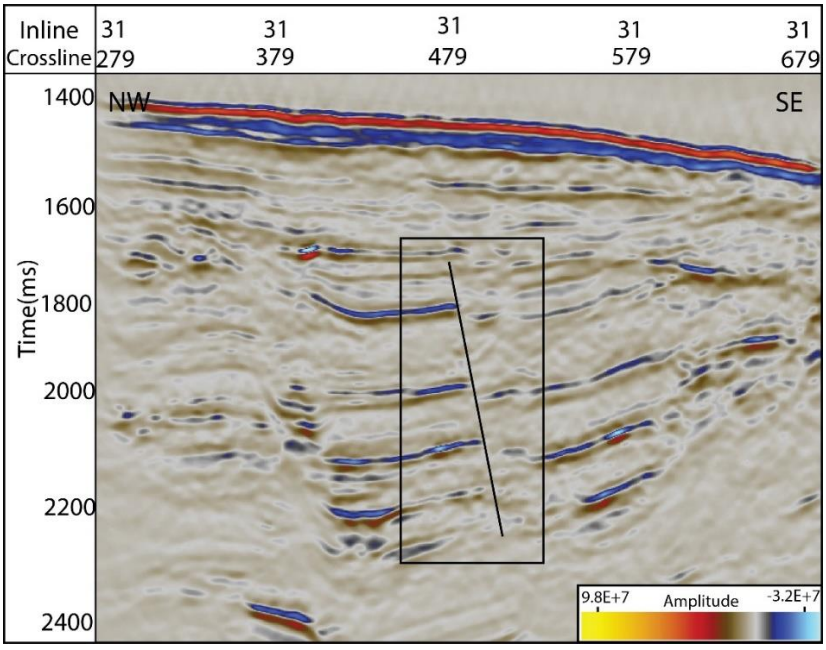


Figure 4. Inline 31 seismic section after median-filter-based conditioning, illustrating noise suppression and preservation of structural discontinuities.

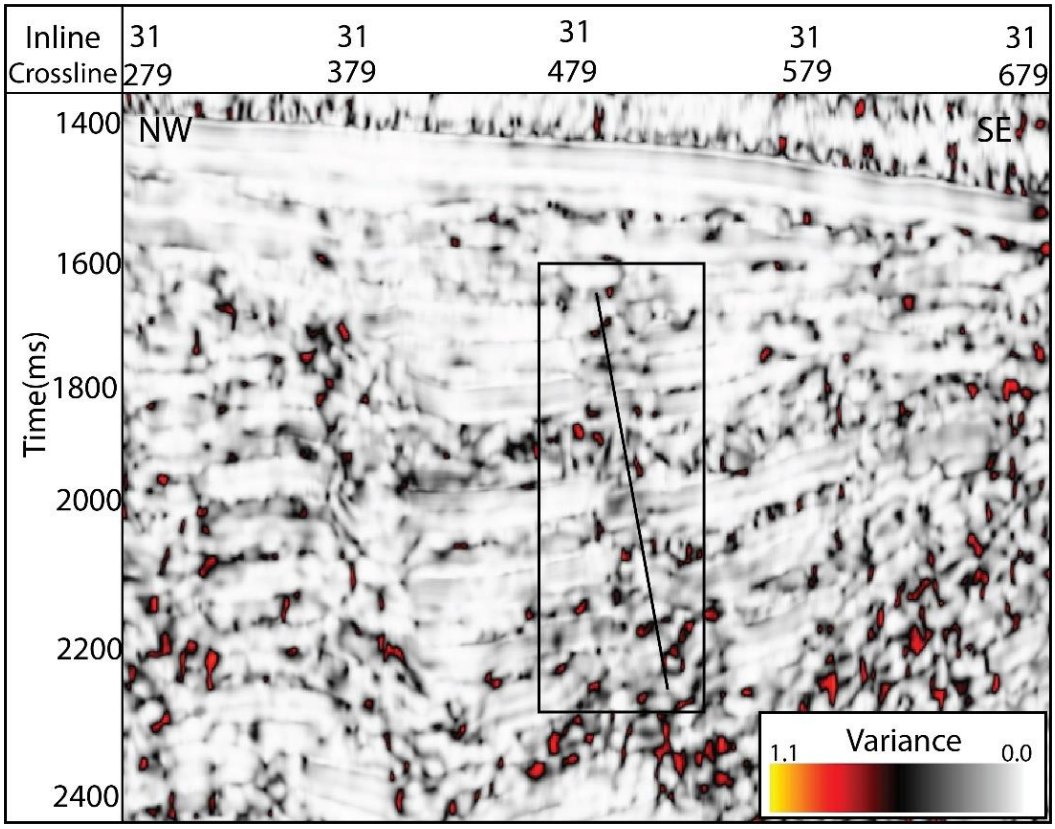


Figure 5. Variance attribute computed from the median-filtered Inline 31 seismic section, highlighting the discontinuity features that serve as the input for subsequent ant-tracking analysis.

The variance attribute computed from the median-filtered seismic volume (Figure 5) clearly shows the enhanced fault- and fracture-related discontinuities by highlighting abrupt lateral changes in seismic reflections of inline 31 and crossline varying from 466 to 500. Compared with the original and conditioned seismic sections, the variance volume provides a clearer representation of structural discontinuities and improves the visibility of potential fracture zones. Application of ant tracking to the variance volume further enhances the continuity and connectivity of these discontinuities. Fracture-related features that appear fragmented in the variance attribute become more continuous and better connected in the ant-tracking volume, enabling clearer delineation of fracture corridors and structural connectivity as shown in Figure 6. Taking cue from this analysis, we have computed the ant tracked volume and extracted the time slices in the window of 1500 ms and 2200 ms.

Interpretation of ant-tracking time slices reveals a prominent seismic discontinuity exhibiting strong lateral continuity and structural connectivity as indicated by black arrow within the purple oval in Figure 7. The feature is identifiable across multiple successive time slices of Inline 31 and becomes most prominent between 1800 and 2100 ms of x-line varying from x-line 468 to x-line 492, indicating that this interval represents the zone of maximum fracture related discontinuity development within the study area. The persistence of the interpreted fracture related discontinuity across adjacent time slices and crosslines suggests vertical structural continuity supporting its interpretation as a connected fracture related feature within the seismic volume. The ant-tracking results provide a clearer and more continuous representation of these discontinuities compared with the variance attribute alone, improving the identification of interpreted fracture related features and their structural connectivity.

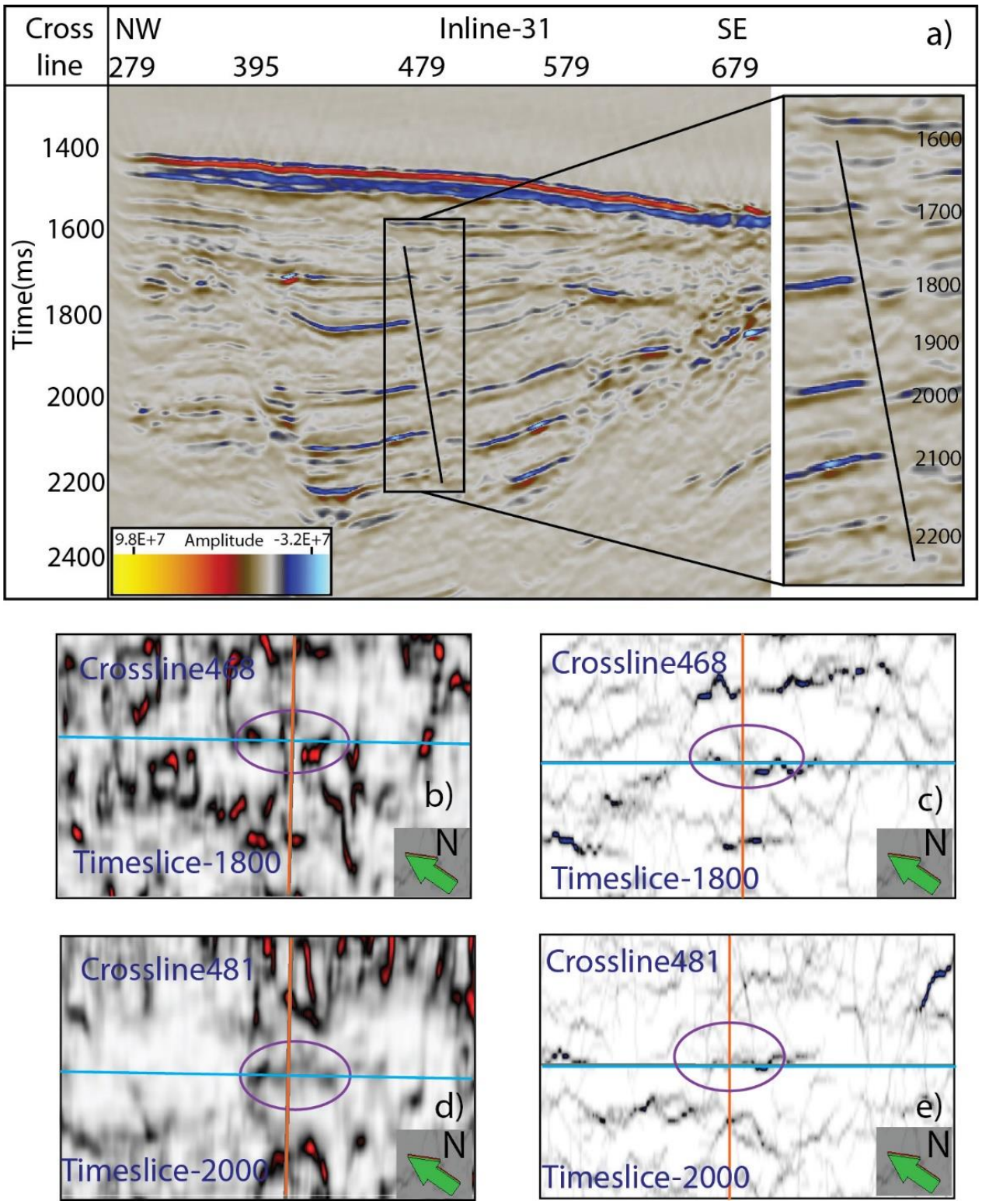


Figure 6. **(a)** Median-filtered seismic section along Inline 31, showing the fracture discontinuity (black line). **(b)** Variance attribute time slice at 1800 ms intersecting crossline 468. **(c)** Corresponding ant-tracking time slice at 1800 ms showing enhanced continuity of the fracture-related feature. **(d)** Variance attribute time slice at 2000 ms intersecting crossline 481. **(e)** Corresponding ant-tracking time slice at 2000 ms.

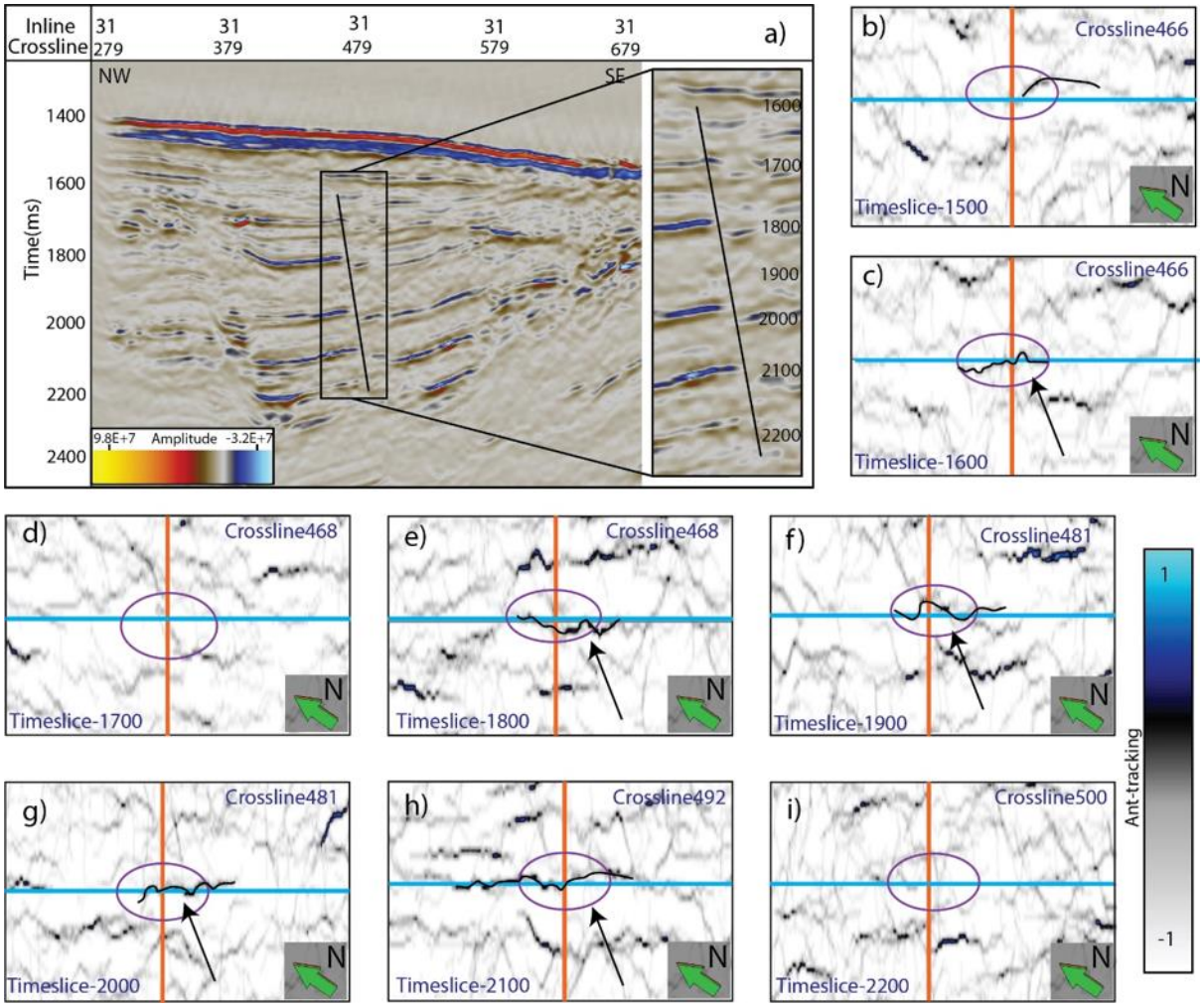


Figure 7. **(a)** Median-filtered seismic section along Inline 31, showing the interpreted fracture related structural feature (black line). **(b-i)** Ant-tracking time slices from 1500 ms to 2200 ms illustrating the vertical continuity of the interpreted fracture conduit across multiple crosslines. The fracture feature is initially observed at 1500-1600 ms (Crossline 466), becomes weak or absent around 1700 ms (Crossline 468), reappears at 1800 ms, and remains visible through 1900-2100 ms (Crosslines 481-492) before diminishing at 2200 ms (Crossline 500). The highlighted regions (purple ellipses) indicate the interpreted fracture pathway, demonstrating its lateral persistence and vertical structural continuity within the study area.

DISCUSSION

The median filter played an important role in improving the quality of the seismic data by suppressing random noise while preserving fault and fracture boundaries, which are essential for discontinuity-based interpretation (Jaglan et al., 2015). The effectiveness of the proposed workflow, highlights the importance of applying seismic conditioning and attribute generation in a systematic sequence. Acuna-Uribe et al. (2021) considered seismic data from New Zealand and Colombia from 3 basins: (1) Kupe Area, southwestern flank of the Taranaki Basin (New Zealand), (2) South-eastern flank of the offshore Taranaki Basin (New Zealand), and (3) The Middle Magdalena valley basin (Colombia), which demonstrated that the success of seismic attribute interpretation depends not only on attribute selection but also on the order in which conditioning and attribute-generation steps are applied.

The work of Zhang et al. (2017) in Taranaki Basin, aimed at enhancing fault and fracture imaging through attribute-based ant-tracking analysis reported that the reliability of ant-tracking results is highly dependent on the signal-processing method and the attribute volume that is used as input. They found that conventional conditioning workflows often fail to preserve small fracture features, leading to incomplete fracture interpretation. To overcome this limitation, we adopted the workflow which includes median filter for further data conditioning before performing attribute analysis. Xie et al. (2022) improved fracture detection by

integrating frequency-divided seismic volumes with ant tracking; however, such workflows require the generation and interpretation of multiple frequency-dependent datasets. In contrast, the workflow proposed in this study uses a single conditioned seismic volume, followed by variance analysis and ant tracking, providing a relatively simple approach for delineating fracture-related discontinuities while maintaining their spatial continuity.

Ant tracking further enhanced the continuity and connectivity of discontinuities compared with the variance volume, improving the delineation of fault- and fracture-related features (Randen et al., 2001; Pedersen et al., 2002; Fehmers and Hocker, 2003). Comparison with previous ant-tracking studies from other basins further validates the results obtained here. Basir et al. (2013) reported improved fault delineation through optimized ant-tracking workflows. In the present study, the custom ant-tracking configuration improved the sensitivity of the workflow to subtle discontinuities, enabling more effective identification and mapping of small-scale fractures and enhancing the continuity of the interpreted fracture network. The interpreted fracture network reveals that fracture development is not uniform throughout the target interval. In several locations, fracture signatures weaken or temporarily disappear before reappearing at deeper levels with slightly modified orientations. As illustrated in Figure 6, a prominent fracture related discontinuity is visible at approximately 1600 ms, becomes less distinct or temporarily disappears around 1700 ms, and reappears at 1800 ms with a similar or slightly modified trend. The fracture feature then remains identifiable and continuous down to approximately 2100 ms. The persistence of this interpreted discontinuity across multiple time slices and crosslines indicates vertical structural continuity and suggests connectivity of the feature within the seismic volume. Such variations may be related to changes in lithology, mechanical properties, structural deformation, or local stress conditions that influence the development and expression of structural discontinuities.

The interpreted fracture corridors have important geological implications within the tectonic framework of the KG Basin. Visual interpretation of the ant-tracking volume suggests that the major fracture corridors generally follow a NE-SW trend, broadly consistent with the dominant regional structural and fault trends of the basin (Rao, 2001; Subrahmanyam and Chand, 2006). The KG Basin is characterized by passive-margin normal faulting and shale tectonism, which can promote the development of secondary faults and fractures (Ramprasad et al., 2011; Badesab et al., 2019). The persistence of fracture-related lineaments across multiple time slices, indicates structurally connected pathways rather than isolated discontinuities. Previous studies have demonstrated that faults and fracture networks can provide pathways for the upward migration of methane-rich fluids in the offshore KG Basin (Riedel et al., 2010; Collett et al., 2019). Therefore, the connected fracture corridors identified in the present study, may represent structurally controlled pathways that could influence subsurface fluid migration and connectivity.

Previous fracture identification and characterization studies in the KG Basin have largely relied on well-based observations; however, the limited spatial coverage of wells, makes it difficult to capture the lateral distribution and connectivity of fracture networks across the subsurface (Singha and Sarkar, 2025). The presence of fractures is established from the well log results from the near-by well, namely NGHP-01-02B well, located approximately 8.9 km from the study area. Resistivity imaging identified a distinct interval of variable resistivity at approximately 192-194 mbsf, which was interpreted possibly as a steeply dipping fault or fracture. This observation provides independent evidence for the presence of localized structural discontinuities within the subsurface. However, a direct correlation of fractures is not carried out owing to the 8.9 km distance from the study area. The occurrence of such features in well-log data is consistent with the fracture-related discontinuities identified from the seismic attribute and ant-tracking analysis in the present study, supporting the interpretation of structurally controlled fracture zones within the target interval. Overall, the results demonstrate that the integration of median filtering, variance attributes, and ant tracking provides a practical and effective approach for delineating seismic discontinuities and interpreted fracture related corridors within the KG Basin. The resulting interpretation improves the understanding of subsurface structural connectivity and provides a valuable framework for future fracture characterization, reservoir studies, and fluid-migration analysis in the basin. However, the ant-tracking workflow has several limitations and associated uncertainties. The extracted discontinuities depend on seismic data quality, seismic resolution, data conditioning, and the selection of variance and ant-tracking parameters. Variance and ant tracking primarily identify seismic discontinuities and cannot independently distinguish fractures from faults, stratigraphic boundaries, processing artefacts, or residual noise. Therefore, the mapped features areto be interpreted cautiously as fracture-related discontinuities based on their seismic characteristics and geological context.

CONCLUSIONS

An integrated workflow comprising median-filter-based seismic conditioning, variance attribute analysis and ant tracking, was successfully applied to a 3D seismic dataset from the KG Basin for qualitative fracture characterization. Median filtering was first applied to the stacked seismic volume, followed by variance attribute generation and ant tracking to delineate fracture-related discontinuities and their spatial continuity. Interpretation of the ant-tracking time slices revealed a prominent fracture-related feature with strong lateral and vertical continuity between 1800 and 2100 ms, indicating enhanced structural connectivity within this interval. The mapped fracture corridor generally follows the regional structural trend of the KG Basin and may represent a potential pathway for subsurface fluid migration and reservoir connectivity. Overall, the workflow provides an efficient approach for qualitative fracture characterization using conventional 3D seismic data. Quantitative comparison of discontinuity density, continuity, and extracted lineament characteristics between the variance and ant-tracking results, remains a potential direction for future work. Similarly, quantitative estimation of fracture orientation and intensity using AVAz analysis will further improve fracture characterization within the study area.

Acknowledgments

The authors express their sincere gratitude to the Director, CSIR-National Geophysical Research Institute, for granting permission to publish this work (Ref. No. NGRI/Lib/2026/Pub-140). We acknowledge the Directorate General of Hydrocarbons (DGH), New Delhi, for supplying the seismic data used in this study. Financial support from the Department of Science and Technology (DST) towards the first author's Ph.D. research, is gratefully acknowledged. Special thanks to Dr. J.V.S.S. Narayan Murthy (Former G.M., ONGC) for his valuable assistance in seismic data processing. Also, thanks extended to Sai Vijay Kumar, P. for the technical support throughout the work. Thanks to Dr. Rowtu Ramu for his assistance in Petrel software.

Author credit statement

Latha Sri Pelluri carried out the seismic data processing and interpretation and prepared the initial draft of the manuscript. Dr. N. Satyavani supervised the research, provided scientific guidance throughout the study, reviewed and revised the manuscript, and contributed to refining the study direction.

Data availability

Data is available at CSIR-NGRI and will be shared on request.

Compliance with ethical standards

No conflict of interest, and authors adhere to copyright norms.

References

Acuna-Uribe, M., Pico-Forero, M.C., Goyes-Peñafiel, P. and Mateus, D., 2021. Enhanced ant tracking: Using a multispectral seismic attribute workflow to improve 3D fault detection. The Leading Edge, 40(7), 502-512.

Aydin, A., 2000. Fractures, faults, and hydrocarbon entrapment, migration and flow. Mar. Pet. Geol., 17(7), 797-814.

Badesab, F., Dewangan, P., Gaikwad, V., Kars, M., Kocherla, M., Krishna, K. S., Sangode, S. J., Deenadayalan, K., Kumar, P., Naikgaonkar, O., Ismaiel, M. and Khan, A., 2019. Magnetic Mineralogical approach for the exploration of gas hydrates in the Bay of Bengal. J. Geophys. Res. Solid Earth, 124(5), 4428-4451.

Basir, H.M., Javaherian, A. and Yaraki, M.T., 2013. Multi-attribute ant-tracking and neural network for fault detection: A case study of an Iranian oilfield. J. Geophys. Eng., 10(1), 015009.

Chopra, S. and Marfurt, K.J., 2005. Seismic attributes-A historical perspective. Geophysics, 70(5), 3SO-28SO.

Chopra, S. and Marfurt, K.J., 2007 a. Seismic attributes for prospect identification and reservoir characterization. Soc. Explor. Geophys. and Eur. Assoc. Geosci. Eng., Tulsa.

Chopra, S. and Marfurt, K.J., 2007b. Seismic attributes for fault/fracture characterization. The Leading Edge, 26(12), 1548-1565.

Collett, T. S., Boswell, R., Waite, W. F., Kumar, P., Roy, S. K., Chopra, K., Singh, S. K., Yamada, Y., Tenma, N., Pohlman, J. and Zyrianova, M., 2019. India National Gas Hydrate Program Expedition 02 Summary of Scientific Results: Gas hydrate systems along the eastern continental margin of India. Mar. Pet. Geol., 108, 39-142.

Dorigo, M., Maniezzo, V. and Colorni, A., 1996. Ant system: Optimization by a colony of cooperating agents. IEEE Trans. Syst. Man Cybern. B, 26(1), 29-41.

Fehmers, G.C. and Höcker, C.F.W., 2003. Fast structural interpretation with structure-oriented filtering. Geophysics, 68(4), 1286-1293.

Jaglan, H., Qayyum, F. and Hélène, H., 2015. Unconventional seismic attributes for fracture characterization. First Break, 33(3), 101-109.

Jibrin, B.W., Turner, J.P., Westbrook, G. and Huck, A., 2009. Application of volumetric seismic attributes to delineate fault geometry: Examples from the outer fold and thrust belt, deepwater Niger Delta. SEG Tech. Program Expanded Abstracts.

Latha Sri, P. and Satyavani, N., 2026. Identification of Gas-hydrates and Free Gas Zones using Acoustic Impedance Inversion Integrated with AVA Analysis. J. Geol. Soc. India, 102(9), 1262–1269

Lavendra Kumar, Ramakrishna, K. and Viswanathan, S., 2015 Overview of basement exploration techniques. Geohorizons, July issue, 9-16.

Nelson, R.A., 2001. Geologic analysis of naturally fractured reservoirs. Gulf Professional Publishing, Houston.

Ngeri, A.P., Tamunobereton-ari, I, and Amakiri, A. R. C., 2015. Ant-tracker attributes: An effective approach to enhancing fault identification and interpretation. IOSR J. VLSI Signal Process., 5(6), 67-73.

Pedersen, S.I., Randen, T., Sonneland, L. and Steen, Oyvind., 2002. Automatic fault extraction using artificial ants. SEG Tech. Program Expanded Abstracts 2002, 512-515.

Ramana, M., Ramprasad, T., Raju, K. K. and Desa, M., 2007. Occurrence of gas hydrates along the continental margins of India, particularly the Krishna-Godavari offshore basin. Int. J. Environ. Studies, 64(6), 675-693.

Ramprasad, T., Dewangan, P., Ramana, M., Mazumdar, A., Karisiddaiah, S., Ramya, E. and Sriram, G., 2011. Evidence of slumping/sliding in Krishna-Godavari offshore basin due to gas/fluid movements. Mar. Pet. Geol., 28(10), 1806-1816.

Randen, T., Pedersen, S.I. and Sønneland, L., 2001. Automatic extraction of fault surfaces from three-dimensional seismic data. SEG Tech. Program Expanded Abstracts, 551-554.

Rao, G.N., 2001. Sedimentation, stratigraphy, and petroleum potential of Krishna-Godavari Basin, east coast of India. AAPG Bull., 85(9), 1623-1643.

Riedel, M., Collett, T., Kumar, P., Sathe, A. and Cook, A., 2010. Seismic imaging of a fractured gas hydrate system in the Krishna-Godavari Basin offshore India. Mar. Pet. Geol., 27(7), 1476-1493.

Sastri, V. V., Raju, A. T. R., Sinha, R. N. and Venkatachala, B. S., 1974. Evolution of the Mesozoic sedimentary basins on the east coast of India. The APEA Journal, 14(1), 29–41.

Satheesh, S., Subrahmanyam, V.S.R. and Veeraiah, B., 2025. Reservoir characterization studies using seismic attributes of onshore 3D seismic data, East Godavari Depression, Krishna-Godavari Basin, India. J. Earth Syst. Sci., 134(3). https://doi.org/10.1007/s12040-025-02592-4

Sheriff, R.E., 2002. Encyclopedic dictionary of applied geophysics. Cambridge Press. Soc. Explor. Geophys., Tulsa.

Sibson, R.H., 1996. Structural permeability of fluid-driven fault-fracture meshes. J. Struct. Geol., 18(8), 1031-1042.

Singha, D. K. and Sarkar, A., 2025. A Comprehensive Study on Fracture Identification and Fractures Properties Estimation from Well Log Data in the Hydrocarbon Bearing Formation Using Semi-automated Machine Learning and Dual Porosity Model. Pure Appl. Geophys., 182(9), 3613–3637.

Subrahmanyam, C. and Chand, S., 2006. Evolution of the passive continental margins of India-A geophysical appraisal. Gondwana Res., 10(1-2), 167-178.

Xie, Q., Zhao, C., Rui, Z., Guan, S., Zheng, W. and Fan, H., 2022. An improved ant-tracking workflow based on divided-frequency data for fracture detection. J. Geophys. Eng., 19(5), 1149-1162.

Zhang, J.H., Xie, Q.H., Zhang, D.T., Zhao, C.D., Yao, Q.C. and Li, Q.S., 2020. Application of an optimized ant-tracking workflow in shale-gas Y1 area of Sichuan. Geophys. Prospect. Pet., 59, 970-997.

Zhang, R., Wen, X.T. and Li, S.K., 2017. Application of frequency division ant-tracking in identifying deep minor fault. Prog. Geophys., 32, 350-356.

Zhao, S., Zheng, M., Liu, S., Li, B., Liu, Y., He, Y., Wang, G. and Qiu, X., 2023. Multi-scale fractures and their influence on shale gas deliverability in the Longmaxi formation of the Changning Block, southern Sichuan Basin, China. ACS Omega, 8(20), 17653–17666.

Received on: 19-06-2026; Revised on: 25-09-2026; Accepted on: 26-09-2026

J. Ind. Geophys. Union, 30(6) (2026), 462-473
http://doi.org/10.71122/JIGU.30(6)2026.0046

Integrated well-log analysis and 3D transient modeling for optimizing reservoir flow in CO_2 storage settings

Tanmoy Chetia[1], Pallavi Banerjee Chattopadhyay[1*], Aakash Jaiswal[1], Nimisha Vedanti[2], Ravi Shankar Dubey[1], and A. D. Sarath[1]
[1]Department of Earth Sciences, Indian Institute of Technology Roorkee-247667, India
[2]CSIR–National Geophysical Research Institute, Hyderabad- 500007, India
*Corresponding Author: cpallavi@es.iitr.ac.in

ABSTRACT

This study presents a coupled analysis of transient flow dynamics and reactive transport processes, providing a comprehensive understanding of reservoir behavior under both baseline and CO_2 injection scenarios. The governing framework integrates Darcy's law (pressure-driven flow) with mineral-dissolution kinetics, enabling dynamic feedback between fluid flow and evolving reservoir properties in the Ankleshwar oil field of the Cambay Basin (India). Unlike conventional approaches that assume constant permeability, this work incorporates pressure-dependent permeability, integrating Darcy's law (pressure-driven flow) with mineral-dissolution kinetics to enable dynamic feedback between fluid flow and evolving reservoir properties in COMSOL Multiphysics. Log-derived petrophysical properties from Well A indicate significant heterogeneity. For Well A, porosity ranges from 14% to 26% and permeability from 144 to 336 mD. Shale volume influences reservoir quality, and the V_{shale}-permeability relationship, is interval-dependent. A mineral dissolution framework was incorporated, in which forward-reaction-based projections indicate absolute porosity increases of 0.06-0.08 percentage points, corresponding to relative increases of approximately 0.1-0.4%, and permeability increases of approximately 1-2% over 50 years. The results show that reservoir behavior is governed by the combined effects of clay content, stress-sensitive permeability, and geochemical alteration.

Keywords: Reservoir characterization; Pressure-dependent permeability; Transient flow simulation; CO_2 sequestration; Mineral dissolution; Reactive transport modeling; Reservoir heterogeneity; Cambay basin

INTRODUCTION

Hydrocarbon reservoirs continue to play a central role in global energy supply, particularly in developing economies where fossil fuels remain a major component of the energy mix (Dixit et al., 2019). At the same time, the growing emphasis on carbon management has renewed interest in using subsurface reservoirs for CO_2 storage, either through dedicated geological storage or CO_2-assisted recovery strategies (Ali et al., 2022; Bargees et al., 2023). These parallel drivers, enhanced recovery, and secure CO_2 storage, make it essential to understand how reservoir heterogeneity governs pressure communication, flow pathways, and injectivity over time (Abdelghany et al., 2021). These parallel drivers enhance hydrocarbon recovery and secure CO_2 storage.

Integrating well-log interpretation with advanced three-dimensional transient numerical modeling, provides a powerful framework for resolving complex subsurface flow behavior and improving reservoir performance assessment (Sen et al., 2020; Radwan and Sen, 2021). Reservoirs are inherently heterogeneous systems in which variations in lithology, clay content, porosity, and permeability control fluid distribution and movement. Traditional reservoir models often assume constant permeability; however, this assumption is not valid in many formations, particularly in tight or clay-bearing reservoirs, where permeability is pressure-dependent. Such pressure-sensitive permeability significantly influences fluid flow, production performance, and reservoir management strategies. Real-world applications of this type of research are significant, particularly for reservoir management. Therefore, incorporating permeability variability and geomechanical effects into reservoir simulations is essential for realistic modeling and production optimization (Chanda and Singh, 2019; Kamal et al., 2019).

Despite advances in reservoir simulation, several challenges remain. One major challenge is integrating multiple data sources, such as well logs, core data, and numerical simulations, into a unified modeling framework (Jin et al., 2022). Well-log data often contain uncertainties and limited spatial coverage, while high-resolution numerical modeling requires careful parameter selection and computational resources (Nair and Srivastava, 2024). Another important challenge is capturing microscale interactions between injected CO_2 and reservoir rocks. These interactions depend on mineralogy, pore structure, wettability, and capillary forces, all of which influence long-term reservoir behavior and storage integrity (Boswell et al., 2017; Kim et al., 2017). As a result, reservoir behavior during CO_2 injection is governed not only by fluid flow but also by geochemical reactions that gradually modify pore structure and permeability.

Geological heterogeneity, particularly the presence of clay and shale, plays a crucial role in controlling reservoir properties, including porosity, permeability, and pore pressure. Clay-rich intervals can act as flow barriers, reducing permeability and altering fluid flow paths, while cleaner sand intervals serve as preferential flow channels. Although previous studies have investigated reservoir flow dynamics and hydrocarbon recovery using numerical simulations and material balance approaches (Collett, 2019;

Jain et al., 2019), the combined effects of permeability variability, pressure sensitivity, and clay content on fluid flow behavior remain insufficiently explored. In particular, the dynamic nature of pressure-sensitive permeability in tight formations represents a significant gap in reservoir engineering studies. In parallel, global greenhouse gas (GHG) emissions continue to rise, with the largest contributions originating from energy-intensive sectors such as industry, buildings, and transportation. Industrial activities account for over 24% of global emissions, while buildings and transport account for approximately 17.5% and 16.2%, respectively. Hard-to-abate sectors such as iron and steel, cement, and petrochemicals also contribute significantly to global emissions, highlighting the urgent need for carbon capture and storage (CCS) technologies. Geological CO_2 storage in depleted or producing reservoirs is widely considered one of the most practical and large-scale solutions for reducing atmospheric CO_2 concentrations. However, the success of CO_2 sequestration depends on reservoir properties, injectivity, fluid flow behavior, and long-term geochemical interactions between CO_2 and reservoir rocks (Xu et al., 2020).

Recent research studies have increasingly focused on coupling reservoir flow simulations with reactive transport modeling to better understand CO_2-rock interactions and their impact on reservoir properties (Delavar, 2022). When CO_2 dissolves in water, it forms carbonic acid, which reacts with minerals such as calcite and feldspars, leading to mineral dissolution or precipitation. These reactions gradually alter the pore structure, thereby altering porosity and permeability. Such changes can influence fluid flow pathways, injectivity, and long-term storage security, underscoring the need to incorporate mineral-dissolution processes into reservoir simulations.

To address these gaps, the present study highlights the importance of depleted oil reservoirs for CO_2 storage in the Ankleshwar oil field, Cambay Basin, India. The well-log interpretation, combined with advanced three-dimensional transient numerical modeling, reveals the roles of petrophysical parameters, heterogeneity, and pressure-dependent permeability. Also, CO_2-brine-rock reaction and reactive transport that representation of subsurface flow processes. The objectives of this study are to, (i) quantify porosity, permeability, and shale variability using well-log data, (ii) incorporate these properties into a 3D transient flow model developed in COMSOL Multiphysics, (iii) simulate reservoir flow behavior under baseline and CO_2 injection scenarios, and (iv) evaluate the long-term impact of CO_2-rock interactions on porosity and permeability evolution.

GEOLOGICAL SETTINGS

The present study was conducted within the Cambay Rift Basin, one of India's most prolific petroleum provinces, located in the western part of the Indian subcontinent. Geographically, the Cambay Basin extends between 21°00′ and 25°00′ N and 71°30′ and 73°30′ E, covering an area of approximately 56,000 km² (Mohan et al., 2008) (Figure 1). The basin is situated within the alluvial plains of Gujarat, where hydrocarbons are produced primarily from Eocene sandstone reservoirs and represents one of the most extensively explored and structurally well-defined sedimentary basins in India. It is geographically bound by the Saurashtra Plateau to the west, the Aravalli Range to the northeast, and the Deccan Traps to the south. The hydrocarbon accumulation is structurally controlled by faulted anticline traps, and the field contains oil with associated natural gas (Ganguli et al., 2018). This sedimentary basin is essential not only for petroleum system analysis but also for evaluating basin-scale hydrogeological processes, CO_2 sequestration potential, salinity migration, and long-term subsurface fluid behavior.

The Ankleshwar oil field lies in the southern part of the Cambay Basin within the Narmada Block, where sediment thickness exceeds 5 km. The stratigraphy, ranging from Eocene to Miocene, records tectonically controlled sedimentation influenced by rift-related faulting and changing depositional environments. Alternating shale and sandstone units reflect marine-to-fluvial-deltaic conditions, forming the reservoir, seal, and source framework of the Ankleshwar petroleum system.

METHODOLOGY

This study adopts an integrated workflow combining well-log interpretation, petrophysical characterization, three-dimensional transient numerical modeling, and coupled flow-reaction simulations to investigate reservoir behavior and evaluate the effects of CO_2 injection in the Ankleshwar oil field, Cambay Basin, India (Figure 1). The methodology consists of four sequential stages, as shown in Figure 2:

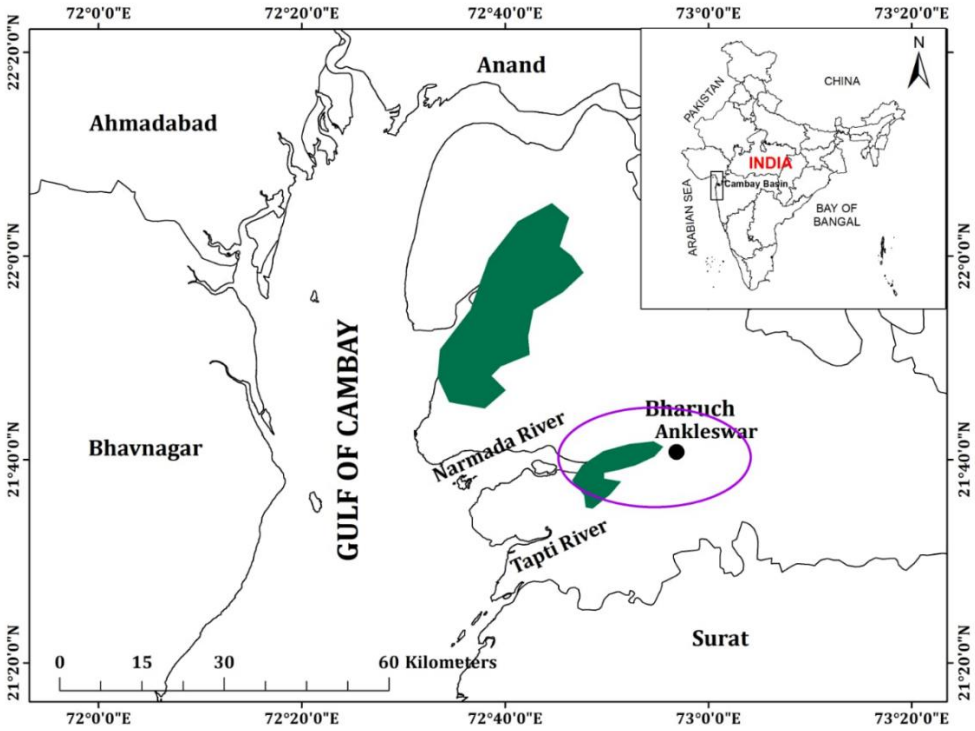


Figure 1. Location map of the study area in the Cambay Basin, western India. The map shows the Gulf of Cambay and the surrounding area, including the Narmada and Tapti rivers. The green-shaded areas represent oil fields, and the purple circle highlights the spatial extent of the Cambay Basin, which is the primary study area (after Nair and Srivastava, 2024)

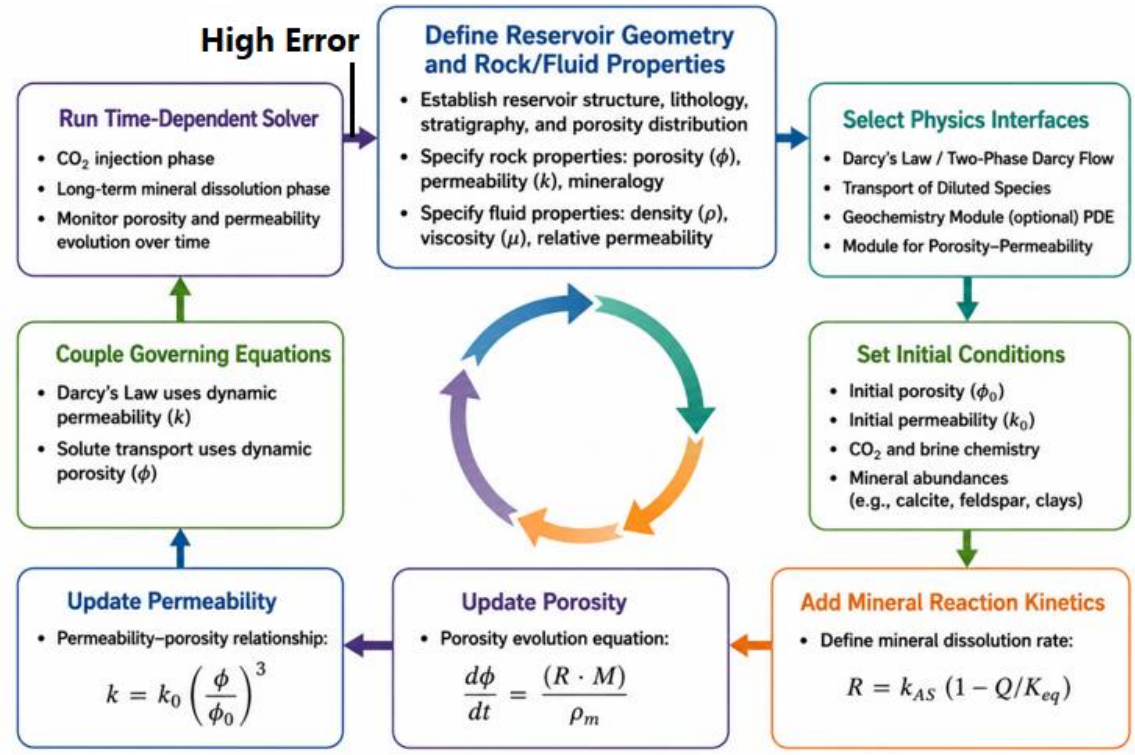


Figure 2. Methodology workflow illustrating the COMSOL Multiphysics-based coupled reactive transport framework, in which mineral dissolution dynamically updates porosity and permeability, which are fully coupled with Darcy flow and solute transport, thereby controlling fluid flow behavior, reservoir permeability evolution, and long-term CO_2 migration

Reservoir characterization from well-log data

Reservoir data were obtained from a well in the Ankleshwar oil field, anonymized as Well A for confidentiality reasons. Seven log intervals from Wells A are selected to derive the parameters like porosity, permeability (mD), water saturation using Archie's equation S_w, hydrocarbon saturation S_h, irreducible water saturation using the Buckley-Leverett relationship S_{wi}, Reservoir Quality Index RQI (µm), Flow Zone Indicator FZI (µm) that are estimated from the available geophysical logs (Figure 3). Average porosity and permeability for Wells A is shown in Table 1. Exact water saturation requires formation-water resistivity and true formation resistivity at each depth from Wells A. Therefore, the calculations below use clearly stated illustrative Archie and Buckles assumptions: a=1, m=2, n=2, and a Buckles constant of 0.06 to estimate irreducible water saturation.

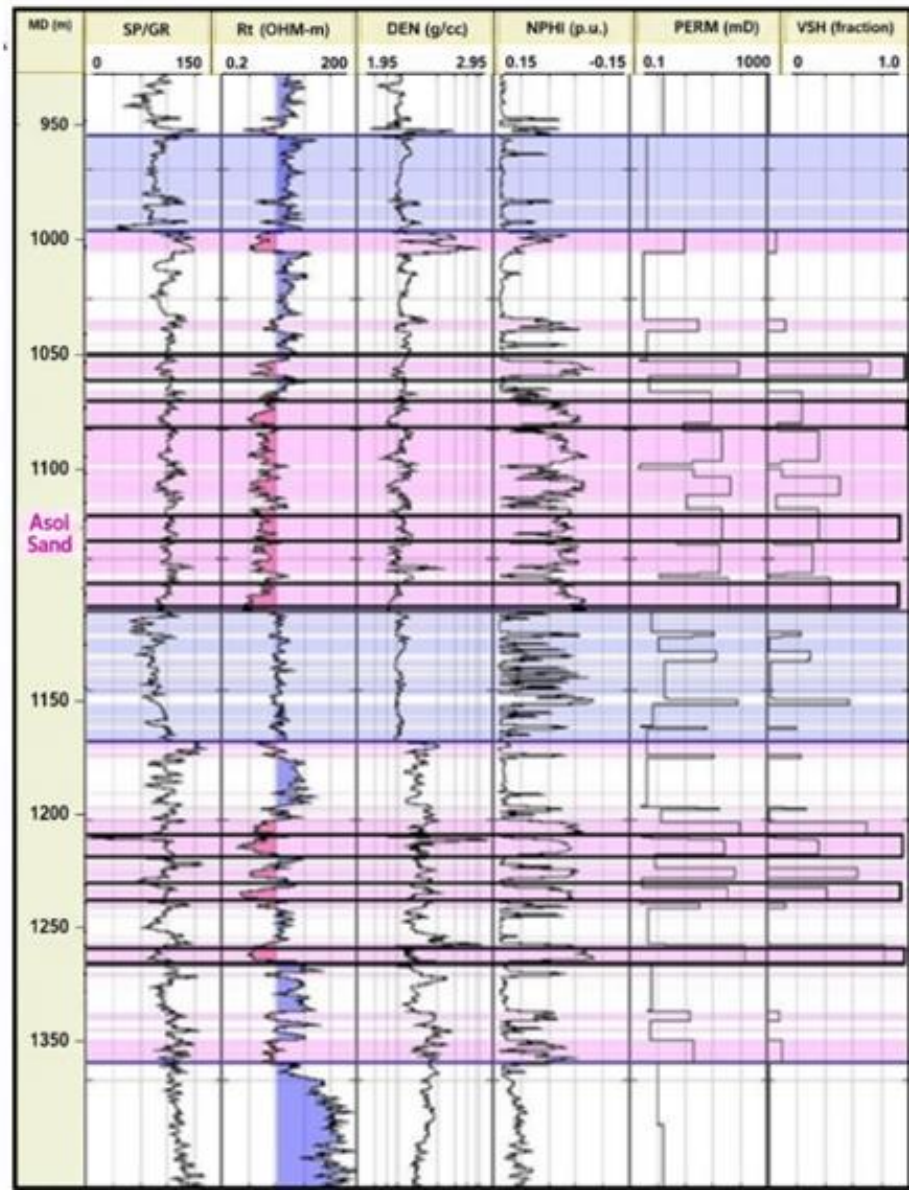


Figure 3. Continuous geophysical well-log interpretation for Well A, showing the vertical distribution of major petrophysical and lithological properties within the Cambay Basin reservoir. The logs include Gamma Ray (GR), true resistivity (R_t), bulk density (ρ_b), neutron porosity (NPHI), permeability (k), and volumetric shale content (V_{sh})

Table 1 Statistical analysis of porosity and permeability for Wells A

Well A		
Parameters	Porosity (%)	Permeability (mD)
Minimum	14.44	142.86
Maximum	25.55	335.72
Mean	20.87	213.29
Standard deviation	3.69	75.17

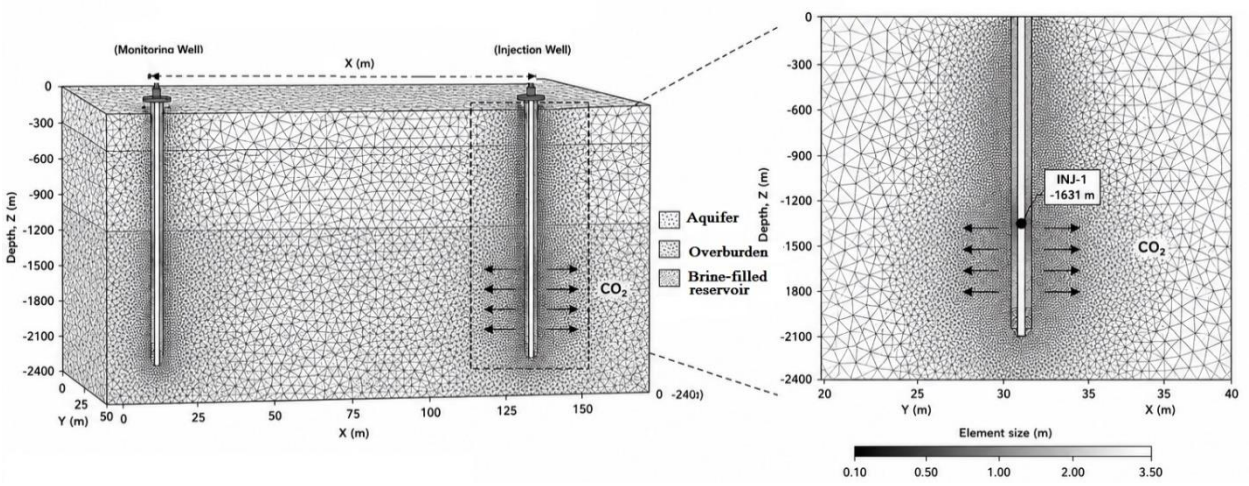


Figure 4. A finite-element mesh of the reservoir model showing the monitoring and CO_2 injection wells used for transient flow simulations, discretized using tetrahedral finite elements.

Table 2. Pressure and operating conditions

S.No.	Operating conditions	Suggested value
1	Initial reservoir pressure, P_{res}	20.10 MPa
2	Far-field boundary pressure	20.10 MP
3	Bottom-hole injection pressure	22.0 MPa
4	Injection overpressure, Δp_{inj}	1.90 MPa
5	Base-case reservoir temperature	75°C
6	Reference injection depth	1200 m
7	Simulation duration	5 years
8	Average porosity and permeability for layer 1 Aquifer	21.5% and 171mD Well A point 1
9	Average porosity and permeability for layer 2 Overburden	16% and 153 mD Well A point 2,3
10	Average porosity and permeability for layer 3 Saline Aquifer	22.5% and 204 mD Well A point 4-7

(i) Development of a three-dimensional finite-element reservoir model

Figure 4 presents the three-dimensional finite-element discretization of the reservoir domain used for transient flow simulations. The computational domain was discretized using tetrahedral finite elements, which offer the flexibility needed to model complex reservoir geometries. Adaptive local mesh refinement was applied around the wellbore to improve the resolution of near-well hydraulic behavior. This graded-mesh distribution provides an optimal balance between computational efficiency and numerical precision for simulations of CO_2 migration and reservoir property evolution.

(ii) Transient Darcy-flow simulation under baseline and CO_2 injection scenarios

Transient fluid flow within the reservoir was simulated using Darcy's Law interface in COMSOL Multiphysics. Two scenarios were investigated over a 50-year simulation period (Table 2):

Baseline reservoir flow without CO_2 injection

The baseline case represents natural reservoir flow without CO_2 injection. An initial reservoir pressure of 20 MPa was assigned throughout the model domain. Constant-pressure boundaries were prescribed at the inlet, and outlet faces to establish a regional hydraulic gradient, while the remaining

boundaries were treated as impermeable, no-flow boundaries.

Continuous CO_2 injection through a centrally located vertical well

The governing equation for transient single-phase flow is:

$$\emptyset c_t \frac{\partial P}{\partial t} = \nabla . \left(\frac{k}{\mu} \nabla P\right) + q \quad (1)$$

where P is reservoir pressure (P_a), ϕ is porosity, c_t is the total compressibility Pa^{-1}, k is permeability (m^2), μ is fluid viscosity ($Pa{\cdot}s$), and q represents fluid injection.

For immiscible oil–water flow, phase velocities are described using relative permeability:

$$u_w = -\frac{k\, k_{rw}}{u_w} \nabla P \quad (2)$$

$$u_o = -\frac{k\, k_{ro}}{u_o} \nabla P \quad (3)$$

The conservation of fluid saturation is represented by the Buckley-Leverett equation, which provides the basis for simulating immiscible two-phase displacement under incompressible flow conditions:

$$\frac{\partial S_w}{\partial t} + \nabla . (f_w V_t) = 0 \quad (4)$$

where S_w is the water saturation, f_w is the fractional flow of water, and V_t is the total Darcy velocity. The governing equations are solved iteratively alongside the reactive transport model, allowing continuous updates to porosity, permeability, pressure, and velocity throughout the simulation.

(iii) Coupled reactive transport modelling to evaluate the evolution of porosity, permeability, and fluid flow

To evaluate the impact of long-term reservoir evolution, Darcy-flow simulations were coupled with a mineral-dissolution model representing CO_2-rock interactions. Injected CO_2 dissolves in formation water to produce carbonic acid, which promotes dissolution of carbonate minerals according to:

$$CaCO_3 + H^+ \rightarrow Ca^{2+} + HCO_3^-$$

The pressure-sensitivity coefficient = $k(P) = k_o \exp[-\alpha\,(P - P_o]$

where *ko* is the reference permeability, *Po* is the reference pressure, and α is the pressure-sensitivity coefficient. Mineral dissolution changes porosity (φ) and, through Kozeny-Carman-type relationships, permeability (k) is estimated.

The dynamically coupled with Darcy flow and property update equations in COMSOL Multiphysics, a reactive transport model to simulate mineral dissolution and its impact on porosity and permeability, the governing relationship is given by:

$$\frac{d\emptyset}{dt} = \frac{1}{\rho_m} \sum_i v_i\, R_i M_i \quad (6)$$

$$\text{R} = k_r A_s \left(1 - \frac{Q}{k_{eq}}\right) \quad (7)$$

$k_r A_s \left(1 - \frac{Q}{k_{eq}}\right)$ = (1-saturation ratio) = reactive factor F (8)

where R is the reaction rate (mol/m³/sk_{eq}); k_{eq} is the equilibrium constant; k_r is the intrinsic rate constant (mol m^{-2} s^{-1}); A is the reactive surface area of the mineral; Q is the ion activity product; φ is porosity; ρ_m = mineral density; v_i is the stoichiometric coefficient; and M_i is the molecular weight.

RESULTS

The Ankleshwar reservoir in the Cambay Basin is a depleted hydrocarbon reservoir that is now largely saturated with saline formation water due to prolonged hydrocarbon production and natural aquifer influx. Although it is not a primary deep saline aquifer, its hydraulic characteristics closely resemble those of a confined brine-filled reservoir, making it a promising geological formation for long-term CO_2 sequestration. The layered reservoir architecture generates heterogeneous pressure and flow fields during CO_2 injection, resulting in distinct migration pathways across the reservoir. Injected CO_2 preferentially migrates through Layer 3, where the relatively high porosity and permeability provide the least hydraulic resistance and the greatest storage capacity. In contrast, Layer 2 acts as a semi-confining interval owing to its comparatively lower permeability, thereby restricting vertical pressure propagation and inhibiting upward CO_2 migration. Layer 1 serves as an additional storage horizon, facilitating pressure redistribution while its moderate permeability limits excessive lateral plume expansion. This stratigraphic heterogeneity enhances overall storage security by promoting efficient CO_2 injectivity within the lower reservoir while minimizing the risk of vertical leakage into overlying formations.

Table 3 summarizes the calculated formation factor (F), water saturation (S_w), hydrocarbon saturation (S_h), irreducible water saturation (S_{wi}), Reservoir Quality Index (RQI), and Flow Zone Indicator (FZI) for Wells A and B using Archie's equation under the assumptions of a = 1, m = 2, n = 2, with a formation water resistivity (R_w) of 0.10 Ω·m, true formation resistivity (R_t) of 20 Ω·m, and a Buckles

constant of 0.06. These parameters provide insights into pore connectivity, fluid distribution, and hydraulic flow characteristics within the reservoir. The calculated formation factor ranges from 15.32 to 47.96. Lower formation factor values correspond to intervals with higher porosity and better pore connectivity, whereas higher values indicate tighter formations with reduced interconnected pore networks. In Well A, the lowest formation factor (15.32) occurs at 1254 m. Overall, the integrated petrophysical evaluation from Table 3 identifies the 1254 m interval in Well A as the most suitable for the reservoir zones. These intervals combine relatively low formation factors, low water saturation, high hydrocarbon saturation, and favorable RQI and FZI values, indicating superior pore connectivity, efficient fluid flow, and enhanced storage capacity. The simulated CO_2 plume exhibits a clear stratigraphic migration pattern (Figure 5), reflecting the strong influence of vertical reservoir heterogeneity. Following injection, CO_2 preferentially migrates within Layer 3, where relatively high porosity and permeability provide favorable flow pathways and greater storage capacity. In contrast, the overlying Layer 2 acts as an effective hydraulic barrier, restricting upward plume migration and limiting vertical pressure propagation due to its lower permeability. As a result, the injected CO_2 remains predominantly confined within the lower reservoir and spreads primarily laterally.

Table 3. Calculated formation factor, water and hydrocarbon saturation, Reservoir Quality Index, Archie, Normalized porosity index, and Flow Zone Indicator using Buckles assumptions (a=1, m=2, n=2, R_w=0.10 Ω·m, R_t=20 Ω·m, and Buckles constant of 0.06)

Point	Depth (m)	Porosity (%)	Permeability (mD)	Formation factor, F	Sw	Sh	Swi	RQI (µm)	FZI (µm)
1	1026	23.88	292.86	17.54	0.296	0.704	0.251	1.100	3.505
2	1046	17.77	242.86	31.67	0.398	0.602	0.338	1.161	5.372
3	1090	14.44	142.86	47.96	0.490	0.510	0.416	0.988	5.852
4	1116	21.66	171.43	21.31	0.326	0.674	0.277	0.883	3.195
5	1212	21.109	142.86	22.44	0.335	0.665	0.284	0.817	3.053
6	1231	21.664	164.30	21.31	0.326	0.674	0.277	0.865	3.127
7	1254	25.55	335.72	15.32	0.277	0.723	0.235	1.138	3.317

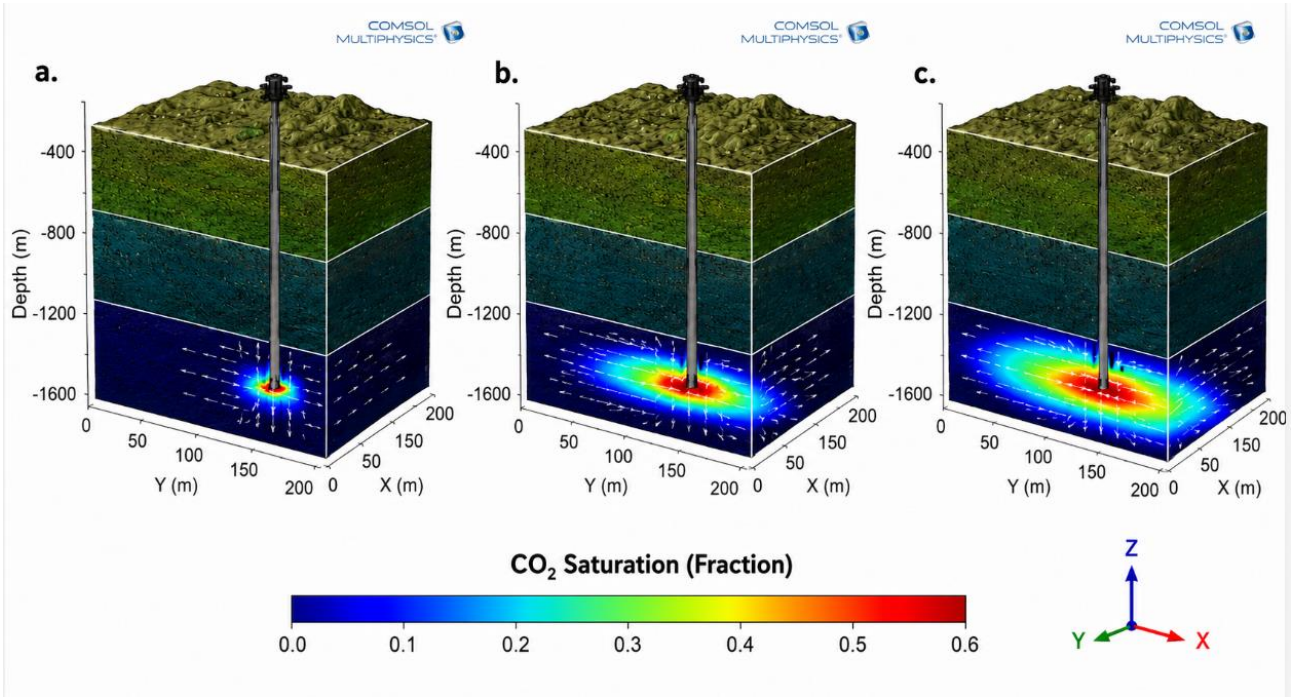


Figure 5. Simulated three-dimensional CO_2 saturation distribution at **(a)** 10 years, **(b)** 30 years, and **(c)** 50 years following continuous injection into Layer 3 of the heterogeneous three-layer depleted hydrocarbon reservoir

Over the five-year simulation period, the plume progressively expands from a localized accumulation near the injection well to an elongated body with a lateral extent of 120-150 m, while vertical migration remains negligible. This behavior demonstrates efficient stratigraphic confinement, stable pressure dissipation, and effective utilization of the high-quality storage interval, highlighting the suitability of the reservoir for secure long-term geological CO_2 sequestration that progressively expands from a localized accumulation near the injection well. The pressure distribution is highly localized near the well during the 1st injection cycle (10 years), then moderate radial pressure propagation with predominantly lateral flow during the 2nd cycle (30 years), and extensive pressure propagation throughout the reservoir, showing lateral migration and pressure dissipation after 50 years.

Reservoir heterogeneity exerts a primary control on fluid flow and CO_2 migration. Well A exhibits lithological variability, with fluctuations in gamma-ray (GR) response and shale volume indicating alternating sandstone and shale intervals. Elevated GR values at points 2 and 3 correspond to shale-rich zones characterized by reduced porosity and permeability, which act as local flow barriers. In contrast, the high-permeability interval at point 7 provides a preferential pathway for fluid movement, highlighting the importance of integrating GR logs and Vpshalep analysis to identify hydraulically favorable injection intervals.

The numerical simulations further demonstrate that CO_2 migration is strongly controlled by the layered reservoir architecture (Figure 5). Throughout the five-year injection period, CO_2 remains predominantly confined within the high-permeability Layer 3, while the overlying low-permeability Layer 2 acts as an effective hydraulic seal, minimizing vertical pressure transmission and plume migration. During the first cycle, the injected CO_2 forms a compact, nearly circular plume with a radius of approximately 20-30 m and a maximum saturation of ~0.6, indicating localized storage around the injection well. After the second cycle, continued injection promotes lateral plume expansion, producing an elongated geometry aligned with preferential high-permeability pathways, while vertical migration remains negligible. By fifty years, the plume extends laterally to approximately 120-150 m, occupying a substantially larger storage volume with a smoother saturation distribution as pressure gradients dissipate. The persistent confinement of CO_2 within Layer 3, together with the asymmetric plume geometry, demonstrates that permeability heterogeneity and anisotropy govern the formation of preferential flow pathways, whereas the intermediate sealing layer provides effective stratigraphic containment. These results confirm favorable injectivity, efficient utilization of the storage reservoir, and robust long-term geological CO_2 sequestration.

The results indicate that the effect of CO_2 injection is spatially variable throughout the reservoir (Table 4). At depths of 1046 m and 1026 m, Darcy velocity approximately doubles or more than doubles because these intervals possess relatively higher permeability and experience stronger pressure gradients generated by the injection process. In contrast, the interval at 1212 m exhibits only a modest increase of approximately 5%, suggesting lower injectivity associated with reduced permeability or higher shale content. These depth-dependent variations highlight the strong influence of petrophysical heterogeneity on fluid migration.

Figure 6 illustrates the spatial distribution of Darcy velocity (dl.U) as a function of radial distance from the CO_2 injection well for three representative reservoir depths. Darcy velocity is highest adjacent to the injection well and decreases progressively with increasing distance, reflecting the dissipation of the pressure gradient generated by continuous CO_2 injection. This trend is consistent with Darcy's law, which states that fluid velocity is directly proportional to the hydraulic pressure gradient. This rapid attenuation reflects the strong pressure gradient immediately surrounding the injector, while the slighter decrease at larger distances indicates progressive pressure equilibration within the reservoir. The observed variation among depths highlights the influence of vertical petrophysical heterogeneity on CO_2 transport. The figure demonstrates that CO_2 migration is primarily controlled by pressure-driven flow near the injection well and by reservoir heterogeneity farther from the well.

Table 4. Depth-wise variation in Darcy velocity before and after CO_2 injection, illustrating the influence of injection pressure and reservoir heterogeneity on fluid-flow behavior

S.N.	Depth (m)	Initial Darcy Velocity (mm/day)	Darcy Velocity after CO_2 Injection (mm/day)	Percentage Change (%)
1	1046	0.73685	1.47370	+100.0
2	1212	0.43344	0.45511	+5.0
3	1026	0.88855	2.22138	+150.0

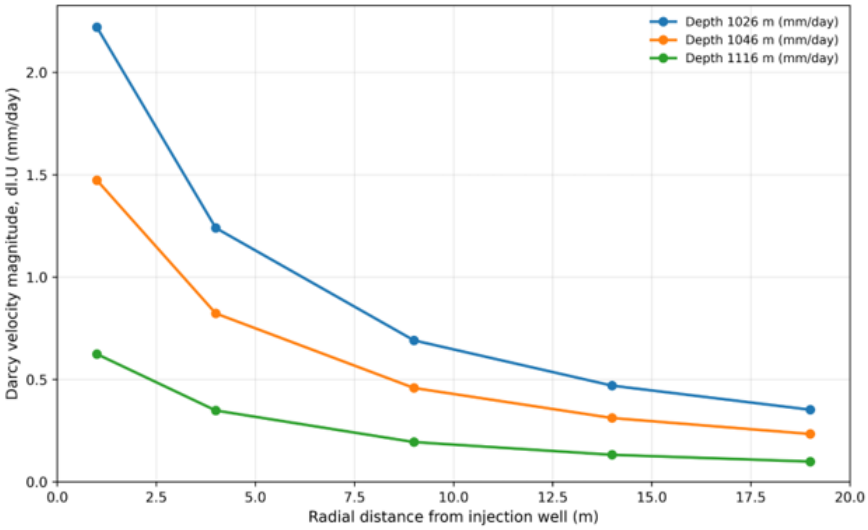


Figure 6. Variation of Darcy velocity magnitude (dl.U) with radial distance (x) from the CO_2 injection well at different reservoir depths

Table 5. Changes in reservoir petrophysical properties due to CO_2-induced mineral dissolution

Parameter	Initial Value	50 Years of CO_2 Injection	Absolute Change	Relative Change	Interpretation
Porosity (%)	22.00	22.08	+0.08 percentage	+0.40%	Minor enhancement due to dissolution of reactive minerals
Permeability (mD)	200	204	+4 mD	+1-2%	Slight increase in pore connectivity
Reservoir Injectivity	Moderate	Slightly improved	Small		Minor reduction in flow resistance
Storage Integrity	Stable	Stable			Caprock integrity remains unaffected

A mineral dissolution framework was incorporated into the numerical model to evaluate the geochemical effects of CO_2-rock interactions during long-term sequestration. Forward reaction-based simulations predict absolute porosity increases of 0.06-0.08 percentage points, corresponding to relative increases of approximately 0.1-0.4%, while permeability increases by approximately 1-2% over a fifty-year injection period. These results indicate that mineral dissolution exerts only a modest influence on the reservoir petrophysical properties over the simulated timeframe. Table 5 is based on initial porosity (22%) and permeability (200 mD), which are representative reservoir-average values. The percentage changes are based on forward reaction-based mineral-dissolution simulations over a 50-year CO_2 injection period.

DISCUSSION

The Cambay Basin is an intra-cratonic rift basin characterized by thick Eocene-Miocene sedimentary successions comprising alternating sandstone and shale units. The Ankleshwar oil field, one of the basin's major hydrocarbon-producing reservoirs, consists predominantly of Eocene sandstone sealed by regionally extensive shale formations. Following prolonged hydrocarbon production, reservoir pressure gradually declines, allowing saline formation water from the surrounding aquifer to occupy the depleted pore space. This transition creates favorable conditions for evaluating depleted reservoirs as potential sites for long-term geological CO_2 storage.

The log analysis demonstrates that the reservoir is highly heterogeneous and cannot be adequately represented by a single permeability value. Variations in Flow Zone Indicator (FZI), Reservoir Quality Index (RQI), porosity, permeability, and shale content reveal the presence of multiple hydraulic flow units with distinct storage and flow characteristics. To

capture this complexity while maintaining computational efficiency, the reservoir was represented using a three-layer numerical model, with each layer reflecting contrasting hydraulic properties derived from the petrophysical interpretation. Transient simulations were conducted using an initial reservoir pressure of 20.10 MPa, an injection pressure of 22.0 MPa, and a reservoir temperature of 75°C over a five-year injection period. Under these conditions, CO_2 remains in a dense supercritical state, maximizing storage efficiency while reducing buoyancy-driven migration. Adaptive mesh refinement around the injection well enabled accurate resolution of steep pressure gradients and near-well flow behavior without significantly increasing computational cost.

The simulation results clearly show that reservoir architecture exerts a fundamental control on CO_2 migration. Injected CO_2 preferentially propagates through the high-permeability sandstone of the lower reservoir, whereas the intervening shale-rich layer acts as an effective hydraulic barrier that limits vertical pressure transmission and upward plume migration. This behavior highlights the importance of stratigraphic heterogeneity in promoting secure geological storage by directing plume migration laterally within the target reservoir while preserving caprock integrity. The observed exponential decrease in Darcy velocity with increasing radial distance from the injection well further confirms that fluid movement is primarily governed by pressure gradients generated during injection.

Integrating geological observations, well-log interpretation, and numerical simulations demonstrates that permeability heterogeneity primarily controls pressure propagation and fluid-flow pathways, whereas porosity largely determines the available storage capacity. High-permeability intervals provide preferential migration pathways that enhance injectivity, while shale-rich intervals compartmentalize the reservoir and improve storage security by restricting vertical communication. The coupled reactive transport model indicates that CO_2-rock interactions have only a modest influence on reservoir properties over the fifty-year simulation period. Mineral dissolution results in slight increases in porosity and permeability, producing localized improvements in injectivity without significantly altering the reservoir's overall hydraulic behavior. Although these changes are relatively small, they demonstrate that geochemical processes gradually modify pore structure and may become increasingly important over longer storage timescales.

The spatial distribution of Darcy velocity further illustrates the interaction between hydraulic forcing and reservoir heterogeneity. From a reservoir management perspective, the results suggest that high-permeability, low-shale zones provide the most favorable targets for CO_2 injection. In contrast, shale-rich intervals contribute to long-term storage security by limiting unwanted vertical migration. Overall, this study demonstrates that integrating well-log interpretation, petrophysical characterization, pressure-dependent transient flow modeling, and coupled reactive transport provides a realistic framework for evaluating depleted hydrocarbon reservoirs as potential CO_2 storage sites. The combined approach improves understanding of pressure evolution, fluid migration, and geochemical alteration while supporting more reliable prediction of injectivity and storage performance. Although the present simulations represent a 50-year injection period, the methodology provides a robust foundation for future investigations.

CONCLUSIONS

1. An integrated reservoir characterization framework combining well-log interpretation, petrophysical analysis, and three-dimensional transient COMSOL modelling, successfully quantified fluid-flow behavior and CO_2 storage performance in the heterogeneous Ankleshwar reservoir.

2. Well-log analysis revealed significant reservoir heterogeneity, with porosity ranging from 14.4-25.6%, permeability from 143-336 mD, and interval-dependent shale distribution.

3. Flow Zone Indicator (FZI) and Reservoir Quality Index (RQI) effectively identified hydraulically favorable intervals, with the 1254 m zone in Well A.

4. Three-dimensional transient simulations demonstrated that injected CO_2 remained largely confined within the lower high-permeability reservoir, while the intermediate low-permeability layer effectively restricted vertical migration.

5. Darcy velocity increased significantly near the injection well owing to injection-induced pressure gradients and decreased rapidly with radial distance.

6. Mineral dissolution produced only minor geochemical alteration during the five-year simulation, increasing porosity by 0.06–0.08 percentage points (0.1-0.4%) and permeability by approximately 1-2%, indicating that

short-term CO_2–rock interactions slightly improve injectivity without compromising storage integrity.

7. High-permeability, low-shale intervals act as preferential flow pathways that enhance injectivity, whereas shale-rich intervals function as effective hydraulic barriers.
8. Overall, the study confirms that reservoir heterogeneity, permeability architecture, and shale distribution are the dominant controls on fluid flow and CO_2 migration, while geochemical reactions play a secondary but beneficial role.
9. The proposed integrated workflow offers a practical decision-support framework for reservoir screening, injection planning, enhanced oil recovery (EOR), and long-term geological CO_2 sequestration in depleted hydrocarbon reservoirs.
10. There are a few scopes to improve the work, as the results rely entirely on COMSOL simulations and there is a lack of validation in terms of production history, CO_2 injection field data, and published benchmarks.

Acknowledgment

The authors gratefully acknowledge the Indian Institute of Technology Roorkee, India, for providing laboratory facilities, computational resources, administrative support, and research infrastructure essential for this study. The authors also sincerely thank the Oil and Natural Gas Corporation Limited (ONGC), India, and the CSIR-National Geophysical Research Institute (CSIR-NGRI), Hyderabad, India, for providing the well-log data used in this research. The authors are deeply grateful to the Editor and the reviewers for their valuable comments, constructive suggestions, time, and the opportunity to revise the manuscript. Their insightful feedback significantly improved the quality of this work by strengthening the well-log interpretation and its integration with transient flow simulation, pressure-dependent permeability, and reactive transport modeling. These revisions have enhanced the scientific rigor, technical relevance, and overall contribution of the study to geological CO_2 storage and reservoir engineering.

Author credit statement

Tanmoy Chetia was responsible for data processing and analysis. Dr. Pallavi Banerjee Chattopadhyay provided valuable supervision, conceptualized the study, and wrote the manuscript. Nimisha Vedanti supplied the well log data and provided final editorial support. Aakash Jaiswal and A. D. Sarath Kumar contributed to the interpretation and analysis of well log data.

Data Availability

The unprocessed input data were provided by Oil and Natural Gas Corporation Limited (ONGC), India, and the computational facilities were provided by IIT Roorkee, India.

Comliance with Ethical Standards

We declare that there are no competing interests related to any financial concerns about the publication of the study. It is being declared that there are no personal relationships with people or organizations that may influence or may be perceived to influence the research work described in this paper. We adhere to copyright norms.

References

Abdelghany, W. K., Radwan, A. E., Elkhawaga, M. A., Wood, D. A., Sen, S. and Kassem, A. A., 2021, Geomechanical modeling using the depth-of-damage approach to achieve successful underbalanced drilling in the Gulf of Suez rift basin. J. Petrol. Sci. and Engin., 196, Article 108311.

Ali, J., Ashraf, U., Anees, A., Peng, S., Umar, M. U., Vo Thanh, H., Khan, U., Abioui, M., Mangi, H. N. and Ali, M., 2022. Hydrocarbon potential assessment of carbonate-bearing sediments in the Meyal Oil Field, Pakistan: Insights from logging data using machine learning and quantitative petrophysical modeling: ACS Omega, 7, 39375–39395.

Bargees, A., Harishidayat, D., Iqbal, N. and Al-Shuhail, A. A., 2023. Automatic gas chimney detection from 3D seismic reflection data using a single amplitude attribute: Marine Petrol. Geol., 152, Article 106231.

Boswell, R., Schoderbek, D., Collett, T. S., Ohtsuki, S., White, M. and Anderson, B. J., 2017. The Ignik Sikumi field experiment, Alaska North Slope: Design, operations, and implications for CO_2–CH_4 exchange in gas hydrate reservoirs: Energy & Fuels, 31, 140–153.

Chanda, S. and Singh, R. P., 2019, Prediction of gas production potential and hydrological properties of a methane hydrate reservoir using an ANN–GA-based framework. Thermal Sci. Engin. Progress, 11, 380–391.

Collett, T. S., Boswell, R., Waite, W. F., Kumar, P., Roy, S. K., Chopra, K., Singh, S. K., Yamada, Y., Tenma, N., Pohlman, J. and Zyrianova, M., 2019. India National Gas Hydrate Program Expedition 02: Summary of scientific results from gas hydrate systems along the eastern continental margin of India. Marine Petrol. Geol., 108, 39–142.

Delavar, M. R., 2022. Hybrid machine learning approaches for classification and detection of fractures in carbonate reservoirs. J. Petrol. Sci. Engin., 208, Article 109327.

Dixit, G., Ram, H. and Kumar, P., 2019, Origin of gas in gas hydrates as interpreted from geochemistry data obtained during the National Gas Hydrate Program Expedition 02, Krishna–Godavari Basin, offshore India. Marine Petrol. Geol., 108, 389–396.

Ganguli, S. S., Vedanti, N., Pandey, O. P. and Dimri, V. P., 2018. Deep thermal regime, temperature-induced overpressured zones, and implications for hydrocarbon potential in the Ankleshwar Oil Field, Cambay Basin, India. J. Asian Earth Sci., 161, 93–102.

Jain, V., Saumya, S., Vij, J., Singh, J., Singh, B., Pattnaik, S., Oli, A., Kumar, P. and Collett, T. S., 2019. A new technique

for accurate porosity estimation from logging-while-drilling nuclear magnetic resonance data, NGHP-02 Expedition, offshore India. Marine Petrol. Geol., 108, 570–580.

Jin, G., Xing, H., Li, T., Zhang, R., Liu, J., Guo, Z. and Ma, Z., 2022. An integrated approach of numerical well testing for wells intersecting fractures based on FMI images. Lithosphere, 2021, Article 4421135.

Kamal, M. M., Morsy, S., Suleen, F., Pan, Y., Dastan, A., Stuart, M. R., Mire, E. and Zakariya, Z., 2019, Determination of in-situ reservoir absolute permeability under multiphase-flow conditions using transient well testing: SPE Reservoir Evaluation & Engin. 22, 336–350.

Kim, Y., Jang, H., Kim, J. and Lee, J., 2017. Prediction of storage efficiency for CO_2 sequestration in deep saline aquifers using artificial neural networks: Appl. Energy, 185(1), 916–928.

Mohan, R., Tiwari, S. N. and Mayor, S., 2008. Evidences of multiple phases of basin inversion in the Narmada Block, South Cambay Basin, Gujarat, India. Proc. Int. Conf. and Exposition on Petrol. Geophys., Hyderabad, p. 1–7.

Nair, P. V. and Srivastava, D. K., 2024. Cambay Basin, India: Geological review and exploration potential of a moderately explored hydrocarbon province. Int. J. Sci. Res., 14(4), ISSN 2319-7064.

Radwan, A. E. and Sen, S., 2021. Stress path analysis for characterization of in situ stress state and the effect of reservoir depletion on present-day stress magnitudes: Reservoir geomechanical modeling in the Gulf of Suez Rift Basin, Egypt. Natural Resources Res., 30, 463–478.

Sen, S., Kundan, A. and Kumar, M., 2020. Modeling pore pressure, fracture pressure, and collapse pressure gradients in offshore Panna, western India: Implications for drilling and wellbore stability. Natural Resources Res., 29, 2717–2734.

Xu, Z., Li, S., Li, B., Chen, D., Liu, Z. and Li, Z., 2020. A review of development methods and enhanced oil recovery technologies for carbonate reservoirs: Petrol. Sci., 17, 990–1013.

Received on: 09-07-2025; Revised on: 27-07-2026; Accepted on: 03-08-2026

J. Ind. Geophys. Union, 30(6) (2026), 474-488
http://doi.org/10.71122/JIGU.30(6)2026.0047

Magnetic methods in delineation and depth assessment of Banded Iron Formation: A case study from Sonbhadra District (Uttar Pradesh), India

Gautam Kumar*, C. B. Tiwari, S. P. Chaubey and Tashmeet Kaur
Geological Survey of India, Northern Region, Vasundhara, Sector E, Aliganj, Lucknow-226024, India
* Corresponding author: gautamphy21@gmail.com

ABSTRACT

The objective of the present survey is to apply ground magnetic method for delineating the Banded Iron Formation (BIF) and to trace its subsurface extensions and depth using various processing techniques. A total of 22 line kilometres were covered with traverse spacing of 100 to 200 m and a station interval of 20 m. The study area lies within Toposheet No. 63L/14, bounded by 24°33'06.70"N - 24°33'50.00" N and 82°48'32" E - 82°51'40"E. Magnetic contour maps reveal anomalies ranging from –6168 nT to +3228 nT, predominantly trending ENE-WSW. A major magnetic high occurs in the central part of the area, with a parallel high in the south, both separated by a strong E–W magnetic gradient, interpreted as a contact zone. Residual anomaly maps highlight shallow, patchy sources attributed to iron-bearing formations. Traverses E1–E18 display strong anomalies associated with Banded Hematite Jasper (BHJ) and Banded Hematite Quartzite (BHQ), while ferruginous phyllites show responses exceeding 1000 nT. In contrast, northern areas under weathered dolerite/phyllite, exhibit weak anomalies (<100 nT), reflecting lithological diversity. Interpretation using Radially Averaged Power Spectrum (RAPS), Euler 3D deconvolution, P-depth sections, SPI and magnetic inversion, indicates predominantly shallow to intermediate magnetic sources, with RAPS identifying principal source-depth levels at approximately 18, 37, 75 and 175 m, while the 3D inversion indicates high-susceptibility sources extending locally to about 140 m depth. High magnetic anomalies are consistent with magnetite-rich iron ore bodies. Boreholes (BH1, BH2, BH4, BH6) drilled in anomaly zones, confirm a close correlation between strong magnetic signatures and iron ore mineralization. The integration of magnetic data and borehole validation, establishes the potential of the surveyed area for iron ore exploration, providing reliable constraints on the depth, extent, and quality of mineralization.

Keywords: Ground magnetic survey, Mahakoshal Group, Banded Iron Formation (BIF), Euler 3D deconvolution, SPI, P-depth, Inversion, Sonbhadra district

INTRODUCTION

Iron ore, particularly that associated with Banded Iron Formations (BIFs), is an important raw material for steel production and a key mineral resource for economic development. In India, BIF-hosted iron ore deposits are widely distributed in Precambrian terrains, including the Central Indian Tectonic Zone (CITZ). The Mahakoshal Group within the CITZ, is an important volcano-sedimentary sequence hosting BIF horizons and associated iron mineralisation, making it a significant domain for iron-ore exploration. In Sonbhadra district (Uttar Pradesh), the Mahakoshal Group occurs along the Vindhyan–Mahakoshal interface, where BIF horizons are associated with metavolcanic, metasedimentary and mafic intrusive rocks. These BIFs, containing hematite and locally magnetite-rich bands, represent important targets for assessing the iron-ore potential of this relatively less explored part of the CITZ.

Geophysical methods, particularly gravity and magnetic techniques, are widely employed in mineral exploration because they provide effective, non-invasive means of characterising subsurface lithological variations, geological structures and concealed mineralised bodies (Grant and West, 1965; Paterson and Reeves, 1985; Nabighian et al., 2005; Mandal et al., 2015; Biswas and Sharma, 2016; Singh, 2019). Among these, the magnetic method is particularly well suited to BIF-hosted iron mineralisation, as iron-bearing minerals such as magnetite, hematite, titaniferous magnetite, goethite and limonite, generate susceptibility contrasts with surrounding relatively non-magnetic rocks. These contrasts enable the delineation of BIF horizons, magnetite-rich bodies and associated structural features such as folds, faults and dykes, as demonstrated in various geological settings (Wennerström and Airo, 1998; Prevec and Morris, 2001; Grauch, 2002; Betts et al., 2003).

The Mahakoshal Group has been the subject of extensive geological and geophysical investigations aimed at understanding its tectonic framework, structural evolution and geological history (Nair et al., 1995). In the Sonbhadra region, previous studies have primarily involved geological mapping and reconnaissance-scale geophysical investigations by the Geological Survey of India (GSI) during successive Field Seasons. Notably, gravity and magnetic surveys conducted during Field Season 2009–2012, identified a prominent gravity high associated with elevated magnetic responses in the southern part of Toposheet No. 63 L/14, which was interpreted in relation to BIF bands of the Mahakoshal Group (Bhattacharya et al., 2012). This finding highlighted the potential for concealed BIF-hosted iron mineralisation and provided a basis for further detailed investigation. However, the lateral continuity and depth extent of the BIF horizons and associated mineralisation, remain inadequately constrained.

The present study aims to delineate BIF horizons, trace their subsurface extensions, and estimate the depth of iron

mineralisation in the Sobhna–Chakariya–Khoriya area of the Mahakoshal Group, Sonbhadra district, Uttar Pradesh, using detailed ground magnetic data. The study involves systematic magnetic data acquisition along closely spaced profiles, followed by data processing and enhancement using various filters and qualitative and quantitative interpretation techniques, including Radially Averaged Power Spectrum (RAPS), Euler deconvolution, P-depth and magnetic inversion. Integration of the magnetic results with available geological information, facilitates the identification and characterisation of potential BIF-hosted iron mineralisation zones in terms of their lateral extent and depth. The results are expected to improve understanding of the subsurface geometry of BIF and provide a cost-effective basis for targeting future drilling and mineral exploration. The study area falls within Toposheet No. 63L/14 and is bounded by 24° 33' 06.70"N to 24° 33' 50.00" N and 82° 48' 32"E to 82° 51' 40" E, as demarcated in Figure 1

GEOLOGIC SETTINGS AND IRON ORE MINERALISATION

The Sonbhadra district, southeastern part of Uttar Pradesh, forms part of the Central Indian Tectonic Zone (CITZ) and the study area lies within the Paleoproterozoic volcano-sedimentary Mahakoshal Group, intruded by mafic–ultramafic bodies and later dykes. Mahakoshal Group records three major deformation phases, comprising E–W to ENE–WSW-trending upright to gently inclined folds, followed by vertical to reclined folds and later broad warps and small-scale N–S-trending folds (Roy and Bandyopadhyay, 1990). Several syn- to post-kinematic granitoids, including Barambaba granite, Jhirgadandi monzodiorite–quartz syenite, Rihand–Makhrohar–Sigrauli granodiorite, Muirpur Granite, Sidhi granitoid and Dudhi Granite Gneiss, intrude the Mahakoshal succession, along with younger Bari–Ainti syenites (Pandey et al., 1998; Sarkar et al., 1998).

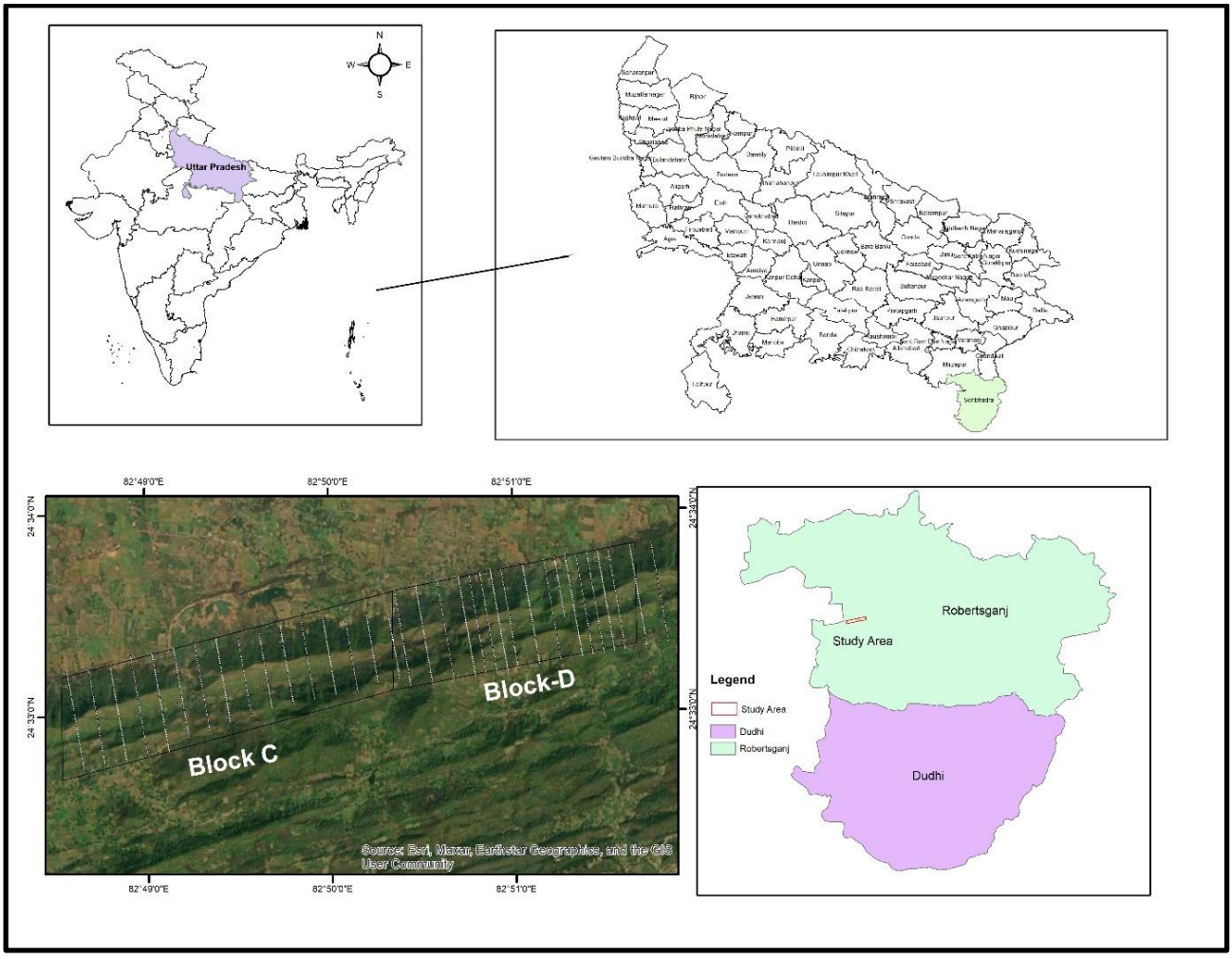


Figure 1. Location Map of the study area (not to scale)

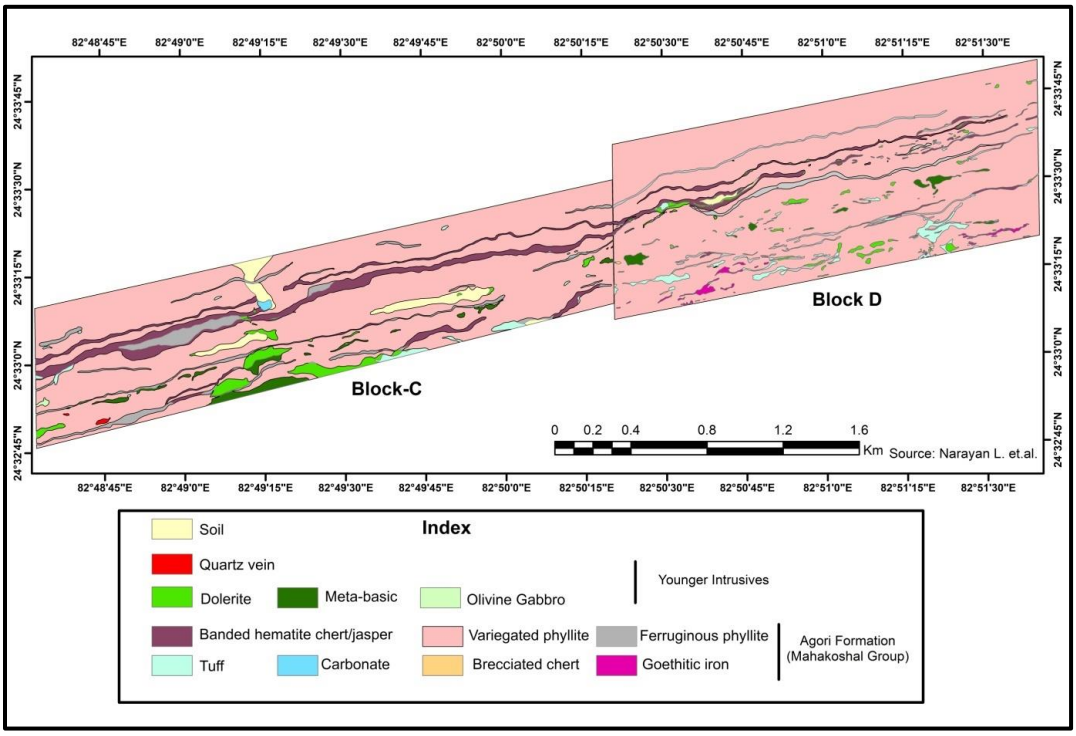


Figure 2. Geological map of the study area

The study area belongs to the Agori Formation, exposed between the Son Fault to the north and the Obra–Amsi–Jiwan Fault to the south. The Geological map of study area is presented in Figure 2. The BIF bands in Blocks C and D form part of a ~20-km-long BIF zone extending from NW of Bijaura to Bharhari. These BHC/J (banded hematite chert/ jasper) horizons generally trend ENE–WSW, with moderate to steep southerly dips, and occur along the northern flank of the Mahakoshal ridge, south of the Son–Narmada North Fault. They are closely associated with variegated and ferruginous phyllite, tuff, dolerite and metabasic intrusions; the most continuous BHC/J horizon occurs near the ridge top, whereas discontinuous exposures occur towards the eastern part of Block D (Prajapati and Ahmad, 2023; Narayan and Ahmed, 2025). However, their subsurface geometry, lateral continuity and depth extent remain poorly constrained, necessitating detailed geophysical investigation.

DATA ACQUISITION AND METHODOLOGY

The magnetic survey was conducted to assess the iron ore potential in Sobhna-Chakariya-Koriya region of Sonbhadra district, Uttar Pradesh. The survey was conducted in two phases, with data for Block C collected under the Geological Survey of India's Field Season Programme 2022–23, and for Block D in the Field Season Program 2023–24. Both blocks are located within the BIF bearing corridor of Sonbhadra district, Uttar Pradesh, India. The layout of the geophysical survey is presented in Figure 3. The baseline was laid in the N80°E direction, and the traverses were laid perpendicular to the baseline, i.e., N10°W direction at a regular intervals of 100 m to 200 m, with station spacing at 20 m. The total length of baseline/ strike length laid was 5.5 km, with a total of 28 primary profile lines ranging in length from 650 m to 950 m. Additional six secondary profile lines of 500 m to 900 m long, were also laid to overlap the two blocks and verify the continuity of the anomaly. Magnetic data were acquired using a Proton Precession Magnetometer with a sensitivity of ±0.01 nT.

The instrument was operated in scalar mode to record the Total Magnetic Intensity (TMI) at each station. A fixed base station was established in a magnetically quiet zone to monitor diurnal variations during the survey. The magnetic data were reduced to the magnetic base established outside of the area under survey. After diurnal correction, the International Geomagnetic Reference Field (IGRF) model 2020, using Seequent (2023) Oasis Montaj Geosoft software, was applied to remove the geomagnetic field (also called the regional magnetic field), thereby obtaining the magnetic field anomaly due to the local source. The corrected magnetic data were gridded using a minimum curvature grid cell size of 25 m. The data processing and preparation of the total intensity magnetic map and other derivative maps were done using Microsoft Office (Excel) and Oasis Montaj Geosoft software.

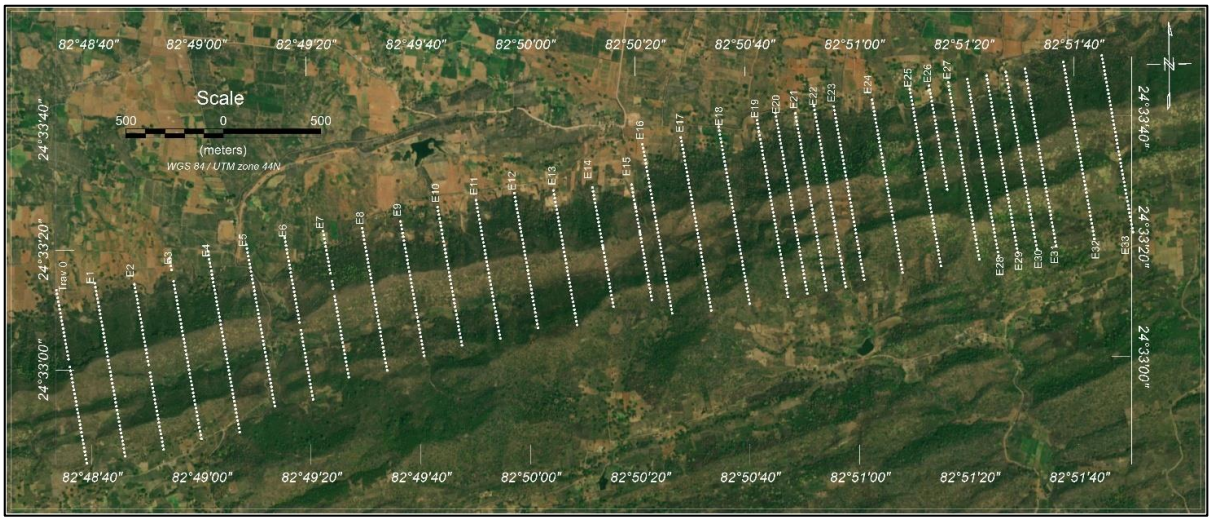


Figure 3. Geophysical layout map of the study area

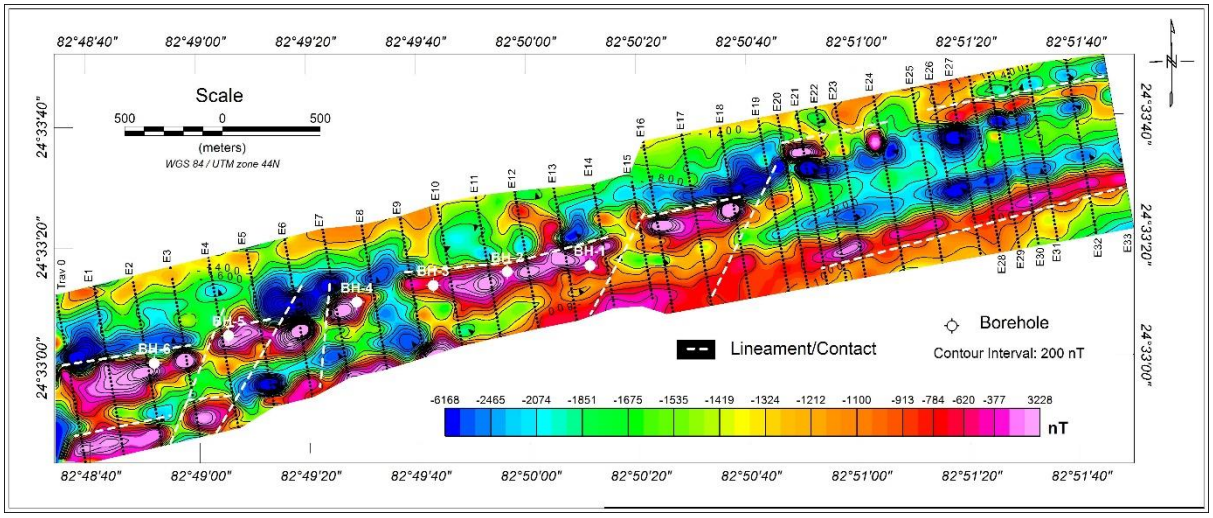


Figure 4. Magnetic anomaly contour map of the study area**.**

QUALITATIVE INTERPRETATION

Total magnetic intensity anomaly map

The Total Magnetic Intensity (TMI) anomaly contour map is shown in Figure 4. It is observed that magnetic anomalies vary from −6168 nT to 3228 nT. The high TMI anomaly is dominant in the central and southern parts of the study area, corroborated by the ENE-WSW trending BIF band. The northern part of the study area is dominated by a low magnetic anomaly, which corroborates the presence of phyllite at the surface. In the study area, two ENE-WSW trending high magnetic linear zones continue across almost all traverses, and the general trend of these anomalies (ENE-WSW) is well corroborated by the geological formations. The shapes of magnetic anomalies are elliptical with ENE-WSW strike and lie over the BIF/ferruginous body/ dolerite. The high magnetic anomalies are indicated in red to pink colour, which may be due to responses from the BIF. The contours in the central and southern parts of the block show a high gradient representing the shear zone/lithological contact. The consistent orientation of magnetic highs and lows indicates a dominant regional structural trend that aligns with the known tectonic trends, probably the Son-Narmada North Fault system. A third linear magnetic high is observed in the northern part, between traverses E20 and E33. This anomaly may be related to NE–SW subsurface structural disturbances and is likely to be associated with BIF or other iron-rich rocks. The pronounced E–W magnetic gradient marks a contact zone, interpreted as a structural or lithological boundary. In contrast, a NE-SW trending lineament may reflect structural disturbances in the subsurface.

Residual map of total magnetic intensity (TMI)

The residual TMI map was generated using a high-pass filter with a cut off wavelength of 500 m in the MAGMAP module of Geosoft. The cutoff wavelength was selected based on the RAPS analysis, which enabled the identification of magnetic sources at different depth levels. A wavelength of 500 m (equivalent to 2 cycles/km) was therefore adopted to enhance short-wavelength magnetic anomalies associated with relatively shallow sources while attenuating the contribution from deeper-seated sources. The residual TMI map (Figure 5) highlights shallow magnetic variations associated with BIF/BHJ and other susceptibility contrasts. Several high and low magnetic patches present in the Residual TMI map (Figure 5) indicate that the magnetic materials (BIF/BHJ) are in discontinuous and formed at variable depths in the study area. Their continuity across multiple traverse lines suggests a fairly uniform structural trend. The moderately high magnetic anomaly (Figure 4) in the central part of traverses E20 to E33 appears as a high magnetic anomaly in the residual magnetic map (Figure 5) and is attributed to BIF bands. The high anomaly in the northern part, from traverses E20 to E33, is attributed to a separate BIF anomaly zone. Hence, in the residual magnetic anomaly map, three linear magnetic anomalies are observed and attributed to the presence of the BIF band in the study area.

Analytic signal of residual magnetic anomaly

The analytic signal (Figure 6) was used to delineate the boundaries of magnetic sources and BIF units, owing to its reduced dependence on magnetization direction. High-amplitude zones (>17.9nT/m) indicate areas with potential for mineralisation (Dentith and Mudge, 2014), whereas lower amplitudes correspond to regions devoid of significant magnetic bodies. High analytical signal values have been observed in the central part due to contrasting susceptibilities of BIF and ferruginous phyllites, relative to greywacke argillite.

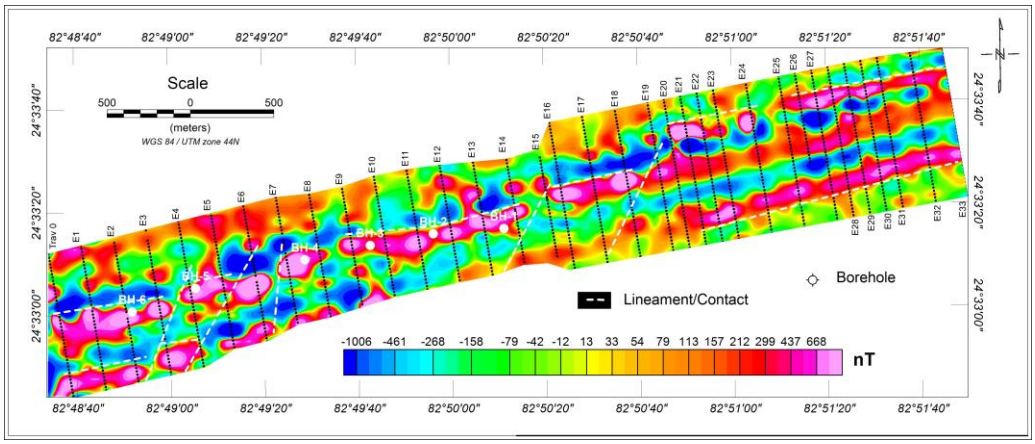


Figure 5. Residual map of magnetic data of the study area

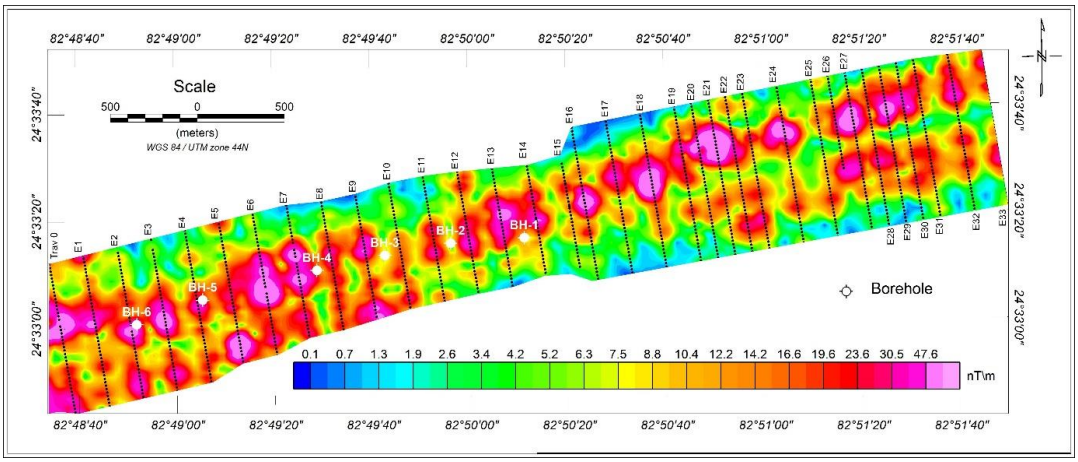
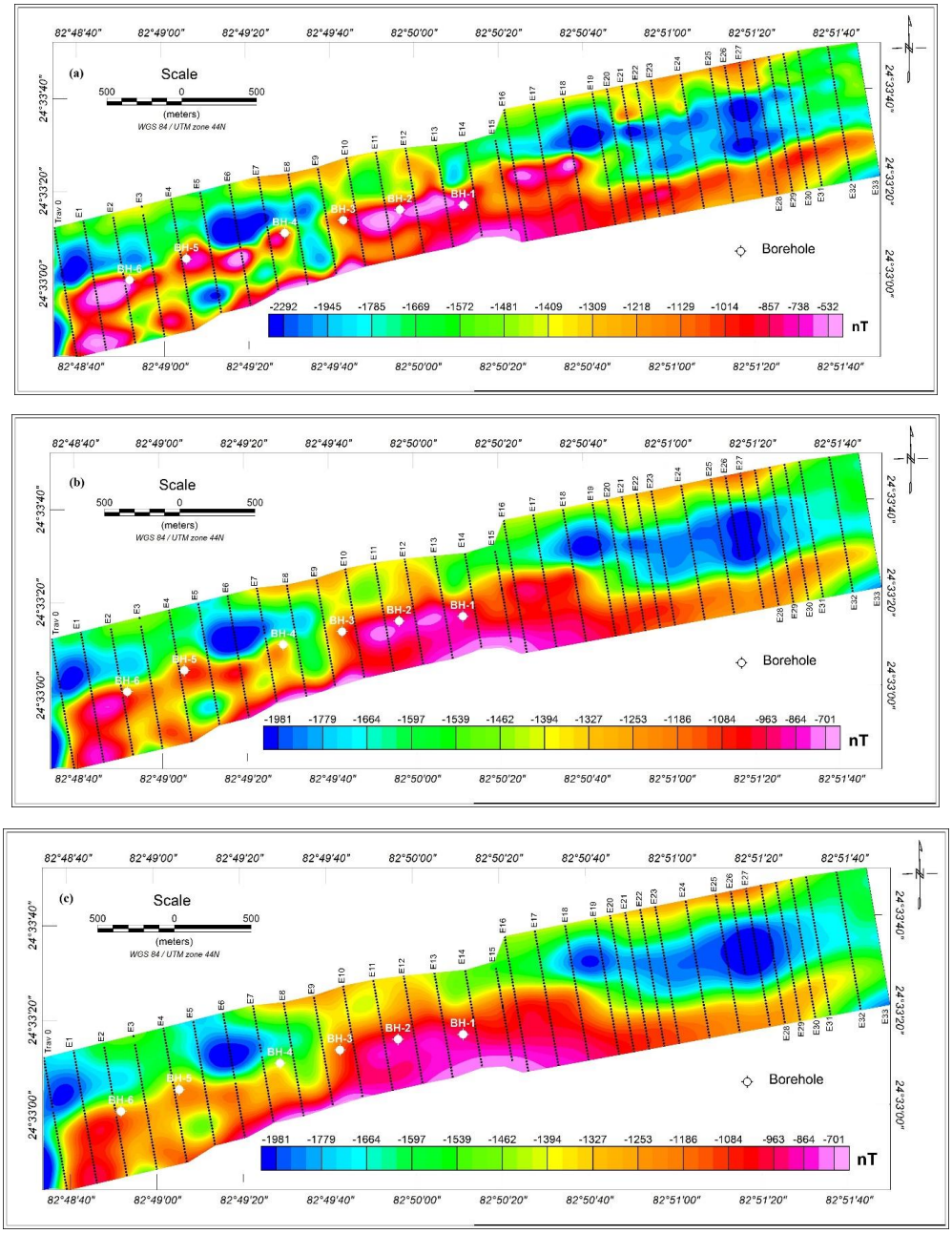


Figure 6. Analytic Signal map of the magnetic anomaly of the study area

Upward continuation of magnetic anomaly

Upward continuation is a technique used to separate regional magnetic anomalies caused by deep sources from the observed magnetic field. Upward continuation is an effective method for regional-residual separation, separating causative sources of various depths (Jacobsen, 1987). By applying this technique, high-frequency signal components associated with shallow magnetic features are attenuated, and deep regional-scale magnetic anomalies tend to be highlighted. It is particularly useful in noise attenuation and source separation. The magnetic anomaly data were upward-continued to elevations of 50 m, 100 m, 150 m, and 200 m (Figures 7a- d). With increasing continuation height, the influence of shallow features gradually diminished. At 200 m continuation (Figure 7d), most of the short-wavelength anomalies were suppressed, suggesting that the majority of the causative sources lie within the upper 100 m.



(Contd.)

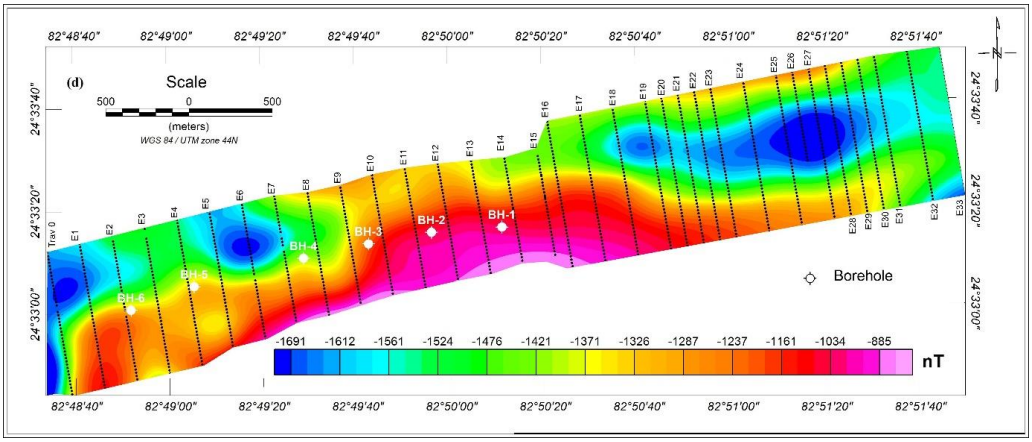


Figure 7. Regional magnetic anomaly map by upward continuation to a height of **(a)** 50m, **(b)** 100m, **(c)** 150m and **(d)** 200m.

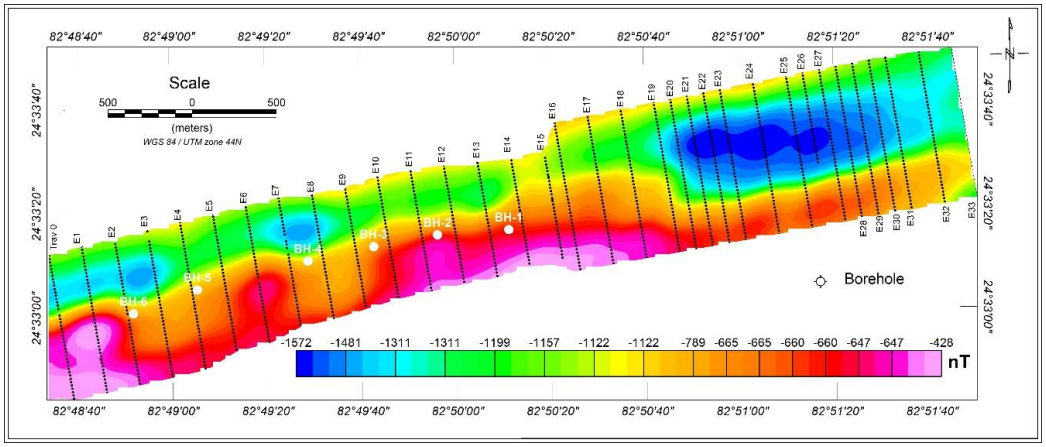


Figure 8. Aeromagnetic map of the study area

Aeromagnetic map of the study area

The aeromagnetic survey over the study area was conducted under the Geological Survey of India's flagship National Aeromagnetic Programme (NAGMP), covering Survey Block 3. The survey was carried out at a terrain clearance of approximately 80 m above ground level (AGL) with a traverse-line spacing of 300 m (Source: Geodata India). The aeromagnetic map of the study area is presented in Figure 8. The aeromagnetic survey exhibits a relatively regional response comparable to the ground magnetic field upward-continued to 150–200 m. The wider line spacing and higher survey altitude limit its ability to resolve near-surface BIF-related anomalies, which are better delineated by the ground magnetic data.

Radially averaged power spectrum (RAPS)

Data have been transformed into the wavenumber domain to determine the source depth of the dominant frequencies. The RAPS of the magnetic anomaly shown in Figure 9, where the depths are statistically estimated as a function of the wavenumber. The RAPS-derived source depth estimates reveal four significant susceptibility contrast levels, occurring at approximately 18 m, 37 m, 75 m, and 175 m. The histogram of the depth obtained from RAPS reveals a right-skewed distribution with a long tail. Most of the depths are concentrated in the 0-50 m range, while a few depth values are beyond 100 m, 150 m, 200 m and 300 m. The frequency sharply decreases with depth. The majority of observations are very shallow, indicating that most of the sources lie at depths of less than 100 m.

3D-Euler depth solutions of magnetic (TF) data

To locate and estimate the depths of geological bodies/structures, the Euler 3D deconvolution operation is applied to magnetic data in the frequency domain. This method generates many solutions from a large database and

performs clustering, providing a three-dimensional visualization of the source depths (Fitzgerald et al., 2004). Several attempts have been made to obtain Euler solutions using the Euler 3D module of Geosoft Oasis Montaj Software with different window sizes and Structural Index (SI) values. Finally, a window length of 250 m and structural index of 1, window size = 10, and depth tolerance = 10% for TMI data has been selected, which has produced the better solutions and superimposed over the TMI anomaly contour map of the study area and shown in Figure 10a. It is clear that, for the Euler-3D solution of magnetic data, most of the depth solutions for the causative sources lie in the range of 30-75m depth; however, some reflection from deep causative sources greater than 75m depth, is mostly due to the dolerite dykes present in the area. The depth solutions are falling over the magnetic gradient at different locations, representing contacts/shear and other linear patterns. It reveals that the depth of lithological contact of the anomalous sources with the host rock ranges from 30 m to 75 m.

The depth histogram (Figure 10b) confirms predominance of shallow-to-intermediate sources, with the highest concentration around 55–65 m and fewer deeper solutions extending to 120–160 m. The dominance of sources within the 30–80 m interval, implies that the principal magnetic anomalies are controlled by moderately shallow geological structures, possibly associated with ferruginous lithologies or mineralized horizons. The presence of deeper solutions, though less frequent, may indicate structurally controlled features such as faults, shear zones, or deep-seated magnetic intrusions that contribute to the anomaly field.

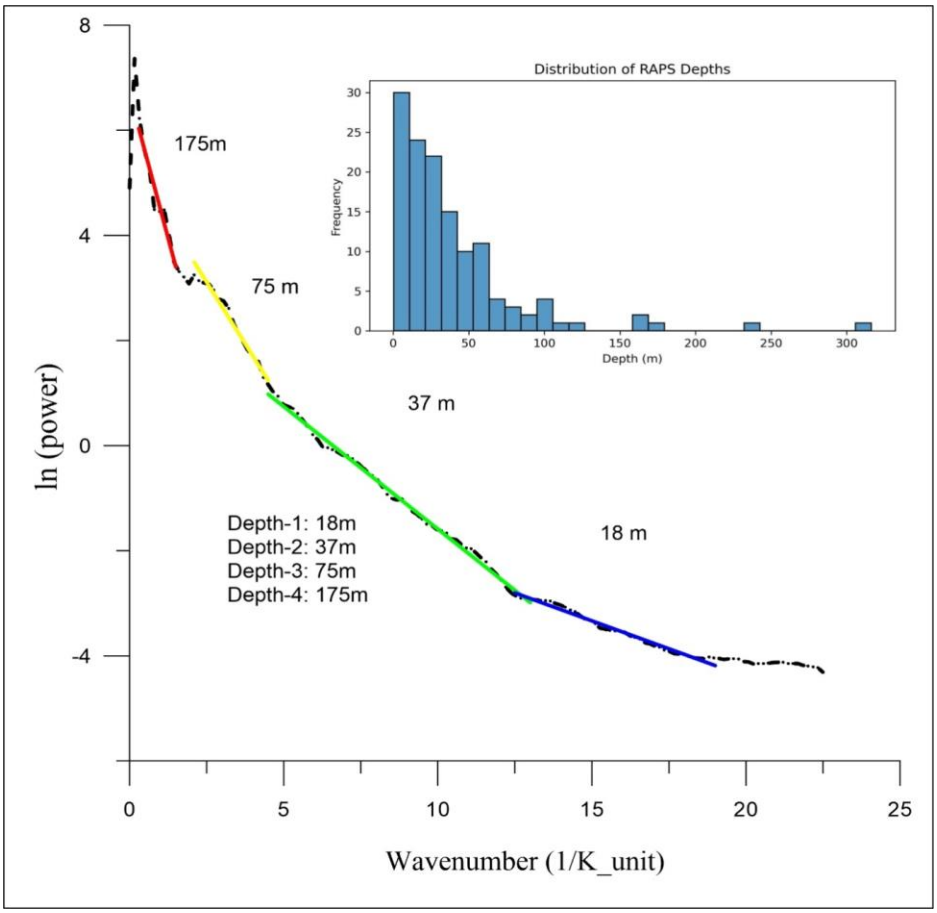


Figure 9. Radially averaged power spectrum of total magnetic intensity

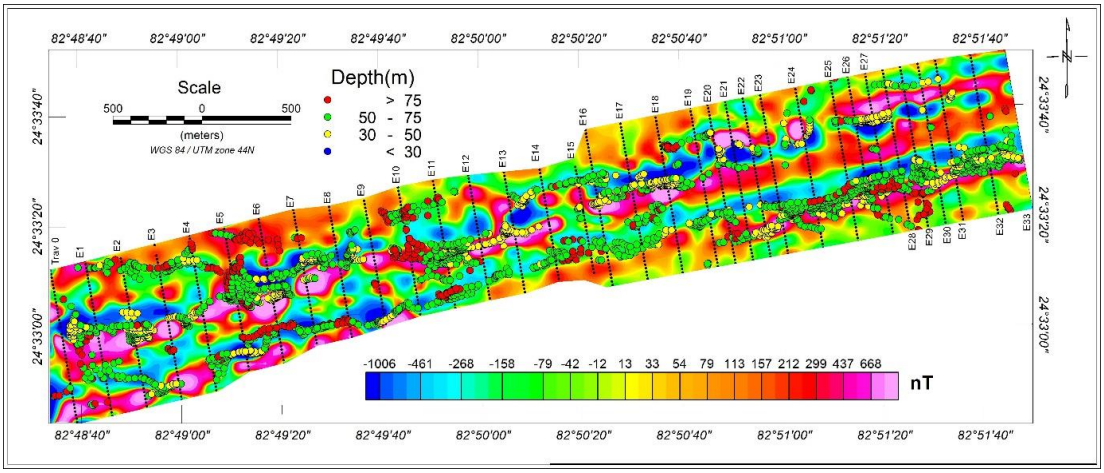


Figure 10a. 3D Euler Depth solution of magnetic data of the study area (Window Length: 250m, SI=1)

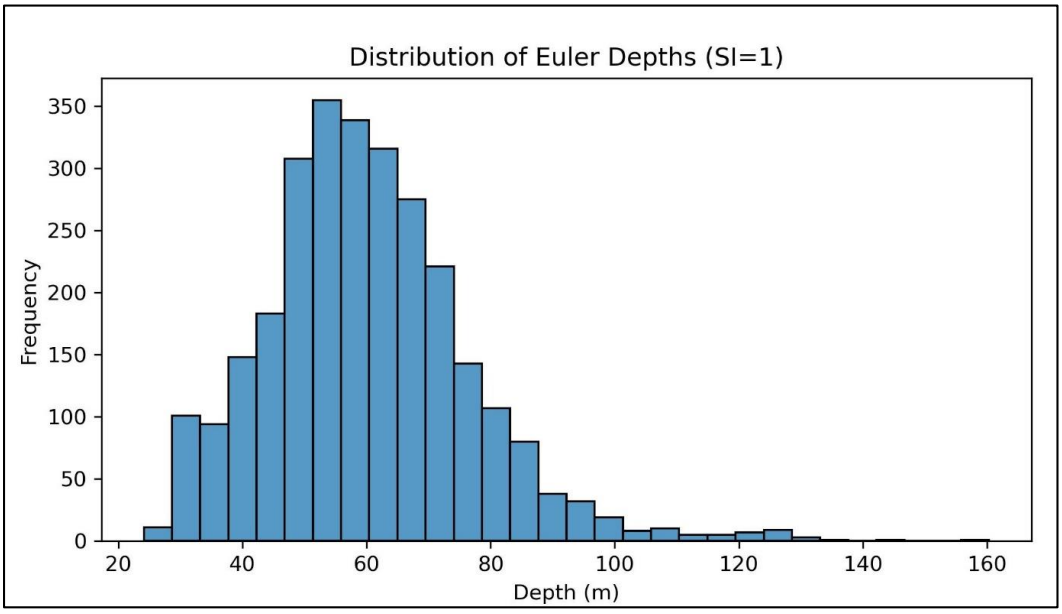


Figure 10b. Histogram of 3D Euler Depth solution of magnetic data of the study area

Source parameter imaging (SPI) of total magnetic intensity data

SPI method estimates the depth of magnetic sources by using the local wavenumber derived from an analytical signal. It is a fast, straightforward, and effective method for calculating depth (Thurston and Smith, 1997). SPI depth has been calculated and shown in Figure 11a, which reveals spatial distribution of depths to magnetic sources in the subsurface. The map clearly shows that the magnetic sources in the central part of the study area occur at shallower depths, compared to those in the northern part. The central part of the area is covered by BIF and ferruginous phyllite, while the northern part is covered by alluvium. A slightly greater source depth is observed near traverses E11 and E20–E23, indicating possible subsurface disturbances in the area.

The histogram of the depth distribution obtained from the SPI (Figure 11b), indicates predominance of shallow anomalies within the study area. The majority of sources are confined to depths between 20 m and 40 m, with peak concentrations in the 25–35 m interval, reflecting the influence of near-surface lithological units such as BIF and ferruginous phyllite. A gradual decline in frequency is observed between 40 m and 60 m, beyond which the number of sources decreases sharply. Sparse occurrences are detected at depths exceeding 100 m, suggesting localised structural disturbances or the presence of deep-seated magnetic bodies.

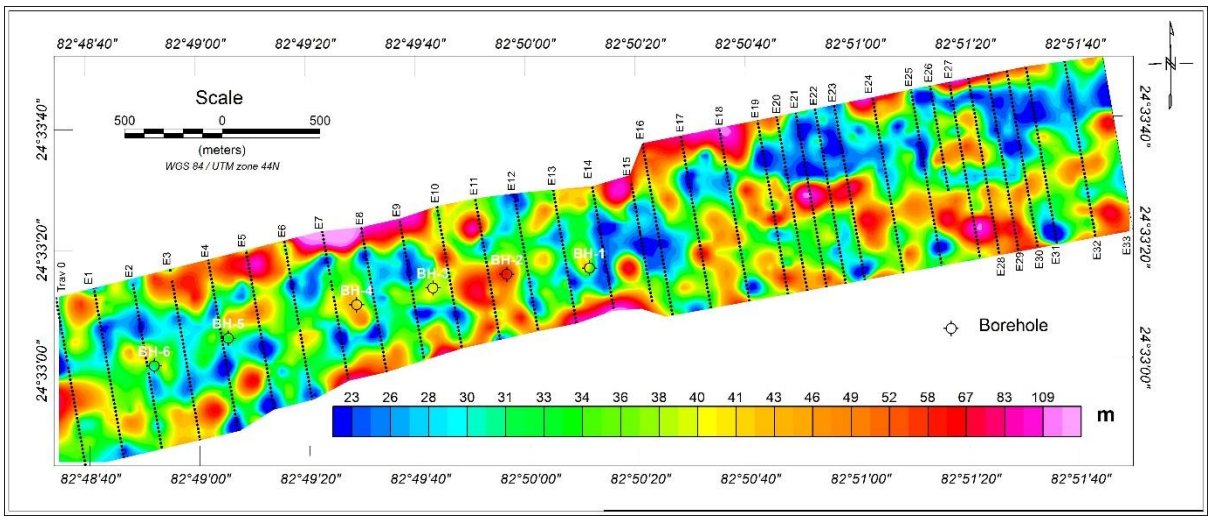


Figure 11a. Source parameter imaging **(**SPI) depth map of the study area

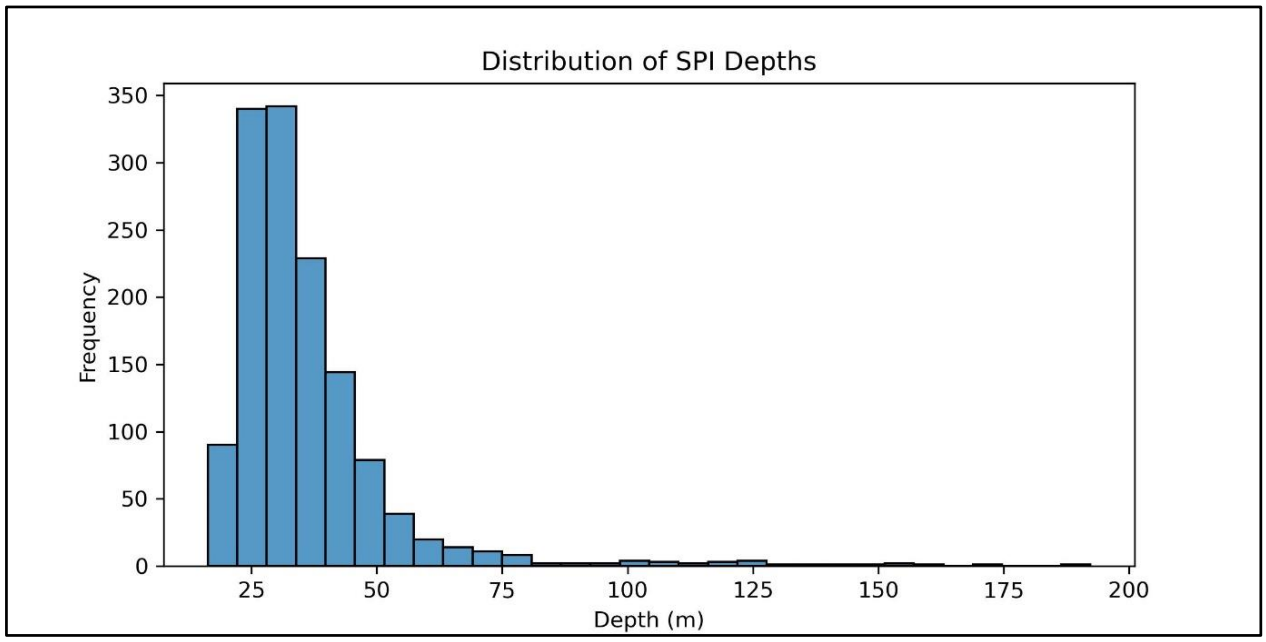


Figure 11b. Histogram of source parameter imaging (SPI) depth of the study area

Profile depth to basement (P-depth) of total magnetic intensity data

In this study, the analytic signal and the Werner Deconvolution methods were applied to estimate basement depths along selected profiles. Both approaches indicate that the source body corresponds to a finite, large dyke or a contact. The profile intersects BIF zones, as evidenced by high magnetic anomalies (MA) and elevated topography. For profile E2 (Figure 12), the analytic signal solutions suggest contact depths ranging from 8 m to 224 m, while Werner solutions indicate a shallower range of 1 m to 71 m. For the dyke, the analytic signal results, show depths ranging from 4 m to 156 m, whereas the Werner method estimates depths between 20 m and 98 m. These results suggest that the subsurface is dominated by significant dykes and contacts associated with BIF zones, which exert strong structural and lithological control on the observed magnetic anomalies.

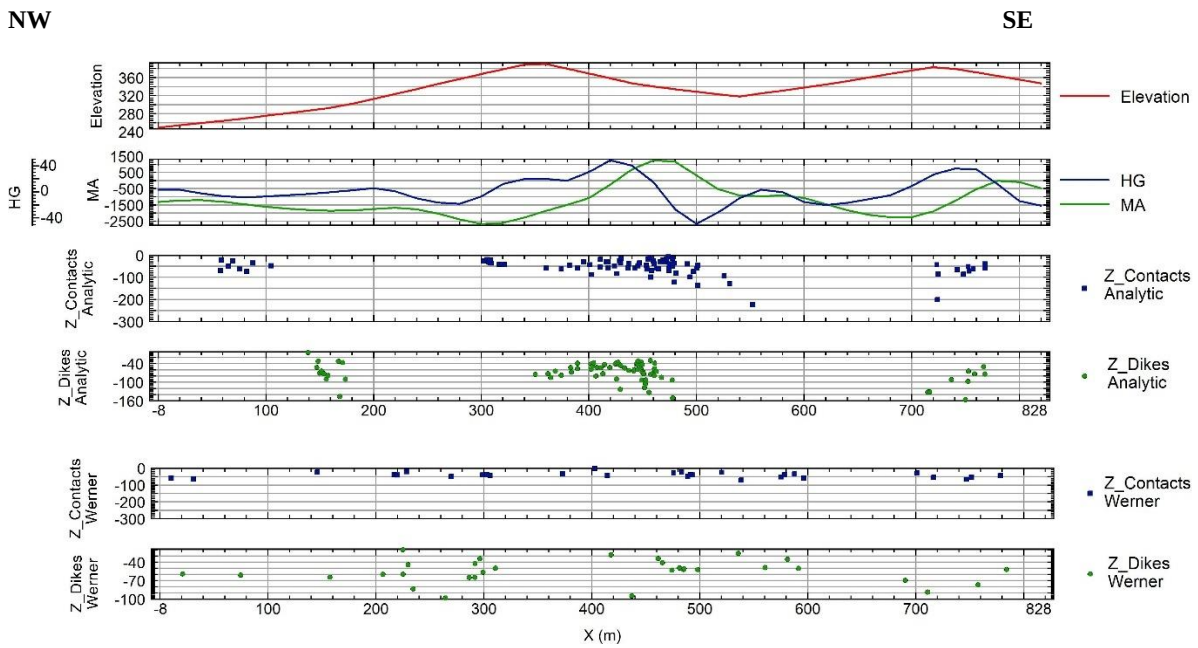


Figure 12. Depth calculated through the P-depth module using analytic signal and the Werner solution on profile E2.

3D geophysical modelling

To produce a 3D geometry model of the BIF for the study area, a 3D inversion using Oasis Montaj Geosoft was performed over the entire block (Figure 13a). The inversion algorithm assumes that there are no remnant magnetization or demagnetization effects present and magnetic data are produced only by induced magnetization (IGRF= 47211 nT, I=38.8, D=0.2). The topographic surface of the study area was incorporated into the 3D inversion model using the SRTM World Elevation 3 Arc-Second DEM. The elevation across the study area ranges from 214 to 460 m above mean sea level. The inversion mesh therefore follows the actual topographic relief, and the Z-coordinates/depths of the recovered susceptibility distribution are referenced to the SRTM-derived surface at each location. Thus, the reported depths represent distances below the local ground surface. The earth model is discretized horizontally in the X and Y directions at 25 m and in the Z direction at 12.5 m. The inversion is presented as a 3D magnetic susceptibility iso-surface rendered at three ranges: 0.1- 0.2 SI, 0.2-0.5 SI and > 0.5 SI as shown in Figure13b. The model enhances the understanding of BIF/ magnetic body in the subsurface. From the figure, it is evident that the depth of the body increases towards the south-west. The 3D magnetic inversion results indicate that BIF-associated magnetic sources with susceptibility values greater than 0.5 SI occur between elevations of approximately +387 and +195 m. When referenced to the SRTM-derived DEM, these high-susceptibility zones extend to a maximum depth of approximately 140 m below the local ground surface. However, the histogram of the inverted susceptibility values indicates that the highest frequency of occurrence is concentrated within the upper approximately 90 m depth range, suggesting that the dominant volume of the high-susceptibility material occurs at relatively shallow depths. These high-susceptibility sources are scattered, with limited depth persistence, and occur randomly in the subsurface, indicating the presence of high-grade magnetite-rich rock. BIF/magnetic sources with susceptibility between 0.2–0.5 SI are observed from +425 m to +75 m. When referenced to DEM, these zones extend up to 300 m depth below the ground surface. However, the highest frequency of occurrence is concentrated within the upper approximately 180 m depth range. These bodies exhibit clear lateral continuity, likely due to the presence of hematite-rich BIF. Similarly, BIF/magnetic sources with susceptibility between 0.1–0.2 SI occur between +437 m and –77 m, When referenced to DEM, these zones extend up to 405 m depth below the ground surface. However, the highest frequency of occurrence is concentrated within the upper approximately 300 m depth range and also exhibit good lateral continuity, indicating the presence of low-grade BIF/ Ferruginous material. Table 1 shows comparison of depth estimates obtained from different geophysical methods and their correlation with the borehole BH-6

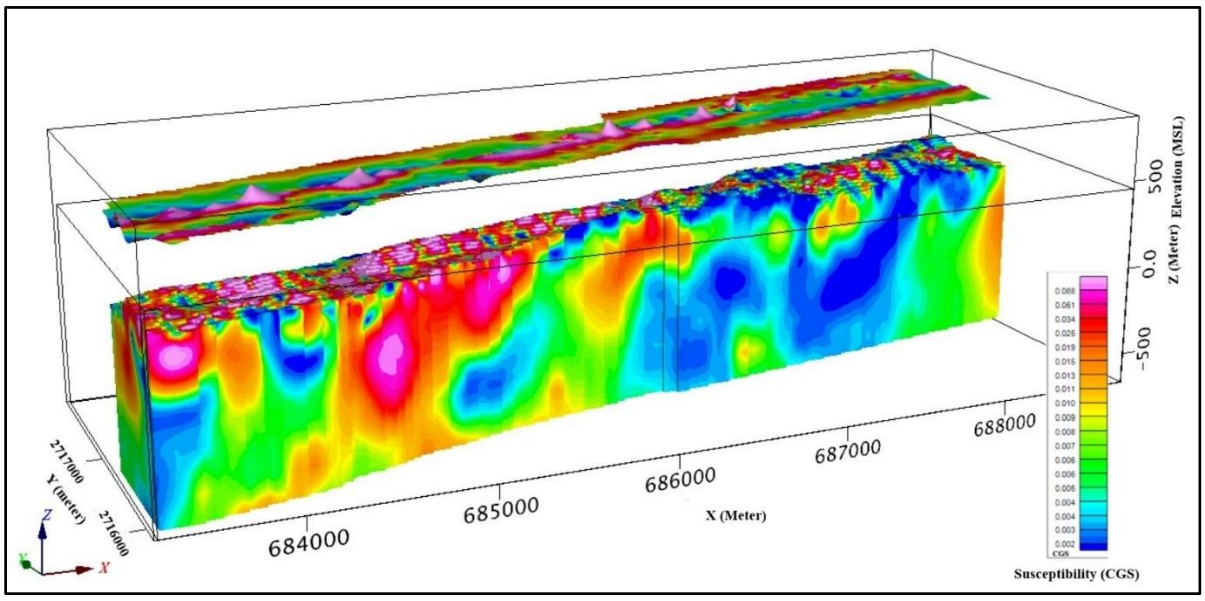


Figure 13a. Prospective view of inverted block

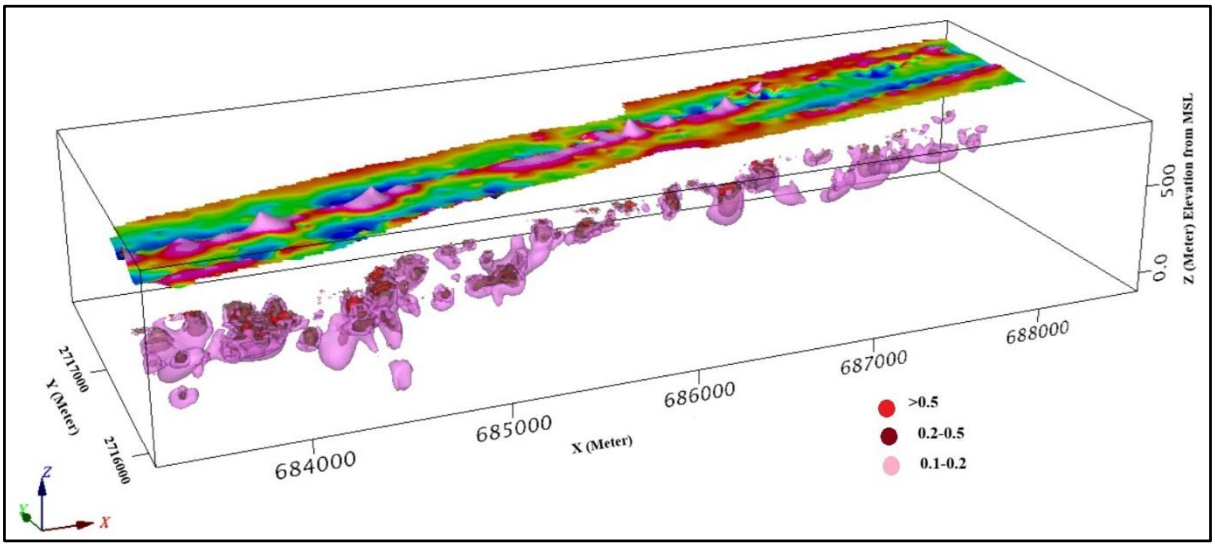


Figure 13b. Subsurface magnetic susceptibility distributions plotted as an iso-surface at, 0.1-0.2SI, 0.2-0.5 SI and >0.5 SI.

Table 1. Comparison of depth estimates obtained from different geophysical methods and their correlation with the borehole BH-6

Geophysical method	*Estimated depth range*	*Key characteristics and correlation*
RAPS	18, 37, 75 and 175 m	The shallow and intermediate levels are broadly consistent with the mineralized zones intersected in the boreholes
Euler 3D Solution	30 m to 90 m	Confirms that the majority of sources are confined to shallow to intermediate depths.
SPI	20 m to 60 m	Provides subsurface constraints on geometry and thickness variation.
Inversion results	20 m to 140 m	Directly substantiates the geophysical disposition of the BIF.
Werner Deconvolution	1–71 m (contact); 20–98 m (dyke)	Corroborates well with the actual BIF thickness obtained in BH-6.

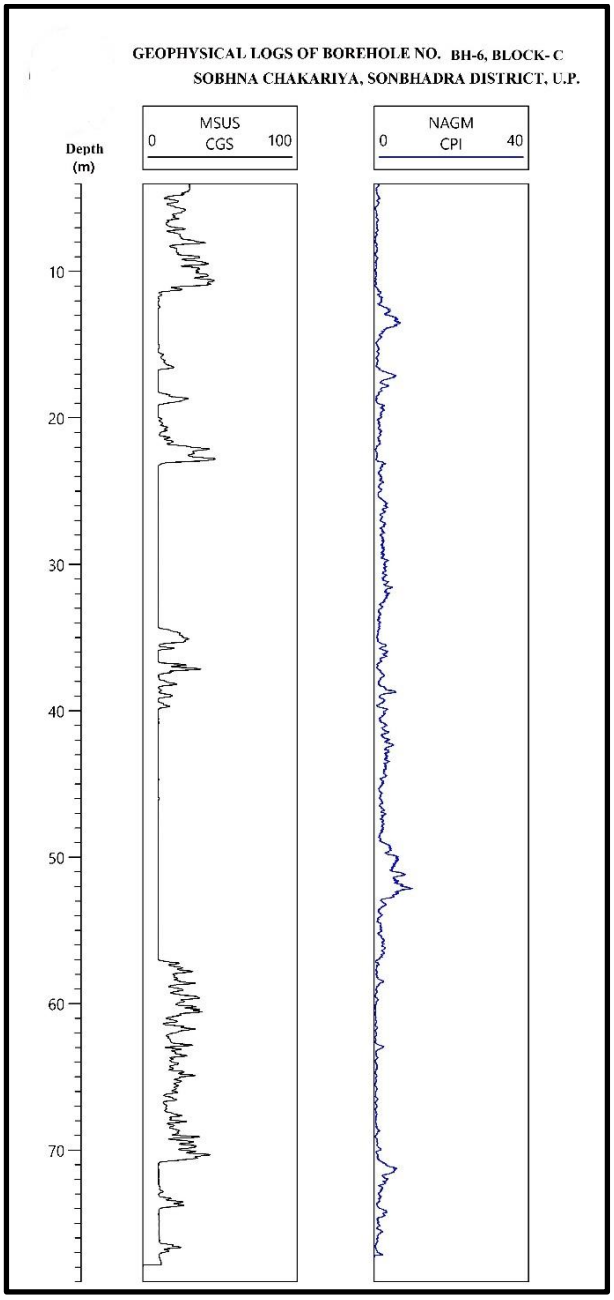


Figure 14. Geophysical log of borehole BH-6

DISCUSSION

Correlation with the drilled boreholes in the study area.

Six boreholes (BH-1 to BH-6) consistently intersected thick zones of BHC/J and banded hematite-magnetite chert/jasper (BHMC/J), with true thickness ranging from ~30 m to ~60 m, thereby confirming the lateral persistence of the BIF band at depth (Narayan and Ahmed, 2025). The eastern boreholes (BH-1 to BH-3), show relatively thinner BHC/J intersections (true thickness ~29.9–48.5 m), with frequent occurrences of dolerite intrusions and a higher proportion of phyllitic horizons. In contrast, the western boreholes (BH-4 to BH-6), consistently intersect thicker and more massive BHC/J bands (true thickness ~49.8–59.8 m), with relatively fewer interruptions by phyllite, though dolerite intrusions remain common. Magnetite bands were observed in BH-4, while BH-5 and BH-6 contained thick, continuous BHC/J horizons with sulphide disseminations and veinlets within cherty-phyllite intervals, highlighting a stronger mineralisation signature in the western sector. Analytical results of borehole BH-1, delineated three mineralized zones at 35% Fe cut off, having true thickness ranging from 2.91 m to 10.98 m. In BH-

2, two mineralized zones at a 35% Fe cut off have been established, having true thicknesses ranging from 3.80 m to 15.21 m. In BH-3, four zones at 35% Fe cut off have been demarcated, with true thicknesses ranging from 2.71 m to 6.58 m. While in BH-4 three mineralized zones were established at a 35% Fe cut off, with true thicknesses ranging from 8.50 m to 19.40 m. In BH-5, mineralized zones at 35% Fe cut off have been observed, having true thickness ranging from 6.33 m to 18.35 m whereas in BH-6, three mineralized zones, have been established, having true thicknesses ranging from 7.53 m to 15.46 m.

Geophysical logging was carried out in borehole BH-6 up to a depth of 78.00 m. The geophysical log is shown in Figure14. In this borehole, three magnetic zones have been observed. These zones may be important from a mineralization perspective. These are the ore zones of the borehole with Fe > 35% (Narayan and Ahmed, 2025). These results substantiate the geophysical disposition of the BIF and provide valuable subsurface constraints on its geometry, thickness variation and associated lithological assemblages, which are critical for assessing the mineralisation potential. The integrated geophysical results, indicate that the majority of the magnetic sources are concentrated at shallow to moderate depths, broadly within 20–60 m, which correlates well with the mineralized zones intersected in the boreholes, although deeper source levels are also indicated by RAPS and inversion. The Werner depth solution obtained in profile E2 is also well corroborated by the BIF thickness obtained in the BH-6. In the geophysical depth analysis, a few deeper depths are also present, which may be related to the deeper source of magnetic bodies and may be intersected in the deeper boreholes.

CONCLUSIONS

The detailed ground magnetic survey in Blocks C and D, in Sonbhadra District, successfully delineated BIF-associated iron mineralisation within the Mahakoshal Group. The magnetic response, ranging from –6168 to +3228 nT, is dominated by ENE–WSW-trending magnetic highs associated mainly with ferruginous BIF horizons and locally with dolerite intrusions. Multiple quantitative interpretation techniques provided consistent constraints on the depth and geometry of the magnetic sources. RAPS indicated principal source depths of approximately 18, 37, 75 and 175 m, while Euler 3D and SPI predominantly indicated shallow to intermediate sources, generally within 20–80 m, with isolated deeper sources extending beyond 100 m. P-depth analysis further identified contacts and dyke-like bodies associated with the BIF zones. The 3D magnetic inversion indicated high-susceptibility sources (>0.5 SI) extending locally to about 140 m depth. The close correspondence between geophysical interpretations and borehole intersections, demonstrates that the principal mineralised horizons occur predominantly at shallow to moderate depths of approximately 20–60 m. Overall, Blocks C and D are prospective for further exploration, with the western sector representing a particularly favourable target owing to its thicker and more massive BIF intersections and identified Fe-rich zones.

Acknowledgement

The authors express their deep sense of gratitude to the Additional Director General and HOD, GSI, NR, for their overall supervision and for providing logistical support for the survey work. They are also thankful to the Director (Geophysics) for their guidance and useful suggestions. Wholehearted cooperation received from every party member is praiseworthy. The authors sincerely thank the anonymous reviewers for their constructive and insightful comments, which have significantly improved the quality and clarity of the manuscript. The authors also gratefully acknowledge Dr O. P. Pandey, Chief Editor of the Journal of Indian Geophysical Union (JIGU), for his valuable suggestions.

Author Credit Statement:

Gautam Kumar: Data acquisition, data processing, project administration, formal analysis, conceptualisation, interpretation of results, writing draft, and manuscript editing; C. B. Tiwari: Data acquisition, data processing, formal analysis, conceptualisation, writing draft, and manuscript editing; S.P. Chaubey: Conceptualisation, supervision and review and editing of the manuscript; Tashmeet Kaur: Data processing, formal analysis, interpretation of results and writing draft.

Data availability

The datasets generated and/or analysed during the current study are available from the corresponding author on reasonable request.

Compliance with ethical standards

The authors declare no competing interests and adhere to copyright norms.

REFERENCES

Betts, P.G., Valenta, R.K. and Finlay, J., 2003. Evolution of the Mount Woods Inlier, northern Gawler Craton, southern Australia: an integrated structural and aeromagnetic analysis. Tectonophysics, 366, 83-111.

Bhattacharya, D., Verma, C.S., Singh, R. P., Singh, M. and Shivlal, 2012. Report on the ground geophysical mapping in parts of Degree Sheet No. 63L (Toposheet no. 63L/1,5,9,13,14,15 & 16), Geol. Surv. India, Kolkata, India (Unpub. Report).

Biswas, A. and Sharma, S. P., 2016. Integrated geophysical studies to elicit the subsurface structures associated with uranium mineralization around South Purulia Shear Zone, India: A review. Ore Geol. Rev., 72, 1307-1326.

Dentith, M. and Mudge, S.T., 2014. Geophysics for the Mineral Exploration Geoscientist, Cambridge University Press, 126.

FitzGerald, D., Reid, A. and McInerney, P., 2004. New discrimination techniques for Euler deconvolution. Comput. Geosci., 30, 461–469.

Grant, F. S. and West, G. F., 1965. Interpretation theory in applied geophysics. McGraw-Hill Book Co., New York, 583.

Grauch, V.J.S., 2002. High-resolution aeromagnetic survey to image shallow faults, Dixie Valley Geothermal Field, Nevada. US Geological Survey, Open-File Report 2002-384.

Jacobsen, B.H., 1987. A case for upward continuation as a standard separation filter. Geophysics, 52, 1138–1148.

Mandal, A., Mohanty, W. K., Sharma, S. P., Biswas, A., Sen, J. and Bhatt, A. K., 2015. Geophysical signatures of uranium mineralisation and its subsurface validation at Beldih, Purulia District, West Bengal, India: a case study. Geophys. Prospect. 2015, 63, 713-726.

Nabighian, M. N., Grauch, V. S., Hansen, R. O., LaFehr, T. R., Li, Y. and Peirce, J. W., 2005. The historical development of the magnetic method in exploration. Geophysics, 70(6), 33–61.

Nair, K.K.K., Jain, S.C. and Yedekar, D.B., 1995. Stratigraphy, structure and geochemistry of the Mahakoshal greenstone. Mem. Geol. Soc. India, 31, 403–432.

Narayan L. and Ahmed S., 2025. Final report on Preliminary exploration for iron ore in Mahakoshal Group, Block 'D', North of Khoriya, Bharhari, Sonbhadra district, Uttar Pradesh (STAGE: G-3), Geol. Surv. India, Kolkata, India, Field season: 2023-24 (Unpub. Report).

Pandey, B.K., Krishna, V. and Chabria, T., 1998. An overview of the geochronological data on the rocks of Chotanagpur Gneiss-granulite Complex and adjoining sedimentary sequences, eastern and central India. In: Int. seminar on Precambrian crust in eastern and central India, pp. 131-135.

Paterson, N. R. and Reeves, C. V., 1985. Applications of gravity and magnetic Surveys: The State-of-the-Art in 1985. Geophysics, 50, 2558-2594.

Prajapati S. K. and Ahmad S., 2023. Preliminary exploration for iron ore in Mahakoshal Group, near Sobna and Chakariya area, Sonbhadra district, Uttar Pradesh (STAGE: G-3), Geol. Surv. India, Kolkata, India, Field season: 2022-23 (Unpub. Report).

Prevec, L. and Morris, W.A., 2001. Enhanced resolution of geological structures from magnetic data: an example from the Abitibi Greenstone Belt of Northern Ontario. Can. J. Earth Sci., 38, 963–974.

Roy, A. and Bandyopadhyay, B.K., 1990. Tectonic and structural pattern of the Mahakoshal belt of Central India: a discussion. Geol. Surv. India, Spl. Publ., No. 28, pp. 226-240.

Sarkar, A., Boda, M.S., Kundu, H.K., Mamgain, V.D. and Shankar, R., 1998. Geochronology and petrochemistry of Mesoproterozoic intrusive plutonites from the eastern segment of the Mahakoshal greenstone belt, Central India. Abstract, Int. Seminar on Precambrian Crust in Eastern and Central India, IGCP-368, pp. 82–85.

Seequent, 2023. Oasis Montaj (Version 2023.2) geophysical data processing software. Seequent, Toronto, Canada.

Singh, A., 2019. Triangular Grid-Based Fuzzy Cross-Update Inversion of Gravity Data: Case Studies from Mineral Exploration. Nat. Resour. Res., 29(1), 459-471.

Thurston, J. B. and Smith, R. S., 1997. Automatic conversion of magnetic data to depth, dip and susceptibility contrast using the SPI (TM) method. Geophysics, 62, 807-813.

Wennerström, M. and Airo, M., 1998. Magnetic fabric and emplacement of the post-collisional Pomovaara Granitic Complex in northern Fennoscandia. Lithos, 45, 131–145.

Received on: 23-09-2025; Revised on:15-08-2026; Accepted on 16-09-2026

J. Ind. Geophys. Union, 30(6) (2026), 489-502
http://doi.org/10.71122/JIGU.30(6)2026.0048

Assessing the impact of saline water intrusion, aquaculture practices and oil–gas operations on groundwater in the Godavari Delta, Andhra Pradesh, India

B. Naga Jyothi[1*], GunnamVenkataRatnalu[2], K. BhimaRaju[3, 4], P.V. Nagamani[5], G. Udaya laxmi[6],
[1]Research Scholar, Department of Geophysics, Osmania University, Hyderabad, Telangana- 500007, India
[2]Department of Geology, Parul Institute of Applied Sciences (PIAS), Parul University, Vadodara, Gujarat- 391760, India
[3]CSIR-National Geophysical Research Institute, Uppal Road, Hyderabad-500007, India
[4]Academy of Scientific and Innovative Research (AcSIR), Ghaziabad- 201002, India
[5]National Remote Sensing Centre, Indian Space Research Organisation, Dept. of Space, Govt. of India, Balanagar, Hyderabad - 500037 India
[6]Department of Geophysics, Osmania University, Hyderabad, Telangana- 500007, India
[*]Corresponding Author: bnjyothi10@gmail.com

ABSTRACT

The objective of this study is to evaluate the impact of saline water intrusion, aquaculture activities, and hydrocarbon exploration on groundwater quality in the Konaseema region of Andhra Pradesh, India. The present study assesses seasonal variations in groundwater quality by monitoring groundwater at 46 locations during the pre- and post-monsoon seasons, which includes groundwater quality parameters, pollution assessment, and heavy metal evaluation. Concentrations of Cr, Mn, Fe, Co, Ni, Cu, Zn, As, Cd, and Pb were analysed along with salinity indicators, and the results were interpreted using correlation analysis and Heavy Metal Pollution Index (HPI). Pre-monsoon results show significant enrichment of Fe (400–5558 µg/L; 100% exceedance) and Mn (45–1044 µg/L; ~70% of samples exceeded permissible limits), while As concentrations (0.13–14.43 µg/L), exceeded Bureau of Indian Standards limits in about 15% of the samples. Post-monsoon groundwater consistently exhibits elevated Fe levels (444–5281 µg/L; 100% exceedance) and Mn (6.9–1281 µg/L; around 60% exceedance), along with increased variability in As, Cd and Pb. Correlation analysis revealed strong positive relationships between Fe–Mn, TDS–Cl^-, and selected metals, suggesting salinity-driven geochemical mobilisation and redox-controlled metal release. Moderate correlations among Ni, Cu, and Zn indicate additional anthropogenic influences, including aquaculture and hydrocarbon-related activities. HPI values ranged from 7.5 to 34.8 in the pre-monsoon and 5.1 to 42.6 in the post-monsoon, indicating groundwater quality from excellent to good, with relatively higher pollution levels observed in coastal zones and areas influenced by aquaculture and oil–gas operations. This suggests enhanced metal dispersion under saline water intrusion and recharge-driven conditions. These findings demonstrate that heavy metal contamination in the Konaseema aquifer is primarily governed by saline water intrusion and redox processes, further intensified by local anthropogenic activities, underscoring the need for sustainable groundwater management in this sensitive deltaic environment.

Keywords: Groundwater quality, Saline water intrusion, Geochemical, Anthropogenic, Heavy Metal Pollution Index (HPI); Godavari delta (India).

INTRODUCTION

Groundwater quality in coastal deltaic regions is increasingly threatened by both natural processes and anthropogenic activities. Among these, saline water intrusion is a major hydrogeological concern, particularly in low-lying coastal aquifers where freshwater–seawater interactions, are highly dynamic. Factors such as excessive groundwater extraction, reduced freshwater recharge, tidal influences, and extreme climatic events (e.g., cyclones and storm surges), contribute to the inland migration of saline water, thereby degrading groundwater quality (CGWB, 2014; Surinaidu et al., 2015). Hydrochemical indicators such as elevated electrical conductivity, high chloride and sodium concentrations, and Na/Cl ratios are widely used to identify seawater intrusion and associated geochemical processes (Subramanian and Saxena, 1983; Surinaidu, 2016). In addition to natural salinisation processes, anthropogenic activities play a significant role in altering groundwater chemistry in coastal regions. The rapid expansion of aquaculture, particularly brackish-water shrimp farming, has been identified as a major contributor to groundwater salinity. Prolonged storage of saline water in aquaculture ponds enhances seepage into shallow aquifers, resulting in increased concentrations of dissolved ions and trace elements (Gopalakrishnan et al., 2019; CGWB, 2019). Previous studies in coastal Andhra Pradesh have reported elevated salinity, nitrate, and trace metal concentrations in groundwater in areas with intensive aquaculture practices (Reddy et al., 2017; Subba Rao et al., 2022).

Furthermore, hydrocarbon exploration and production activities in sedimentary basins can introduce additional environmental stressors. The handling of drilling fluids, mud additives, and produced water, often containing dissolved salts and heavy metals, poses a risk to soil and groundwater systems if not properly managed (Veerabhadrappa and Kumar, 2012; MoEFCC, 2016). Improper disposal of drilling wastes, inadequate containment systems, and accidental spills may lead to contamination by metals such as chromium, nickel, lead, and cadmium (CPCB, 2010). Regulatory assessments have emphasized the need for improved waste management practices, well integrity, and continuous groundwater monitoring in such regions (MoEFCC, 2016). The combined influence of saline water intrusion, aquaculture, and hydrocarbon activities, results in complex hydrogeochemical interactions that control the distribution and mobility of dissolved ions and trace metals in coastal aquifers. Despite several regional studies, there remains a

need for integrated seasonal assessments that link salinity processes with heavy metal behaviour. This study aims to evaluate the combined effects of saline water intrusion, aquaculture practices, and upstream oil–gas operations on groundwater quality in the Godavari delta, with particular emphasis on trace metal contamination and the geochemical processes governing their distribution.

STUDY AREA AND GEOLOGICAL SETTING

Study area

The study region is located in the Konaseema area of Dr. B.R. Ambedkar Konaseema District, situated at the central part of the Godavari Delta along the eastern coast of Andhra Pradesh, India. This coastal deltaic system is highly productive yet environmentally fragile, bounded by the Bay of Bengal to the east and intersected by numerous distributaries of the Godavari River. The region is characterised by low-lying terrain, shallow groundwater conditions, and extensive dependence on groundwater for domestic, agricultural, and aquaculture uses. These features make the aquifer system highly vulnerable to salinisation and contamination from both natural processes and human activities (Subramanian, 1994; Surinaidu, 2016). The study area covers approximately 480 km² in the Razole constituency of Dr B. R. Ambedkar Konaseema district, located along the eastern coast of Andhra Pradesh, India. It encompasses the mandals of Mamidikuduru, Razole, Malkipuram, and Sakhinetipalle. Geographically, the area lies between 16°18′N and 16°37′N and 81°41′E and 82°01′E (Figures 1 and 2). The terrain is predominantly flat and low-lying, with elevations close to mean sea level, making it highly susceptible to flooding, tidal influences, and saline water intrusion. Groundwater in the region occurs under shallow conditions and serves as a primary resource for domestic use, irrigation, and aquaculture. The climatic setting is tropical, with significant seasonal variation driven by the southwest and northeast monsoon. The combination of low relief, high water demand, and coastal proximity, makes the aquifer system particularly vulnerable to salinisation and contamination.

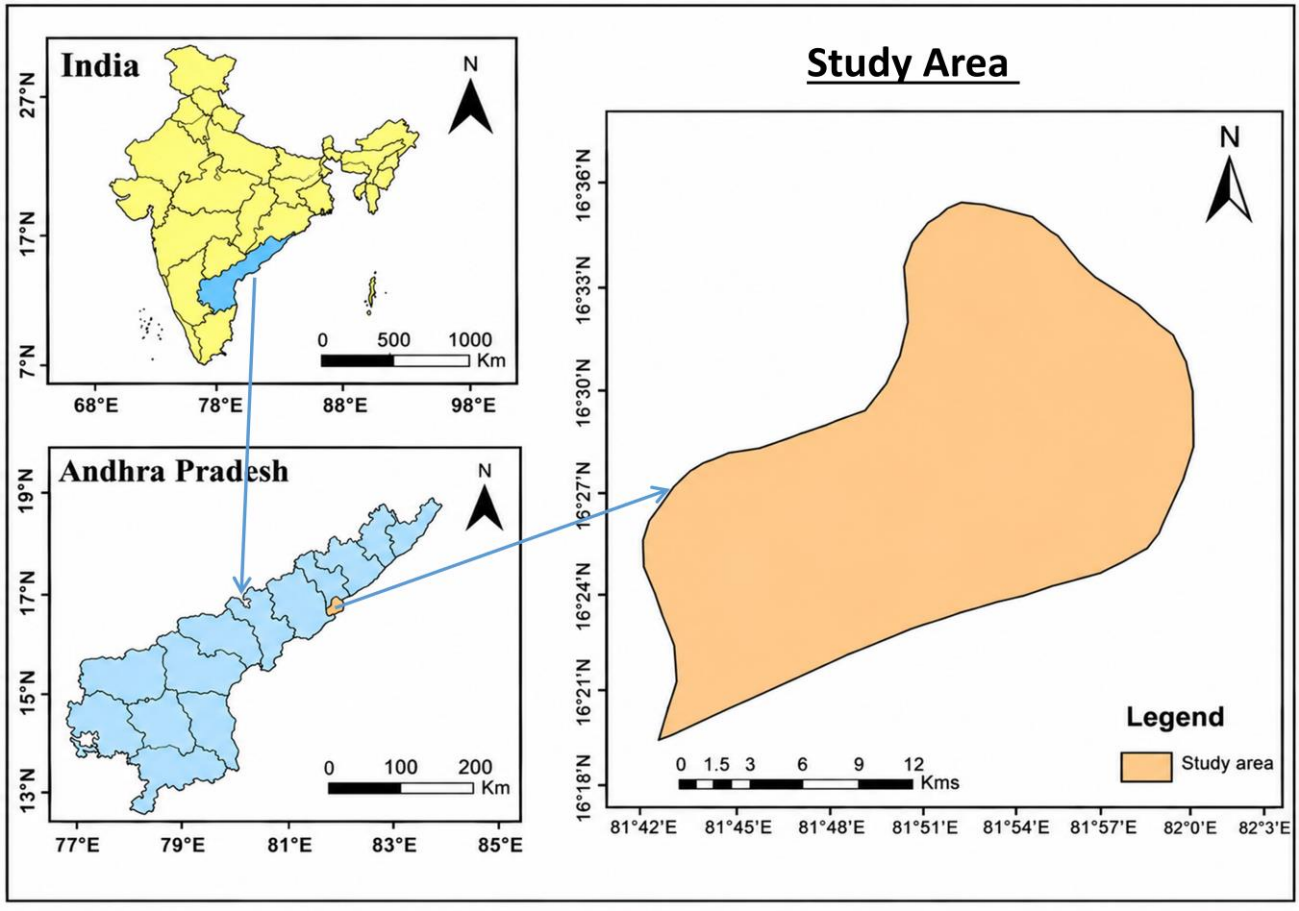


Figure 1. Geographic location of the study area in Andhra Pradesh, India

GEOLOGICAL SETTING

The study area forms part of an extensive alluvial plain of the Godavari delta, developed through prolonged fluvial sedimentation during the late Quaternary period. The regional geology is characterised by thick sequences of unconsolidated to semi-consolidated alluvial and deltaic sediments, overlying older sedimentary formations of the Krishna–Godavari Basin (Rao, 1975; Subramanian, 1994).The deltaic deposits predominantly consist of alternating layers of clay, silt, silty clay, and fine- to medium-grained sand, with occasional peat horizons. The mineralogical composition of deltaic sediments comprises quartz, feldspars, clay minerals (illite, kaolinite, smectite), and iron-rich minerals. These sediments were deposited under diverse environmental conditions, including fluvial, floodplain, estuarine, tidal flat, and shallow-marine settings (Rao and Radhakrishna, 1985). The dominance of clay-rich layers in the shallow subsurface, results in low hydraulic conductivity, restricted groundwater flow, and the development of reducing geochemical conditions.

Stratigraphically, the Quaternary alluvium rests unconformably over Tertiary formations composed of sandstone, shale, and claystone sequences, deposited in deltaic to shallow-marine environments (Rao, 1975; ONGC, 2010). These formations are known to host significant hydrocarbon reserves, supporting extensive onshore oil and gas exploration activities in the region. Structural elements such as gentle folds, growth faults, and subsurface lineaments, influence sediment thickness and groundwater flow dynamics, particularly near hydrocarbon-bearing zones. Iron and manganese oxides commonly occur as coatings and nodules within clay layers, act as important geochemical sinks for trace metals (Subramanian and Saxena, 1983; Surinaidu, 2016). Under reducing and saline conditions, these Fe–Mn oxides tend to dissolve, releasing associated metals such as arsenic, zinc, and lead into groundwater.

The proximity to the Bay of Bengal, along with the presence of tidal channels and palaeo-estuarine features, facilitates seawater intrusion into shallow aquifers. The flat topography further enhances inland saline water movement, especially during periods of reduced river discharge and extreme weather events such as cyclones (CGWB, 2014; Surinaidu et al., 2015). These hydrogeological processes significantly influence groundwater salinity, trace metal mobilisation, and spatial variability in water quality across the region. When combined with intensive aquaculture and hydrocarbon exploration activities, this geological framework exerts a strong control on the hydrogeochemical evolution of groundwater in the Konaseema region.The Land Use Land Cover map of the study area (Naga Jyothi, 2026), indicates that the primary occupations of the people in this area, according to 2011-12 data, are coconut plantations, paddy cultivation, and aquaculture. About 157 sq. km (33%) is primarily coconut plantations, around 145 sq. km (30%) is dedicated to agriculture, mainly paddy, and aquaculture occupies 60 sq. km (13%).

OIL AND GAS DRILLING SITES

The Konaseema district, located within the hydrocarbon-rich Krishna–Godavari (KG) Basin, hosts several major onshore oil and natural gas production facilities operated by ONGC**.** Figure3 illustrates the spatial distribution of the major drilling sites identified through field surveys and Google Earth Pro historical imagery (timeline analysis). The red circles represent the major gas collecting stations (GCS), namely Tatipaka, Ponnamada, Kesanapalli, Adavipalem, and Mori, which serve as central gathering and processing facilities for natural gas produced from surrounding wells before its transmission through the regional pipeline network. The yellow markers indicate the major villages associated with hydrocarbon exploration and production activities, including LankalaGannavaram, Pasarlapudi, Mamidikuduru, Razole, Gudimellanka, Sakhinetipalli, Malikipuram, GudimulaKandrika, and Kesavadasupalem. The numerous white circular points denote the locations of drilling rigs and production well pads, identified during field investigations and verified using Google Earth historical imagery, which enabled the detection of drilling sites, well pads, access roads, and associated infrastructure developed over different periods. A dense concentration of drilling rigs is observed around the Tatipaka–Pasarlapudi–Ponnamada–Kesanapalli corridor, indicating the principal hydrocarbon-producing zone within the study area, while comparatively fewer active drilling sites are presently observed in the northwestern part of the study area near Sakhinetipalli and Gudimellanka. According to information obtained during field visits from local villagers, hydrocarbon exploration and drilling activities were carried out in these northwestern areas several years ago, after which the drilling rigs and associated temporary infrastructure were dismantled and removed following the completion of exploration or production activities. Consequently, these older drilling locations could not be identified during the present field investigation or from recent Google Earth imagery, although their previous existence was consistently reported by local residents.

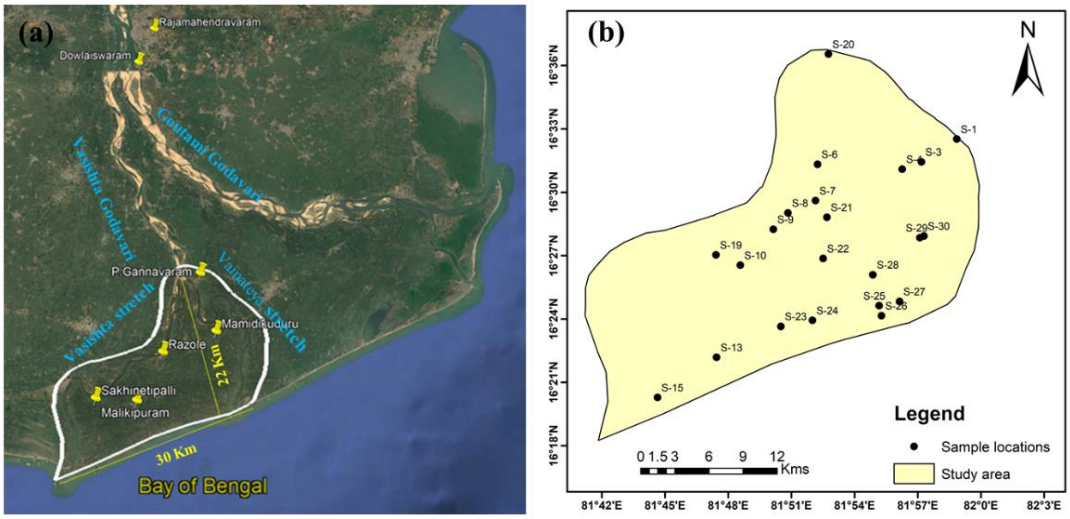


Figure2. Map showing **(a)** Location of study area in Konaseema region of Dr B.R. Ambedkar Konaseema District; **(b)** Study area map along with sampling points (represented by black dots)

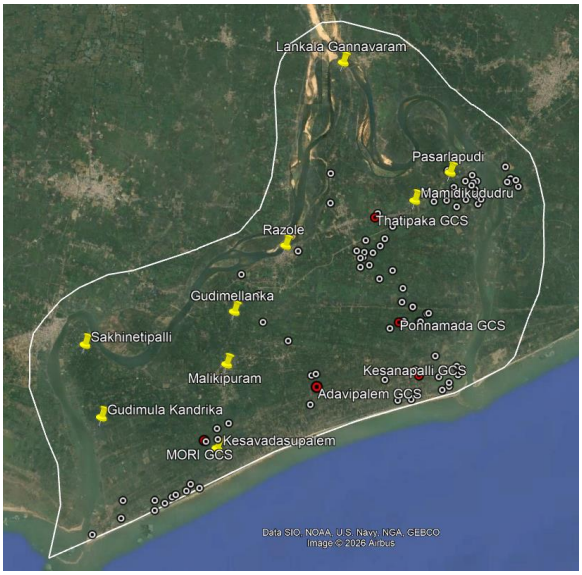


Figure3. Spatial distribution of major oil and gas drilling sites in the Dr B.R. Ambedkar Konaseema district, Andhra Pradesh, showing gas collecting stations (red circles), major villages (yellow markers), and drilling rigs/well locations (white circles) identified through field surveys and Google Earth Pro historical imagery (timeline analysis).

Thus, the integration of field reconnaissance, local knowledge, and temporal satellite image interpretation, provided a more comprehensive understanding of both existing and historical oil and gas exploration activities across the Konaseema coastal delta, thereby establishing a valuable spatial framework for evaluating the environmental and groundwater impacts of hydrocarbon development.

METHODOLOGY

Groundwater sampling and preservation

Groundwater samples were collected from representative locations across the study area, including coastal zones, aquaculture regions, agricultural lands, and areas influenced by oil and gas activities. Sampling was conducted during both the pre-monsoon and post-monsoon seasons to assess seasonal variations in groundwater quality. A total of 46 groundwater samples were collected, comprising 23 samples during the pre-monsoon period and 23 samples during the post-monsoon period. Samples were obtained from bore wells and hand pumps after purging for 5–10 minutes to remove stagnant water and ensure collection of representative groundwater. The geographic coordinates of each sampling location were recorded using a handheld GARMIN GPS device.

For heavy metal analysis, groundwater samples were collected in 200 ml pre-cleaned high-density polyethylene (HDPE) bottles. Immediately after collection, samples were preserved by acidification with ultrapure nitric acid (HNO_3) to pH < 2, following standard procedures recommended by APHA (2017), to prevent metal precipitation and adsorption onto container walls. Separate unacidified samples were collected for the determination of physicochemical parameters such as total dissolved solids (TDS) and chloride (Cl^-).

Sample preparation

Prior to analysis, preserved water samples were filtered through 0.45 µm membrane filters to remove suspended particulate matter. The filtered samples were stored at 4°C until laboratory analysis. No further digestion was required because dissolved heavy metals were targeted in this study. Unacidified samples were analysed for TDS and chloride using standard analytical procedures. TDS was determined using the gravimetric method, while chloride concentration was measured by standard conductivity/titrimetric methods in accordance with APHA (2017) guidelines.

Heavy Metal Analysis

The concentrations of iron (Fe), manganese (Mn), chromium (Cr), cobalt (Co), nickel (Ni), copper (Cu), zinc (Zn), arsenic (As), cadmium (Cd), and lead (Pb) were determined using Atomic Absorption Spectrophotometry (AAS) (Model: iCE FIOS, Thermo Fisher Scientific India Pvt. Ltd., Nashik, India). The instrument was operated under optimized conditions using element-specific hollow cathode lamps and appropriate analytical wavelengths for each metal. Calibration was performed using multi-element standard solutions prepared from certified reference materials (Merck standards) over suitable concentration ranges. Instrument calibration curves exhibited correlation coefficients (R^2) greater than 0.995 for all analyzed metals.

The method detection limits (MDLs) ranged from 0.001 to 0.01 mg/L depending on the element. Measured concentrations were compared with the drinking water standards specified by APHA (2017) and BIS (2012).

Quality Assurance and Quality Control (QA/QC)

Quality assurance and quality control procedures were implemented throughout sampling, preparation and analysis to ensure data reliability. All sampling containers were acid-washed and rinsed with deionized water before use. Field blanks, laboratory blanks, and duplicate samples were analyzed periodically to assess contamination and analytical precision. Instrument calibration was verified using quality control standards at regular intervals during analysis. Recovery studies were performed using spiked samples, and metal recoveries were maintained within ±10% of the certified values. Analytical measurements were accepted only when calibration standards, blanks, and duplicate analyses met the prescribed quality control criteria.

Table 1. Statistical summary of trace metal constituents (*practical unit, no specific BIS/WHO standard exists for that element)

Parameter	Pre-monsoon				Post-monsoon				BIS Standard (2012)
	Min	Max	Mean	SD	Min	Max	Mean	SD	
Cr	2.90	11.85	5.33	2.01	3.22	9.29	4.24	1.35	50
Mn	44.76	1044.30	403.42	294.38	6.93	1280.67	468.97	448.01	100
Fe	400.22	5557.67	2013.38	1162	444.16	5280.58	1967.76	1212.7	300
Co	0.15	1.28	0.68	0.32	0.16	2.74	0.80	0.64	5*
Ni	0.90	9.78	2.01	1.71	0.95	5.66	1.86	1.06	20
Cu	0.44	23.48	3.12	4.89	0.63	4.59	1.74	0.94	50
Zn	10.33	703.03	66.61	141.33	16.36	56.34	36.26	12.03	5000
As	0.13	14.43	3.30	3.47	0.08	14.92	2.94	3.79	10
Cd	0.002	0.16	0.027	0.033	0.01	0.15	0.04	0.03	3
Pb	0.08	7.26	1.12	1.47	0.07	1.61	0.70	0.41	10

Heavy Metal Pollution Index

(HPI)

The Heavy Metal Pollution Index (HPI) was calculated to assess the overall impact of heavy metals on groundwater quality. HPI integrates the concentrations of multiple heavy metals into a single numerical value representing the composite pollution status of groundwater.

The HPI was calculated using the weighted arithmetic index method:

$$HPI = [\Sigma(W_iQ_i)] / [\Sigma W_i] \quad (1)$$

where,

W_i = Unit weight of the i^{th} heavy metal,

Q_i = Sub-index of the i^{th} heavy metal.

The sub-index (Q_i) was computed as:

$$Q_i = [(M_i - I_i) / (S_i - I_i)] \times 100 \quad (2)$$

where,

M_i = Monitored concentration of the i^{th} heavy metal (mg/l),

I_i = Ideal value of the i^{th} heavy metal in drinking water (usually 0),

S_i = Standard permissible value of the i^{th} heavy metal (mg/l).

The unit weight (W_i) was determined as:

$$W_i = k / S_i \quad (3)$$

where, k = Proportionality constant.

Higher HPI values indicate greater heavy metal contamination and poorer groundwater quality. An HPI value below 100 generally indicates low pollution, whereas values exceeding 100 suggest significant contamination and potential health concerns.

Statistical analysis

Statistical analyses were conducted separately for pre-monsoon and post-monsoon datasets to evaluate seasonal differences. Pearson correlation analysis was performed to identify relationships among heavy metals and infer possible geochemical controls and contamination sources. Heavy Metal Pollution Index (HPI) values were computed for all sampling locations to assess groundwater suitability for drinking purposes. All statistical analyses and graphical visualizations were performed using appropriate statistical software, and the results were interpreted with reference to BIS IS 10500:2012 drinking water standards

RESULTS AND DISCUSSION

Groundwater quality was assessed during the pre- and post-monsoon seasons and compared with BIS (2012) drinking water standards. The statistical summary of heavy metals is presented in **Table 1**. Additionally, the spatial distribution maps for these parameters during the pre-monsoon are shown in Figures 4 and 5 and those during the post-monsoon are shown in Figures 6 and 7. Statistical analysis was performed separately for both datasets. Correlation patterns between heavy metals and salinity indicators (TDS and Cl^-) (Figure8), reveal the influence of salinity and geochemical processes on metal mobility and possible sources. HPI values indicate overall groundwater quality with respect to metal contamination. The observed concentrations are evaluated against BIS drinking-water standards to assess groundwater suitability.

Seasonal variability of heavy metals in groundwater

A detailed comparison of heavy-metal concentrations between the pre- and post-monsoon seasons was conducted to assess the effects of saltwater intrusion, aquaculture, and hydrocarbon exploration on groundwater chemistry in Konaseema area. Seasonal average metal concentrations are presented and analysed in relation to the hydrogeochemical processes occurring in the deltaic aquifer.

Chromium (Cr)

The statistical analysis of Cr concentrations reflects an approximate 20% dilution due to monsoonal recharge. The overall range indicates moderate spatial variability, with persistent hotspots at Thatipaka and Ponnamada (Figures 4a and 6a) suggesting a dominant lithogenic source from Cr-bearing detrital minerals. Cr mobility is governed by redox–pH conditions (mobile Cr(VI) under oxidising–alkaline conditions vs. immobile Cr(III) under reducing environments), along with sorption–desorption reactions involving Fe–Mn oxides and clays. Elevated salinity enhances desorption through anion competition (e.g., Cl^-) during seawater intrusion. Anthropogenic inputs from oil–gas activities and aquaculture are sporadic and secondary, mainly influencing Cr indirectly through changes in TDS, DOC, and redox conditions. All observed Cr values remain well within the BIS limit (50 ppb), indicating no direct health risk.

Manganese (Mn)

Mn shows a clear seasonal increase from pre-monsoon (Figure 4b) to post-monsoon (Figure 6b), indicating enhanced reducing conditions after recharge. The observed range highlights strong spatial heterogeneity, with elevated values at Pasarlapudi and Ponnamada. Mn enrichment is primarily driven by reductive dissolution of Mn-oxides under low-oxygen conditions in organic-rich sediments. Salinity intrusion further promotes Mn release by increasing ionic strength and modifying redox gradients.

Anthropogenic influences (oil-field fluids, aquaculture effluents) act as supporting factors, enhancing oxygen depletion and microbial activity. Mn frequently exceeds the BIS permissible limit (100 ppb), particularly in post-monsoon samples, indicating potential groundwater quality concerns.

Iron (Fe)

Fe concentrations remain consistently high across seasons in pre-monsoon (Figure 4c) to post-monsoon (Figure 6c), with localized post-monsoon enrichment at sites such as Pasarlapudi and Gudimellanka. The wide range reflectsstrong geogenic control from iron-bearing minerals and deltaic sediments. Post-monsoon conditions favour reductive dissolution of Fe-oxides due to water logging and oxygen depletion. Salinity mixing at the freshwater–seawater interface further enhances Fe mobilisation through changes in pH, ionic strength, and redox gradients. Anthropogenic contributions (oil–gas leakage, aquaculture seepage) are localized but secondary, mainly accelerating reducing conditions. Fe concentrations significantly exceed the BIS limit (300 ppb) in most samples, indicating widespread iron contamination in groundwater.

Copper (Cu) and Zinc (Zn)

Cu and Zn exhibit higher pre-monsoon concentrations (Figures 4d and 5a) followed by a marked post-monsoon decline (Figures 6d and 7a), indicating strong seasonal dilution and flushing effects. Their spatial variability corresponds closely with aquaculture zones, identifying it as the primary source (Cu-based algicides, Zn-rich feed and fertilisers). While salinity intrusion may enhance mobility through pH and ionic changes, its role is secondary. No consistent enrichment near oil–gas sites suggests minimal industrial contribution. Overall, Cu and Zn are anthropogenically controlled with clear seasonal variability. Both Cu (limit: 50 ppb) and Zn (limit: 5000 ppb), remain within BIS permissible limits across all samples.

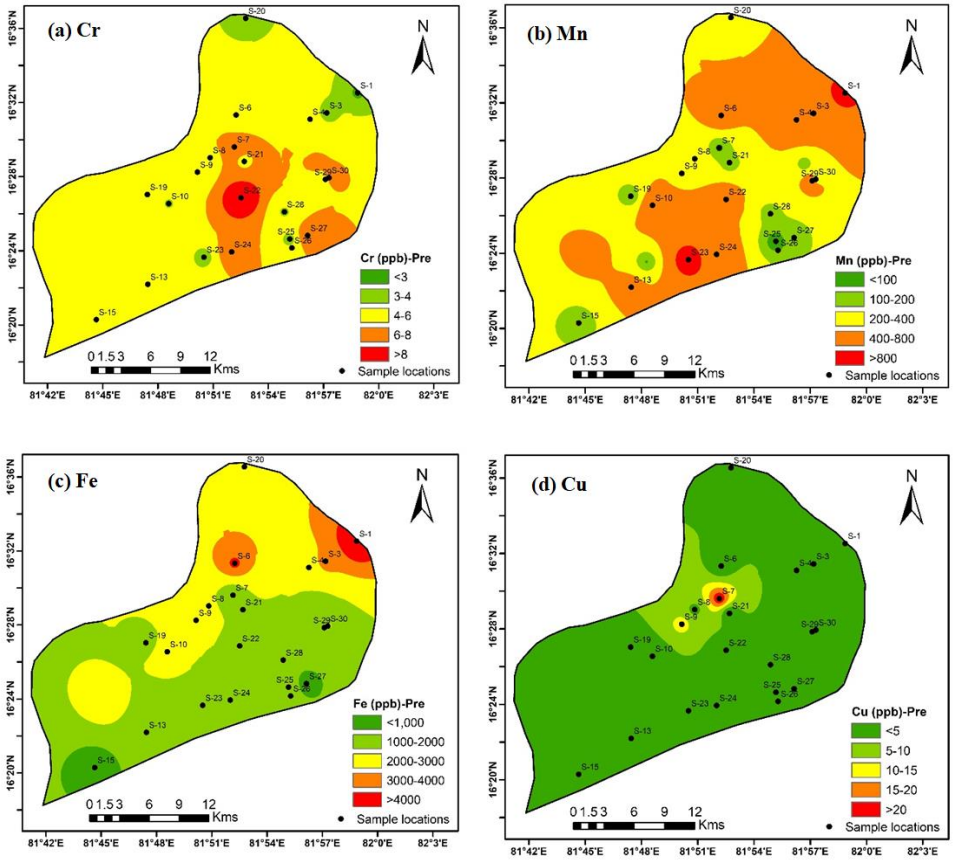


Figure4. Spatial distribution maps of metals, **(a)** Cr, **(b)** Mn, **(c)** Fe, and **(d)** Cu in Konaseema region during the Pre Monsoon

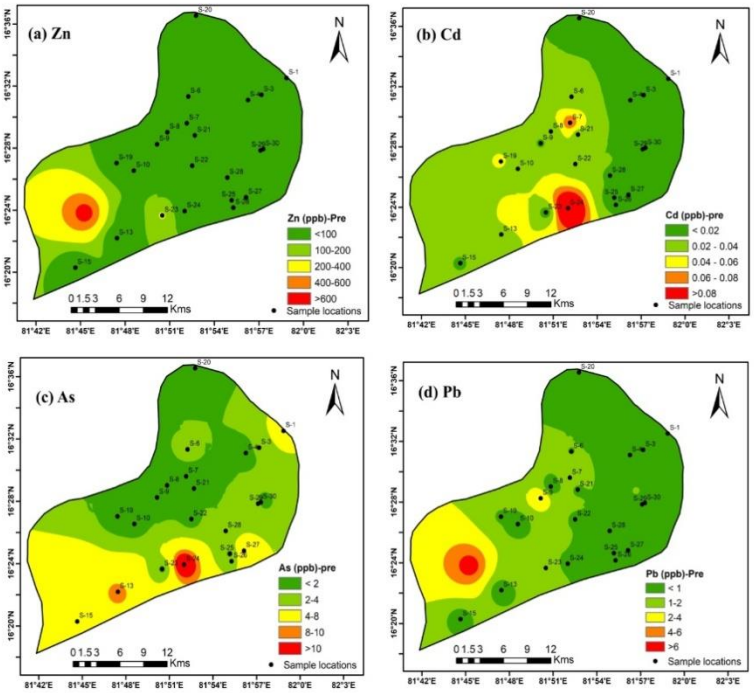


Figure5. Spatial distribution maps of metals, **(a)** Zn, **(b)** Cd, **(c)** As, and **(d)** Pb in Konaseema region during the Pre Monsoon

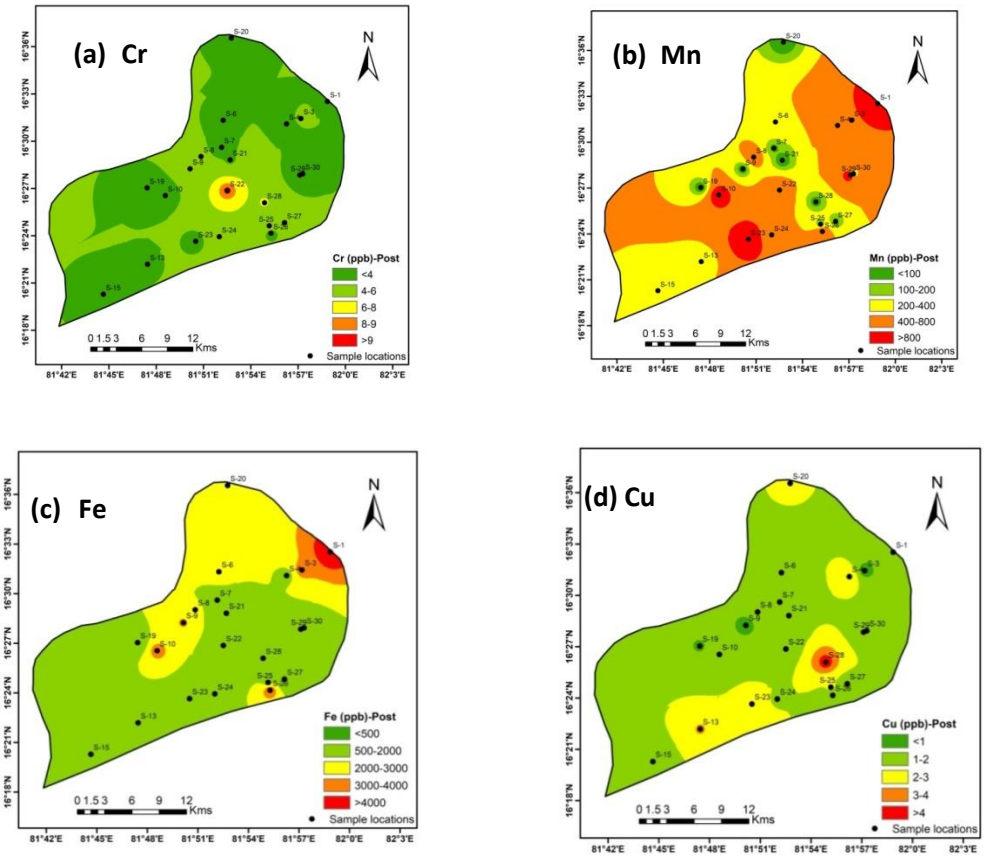


Figure6. Spatial distribution maps of metals **(a)** Cr, **(b)** Mn, **(c)** Fe, and **(d)** Cu in Konaseema region during the Post Monsoon

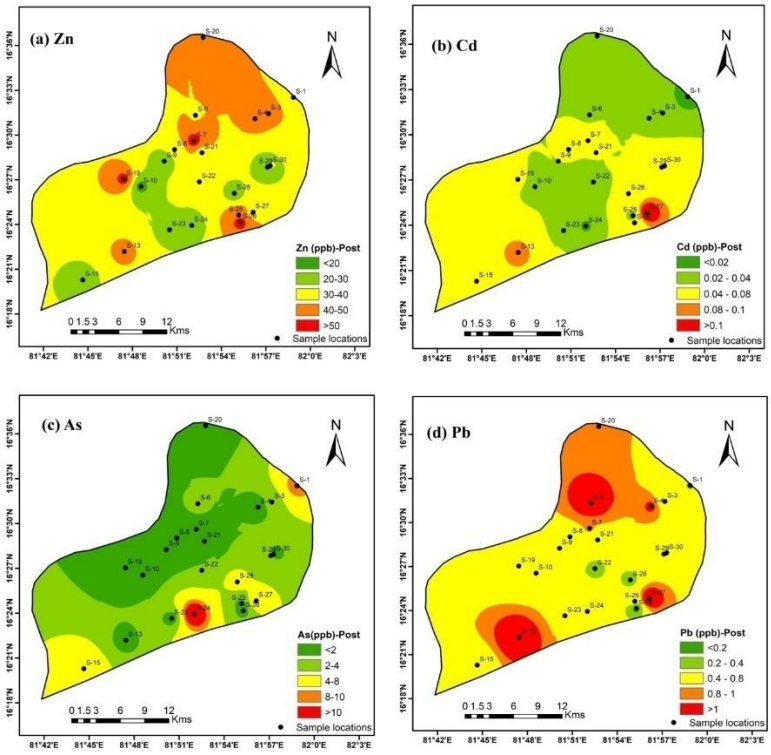


Figure7. Spatial distribution maps of metals, **(a)** Zn, **(b)** Cd, **(c)** As, and **(d)** Pb in Konaseema region during the Post Monsoon

Cobalt (Co) and Nickel (Ni)

Co and Ni occur at low concentrations with narrow ranges in both seasons (Table 1), indicating stable geogenic control. Minor post-monsoon variation in Co is linked to pH–redox-driven release from Fe–Mn oxides, while Ni shows dilution due to recharge. The limited variability and absence of spatial anomalies, suggest minimal influence from salinity intrusion or anthropogenic sources. Ni concentrations remain well within the BIS limit (20 ppb), while no specific BIS standard is prescribed for Co.

Cadmium (Cd), Arsenic (As) and Lead (Pb)

Cd remains very low with minimal seasonal variability (Figures 5b and 7b), indicating limited mobility and dominant geogenic origin. In contrast, As shows notable spatial variability (Figures5c and 7c), particularly at Pasarlapudi and Adavipalem, controlled by reductive dissolution of Fe–Mn oxyhydroxides under post-monsoon reducing conditions. Salinity intrusion further enhances As mobilisation through competitive desorption and ionic effects. Pb exhibits higher pre-monsoon concentrations (Figure5d) near aquaculture areas, followed by significant post-monsoon dilution (Figure7d), indicating anthropogenic input from aquaculture practices. Overall, As is redox-controlled and geogenic, Cd is immobile, and Pb reflects localized anthropogenic influence. As occasionally exceeds the BIS limit (10 ppb) at specific locations, whereas Cd (limit: 3 ppb) and Pb (limit: 10 ppb) remain within permissible limits.

Assessing anthropogenic controls on heavy metal co-occurrence

The correlation patterns of heavy metals in the Konaseema region (Figure8), reveal how oil and gas drilling, aquaculture activities, land-use practices, and subtle saltwater intrusion collectively influence groundwater quality across seasons. During pre-monsoon, strong correlations such as Ni–Cu (r = 0.85) and Zn–Pb (r = 0.88) point to common anthropogenic sources, likely arising from metal-rich drilling mud additives, corrosion inhibitors, and well-pad leakages, which tend to accumulate during low groundwater conditions. Moderate correlations between Cd–As (r = 0.58) and Cd–Ni (r = 0.46) suggest co-mobilisation of metals from drilling residues and phosphate fertilisers, which often contain trace Cd. Fe and Mn exhibit a moderate correlation (r = 0.45) but exceed drinking-water standards, reflecting premonsoon desorption, organic inputs from aquaculture, and early effects of saline water intrusion (Naga Jyothi, 2026) , where increased ionic strength promotes competitive ion exchange and releases Fe, Mn, and Cd from sediments.

During post-monsoon, correlation patterns shift toward redox-driven processes, intensified by monsoonal recharge, sediment–water interactions, and saline mixing in low-lying delta zones. Strong correlations among Co–Ni (r = 0.81), Mn–Co (r = 0.74), and Mn–Fe (r = 0.50), indicate the dissolution of Fe–Mn oxyhydroxides and concomitant release of trace metals following recharge. Organic-rich seepage from aquaculture ponds and drilling further enhances reducing conditions. A strong Pb–Cd correlation (r=0.62) and moderate Co–Fe correlation (r=0.29) after the monsoon suggest remobilisation of metals from sediments due to variations in pH, redox potential, and salinity. Saline water intrusion during and after the monsoon also increases the mobility of Pb, Cd, and Zn through competitive adsorption and ion displacement. Metals such as Cr and Zn, which show weak or negative correlations in both seasons, are likely influenced by distinct lithological sources or anthropogenic pathways less sensitive to redox or salinity changes. Overall, seasonal correlation patterns Table 2 demonstrate that human activities, including drilling fluids, agricultural chemicals, and aquaculture seepage, predominantly control pre-monsoon metal concentrations, while post-monsoon metal dynamics (Fe, Mn, Co, Ni) are largely governed by redox conditions, sediment interactions, and saline water intrusion (Naga jyothi, 2026). These findings underscore the Konaseema aquifer's vulnerability to monsoonal fluctuations, land-use pressures, and coastal saltwater intrusion.

Heavy Metal Pollution Index (HPI)

Detailed HPI values and classifications are provided in Table 3. The Heavy Metal Pollution Index (HPI) was calculated by assigning relative weights of each parameter (Table 4) for groundwater samples collected during pre- and post- monsoon seasons to assess the impact of heavy metal contamination using BIS Standards

During the pre-monsoon season, HPI values ranged from 8 to 35, indicating excellent to good groundwater quality with respect to heavy metals. Approximately 63% of the samples belonged to the excellent category (HPI < 25), with groundwater from Razole, Gudimellanka, Malkipuram, GudimulaKandrika, Kesavadasupalem, Sakhinetipalli, Mori, LankalaGannavaram, Pasarlapudi, and Mamidikuduru, showing minimal heavy-metal contamination. The remaining samples fell within the good category (HPI = 25–50), mainly in Thatipaka, Ponnamada, Kesanapalli, and Adavipalem, reflecting slightly elevated metal concentrations that remained well below the critical HPI threshold (100). These findings indicate that groundwater in the study area was not significantly affected by heavy-metal pollution during the pre-monsoon period.

In the post-monsoon season, HPI values ranged from 5 to 43, also indicating excellent to good groundwater quality. Groundwater from LankalaGannavaram, Razole, Gudimellanka, Malkipuram, GudimulaKandrika, Sakhinetipalli, Mori, Pasarlapudi, Mamidikuduru, Thatipaka, Ponnamada, Kesanapalli, and Adavipalem exhibited excellent quality with minimal heavy-metal contamination following monsoonal recharge. Good-quality groundwater was observed at a few locations around Thatipaka, Ponnamada, and Adavipalem, where metal concentrations remained within the permissible limits. The highest HPI value (43) was recorded in the Pasarlapudi–Mamidikuduru sector, indicating relatively greater post-monsoon metal mobilisation; however, the value remained well below the critical threshold of 100, confirming that groundwater throughout the study area remained suitable for drinking with respect to heavy metals.

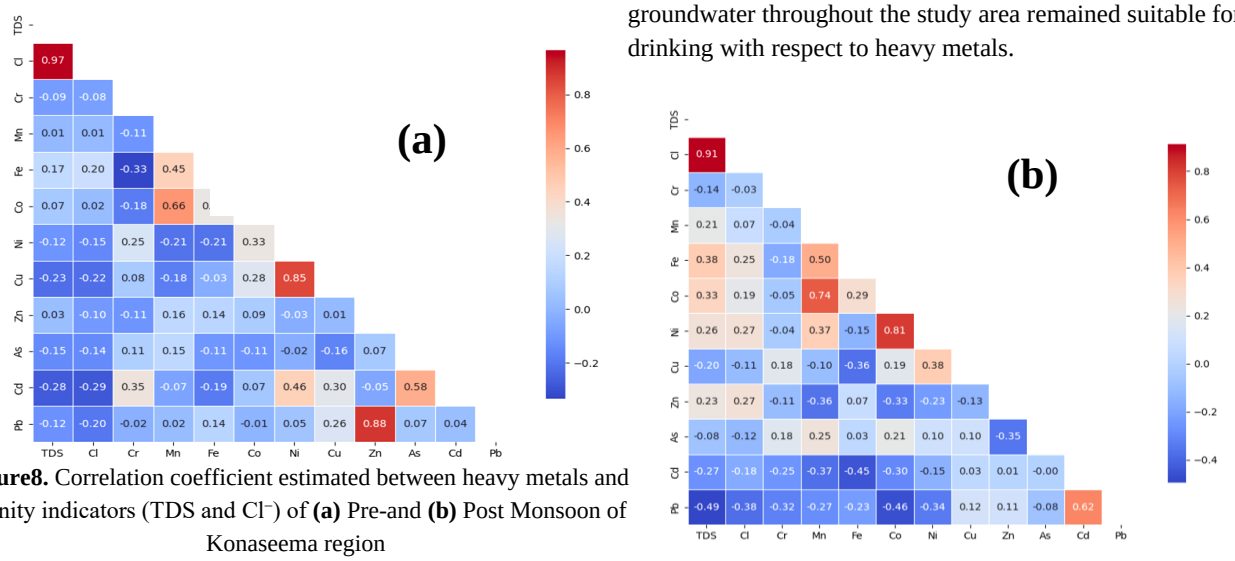


Figure8. Correlation coefficient estimated between heavy metals and salinity indicators (TDS and Cl^-) of **(a)** Pre-and **(b)** Post Monsoon of Konaseema region

Table 2. Interpretation of heavy metal correlation patterns in pre (PRM) and post (POM) monsoon seasons of the Konaseema region

Metal pair	Correlation coefficient (PRM)	Correlation coefficient (POM)	Interpretation
TDS – Cl	0.97	0.91	Very strong positive correlation in both seasons, indicating that chloride is the principal contributor to groundwater salinity. This reflects seawater intrusion and saline water mixing in the coastal aquifer.
Ni – Cu	0.85	0.38	Strong pre-monsoon association from drilling mud additives and corrosion inhibitors; weaker post-monsoon due to dilution and redox shifts
Zn – Pb	0.88	0.11	Co-occurrence from industrial/aquaculture inputs; strong dry-season accumulation, reduced influence after recharge
Cd – As	0.58	−0.00	Trace-metal co-mobilization from phosphate fertilizers; minimal post-monsoon linkage due to dilution and redox changes
Cd – Ni	0.46	−0.15	Mixed agricultural and drilling influences; negative post-monsoon value suggests different mobilization pathways under altered chemistry
Fe – Mn	0.45	0.50	Coupled release from Fe–Mn oxyhydroxides; stronger post-monsoon due to reductive dissolution during recharge
Mn – Co	0.66	0.74	Strong redox-controlled association; Co released with Mn under reducing conditions in both seasons
Co – Ni	0.33	0.81	Weak pre-monsoon linkage; very strong post-monsoon redox-driven release enhanced by aquaculture and drilling disturbances
Pb – Cd	0.03	0.62	Weak relationship in dry season; strong post-monsoon coupling from sediment remobilization and saline/organic-driven desorption
Cr – others	Weak	Weak	Largely lithogenic, limited anthropogenic influence; not significantly redox- or salinity-controlled
Zn – others	Weak	Weak to negative	Controlled by separate anthropogenic pathways; minimal seasonal geochemical coupling

Table 3. Water classifications based on HPI scores in Konaseema region

Range	Type of water	% of PRM samples	% of POM samples
<25	Excellent water	88	73
25–50	Good water	12	27
50–75	Poor water	–	–
75–100	Very poor water	–	–
>100	Water unsuitable for drinking	–	–

Table 4. Assigned relative weights of each parameter in Konaseema region

Chemical parameters	BIS (2012)	Relative weight (Wi)
Cr	50	0.02
Mn	100	0.01
Fe	300	0.003
Co	5	0.2
Ni	20	0.05
Cu	50	0.02
Zn	5000	0.0002
As	10	0.1
Cd	3	0.33
Pb	10	0.1

Seasonal Response of HPI to LULC and Coastal Processes

Higher HPI levels following the monsoon indicate that recharge improves both dilution and metal transport, particularly in aquaculture and coastal regions. Although aquifer resilience remains, intensified land use could heighten associated risks. Saltwater intrusion primarily causes heavy metal mobilisation, with localised impacts from aquaculture and oil and gas activities. While existing HPI levels are not alarmingly high, their spatial correlation with stressed areas highlights the need for targeted groundwater management and ongoing monitoring.

Influence of seawater intrusion, aquaculture, and oil–gas activities on trace metal distribution

Spatial heterogeneity and seasonal variations reflect hydrogeochemical processes, seawater intrusion and human activities in the coastal aquifer (Werner et al., 2013; Prustyand Farooq, 2020). Iron (Fe) shows broad, asymmetric seasonal distributions, indicating high spatial variability. Elevated Fe levels, especially after the monsoon, suggest increased mobilisation under reducing conditions. In coastal deltaic aquifers, saline-water mixing promotes reductive dissolution of iron-bearing minerals, increasing Fe concentrations (Melloul and Goldenberg, 1997; Appelo and Postma, 2005). Similar Fe enrichment linked to seawater intrusion has been reported from the Godavari delta and other Indian coastal aquifers (Surinaidu et al., 2016; CGWB, 2019). Manganese (Mn) shows broad, bimodal patterns, especially after the monsoon, indicating spatial variability. Mn mobilisation occurs via redox-sensitive dissolution of Mn oxides under saline and reducing conditions (McArthur et al., 2008). In Indian coastal areas, seasonal recharge and saline water intrusion enhance the release of Mn from groundwater (Rao et al., 2017). Arsenic (As) exhibits moderate variability with right-skewed distributions, suggesting localised enrichment. Its release primarily results from reductive dissolution of Fe–Mn oxyhydroxides, especially in saline and organic-rich environments (Smedley and Kinniburgh, 2002). Aquaculture activities, particularly shrimp farming, introduce organic matter and nutrients that create reducing conditions, facilitating As mobilisation (Chowdhury et al., 2021). Similar patterns of arsenic behaviour have been observed in deltaic aquifers of eastern India (Gopalakrishnan et al., 2019). Cobalt (Co) exhibits seasonal variability, with a wider distribution after the monsoon, suggesting sensitivity to redox changes and saline mixing. In contrast, Cadmium (Cd) remains low with minimal variation, indicating limited human influence and strong geochemical retention (Alloway, 2013). Chromium (Cr), Copper (Cu), and Nickel (Ni) are relatively concentrated, with occasional peaks, possibly linked to upstream oil and gas activities involving drilling muds, corrosion inhibitors, and produced water that contain trace metals affecting groundwater if containment fails (Neff, 2005; Darbra et al., 2018). Studies of Indian sedimentary basins also report localised Cr, Cu, and Ni enrichment near hydrocarbon exploration (Veerabhadrappa and Kumar, 2012). Zinc (Zn) and Lead (Pb) have low, stable concentrations with minimal seasonal variation, showing limited impact from industrial or agricultural sources. Their stability indicates strong adsorption to aquifer materials and restricted mobility under current conditions (Appelo and Postma, 2005). Overall, the spatial distribution map shows seawater intrusion mainly drives Fe and Mn enrichment, while aquaculture improves conditions that facilitate As mobilisation. Oil and gas activities locally add trace metals such as Cr, Cu, and Ni, but don't control regional groundwater chemistry. Seasonal monsoon recharge affects these processes by changing redox conditions and dilution, leading to more metal mobilisation post-monsoon.

The rise in Mn and Co after the monsoon signals improved reducing conditions and mixing of saline and freshwater. The decline in metals such as Cr, Ni, Cu, Zn, Pb, and As, suggests dilution from monsoon recharge and reduced human activity. Persistent metals such as Fe and Mn remain high due to hydrogeochemical controls and tidal effects from the Bay of Bengal. Indicators of saltwater intrusion include increases in Mn, high Fe, localised increases in As, and stable Ni, reflecting shifts in the aquifer along the saline–freshwater interface in the coastal delta. Stable, low levels of Cr, Co, and Ni indicate minimal metal contamination from drilling, though drilling can disrupt deep aquifers and introduce trace metals. The pre-monsoon rise and post-monsoon fall in Cu, Zn, and Pb concentrations from feeds, lime, fertilisers, and algicides suggest that aquaculture contributes to metal loading.

Influence of anthropogenic activities and hydrogeochemical processes on HPI

The distribution of Heavy Metal Pollution Index (HPI) values in the Konaseema region suggests possible influence of anthropogenic activities and coastal hydrogeochemical processes. Although most groundwater samples fall within the good HPI category in both pre- and post-monsoon seasons, localized increases indicate the influence of site-specific anthropogenic and natural factors. Oil and gas exploration—including drilling operations, fluid storage,

cuttings disposal, and accidental leaks—can indirectly elevate HPI levels at certain locations by introducing trace metals such as Cr, Ni, Pb, and Cd into the environment. Groundwater with higher HPI (good to moderate) is often associated with areas where protective clay layers are thin or discontinuous. The absence of HPI values exceeding 100, suggests limited large-scale contamination from oil and gas activities, with metal inputs likely localized and mitigated by regional groundwater flow and monsoonal recharge. Aquaculture, which dominates the Konaseema coast, also affects groundwater quality. Seepage and pond pumping can transport metals such as Cu, Zn, Fe, and Mn from fish feed, antifouling agents, and pond additives into shallow aquifers. Even groundwater classified as good in HPI terms may show diffuse metal inputs after the monsoon, highlighting the vulnerability of shallow aquifers to surface infiltration. Natural processes, particularly saltwater intrusion, further influence HPI distribution by increasing ionic strength, chloride concentration, and electrical conductivity, thereby promoting desorption and dissolution of metal minerals. Elevated post-monsoon HPI values at certain stations correspond to areas prone to saline water intrusion, indicating that salinity-driven mobilisation of Fe, Mn, and As contributes to changes in groundwater metal chemistry. Reductive dissolution of iron oxy hydroxides releases trace metals, raising HPI values without causing severe contamination, reflecting the combined effects of natural and anthropogenic controls. In the absence of quantitative LULC analysis, interpretations are based on field observations and known regional activities

CONCLUSIONS

1. Groundwater quality in the Konaseema coastal delta is controlled by seawater intrusion, natural hydrogeochemical processes, aquaculture, and localized oil and gas activities, with clear seasonal variations. HPI values indicate excellent to good groundwater quality, confirming its overall suitability for drinking with respect to heavy metals.
2. Elevated Fe and Mn are the major groundwater quality concerns, mainly controlled by reductive dissolution, saline–freshwater mixing, and reducing conditions, while localized As enrichment is linked to similar geochemical processes.
3. Higher metal enrichment and HPI values occur around Tatipaka, Pasarlapudi, Ponnamada, Kesanapalli, Adavipalem, Mori, Mamidikuduru, and Razole, where multiple stressors coexist. However, contamination remains localized, with no evidence of widespread impacts from hydrocarbon exploration alone.
4. Coastal villages such as Malikipuram, Sakhinetipalli, Gudimellanka, GudimulaKandrika, Kesavadasupalem, and LankalaGannavaram, are most vulnerable to seawater intrusion and trace-metal mobilisation due to coastal proximity, low elevation, and intensive aquaculture.
5. Post-monsoon recharge dilutes anthropogenic metals (Cu, Zn, Pb, Cr, and Ni), whereas Fe and Mn remain elevated due to geogenic and redox-controlled processes. Groundwater chemistry is mainly influenced by anthropogenic activities in the pre-monsoon and by natural processes after the monsoon.
6. Groundwater is presently suitable for drinking with respect to heavy metals, but expanding aquaculture, hydrocarbon development, and seawater intrusion may increase future vulnerability. This study provides a scientific baseline for sustainable groundwater management in the Konaseema coastal aquifer.

Acknowledgement

I express my sincere gratitude to the support extended by the APPCB during the laboratory analyses. I also acknowledge the valuable assistance of my colleagues, Mr. S. Eswar, Dr. V. Ajaykumar, and Mr. U. Nanaji in the processing of data. Finally, I extend my heartfelt appreciation to my husband Mr. Y. Rajashekar Reddy and all my family members for their constant encouragement, which greatly contributed to the successful completion of this research.

Author credit statement

B. Naga Jyothi: Conceptualization, data acquisition, data analysis and interpretation, writing of the original draft, and review and editing of the manuscript; K. Bhima Raju: Conceptualization, data acquisition and review and editing of the manuscript; GunnamVenkataRatnalu: Conceptualization, review and editing of the manuscript; P. V. Nagamani: Review and editing of the manuscript; G. Udaya laxmi: Review and editing of the manuscript.

Data availability

The data can be made available on a reasonable request from the corresponding author.

Compliance with ethical standards

The authors declare that they have no conflicts of interest and adhere to copyright norms.

References

Alloway, B.J., 2013. Heavy metals in soils: trace metals and metalloids in soils and their bioavailability. 3rd ed. Springer, Dordrecht.

APHA, 2017. Standard methods for the examination of water and wastewater. 23rd ed. American Public Health Assoc., American Water Works Assoc. (AWWA) and Water Envi.Fed. (WEF), Washington, DC.

Appelo, C.A.J. and Postma, D., 2005. Geochemistry, groundwater and pollut. 2nd ed. Balkema, Rotterdam.

BIS, 2012. BIS-Indian Standard: Drinking water specification (IS 10500:2012). Bureau of Indian Standards, New Delhi.

CGWB, 2014. Groundwater Year Book – Andhra Pradesh. Central Ground Water Board, Govt. of India.

CGWB, 2019. Impact of aquaculture on groundwater quality in coastal Andhra Pradesh. Central Ground Water Board, Govt. of India.

Chowdhury, A., Naz, A., Bhattacharyya, S., and Sanyal, P., 2021. Dynamics of salinity intrusion in surface and groundwater of the Bengal delta. IOP Conference Series: Earth and Envi.Sci., 944(1), Article 012061.

CPCB, 2010. Status of water quality in India. Central Pollut. Control Board, Govt. of India.

Darbra, R.M., Ronza, A., Casal, J.and Lomas, T.,2018. Environmental impacts of oil and gas exploration and production. J. of Petr. Sci. and Engin.,162, 486–501. https://doi.org/10.1016/j.petrol.2018.05.037

Gopalakrishnan, G., Chatterjee, A. and Chandra, R., 2019. Arsenic mobilization in deltaic aquifers of eastern India. Envi.Monit. Assess., 191(12), Article 783.

McArthur, J. M., Herczeg, A. L., Kőhler, S. J. And Islam, F., 2008. Natural organic matter controls on groundwater redox conditions. Chem. Geol., 247(1–4), 1–17.

Melloul, A.J. and Goldenberg, L.C., 1997. Monitoring of seawater intrusion in coastal aquifers: basics and local concerns. J.Envi.Manag., 51, 73–86.

MoEFCC, 2016. Environmental guidelines for onshore oil and gas exploration. Ministry of Envi., Forest and Climate Change, Govt. of India.

Naga Jyothi, B., Bhimaraju,K., GunnamVenkataRatnalu, Nagamani, P.V. andUdayalaxmi, G., 2026. HydrogeochemicalAssessment of Groundwater Degradation and Seawater Intrusion in the Coastal Aquifers of Dr.B.R.AmbedkarKonaseema District, Andhra Pradesh, India. J.Geophys., XLVI (2), 23-38.

Neff, J.M., 2005. Composition, Environmental fates, and biological effects of water-based drilling muds and cuttings discharged to the marine Envi. Sci. Tech., 39(7), 234A–241A.

ONGC, 2010. Geological framework and hydrocarbon prospects of the Krishna–Godavari Basin. Oil and Natural Gas Corporation Limited, Dehradun.

Prusty, P. and Farooq, S. H., 2020. Seawater intrusion in the coastal aquifers of India: A review. Hydro. Research, 3, 61–74.

Rao, K.L., 1975. India's water wealth: Its Assess., uses, and projections. Orient Longman, New Delhi.

Rao, K.N. and Radhakrishna, B.P., 1985. Geology of India. Vol. 2. Geol. Soc. India, Bangalore.

Rao, N. S., Vidyasagar, G., Rao, P. S.and Bhanumurthy, P., 2017. Chemistry and quality of groundwater in a coastal region of Andhra Pradesh, India. Appl. Water Sci., 7, 285–294.

Reddy, D. V., Nagabhushanam, P., Sukhija, B. S., Reddy, A. G. S.and Smedley, P. L., 2017. Geochemical processes controlling groundwater quality in the deltaic aquifers of Andhra Pradesh, India. Envi. Earth Sci., 76, 655.

Smedley, P.L. and Kinniburgh, D.G., 2002. A review of arsenic in groundwater. Appl. Geochem., 17, 517–568.

Subba Rao, N., Das, R. and Gugulothu, S., 2022. Understanding the factors contributing to groundwater salinity in the coastal region of Andhra Pradesh, India. J. Contaminant Hydrol., 250, 104053.

Subramanian, V., 1994. Sediment and water quality in Indian River deltas. Envi. Geol., 24, 1–10.

Subramanian, V. and Saxena, K.K., 1983. Hydrogeochemistry of coastal aquifers in India. J.Hydrol., 62, 49–66.

Surinaidu, L., 2016. Role of hydrogeochemical processes in increasing groundwater salinity in the central Godavari delta, India. Hydrol. Res., 47(2), 373–389.

Surinaidu, L., Rao, M. S., Reddy, D. V., Mahesh, J. and Prasad, K. M., 2015. Seawater intrusion and groundwater quality in the coastal aquifers of India. Envi. Earth Sci., 73, 5935–5947.

Surinaidu, L., Satyanarayana Rao, M., Das, A., Swarnkar, K., Durga Prasad, R. and Mishra, S. K., 2016. Coastal aquifer salinization and its influence on groundwater chemistry in the Godavari delta, India. Environ. Earth Sci., 75, 1252.

Veerabhadrappa, R. and Kumar, P., 2012. Environmental issues related to oil and gas exploration in India. International J.Envi. Sci. and Tech., 9, 547–560.

Werner, A. D., Bakker, M., Post, V. E. A., Vandenbohede, A., Lu, C., Ataie-Ashtiani, B., Simmons, C. T.and Barry, D. A., 2013. Seawater intrusion processes, investigation and management: Recent advances and future challenges. Adv. Water Res., 51, 3–26.

Received: 10-03-2026; Revised on: 30-04-2026; Accepted on: 30-04-2026

J. Ind. Geophys. Union, 30(6) (2026), 503-519
http://doi.org/10.71122/JIGU.30(6)2026.0049

District level long range forecast of rainfall during Monsoon

Onkari Prasad[1*], K. Prasad[2] and O. P. Singh[3]
[1]43, Ritu Apartments, A-4 PaschimVihar, New Delhi-110063, India
[2]D-104, Seema Apartments, Sector 11, Dwarka, New Delhi-110085, India
[3]B44, First Floor, Parshvnath Paradise, Mohan Nagar, Ghaziabad (U.P.)-201007, India
*Corresponding author:ponkari630@gmail.comEah

ABSTRACT

Based on the South Indian Ocean Convergence Zone (SIOCZ) model, district level long range forecast of southwest monsoon seasonal rainfall are being issued for the states of Tamil Nadu, Himachal Pradesh, Andhra Pradesh, Telangana and Maharashtra including Goa since 2005, 2008, 2015, 2015 and 2016, respectively. For the state of Tamil Nadu, district level monthly forecast of rainfall during southwest and northeast monsoons are being issued since 2014 and 2023, respectively. Development of SIOCZ model for district level forecast of rainfall in Tamil Nadu and its performance has been discussed. For further improvement in monthly forecast, improvement in forecast updates and their issue at a regular interval say at the beginning of each month is required. For further improvement in monthly updates,information on the influence of major oscillations in Indian and Pacific Oceans, i.e., Madden Julian Oscillation (MJO), Indian Ocean Dipole (IOD) and ENSO (El Nino/Neutral/La Nina) on monsoon rainfall in India are considered important. Influence of these oscillations on rainfall during 2023 southwest and northeast monsoons has been discussed here. We find that MJO plays the most important role in intra-seasonal oscillations in Indian monsoon rainfall and that the forecast of location and strength of MJO available from the Bureau of Meteorology, Australia, NOAA and ECMWF are helpful in issuing long range forecast of rainfall in India and its monthly updates.

Keywords: Indian monsoon, Long range forecast, South Indian Ocean Convergence Zone model, Madden-Julian Oscillation, Indian Ocean Dipole, ENSO, Forecast update

Nomenclature

ENSO:	El Nino Southern Oscillation	IAV:	Inter-Annual Variability
IOD:	Indian Ocean Dipole	ISV:	Intra-Seasonal Variability
LRF:	Long Range Forecast	MJO:	Madden-Julian Oscillation
OLR	Outgoing Long-wave Radiation	RMM:	Real-time Multivariate MJO
MCZ:	Maximum Cloud Zone	SIOCZ:	South Indian Ocean Convergence Zone
SAI:	SIOCZ Activity Index	SST:	Sea Surface Temperature

INTRODUCTION

Long Range Forecast (LRF) of rainfall has application in several sectors. Agriculture sector happens to be the main beneficiary of these forecasts. LRF of monthly rainfall at district level, is required for agricultural planning and operations. Choosing a crop, other than the traditional one, could be greatly facilitated, if reliable LRF of quantum of seasonal rainfall is made available at district level in the beginning of the season. Based on a new approach to long range forecasting of monsoon rainfall, South Indian Ocean Convergence Zone (SIOCZ) Model had been proposed earlier by the authors (Gupta and Onkari Prasad, 1992,1993; Onkari Prasad et al., 2010a; Onkari Prasad and Singh, 2012, 2013). Hereafter, SIOCZ has been referred to as The Convergence Zone, SIOCZ Activity Index as The Activity Index, and SIOCZ Model as The Model. Based on The Model, district level seasonal forecast of rainfall during southwest monsoon are being issued, on an operational basis, for the states of Tamil Nadu, Himachal Pradesh, Andhra Pradesh, Telangana and Maharashtra including Goa since 2005, 2008, 2015, 2015 and 2016, respectively (Onkari Prasad and Singh, 2008; Onkari Prasad et al., 2010b; Onkari Prasad et al., 2016a-c). Issuing forecast for the subdivisions of southern peninsular India for northeast monsoon has started recently (Onkari Prasad et al., 2022, 2023a) and the district level monthly and seasonal forecast during northeast monsoon in the state of Tamil Nadu is being issued since 2023. Availability of district level LRF of rainfall for the state of Tamil Nadu for both the monsoon periods, may be considered as a significant improvement in The Model. The paper contains two parts: Issuing district level LRF of seasonal and monthly rainfall, on an operational basis, is discussed in the first part. In the context of improving district level monthly forecast, understanding the role played by the major oscillations in Indian and Pacific Oceans, i.e., Madden Julian Oscillation (MJO) (Madden and Julian, 1972; Wheeler and Hendon, 2004), Indian Ocean Dipole (IOD) (Saji et al., 1999; Kriplani and Pankaj Kumar, 2004; Singh and Onkari Prasad, 2011) and ENSO (El Nino/Neutral/La Nina) on rainfall during monsoon becomes important. The preliminary results relating to a comprehensive study on the influence of these oscillations on monsoon rainfall in India are discussed, in brief, in the second part of the paper.

DATA AND METHOD OLOGY

The data used in the study include: (i) Time-latitude plots of NOAA OLR total and OLR anomalies for the period from October 2022-December 2023, (ii) Estimate of satellite observed cloudiness from Indian Ocean region for the period November 2022 -December 2023, (iii) Real-time Multivariate MJO (RMM) Phase Diagram for the period November 2022-December 2023, (iv) IOD mode index values during May 2023-February 2024, (v) monthly SST anomaly data for Nino regions of Pacific, (vi) 3-monthly average SST anomaly data for Nino 3.4 region during 2023, (vii) weekly rainfall for four broad regions of India and India as a whole during 2023 southwest monsoon, weekly monthly and seasonal rainfall in the subdivisions of south peninsular India during 2023 northeast monsoon.

RESULTS

Subdivision level long range forecast

The values of The Activity Index, as the one used for preparing LRF of southwest monsoon seasonal rainfall, for India as a whole, has been used for developing regression equations between The Activity Index and monthly and seasonal rainfall in the subdivisions also. A total of 30 forecasts had been issued till 2019. The results of verification are included in Table 1. The correlation coefficient between The Activity Index and southwest monsoon seasonal rainfall was not significant in 9 subdivisions of East and Northeast India (Subdivision Nos. 1-9), Tamil Nadu, Coastal Karnataka, North Interior Karnataka, South Interior Karnataka and Kerala. (Table1). Subsequently, the correlation coefficient had been improved for the subdivision of Tamil Nadu (Onkari Prasad et al., 2010b). For developing The Model for an individual subdivision, Tamil Nadu had been chosen as a test case: (i) In Tamil Nadu, monthly and seasonal rainfall amounts are small and there is large spatial variation of rainfall at district level, (ii) The model once developed for southwest monsoon could be extended for northeast monsoon rainfall in Tamil Nadu. The Model for the subdivision of Tamil Nadu was developed in 2005 (Onkari Prasad et al., 2010b). The summary of the results of verification is given in Table 1. Verification has been carried out in those subdivisions only where the correlation coefficient was significant at 95% or a better confidence level. The number of such subdivisions for the month of June, July, August and September and for the season as a whole (June-September) is 6, 17, 9, 17 and 26, respectively. It follows from the results that improvement is required in monthly forecasts. The authors had attempted to develop The Model for northeast monsoon also (Onkari Prasad et al., 2022, 2023a). Issuing subdivisions level forecast for northeast monsoon, on an operational basis, started since 2022 and for the districts of Tamil Nadu since 2023 (Onkari Prasad et al., 2022, 2023b). The summary of the results of verification of subdivision level LRF of northeast monsoon for the years 2022 and 2023 is given in Table 2. The criteria for verification remained the same as it was used for southwest monsoon rainfall. The summary of the verification of district level forecast is given in Table -3

District level rainfall data became available from India Meteorological Department (IMD) in 2010 (IMD, 2010). Data for the period 1975-2000 had been used to improve the correlation coefficients. The values of the Activity Index are given in Table 4. The correlation coefficient for all the districts and the regression constants (straight line) for those districts only where the correlation coefficient is significant at 95% level are given in Table 5. Verification of forecast has been carried out for 3 groups of years, i.e., model development period (1975-2000), forecast verification period (2001-2013) and real time forecast verification period (2014-2023). The results of verification have been included in Table 6. The criteria used in IMD for categorization of departures of rainfall from its long period average, i.e., Large Excess (LE, ≥60%), Excess (E, 20-59%), Normal (N, ±19%), Deficient (D, -20 to -59%), Large Deficient (LD, -60% to -99%) and No Rain (NR, -100%) have been followed here also. For the purpose of verification, the % departure ranges of 'LE','E', 'N', 'D','LD' and 'NR' have been clubbed into two broad departure ranges only, i.e., 'LE/E/N' and 'D/LD/NR'. A forecast has been considered useful if both, i.e., the forecast and the realised rainfall are in the same broad category or it becomes so when Model Error (ME) is taken into account. The average ME for the subdivision of Tamil Nadu for the months of July, August, September and for the season is ±7% and for the districts of Tamil Nadu it is ±14%, ±10%, ±9% and ±8%, respectively. The ME is based on the assumption that there could be an error of ±2 in assigning The Activity Index in a year. Forecast has been considered useful when the average of monthly and seasonal forecast in a district is 60% or more. Considering those districts only for which the forecasts were available, the average % of useful monthly and seasonal forecast for 3 groups of years is given at the bottom of Table 6. If the average percentage of monthly and seasonal forecast in a district is less than 60% years, the forecast in that district has been considered as not-useful.

Table 1. Summary of the results of verification of subdivision level monthly and seasonal long range forecast for the 30 year period of 1990-2019. *Verification Criteria*: A forecast has been considered 'Useful', if both, realized as well as the forecast rainfall, were in the same broad categories of 'Large Excess (LE)/Excess (E)/Normal (N)' or 'Deficient(D)/Large Deficient (LD)/No Rain (NR)' or they become so after Model Error (ME) was taken into account. The ME is different for monthly and seasonal rainfall and it differs for subdivisions also. The correlation coefficient are not significant at 95% level in subdivisions at S.Nos. 1-9, 35 (Kerala) and 36 (Lakshadweep). They are not included in the table.

S. No. and name of the subdivision	% of years when forecast was in useful category				
	Jun	Jul	Aug	Sep	Jun-Sep
10. East Uttar Pradesh			87		87
11. West Uttar Pradesh	83	83		67	87
12. Uttarakhand				80	83
13.Har.,Chandi. & Delhi	70	83		77	80
14. Punjab		83		70	93
15. Himachal Pradesh		70		67	77
16. Jammu,Kashmir, Laddakh		80		60	83
17. West Rajasthan	90	90			87
18. East Rajasthan	90	83		83	93
19. West Madhya Pradesh.	80			73	83
20. East Madhya Pradesh.	73	70			90
21. Gujarat Region		77		70	90
22. Saurashtra & Kutch		63		70	83
23. Konkan & Goa				73	93
24.Madhya Maharashtra		83		70	90
25. Marathwada		67	73	67	87
26.Vidarbha		77		70	87
27. Chhattisgarh				68	93
28.Costal Andhra Pradesh		80	83		90
29. Telangana		73	87	67	93
30. Rayalaseema		73	90		83
31.Tamil Nadu		60	67		87
32. Coastal Karnataka				77	87
33. North Interior Karnataka			80		
34. South Interior Karnataka		77	83		

Table 2. Summary of the results of verification of subdivision level monthly and seasonal long range forecast of rainfall during 2022-23 northeast monsoon. The number of subdivisions where verification has been carried out are 2 for October. i.e., Tamil Nadu and Kerala; 4 for November, i.e., Tamil Nadu, Rayalaseema, South Interior Karnataka and Kerala; 4 for December, i.e., Tamil Nadu, Coastal A.P., Rayalaseema and Kerala and in all the five subdivisions for seasonal (Oct-Dec) rainfall

Number of subdivisions, out of 5, where CC between The Activity Index and rainfall is significant)	Oct (2/5)	Nov(4/5	Dec(4/5)	Oct-Dec (5/5)
Year 2022				
Number of subdivisions where forecast was in useful category	1	3	2	3
Year 2023				
Number of subdivisions where forecast was in useful category	2	4	3	3

Table 3. Summary of the results of verification of district level seasonal forecast during southwest monsoon. *Verification Criteria*: Same as that used for subdivision level forecast

Subdivision/State	No. of districts for which verification has been carried out/ Total No. of districts	Period for which forecast was issued	Range (%) of districts where forecast was in useful category and its average (%)	
			Range (%)	Average (%)
Tamil Nadu	28/32	2005-19	46-100	73
Himachal Pradesh	6/12	2008-19	66-100	85
Andhra Pradesh	12/13	2015-19	50-100	87
Telangana	10 /10	2015-19	70-100	84
Maharashtra	30/34	2016-19	63-93	76
Goa	2/2	2016-19	100 in each year	100

Table 4. SIOCZ Activity Index (SAI) used in the development of The Model for district level LRF of monthly and seasonal rainfall in Tamil Nadu during southwest monsoon. The period of data used is 1972-2023, except 1978. Beginning from 2010, forecast updates are being issued during the season. For preparing an update, The SAI value assigned at the beginning of the season is modified. The modified value of SAI has been given in the bracket.

Year	1972	1973	1974	1975	1976	1977	1979	1980	1981	1982	1983	1984	1985
SAI	9	7	7	2	7	8	7	17	3	14	4	6	3
Year	1986	1987	1988	1989	1990	1991	1992	1993	1994	1995	1996	1997	1998
SAI	15	14	3	9	13	8	9	12	16	10	1	13	8
Year	1999	2000	2001	2002	2003	2004	2005	2006	2007	2008	2009	2010	2011
SAI	18	10	13	20	9	12	13	15	8	9	10	4(7)	7(11)
Year	2012	2013	2014	2015	2016	2017	2018	2019	2020	2021	2022	2023	
SAI	18	4	9	13	12	15	7	12(10)	14(10)	13	12(10)	8	

Table 5. Correlation coefficient (CC) between SAI and monthly and seasonal rainfall in the subdivision of Tamil Nadu and the districts of the state of Tamil Nadu and the regression constants(a and b). The period of data used for working out correlation coefficient is 25 years (1975-2000) and the value of correlation coeficients equal to ± 0.38 is significant at 95% level. The number of districts where CC is significant at 95% or a better confidence level is given in the bracket after the name of the month.The values of regression constants (a and b) have been given for those districts only where correlation coefficient is significant. Correlation coefficient is not significant for rainfall in June for the subdivision and also for any of the district of the state of Tamil Nadu. Correlation coeficientis also not significant in any of the month as well as for the season in the districts of Kanyakumari, Tirunelveli, Tenkasi and Thoothukudi. These four districts have not been included in the table.

Subdivision of Tamil Nadu and districts of the state of Tamil Nadu/ total number of district	Jul (25/34) CC a b	Aug (15/34) CC a b	Sep (21/34) CC a b	Jun-Sep (31/34) CC a b
Subdivision of Tamil Nadu	-.50 -3.1 106.9	-.49 -3.3 126.4	-.64 -4.2 167.9	-.81 -11.3 469.6
Ariyalur	-.45 -3.7 97.0	-.37	-.29	-.61 -12.5 461.4
Chennai	-.38 -3.9 143.9	-.22	-.52 -7.4 203.5	-.48 -12.6 564.3
Coimbatore	.15	-.23	-.56 -6.2 191.1	-.29
Cuddalore	-.47 -4.2 118.9	-.33	-.28	-.68 -10.0 469.0
Dharmapuri	-.31	-.29	-.43 -5.4 226.1	-.50 -11.7 507.0
Dindigul	-.53 -3.9 88.2	-.53 -4.2 109.5	-.33	-.58 -11.9 439.5
Erode	-.17	-.01	-.44 -6.1 200.6	-.16
Kanchipuram	-.50 -7.9 187.2	-.20	-.51 -8.1 236.2	-.66 -24.1 730.5
Chengalpattu	-.50 -5.6 139.9	-.08	-.42 -5.6 185.4	-.68 -16.9 589.6
Karur	-.52 -3.0 57.9	-.40 -3.0 72.5	-.33	-.53 -9.1 294.6
Krishnagiri	-.45 -3.6 99.5	-.42-4.9 143.8	-.26	-.56 -11.4 501.0
Madurai	-.38 -2.6 93.9	-.25	-.36	-.46 -7.7 417.1
Nagapattinam	-.41 -3.9 94.1	-.60 -5.5 126.0	-.53 -5.3 142.8	-.77 -15.9 407.8
Mayiladuthurai	-.37	-.38 -5.7 153.3	-.30	-.59 -12.1 420.9
Namakkal	-.64 -5.4 123.4	-.47 -5.0 147.8	-.24	-.63 -13.5 495.5
Nilgiris	.07	-.41 -6.0 286.5	-.75 -9.5 281.6	-.39 -14.3 076.4
Perambalur	-.36	-.46 -4.5 115.3	-.45 -6.0 173.5	-.64 -15.6 403.0
Pudukkottai	-.48 -3.0 92.8	.53 -5.1 147.2	-.52 -4.4 157.2	-.77 -12.8 446.0
Ramanathpuram	-.52 -2.6 50.0	-.48 -2.0 50.1	-.33	-.65 -7.4 202.3
Salem	-.40 -3.2 114.9	-.36	-.34	-.56 -10.5 515.3
Sivaganga	-.32	-.33	-.13	-.39 -7.6 398.2
Thanjavur	-.48 -3.7 98.8	-.54 -5.6 151.5	-.72 -6.6 185.8	-.89 -17.1 481.9
Theni	-.06	-.13	-.38 -3.3 25.7	-.20
Tiruvallur	-.47 -4.7 146.9	-.29	-.50 -5.7 192.5	-.65 -16.9 604.4
Tiruvannamalai	-.52 -6.2 156.4	-.30	-.50 -6.3 29.3	-.69 -18,5 654.3
Tiruvarur	-.43 -4.0 104.0	-.62 -6.1 149.6	-.44 -4.5 156.2	-.83 -16.1 459.1
Tirupur	-.29	-.34	-.35	-.46 -6.7 229.5
Tiruchirapalli	-.57 -3.9 82.7	-.27	-.44 -4.2 176.9	-.63 -11.2 392.7
Vellore	-.48 -6.9 169.9	-.32	-.41 -6.0 225.0	-.69 -20.5 675.7
Ranipet	-.44 -5.3 150.6	-.20	-.47 -6.6 207.6	-.68 -19.0 652.5
Tirupattur	-.60 -8.3 168.2	-.53 -9.4 210.4	-.49 -8.7 240.0	-.84 -29.7 717.8
Villupuram	-.47 -6.9 152.6	-.31	-.49 -4.2 168.6	-.55 -13.3 515.6
Kallakurichi	-.50 -6.0 133.8	-.44 -6.3 188.7	-.38 -5.0 213.2	-.70 17.7 588.5
Virudhunagar	-.39 -3.0 69.0	-.63 -4.4 90.7	-.11	-.59 -8.3 287.5

Table 6. Average % of 'Useful' monthly and seasonal rainfall forecast during southwest monsoon in the subdivision of Tamil Nadu and those districts of the state of Tamil Nadu where correlation coefficient between SAI and rainfall is significant at 95% or a better confidence level. The number of such districts for July, August, September and June-September is 25, 15, 21 and 31, respectively. The correlation coefficients are not significant for any of the district for the month of June. Similarly, the correlation coefficient is not significant in any of the month as well as for the season in the districts of Kanyakumari, Tirunelveli, Tenkasi and Thoothukudi. The name of these districts have not been included in the table.

Subdivision of Tamil Nadu and districts of the state of Tamil Nadu/ total number of district	Average % of useful monthly and seasonal forecasts in the districts during											
	Model development period (1975-2000)				Forecast verification period (2001-13)				Real time forecast Verification period (2014-23)			
	Jul (25/34)	Aug (15/34)	Sep(21/34)	Jun-Sep (31/34)	Jul (25/34)	Aug(15/34)	Sep (21/34)	Jun-Sep (31/34)	Jul (25/34)	Aug(15/34)	Sep (21/34)	Jun-Sep (31/34)
Subdivision of Tamil Nadu	80	84	84	96	61	77	92	92	70	80	80	70
Ariyalur	80			92	*58*			81	80			70
Chennai	*52*		80	72	85		70	*54*	*50*		70	100
Coimbatore			76				69				70	
Cuddalore	76			100	69			69	70			90
Dharmapuri			80	92			61	85			*40*	60
Dindigul	80	80		88	69	61		61	80	60		70
Erode			68				*54*				70	
Kanchipuram	64		80	84	69		92	85	70		60	100
Chengalpattu	72		88	92	61		77	69	100		67	80
Karur	72	76		80	61	61		77	90	60		90
Krishnagiri	76	76		88	61	61		69	90	90		80
Madurai	80			92	61			*38*	50			80
Nagapattinam	68	*56*	92	88	*54*	92	*54*	61	60	70	60	60
Myiladuthurai		72		96		85		78		80		70
Namakkal	84	72		92	*54*	100		*54*	60	70		60
Nilgiris		84	92	100		85	77	92		90	90	100
Perambalur		80	76	76		83	*58*	90		*50*	60	*40*
Pudukkottai	88	72	84	96	77	77	69	77	90	80	80	80
Ramnathpurm	60	80		80	*43*	92		69	*40*	60		70
Salem	76			88	77			77	80			80
Sivaganga				96				85				100
Thanjavur	84	68	84	100	69	87	69	69	70	70	70	60
Theni			60				69				*50*	
Tiruvallur	60		76	76	70		69	69	60		80	90
Tiruvanamalai	72		88	88	69		85	85	80		80	90
Tiruvarur	76	*56*	76	100	69	85	61	77	80	90	*50*	70
Tirupur				72				69				80
Tiruchirapalli	76		84	100	*54*		*54*	85	70		70	70
Vellore	72		80	88	69		69	61	60		80	90
Ranipet	80		84	92	67		77	61	80		83	100
Tirupattur	76	76	64	92	69	85	*46*	77	67	83	83	80
Villupuram	60		88	88	77		77	85	80		80	90
Kallakurichi	68	76	92	96	69	*54*	61	80	60	67	*50*	70
Virudhunagar	*52*	*56*		84	*54*	70		*54*	70	70		60
Average % of useful forecast	72	72	81	89	68	84	72	75	71	78	69	80

The figure giving average % of not-useful forecasts has been shown in italics in Table 6. There is no district in not-useful category during September of model development period and also for the season as a whole. The number of districts where forecast was in not-useful category was 2 (or 4%) in July, and 3 (or 20%) during August. During forecast verification period, there were 6 (or 24%) districts in not-useful category during July. The number of such district was 1 (or around 7%) during August, 5 (or 24%) during September and 3 (or 10%) for the season as a whole. During the period of real time forecast verification, the number of such districts was 3 (or 12%) during July, 1 (or 7%) in August, 4 (or 19%) in September and 1 (or 3%) during the season as a whole. Thus, the percentage of

districts where forecasts were in not-useful category is very small compared to the percentage of districts where forecasts were in useful category.

In order to further examine The Model's ability to produce useful district level forecast, the data on useful forecast contained in Table 6 have been re-grouped in 5 categories: 'Excellent', 'Very Good', 'Good', 'Average' and 'Below Average'. A forecast in a district has been considered as 'Excellent', if it was in useful category in all the years, 'Very Good' if it was useful in 99-81% years, 'Good' if it was useful in 80-61% years, 'Average' if it was useful in 60-51% years and 'Below Average' if it was useful in 50% years or less. The percentage of districts falling in different categories of forecast is given in Table 7. It follows from Table 7 that the forecasts were in 'Excellent' category for seasonal rainfall in only 16% districts during model development and real time forecast verification periods. 'Excellent' forecasts were not available for monthly rainfall. Forecasts were in 'Very Good' category for monthly as well as seasonal rainfall during all the 3 groups of years. The percentage of districts where forecasts were in 'Very Good' category has ranged from 12% in July of model development period to 72% during forecast verification period. For seasonal rainfall, the percentage of districts in 'Very Good' category of forecast was 65% during model development period, 29% during forecast verification period and 19% during real time forecast verification period. The % of districts where forecasts were in 'Good' category has ranged from 20% in July to 80% in August during model development period. The figures for seasonal rainfall are 19% during model development period, 58% during forecast verification period and 46% during real time forecast verification period. The % of districts with useful forecasts belonging to 'Very Good' and 'Good' categories put together during the 3 groups of years and for the months of July, August, September and for the season were, 80, 80, 95, 92; 92, 86, 76, 87 and 64, 73, 67, and 65, respectively. The % of districts with useful forecast belonging to 'Average' category has ranged from 4% in July of forecast verification period to 20% in July and August of real time forecast verification period. For seasonal rainfall, the figure was 10% during forecast verification period and 16% during real time forecast verification period. The percentage of districts with useful category of forecasts belonging to 'Below Average' category was 5% and 3% during September and for the season as a whole, respectively, during forecast verification period and 12%,7%,19% and 3% during July, August, September and for the season as a whole, respectively. The percentage of useful forecasts in 'Average' and 'Below Average' categories were more during real time forecast verification period. However, the percentage of useful forecast in these two categories was either 20% or less. The percentage of districts with useful forecasts belonging to 'Very Good' and 'Good' categories put together during the 3 groups of years and for the months of July, August, September and for the season as a whole were: 80, 80, 95, 92; 92, 86, 76, 87 and 64, 73, 67 and 65, respectively. The verification results have shown that The Model has been able to produce useful LRF of southwest monsoon seasonal rainfall, on real time basis, in a large number of districts. The model is also capable of producing useful LRF of monthly rainfall in some of the districts. Further work is required to improve the number of districts falling in useful category of forecast of monthly rainfall. This calls for improvement in forecast updates and their issue before the commencement of a month.

Table 7. Percentage of districts falling in different categories of useful forecast during 3 groups of years

Forecast category	Percentage of districts in different categories of useful forecast during											
	Model development period (1975-2000)				Forecast verification period (2001-2013)				Real tine forecast verification period (2014-2023)			
	Jul	Aug	Sep	Jul-Sep	Jul	Aug	Sep	Jul-Sep	Jul	Aug	Sep	Jul-Sep
Excellent				16	4	7			4			16
Very good	12		43	65	72	53	9	29	12	20	14	19
Good	68	80	52	19	20	33	67	58	52	53	53	46
Average	20	20	5		4	7	19	10	20	20	14	16
Below Average							5	3	12	7	19	3

Legend: Excellent: The forecast were in useful category in all the years. Very Good: in 99-81% years, Good: in 80-61% years, Average: in 60-51% years and Below Average: in 50% or less percentage of years.

During northeast monsoon

Development of northeast monsoon and its LRF of monthly and seasonal rainfall in the subdivisions of southeast peninsular India have been recently reported by Onkari Prasad et al. (2022, 2023a). It has been shown that the correlation coefficient between The Activity Index and rainfall in Tamil Nadu are significant at 95% level in 12 districts for October rainfall, 35 districts for November rainfall, 37 districts for December rainfall and at 99% level in all the 38 districts of the state for seasonal rainfall. Due to carving out of new districts in Tamil Nadu, the number of districts has increased from 34 to 38. Issuing district level LRF of monthly and seasonal rainfall on real time basis for the state of Tamil Nadu has begun since 2023. Verification of monthly and seasonal forecast for the year 2023 (table not reproduced) has shown that the percentage of districts where forecast was in useful category was at 100%, 91%, 94% and 92%, respectively. The criteria used for verification were the same as that used for rainfall during southwest monsoon. One of the requirements of preparing reliable district level LRF of rainfall during monsoon is to improve the correlation coefficient between The Activity Index and subdivision level seasonal rainfall. Once this is done, the best fit values of The Activity Index could be used to find the correlation coefficient and regression constants (straight line) for the districts of the subdivision also. Preparation of district level forecast of monthly and seasonal rainfall during northeast monsoon has been demonstrated for the state of Tamil Nadu, the details of which being reported separately. The other requirement for better forecasts is to improve the updates and issue them before the commencement of a month.

The Model assumes that Inter-Annual Variability (IAV) signals that develop during the period November of the previous year-March of the current year and Intra-Seasonal Variability (ISV) signals that develop during pre-monsoon months of April-May of the current year, continue to recur during southwest and northeast monsoons. When, an IAV/ISV signal was going to recur or when a new ISV signal was going to develop, are not known. A typical example is the case of 2023 southwest monsoon, when recurrence of IAV signal took place thrice, i.e., during June, July and September. The ISV signal had recurred during June-July and August 2023. How to foresee the interplay of IAV and ISV signal during the season is the most difficult aspect of improvement in updates. In this context, understanding the influence of Madden Julian Oscillation (MJO) (Madden and Julian, 1972; Wheeler and Hendon, 2004), Indian Ocean Dipole (IOD) (Saji et al., 1999; Kriplani and Pankaj Kumar, 2004; Singh and Onkari Prasad, 2011) and ENSO (El Nino/Neutral/La Nina), becomes crucial. Once, the influence of these oscillations on rainfall over India is known, their forecast available from the climate models of the lead centres, could be utilized in improving updates. Eastward and northward movement of a MJO pulse in OLR Anomalies (OLRA) and 850-hPa wind vector anomalies (u850A, and v850A) has been shown by Wheeler and Hendon (2004). The composite, depicts the structure and evolution of the MJO and thus identifies the cause behind intra-seasonal variability of Indian monsoon. They have also given a method for finding an all-season Real-Time Multivariate MJO (RMM) index and its prediction. Following Wheeler and Hendon (2004), information on recent evolution, current status and forecast of location and strength of MJO are available one month in advance from the Bureau of Meteorology, Australia, NOAA and ECMWF. The preliminary results relating to influence of MJO, IOD and El Nino on rainfall during 2023 southwest and northeast monsoons are discussed below, in brief. Both, IOD and El Nino had developed during 2023.

Influence of MJO

The location and strength of Real-Time Multivariate MJO (RMM) index during the period June-December 2023, is given in Table 8 (Bureau of Meteorology, Australia, 2023). Duration of RMM over Indian Ocean sector, development of convection in The Convergence Zone (Eq.-10ºS, 40-100ºE), near equatorial regions of north Indian Ocean (Eq.-5ºN, 40-100ºE), Arabian Sea, mainland India and Bay of Bengal during 2023 southwest monsoon is given in Table 9. A positive influence of MJO is seen on the rainfall. With each case of arrival of MJO pulse over Indian Ocean, there was an enhancement in rainfall over India. The only exception was the presence of a very weak pulse of MJO for a short duration of 3 days during 29-31 August 2023. The weak MJO pulse remained located in Unit Circle (UC) of RMM phase diagram.

Table 8. Duration of RMM over Indian Ocean and its strength during June-December 2023 (Source:http://www.bom.gov.au/climate/mjo/#tabs=Monitoring)

Month	Duration of MJO over Indian Ocean sector and its strength
Jun	7-18 Jun: moderately strong during 7-15 Jun and weak during 16-18 Jun; 24-30 Jun: moderately strong during 24-25 Jun, very weak during 26-27 Jun and weak during 28-30 Jun
Jul	5-14 Jul: moderately strong during 5-7 Jul and weak thereafter
Aug	MJO did not enter Indian Ocean sector till 28 Aug. A weak pulse of MJO entered Unit Circle of RMM phase diagram on 29th Aug and stayed there up to 31st Aug
Sep	1-8 Sep: very weak during 1-4 Sep, moderately strong during 5-8 Sep. A very weak pulse during 15-20 Sep
Oct	MJO did not enter Indian Ocean sector
Nov	3-7 Nov: very weak, and a strong pulse during 22-30 Nov
Dec	Moderately strong pulse during 1-3 Dec and again during 30-31 Dec

Table 9. Duration of MJO over Indian Ocean sector, development of convection in The Convergence Zone, the near equatorial regions of north Indian Ocean, Arabian Sea, mainland India and Bay of Bengal and rainfall over India

Duration of MJO over Indian Ocean during Jun-Sep, 2023	Development of convection		rainfall
	Over SIOCZ and the near equatorial regions of north Indian Ocean	Over Arabian Sea, mainland India and the Bay of Bengal	
7-18 Jun	A MCZ developed in SIO during week ending 14th Jun. The pre-existing weak convection in SIOCZ got organized by 9th Jun. A well developed W-E oriented cloud band formed around 5ºS, between 60-75ºE on 15th Jun.	A MCZ, which had developed close to equator during week ending 7th Jun had moved up to 5º lat. belt of 10-15ºN by week ending 14th Jun.	Rainfall for India as a whole, which was on the lower side of Long Period Average (LPA) up to 7th June, improved during the next two weeks. Improvement in rainfall had occurred over the south Peninsular India, North East India, Gujarat and Rajasthan.
24-30 Jun	Isolated moderate convection persisted over SIOCZ.	A MCZ developed between 15-25ºN over mainland India during week ending 28 Jun.	Significant improvement in rainfall occurred during 25 Jun- 1Jul. Rainfall, for India as a whole, during the week 22-28 June, was 18% above LPA. Improvement in rainfall had occurred over the majority of the subdivisions and it was significant over Central and West India.
5-14 Jul	A MCZ developed over the equator during week ending 5th Jul, rapidly moved northward up to 20ºN during the same week. Another MCZ developed in SIOCZ during the next week, persisted for one more week and weakened, in situ.	Convection increased over mainland India and the Bay of Bengal.	Jul 2023 witnessed an active phase of southwest monsoon. Rainfall for India as a whole was 34% more, 1% less and 20% more than LPA during the weeks, 6-12, 13-19 and 20-26 Jul, respectively. Improvement in rainfall was most significant during the week 6-12 Jul. Jul rainfall, for India as a whole, was 13% more than LPA.
29-31Aug	A spell of active SIOCZ developed close to equator on 27th Jul and weakened on the next day.	Convection increased in Arabian Sea south of 10ºN and it extended up to Bay of Bengal during 29-31 Aug.	Except Northeast India, no enhancement of rainfall took place. Rainfall, for India as a whole, during week ending 30th August 2023 was 40% less than LPA.
1-8 and 15-20 Sep	A MCZ developed between equator and 5ºS during week ending 13 Sep and moved up to 20ºN during the next week. Convection remained confined to the areas north of equator till the end of the month.	On 1st Sep, convection existed over Arabian Sea south of 8ºN and Eq.-10ºN over Bay of Bengal. It was absent over mainland India. Convection moved northward, reached 30ºN by 10th Sep. It increased over mainland on 14th and 15th Sep. It moved westward over north Arabian Sea by 20th Sep.	Rainfall, for India as a whole, was on the lower side of LPA during the first 6 days of Sep, but increased thereafter and remained on the higher side of normal up to 23rd Sep. Rainfall during Sep, for India as a whole, was 13% more than LPA.

Absence of MJO over Indian Ocean during August and October 2023

A very weak pulse of MJO moved across Indian Ocean part of UC of phase diagram for 3 days only, i.e., during 29th-31st August (Tables 8-9 ; Figure 1). In other words, MJO was practically absent over Indian Ocean sector during four consecutive weeks of August 2023. August rainfall, for India as a whole, was 36% less than the long period average. It was the record lowest for August since 1901 (IMD, 2023). Daily rainfall figures, for India as a whole, were on the higher side of long period average on 4 days only during August 2023 and it was less by 50% to 80% on 10 Days. Weekly rainfall data, for India as a whole and in individual subdivisions, show that large reduction in rainfall had occurred for four weeks, in continuation, during August 2023. The Convergence Zone had remained active during these four weeks of August 2023. It is interesting to note that a similar situation had developed during July 2002 also. At 51% less than the long period average rainfall, for India as a whole, July 2002 had recorded the lowest rainfall for the month since 1901. MJO was practically absent over Indian Ocean sector during July 2002 also (figure not reproduced). Thus, the presence of an active spell of The Convergence Zone and simultaneous absence of a MJO pulse over Indian Ocean sector for four consecutive weeks, resulted in large reduction in rainfall for that month. This is an important observation, useful in issuing LRF and its monthly updates. The forecastof MJO, one month in advance, were available during 2023 from the Bureau of Meteorology, Australia. Another similar situation had developed during October 2023 also. We had made use of the forecast of likely absence of a MJO pulse over Indian Ocean sector during October 2023 available in the outlook on MJO from the Bureau of Meteorology, Australia, on real time basis, in our LRF of reduction in rainfall over south peninsular India during October 2023. The duration of MJO, development of convection and rainfall during 2023 northeast monsoon are given in Table 10. It follows from this table that the enhanced rainfall had occurred in the subdivisions of southeast peninsular India during each spell of arrival of a MJO pulse over Indian Ocean sector.

Table 10. Duration of MJO over Indian Ocean sector, development of convection in The Convergence Zone, the near equatorial regions of north Indian Ocean, Arabian Sea, South Peninsular India, Bay of Bengal and rainfall over Coastal A.P., Rayalaseema, Tamil Nadu, South Interior Karnataka and Kerala during 2023 northeast monsoon

Duration of MJO over Indian Ocean during Oct-Dec, 2023	Development of convection over		Rainfall over Coastal A.P., Rayalaseema, Tamil Nadu, South Interior Karnataka and Kerala
	The Convergence Zone	Arabian Sea, mainland India and the Bay of Bengal	
3-7 Nov	Convection developed on 3rd and 4th Nov between 40-60ºE. It reduced thereafter.	Moderate convection developed over Arabian Sea, South Peninsula and the Bay of Bengal south of 10ºN lat. on 3rd Nov. It increased and moved northward up to 14ºN by 6th and weakened on 7th Nov.	During the week 2-8 Nov, rainfall was Excess in Tamil Nadu and Large Excess in South Interior Karnataka and Kerala. Rainfall was normal in Coastal A.P. and Rayalaseema.
22-30 Nov	Moderate convection developed between 70-90ºE on 22nd and 23rd Nov. Thereafter, the convection reduced and re-appeared on 29th and 30th Nov.	Moderate convection developed on 22nd and 23rd Nov. It moved northward during 24th-26th Nov. On 27th it had reached up to 30ºN over mainland India and also over Arabian Sea. Convection reduced on 29th Nov, but increased over the Bay of Bengal on 30th Nov.	Rainfall was normal in South Interior Karnataka, Excess in Coastal A.P. and Rayalaseema and Large Excess in Tamil Nadu and Kerala during the week 23-29 Nov.
1-3 Dec	Convection did not develop.	On 1st Dec, the main convection was between Eq.-12ºN in the Bay of Bengal. It moved up to 20ºN by 3rd Dec.	During week 30th Nov- 6th Dec, rainfall was Large Excess in Coastal A.P. and Rayalaseema, Excess in Tamil Nadu and Kerala and Deficient in South Interior Karnataka.

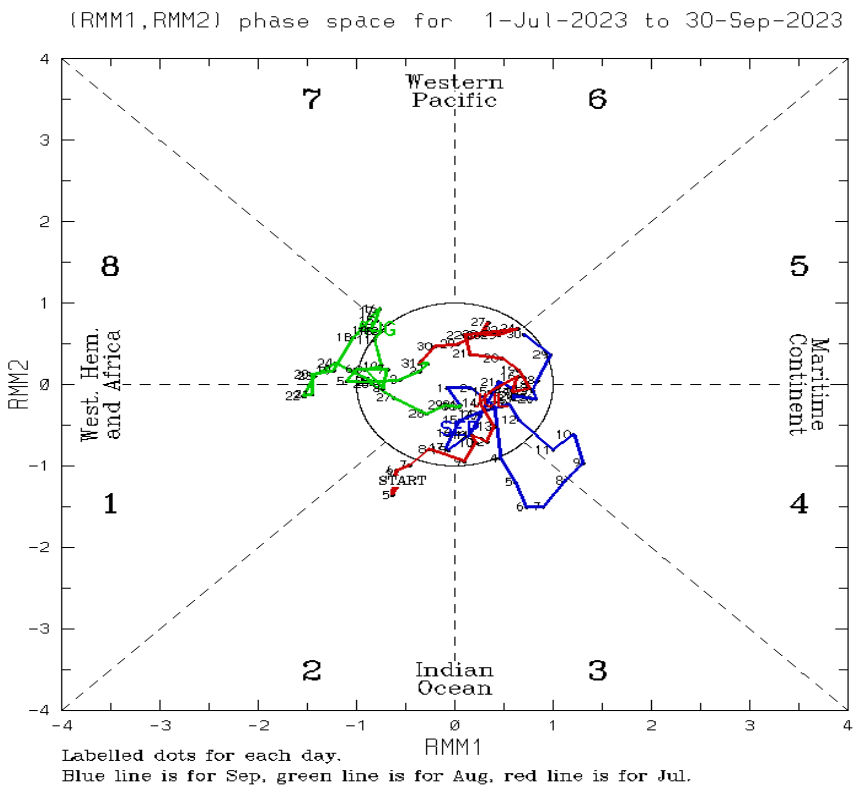


Figure 1. Location and strength of MJO during July-September 2023 (Source: Bureau of Meteorology, Australia, http://www.bom.gov.au/climate/mjo/#tabs=Phase)

As was the case in August (Figure 1), MJO did not enter Indian Ocean sector during October 2023 also (Fig. not reproduced). Forecast of MJO not entering Indian Ocean sector during October 2023 was available, one month in advance, in the outlook on MJO from the Bureau of Meteorology (BoM) Australia (2022-23). This had helped us in formulating the forecast for 2023 northeast monsoon issued on 30th September 2023 (Onkari Prasad, et al., 2023b): Large reduction in rainfall had taken place during October 2023. The forecast from The Model issued at the end of September 2023 had thus captured the reduction in rainfall during October 2023. Similarly, the enhancement of rainfall during November 2023 had also been captured well in the update issued at the end of October 2023. However, the update issued on 30th November 2023 could not capture the large excess rainfall received during week ending 6th December 2023 in Coastal A.P., Rayalaseema, Tamil Nadu and Kerala.

Large excess rainfall over south peninsular India during the first week of December 2023

The percentage departure of realised rainfall from its long period average during December 2023 in the subdivisions of Coastal A.P., Rayalaseema, Tamil Nadu, South Interior Karnataka and Kerala was 521%, 221%, 43%, -40% and 129%, respectively. In the LRF of northeast monsoon based onThe Model and issued on 30th September 2023, rainfall for December in the subdivisions was 10%, 6%, -1%, -6% and -22%, respectively. The same had been lowered to -36%, -20%, -1%, -6% and -22%, respectively in the update issued on 30th November 2023. Rainfall during December 2023 could not be captured in the update: Large excess rainfall during northeast monsoon occurs in a day or two in association with development of a cyclonic storm in southwest Bay of Bengal when it tracks northwards, crosses Tamil Nadu-Andhra Pradesh coast. This was the case during the first week of December 2023 also. The system had developed into a cyclonic storm on 4th December, moved northwards along the coastline, and made landfall between Nellore and Machilipatnam in Andhra Pradesh on 5th December 2023. A mosaic of INSAT visible cloud imagery for the period 30 November to 5 December 2023 is given in Figure 2 and the track of the system in Figure 3. A moderately strong MJO pulse was moving across Indian Ocean during 1-3 December 2023 (Table 8) and that had worked as a trigger in the

development of a cyclonic storm in the Bay of Bengal. Thus, beforehand information on likely strengthening of northeast monsoon during the first weekof December 2023 was available in the outlook on MJO from the Bureau of Meteorology, Australia. But, climatology had been given more weight while issuing the update for December 2023 rainfall. Two factors should had been given weight while issuing the update for December 2023 rainfall, (i) Likely presence of a pulse of MJO in Indian Ocean sector which was available in the outlook from Bureau of Meteorology, (ii) Southward shift in the influence of MJO during northern hemisphere winter. In summary, it may be said that enhancement in rainfall had occurred over south peninsular India during 2023 northeast monsoon whenever a MJO pulse had passed over Indian Ocean.

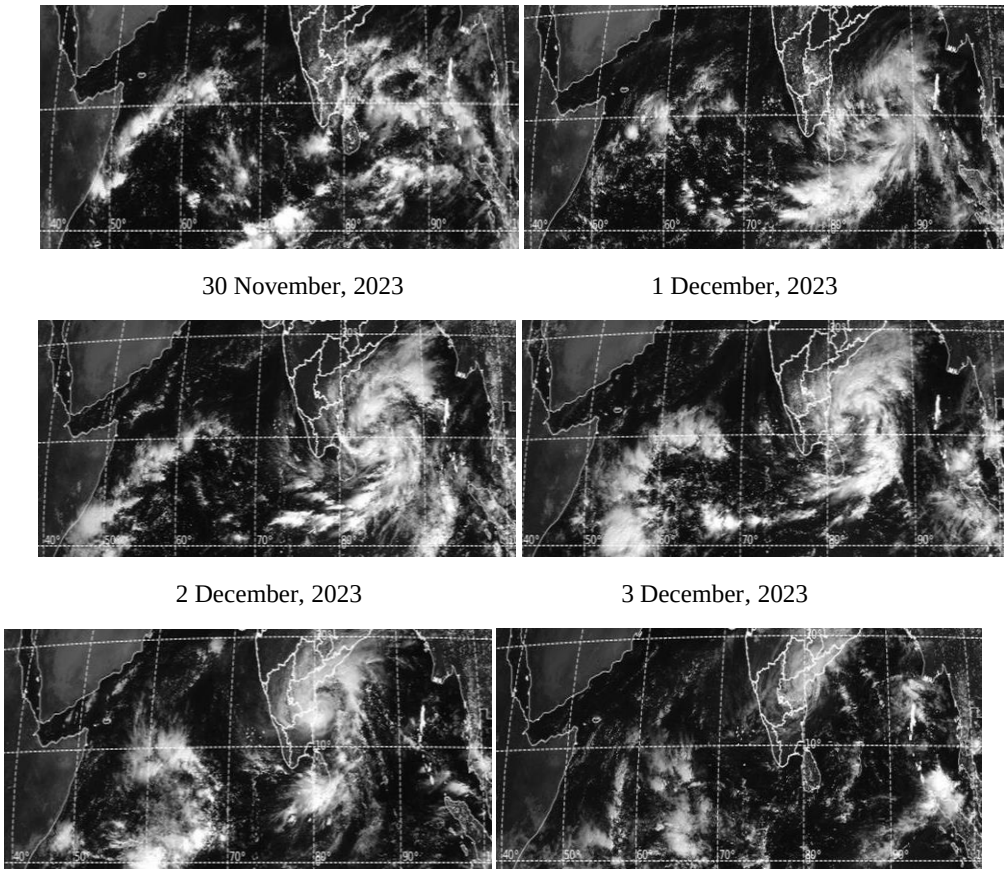


Figure 2. Development of a cyclonic storm in the Bay of Bengal during 30th November-5th December 2023 (Source of cloud imagery: IMD).



Figure 3. Track of severe cyclonic storm Michaung, 1-6 December 2023 (Source: Internet, Wikipedia)

Influence of positive Indian Ocean dipole

The values of Indian Ocean Dipole (IOD) mode index, during the period May 2023-February 2024 are given in Table 11. The threshold for a positive IOD (+IOD) event is a +.4ºC anomaly in Dipole Mode Index (DMI). DMI had reached +1.05°C on 29th August 2023. It had further increased to +1.85°C on 10th October. Thus, a positive IOD(+IOD) event had developed just before the commencement of September 2023. Large increase in rainfall had occurred over South Interior Karnataka, Tamil Nadu and Kerala during week 2-8 November 2023 (Table 12). Convection had increased over east Arabian Sea south of 15ºN from 3rd to 6th November 2023. The presence of a weak pulse of MJO over Indian Ocean during 3-7 November (Table 9) coincided with the period of increased convection over Arabian Sea. The development of convection over east Arabian Sea may be attributed to the presence of a +IOD event for the following two reasons: (i) Climatologically, the region of development of convection during October-December is the Bay of Bengal and not east Arabian Sea (ii) The DMI was at +1.85°C on 10th October, The positive phase of IOD, which had commenced in the beginning of September, had reached its peak intensity before the commencement of enhanced convection in east Arabian Sea. In order to illustrate the development of convection and its movement, a mosaic of 0600 UTC visible INSAT 3D cloud imagery from 1-8 November 2023 covering the area between 10ºS-20ºN, 40-100ºE, is given in Figure 4. There was very little convection over Arabian Sea on 1st November 2023. Convection increased from 2nd November and it moved eastward over east Arabian Sea. Convection had started decreasing from 7th November 2023. Rainfall, which was in Deficient/Large Deficient category in the subdivisions of southeast peninsular India, during week ending 1st November 2023, increased and it was in Large Excess in South Interior Karnataka, Excess in Kerala and Tamil Nadu and Normal in Coastal A.P. and Rayalaseema during the week ending 8th November 2023 (Table 11). The presence of a MJO pulse over Indian Ocean during 3-7 November 2023 does not allow us to conclude that the increased rainfall over south peninsular India during the week 2-8 November 2023, was exclusively due to the influence of +IOD. It could as well be concluded that large increase in rainfall during week 2-8 November had resulted due to the combined influence of MJO and +IOD. While the presence of + IOD had created favourable environment,the arrival of a pulse of MJO had acted as a trigger for development of convection in the Arabian Sea.

Table 11. IOD mode index during May 2023-February 2024. IOD threshold is ± 0.4°C (Source: Archives of Climate Driver Update, Bureau of Meteorology, Australia, www.bom.gov.au/climate/enso/wrap-up/archive)

Date of issue of climate driver update	IOD mode index	Date of issue of climate driver update	IOD mode index
9 May 2023	Neutral	23 May	Neutral
6 Jun	Neutral (+0.32°C)	20 Jun	Neutral
4 July	Neutral	18 Jul	Neutral
1 Aug	Neutral	15 Aug	Neutral
29 Aug	+1.05°C	12 Sep	+1.13°C
26 Sep	+1.45°C	10 Oct	+1.85°C
24 Oct	A positive IOD is underway	8 Nov	The positive IOD event continues
21 Nov	The positive IOD event continues and is currently tracking at strong levels	5 Dec	The positive IOD event continues and is currently tracking at strong levels
19 Dec	The positive IOD event remains active, but is weakening steadily	9 Jan 2024	The positive IOD event is weakening steadily
23 Jan 2024	The positive IOD event had weakened from the strong values seen in late 2023	30 Jan	IOD index was below +0.4°C on 28th Jan 2024
6 Feb 2024	The IOD has returned to neutral, with the latest weekly IOD index (to 4 February 2024) being below +0.4°C for the second consecutive week	20 Feb	The IOD is neutral

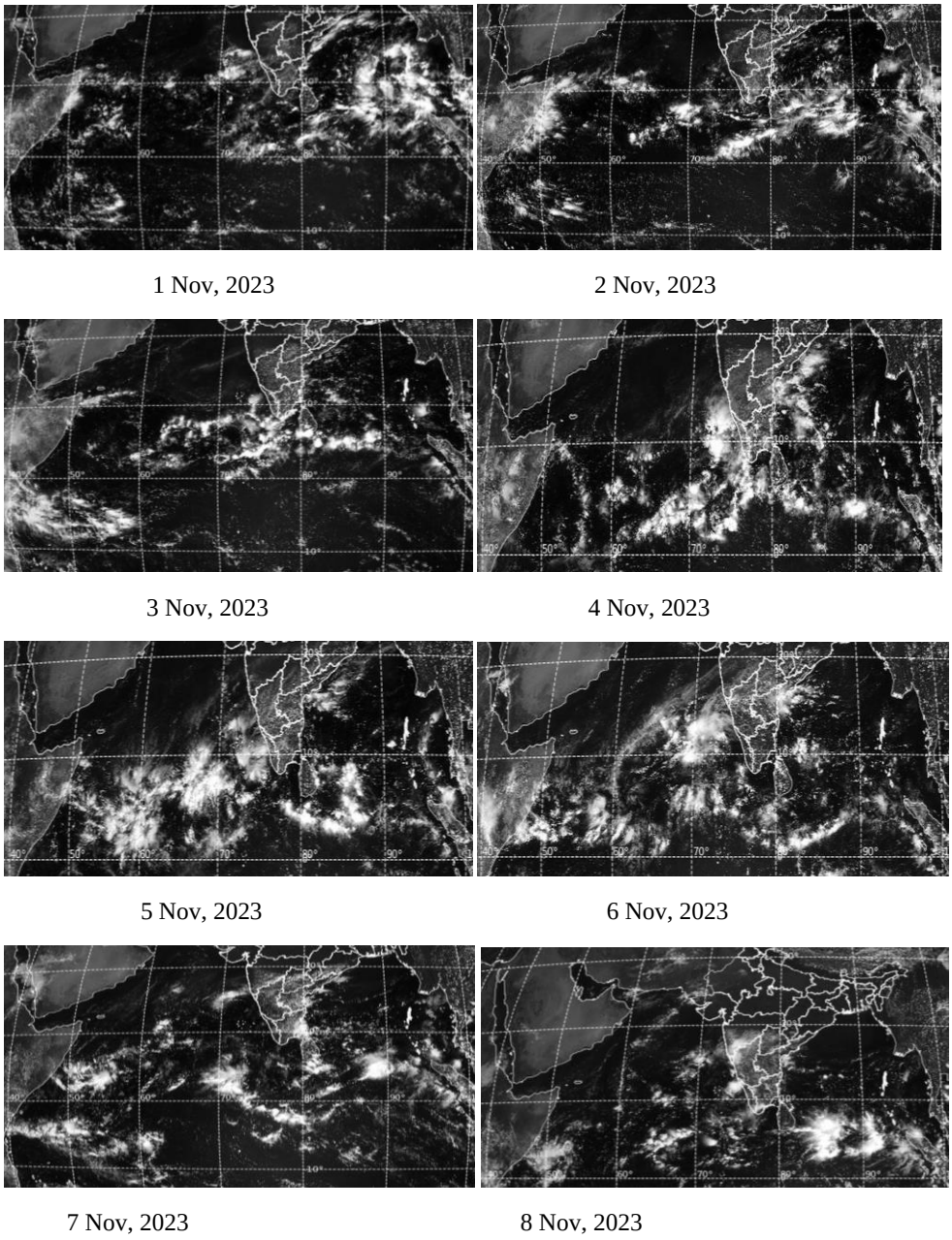


Figure 4. Development of convection over Arabian Sea during 1-8 November 2023 (Source of satellite cloud imagery: IMD).

Influence of El Nino

In general, deficient rainfall had occurred in India in the years of development of an El Nino in Pacific. Another factor invariably associated with deficient rainfall during Indian monsoon has been found to be the presence of The Convergence Zone for 4-5 weeks, in continuation. Identifying this feature in cloud/OLR data has proved to be useful in foreshadowing a deficient monsoon season. Development of both, i.e., El Nino in Pacific and a spell of The Convergence Zone remaining active for 4-5 weeks, in continuation, had occurred during 2023 also. Development of The Convergence Zone for 4-5 weeks, in continuation, during pre-monsoon months of April-May 2023was the prominent ISV signal of the year. The development of an active spell of The Convergence Zone had been noted in cloud data of March 2023 and the same had been mentioned in the LRF Bulletin No.1 issued on 30th March 2023. Thereafter, this feature had recurred during June-July and August 2023. Development of an active spell of The Convergence Zone occurs in association with the presence of positive SST anomalies in near equatorial regions of

south Indian Ocean (Onkari Prasad et al., 2020). Figures 5 and 6 (NOAA/PSL, 2023) show the SST anomaly field during April and May 2023, respectively. Positive SST anomalies were present over the near equatorial regions of south Indian Ocean during April 2023. In Pacific, SSTs had been rising in all the four Nino regions from January 2023 onwards (Table 12). The SST anomalies in Nino 3.4 peaked during June 2023. The threshold of El Nino, i.e., SST anomalies in Nino region 3.4 becoming +0.5ºC or more was reached during the three monthly period of April-May-June. A MCZ, as seen in low OLR values, had developed in The Convergence Zone for 5 weeks, in continuation, during week ending 16 April-week ending 21 May **(**Figure 7). Positive SST anomalies (of the order of +0.5º to 1.0ºC) had occupied The Convergence Zone (Figure showing SST anomalies not reproduced). In Pacific, positive SST anomalies were confined to east of 120ºW in April 2023 and east of 150ºW in May 2023, respectively. Thus, the development of positive SST anomalies in Indian Ocean was not influenced by westward propagation of positive SST anomalies of Pacific. Recurrence of intra-seasonal variability signal took place for 5 weeks during Jun-Jul 2023. It recurred once again for 5 weeks during week ending 31st July- week ending 28 August 2023. This is seen in low OLR values in SIOCZ during week ending 31st July-week ending 28 August 2023 (Figure 8). This time also the positive SST anomalies of Pacific had not entered Indian Ocean (Figs. not reproduced). The SST anomaly in Nino 3.4 region during three monthly period of March-April-May was 0.2ºC.Thus the development of positive SST anomalies in Indian Ocean during April-May 2023, took place independent of westward propagation of Pacific SST anomalies associated with a developing El Nino in Pacific. This implies that development of El Nino of 2023 in Pacific had little/no influence on development of an active spell of The Convergence Zone for 4-5 weeks, in continuation, before the commencement of 2023 southwest monsoon and also its recurrence twice during the season. The linkage, if any, between an El Nino developing in east Pacific and development of an active spell of The Convergence Zone in Indian Ocean lasting for 4-5 weeks, in continuation, was not seen during 2023 southwest monsoon.

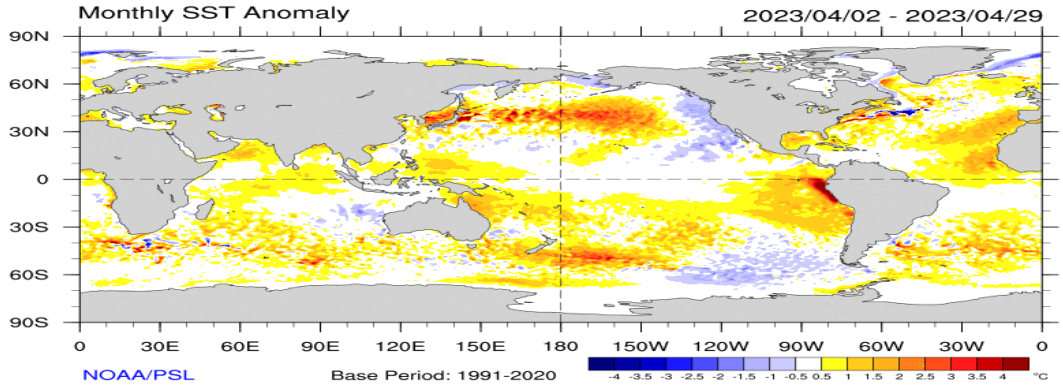


Figure 5. SST anomalies during April 2023

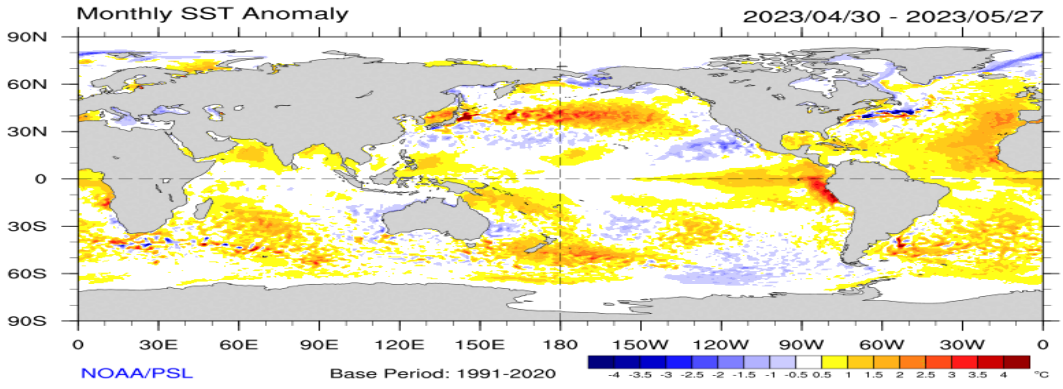


Figure 6. SST anomalies during May 2023

Table 12. Monthly SST in Nino regions and three-monthly SST anomalies in Nino 3.4 region Numbers in red colour refers to El Nino period.

Nino Region	Jan 2023	Feb	Mar	Apr	May	Jun	Jul	Aug	Sep	Oct	Nov	Dec
Nino 1+2	24.00	26.58	27.97	28.15	26.63	25.97	24.86	24.29	23.22	23.36	23.72	24.42
Nino 3	24.94	25.88	27.34	28.10	27.96	27.80	27.30	27.09	26.86	26.86	27.10	27.07
Nino 3.4	25.83	26.29	27.18	27.96	28.40	28.54	28.30	28.21	28.31	28.38	28.72	28.67
Nino 4	27.66	27.64	28.06	28.75	29.21	29.51	29.57	29.72	29.84	29.96	30.21	30.05

Three-monthly mean SST anomalies in Nino region 3.4

Year	DJF	JFM	FMA	MAM	AMJ	MJJ	JJA	JAS	ASO	SON	OND	NDJ
2022-23	-0.7	-0.4	-0.1	0.2	**0.5**	**0.8**	**1.3**	**1.3**	**1.5**	**1.8**	**1.9**	**2.0**

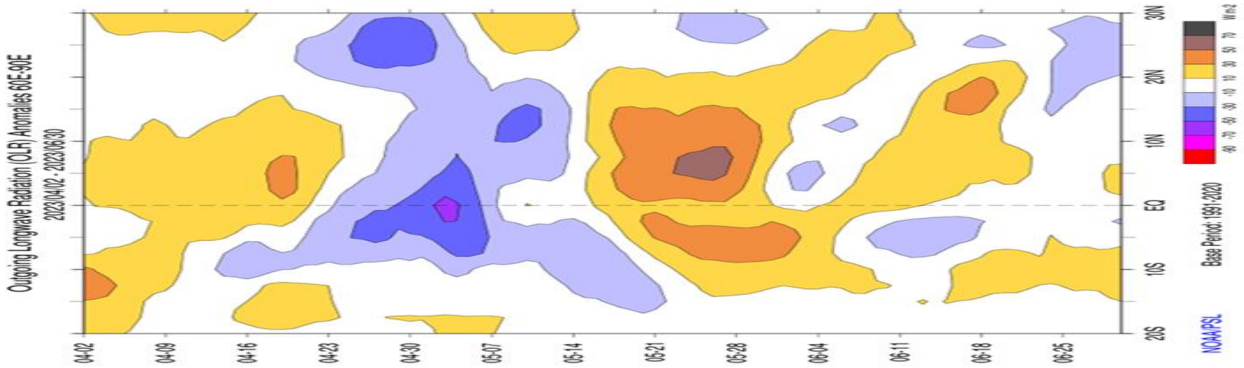


Figure 7. Time-latitude section of weekly mean OLR anomaly over the sector 60-90ºE for the period 2 April-30 June 2023

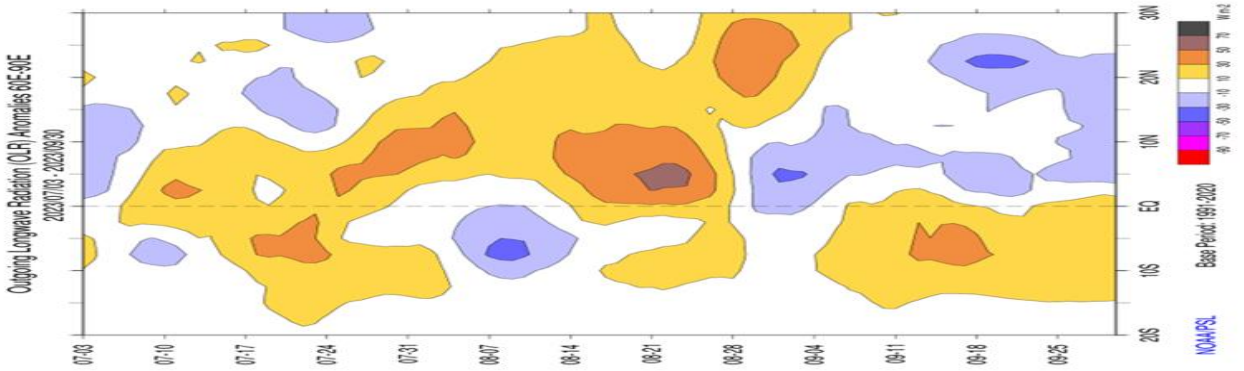


Figure 8. Time-latitude section of weekly mean OLR anomaly over the sector 60-90ºE from 3 July-30 September 2023

CONCLUSIONS

1. The forecast of 2023 southwest and northeast monsoon seasonal rainfall were in useful category in 80% and 92% districts of Tamil Nadu, where the correlation coefficient between South Indian Ocean Convergence Zone Activity Index and rainfall was significant at 95% level.

2. The forecast for the months of July, August and September were in useful category in 71%, 78% and 69% of those districts of Tamil Nadu where the correlation coefficient between South Indian Ocean Convergence Zone Activity Index and monthly rainfall is significant at 95% level.

3. The interplay of Inter-Annual and Intra-Seasonal Variability signals during 2023 southwest monsoon was a rare development. The samehad been clearly brought out in the analysis of cloud and OLR data.

4. The observations that the presence of MJO over Indian Ocean in enhancement of rainfall and its absencefor 4-6 weeks, in continuation, in reduction of rainfall are useful in issuing long range forecast and its updates.

5. There was no signal in Indian Ocean Dipole mode index relating to development of an inter-annual variability signal relating to active southwest monsoon and also an intra-seasonal variability signal relating to reduction in rainfall during 2023.

6. Linkage, if any, between the simultaneous development of El Nino in east Pacific and development of an active spell of The Convergence Zone in Indian Ocean lasting for 4-5 weeks, in continuation, was not seen during 2023 southwest monsoon.

Acknowledgements

The estimates of cloudiness had been obtained from 0600 UTC visible cloud imagery made available by IMD on Internet. Rainfall data had been obtained from IMD. Figures showing MJO location and strength had been downloaded from the site of Bureau of Meteorology, Australia. IOD index values had been noted down from the Archives of Climate Driver Update, Bureau of Meteorology, Australia. OLR anomaly and SST anomaly charts had been downloaded from "Data/image provided by the NOAA/OAR/PSL, Boulder, Colorado, USA, from their Web site at https://psl.noaa.gov/".Monthly SST in Nino regions and three-monthly anomaly in Nino 3.4 region had been downloaded from the site of NOAA. We gratefully acknowledge the continued support and encouragement received from Dr. O. P. Pandey, Chief Editor of the Journal of Indian Geophysical Union (JIGU). We sincerely thank the reviewers for their critical comments.

Author credit statement

Preparation of the estimate of weekly mean cloud data on real time basis was done by Onkari Prasad. Figures were prepared done by K. Prasad. Preparation of first draft of the manuscript was jointly done by K. Prasad and Onkari Prasad. Improvement in the manuscript and its finalisation was done by O.P. Singh.

Data availability

The OLR data are available from NOAA. Phase diagrams showing location and strength of Real-Time Multivariate MJO (RMM) are available from the web-site of the Bureau of Meteorology, Australia. Rainfall data are available from India Meteorological Department. The estimates of weekly mean cloudiness data are available from the authors.

Compliance with ethical standards

The authors declare that they have no conflict of interest and adhere to copy right norms.

References

Bureau of Meteorology, Australia, 2023. Archive of RMM phase Diagram for the period 1 Oct 2022 to 31 Dec 2023. http://www.bom.gov.au/climate/mjo/#tabs=Tropical-update

Gupta, G.R. and Onkari Prasad, 1992. Role of Southern Hemispheric Equatorial Trough in long range forecasting, Jalvigyan Sameeksha,7,83-97.

Gupta, G.R. and Onkari Prasad, 1993. Southern Hemispheric Equatorial Trough model of long range forecast of monthly rainfall during southwest monsoon, J. Indian Association Hydrologists, 16,49-76.

I.M.D., 2010, CD of rainfall data.

I.M.D., 2023, End of season report on 2023 Southwest monsoon.

Kripalani, R. H. and Kumar, P., 2004. Northeast monsoon rainfall variability over south peninsular India vis-à-vis the Indian Ocean dipole mode, Int. J. Climatol.,24, 1267-1282.

Madden, R.A. and Julian, P. R., 1972. Description of global-scale Circulation cells in the Tropics with a 40–50 day period. J. Atmos. Sci., 29, 1109–1123.

NOAA/ PSL, 2023. Monthly SST anomaly charts for the months of April-August 2023 down loaded on real time basis from the site [https://psl.noaa.gov/map/clim/sst.shtml]

Onkari Prasad and Singh, O.P., 2008. District level long range forecast of seasonal rainfall during southwest monsoon, Vayu Mandal, 34,51-56.

Onkari Prasad and Singh, O.P., 2012. South Indian Ocean Convergence Zone Model: A new approach to long range forecasting of summer monsoon rainfall in India Part II:Forecast of rainfall for India as a whole, J. Ind. Geophys. Un.,16,1-10.

Onkari Prasad and Singh, O.P., 2013. South Indian Ocean Convergence Zone Model: A new approach to long range forecasting of summer monsoon rainfall in India Part III: Forecast of rainfall in meteorological subdivisions. J. Ind. Geophys. Un., 17, 75-91.

Onkari Prasad, Singh, O.P. and Sant Prasad, 2010a. South Indian Ocean Convergence Zone Model: A new approach to long range forecasting of summer monsoon rainfall in India Part I: Role of South Indian Ocean Convergence Zone in development of Indian summer monsoon. J. Ind. Geophys. Un., 14, 233-248.

Onkari Prasad, Singh, O.P. and Subramaniam, S.K., 2010b. Seasonal forecast of southwest monsoon rainfall- District level. J. Ind. Geophys. Un.,14, 93-113.

Onkari Prasad, Singh, O.P. and Prasad, K., 2016a. District level long range forecast of rainfall during southwest monsoon in Andhra Pradesh, J. Ind. Geophys. Un., 20, 254-264.

Onkari Prasad, Singh, O.P. and Prasad, K., 2016b. District level long range forecast of rainfall during southwest monsoon in Telangana. J. Ind. Geophys. Un.,20,434-441.

Onkari Prasad, Singh, O.P. and Prasad, K., 2016c. Long range forecast of rainfall during southwest monsoon in the states of Maharashtra and Goa. J. Ind. Geophys. Un.,20, 586-595.

Onkari Prasad, Singh, O.P. and Prasad, K., 2020. Forecast of intraseasonal variations in monsoon rainfall over India based on developments in the convergence zone and SST over south Indian Ocean- a case study from 2019. J. Ind.Geophys. Un.,24, 34-47.

Onkari Prasad, Singh, O.P. and Prasad, K., 2022. Development of northeast monsoon and its long range forecast-Pt I Development. J. Ind. Geophys. Un., 26,521-540.

Onkari Prasad, Singh, O.P. and Prasad, K., 2023a. Development of northeast monsoon and its long rangeforecast-Pt II. J. Ind. Geophys. Un., 27, 292-310.

Onkari Prasad, Singh, O.P. and Prasad, K., 2023b. Forecast of 2023 northeast monsoon issued on 30th September and updates issued on 31st October and 30th November 2023 were submitted to IMD and some other user agencies as an E–mail attachment.

Saji, N. H., Goswami, B. N., Vinayachandran, P. N. and Yamagata, T., 1999.A dipole mode in the tropical Indian Ocean. Nature, 401, 360-363.

Singh, O.P. and Onkari Prasad, 2011. District-level forecast of northeast monsoon rainfall over Tamil Nadu using Indian Ocean Dipole mode index, Mausam, 62, 229-234.

Wheeler, M. and Hendon, H. H., 2004. An All-Season Real-Time Multivariate MJO Index: Development of an Index for Monitoring and Prediction. Mon. Wea. Rev., 197-132.

Received on: 30-01-2026; Revised on: 09-09-2026; Accepted on: 10-09-2026

J. Ind. Geophys. Union, 30(6) (2026), 520-527
http://doi.org/10.71122/JIGU.30(6)2026.0050

Rare Earth Element (REE) geochemistry of placer ilmenites from the east coast of India: Implications for provenance and genetic parentage

Mokka Jagannadha Rao[1]*, G. Sandeep and J. Venkataramana
Department of Geology, Andhra University, Visakhapatnam-530003, Andhra Pradesh, India
[1]Presently with Department of Geophysics, Andhra University, Visakhapatnam-530003, Andhra Pradesh, India
*Corresponding author: mjrao.geology@gmail.com

ABSTRACT

The Rare Earth Element (REE) geochemistry of placer ilmenites from four major east coast deposits of India, namely Kakinada, Bhimunipatnam (Bhimili), Srikurmam and Chatrapur, has been investigated to constrain their provenance and genetic parentage. Chondrite-normalized REE patterns reveal pronounced enrichment of light rare earth elements (LREEs) over heavy rare earth elements (HREEs), expressed by consistently high La/Yb_N ratios and moderate negative Eu anomalies. These fractionation patterns are incompatible with derivation exclusively from metamorphic or metasedimentary source rocks of the Eastern Ghats Belt, which are generally Ti-poor and commonly exhibit flatter REE distributions. Instead, integration of REE signatures with major element chemistry, indicates derivation from igneous protoliths, particularly felsic granitoids, alkaline intrusives and mafic to basic magmatic bodies of Archean to Mesoproterozoic age (~3.0–1.6 Ga), which pre-date or represent early crustal precursors assimilated in Eastern Ghats orogeny. High TiO_2 contents and coherent REE systematics across geographically separated deposits, further support a dominantly igneous provenance. Comparative evaluation with published global placer ilmenite datasets, demonstrates strong affinity with ilmenites derived from the felsic to alkaline igneous terranes. The results highlight the utility of REE systematics in provenance analysis and heavy mineral exploration.

Keywords: Placer ilmenite; Rare earth elements; Provenance; Eastern Ghats; East coast of India; Genetic history.

INTRODUCTION

India possesses an extensive coastline of approximately 6,000 km that hosts a wide range of coastal geomorphic environments conducive to the accumulation of economically significant heavy mineral placers. The interaction of fluvial sediment supply, coastal hydrodynamics, wave sorting, longshore currents, lithological controls and climatic variability has resulted in substantial concentrations of ilmenite, rutile, zircon, monazite, garnet, sillimanite and leucoxene along both the eastern as well as western continental margins of the Indian Peninsula (Ravi et al., 2001; Ali et al., 2021). Among these, the east coast placer deposits of Odisha and Andhra Pradesh are particularly important owing to their exceptionally high titanium content and associated strategic minerals (Figure 1).

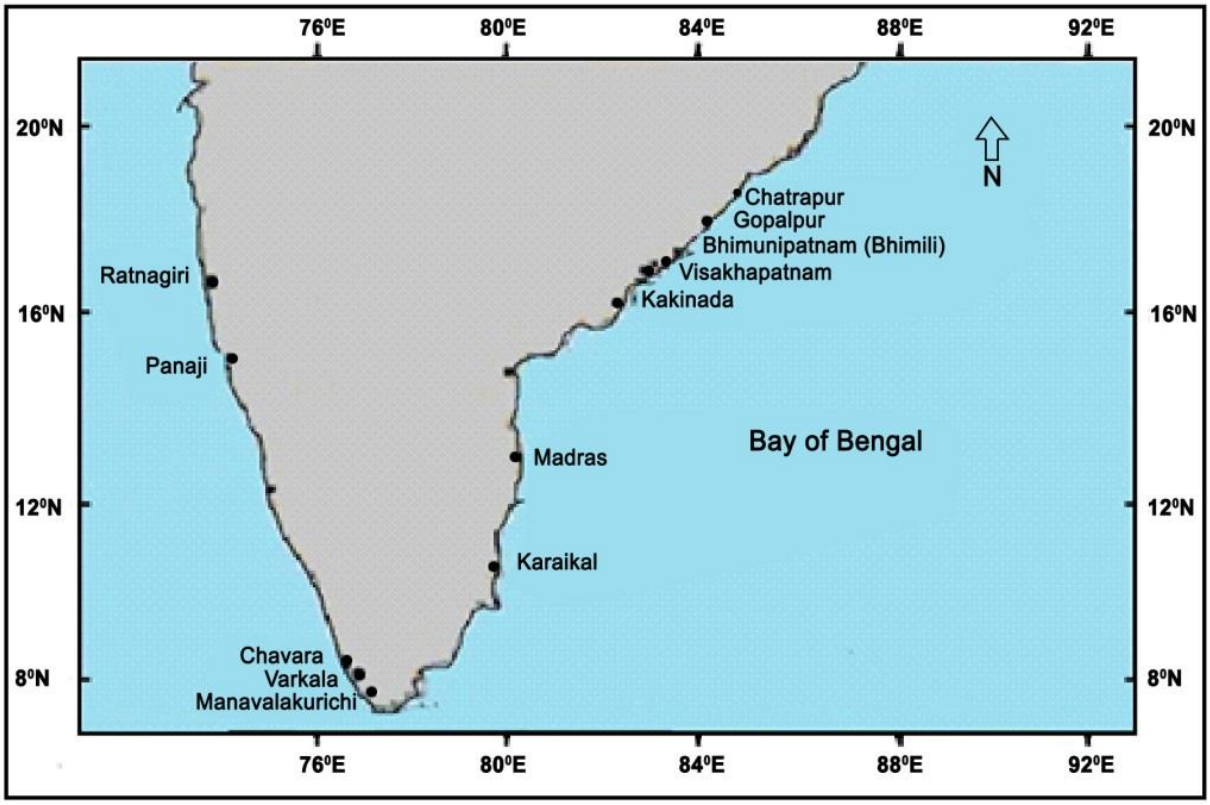


Figure 1. Placer deposits located along eastern and western coasts of India

Early documentation of black sand concentrations along the Visakhapatnam coast dates back to the pioneering observations of Mahadevan and Sri Ramdas (1948), who recognized the economic significance of coastal heavy mineral accumulations. Subsequent investigations primarily focused on reserve estimation, mineral beneficiation, ore mineralogy and geochemical characterization of placer ilmenites from the Visakhapatnam–Bhimunipatnam and Srikurmam sectors (Jagannadha Rao et al., 2005; Jagannadha Rao et al., 2016). However, systematic investigations dealing specifically with Rare Earth Element (REE) geochemistry and its implications for provenance and genetic parentage remain comparatively limited. Rare earth elements provide robust geochemical fingerprints capable of distinguishing between igneous, metamorphic and sedimentary source lithologies (McLennan, 1989). Chondrite-normalized REE patterns, elemental fractionation trends and Eu anomalies are particularly sensitive indicators of magmatic differentiation, sedimentary recycling and crustal evolution processes. Because REEs generally remain immobile during weathering and transportation, they preserve valuable information regarding source rock characteristics even within detrital heavy mineral assemblages.

The Eastern Ghats Belt (EGB), constituting the major hinterland for the east coast placer deposits, comprises granulite-facies metamorphic rocks including khondalites, charnockites, leptynites, migmatites, granite gneisses and basic granulites. Although several of these lithologies contain Ti-bearing accessory minerals, the exact genetic parentage of placer ilmenites remains debatable. In this context, REE geochemistry offers an effective approach for evaluating provenance and identifying possible source lithologies. The present study therefore aims to characterize the REE geochemistry of placer ilmenites from four representative east coast deposits of India and evaluate their provenance and genetic significance using REE systematics and major element chemistry.

GEOLOGICAL SETTING

The studied placer deposits occur along the coastal tracts of Andhra Pradesh and Odisha within the northeastern segment of the Indian Peninsular Shield. The regional geological framework comprises the eastern block of the Dharwar craton, the marginal transitional zone, the Godavari graben and the Eastern Ghats Belt (EGB). The EGB is a high-grade granulite-facies terrain extending for nearly 900 km along the east coast of India. Lithologically, the belt consists predominantly of khondalites, charnockites, basic granulites, leptynites, migmatites and granite gneisses. Khondalites represent dominant metasedimentary assemblages composed mainly of garnet–sillimanite–graphite gneisses, whereas charnockites and associated granitoids record multiple episodes of magmatic activity. Basic granulites are interpreted as metamorphosed tholeiitic basalts emplaced within extensional tectonic settings (Subba Rao and Divakara Rao, 1999).

Geochronological studies indicate that the EGB records multiple tectono-magmatic events ranging from Archean to Mesoproterozoic age. Granitoid and charnockitic protoliths yield ages between ~3.0 and 1.6 Ga, whereas high-grade granulite-facies metamorphism and tectonic reworking are generally attributed to Grenvillian-age events (~1.0–0.9 Ga) (Dobmeier and Raith, 2003; Ramakrishnan and Vaidyanadhan, 2010). These ancient igneous crustal components constitute probable source terranes for the placer ilmenites investigated in the present study. The coastal placer deposits of Kakinada, Bhimili, Srikurmam and Chatrapur occur within beach ridges, foreshore zones, backshore environments and coastal dune systems developed during Quaternary marine transgressions and regressions. Sediment supply is largely controlled by erosion of crystalline rocks from hinterland and subsequent transportation through major east-flowing river systems.

FIELD OCCURRENCE OF PLACER ILMENITE

Placer ilmenite occurs predominantly within the three principal coastal geomorphic zones: foreshore, backshore and coastal dune environments. In the foreshore zone, wave swash and backwash processes facilitate efficient hydraulic sorting, producing thin laminae enriched in heavy minerals beneath lighter quartz-rich sands. The backshore environment is characterized by aeolian deflation and episodic marine inundation, leading to discontinuous black sand streaks and localized placer pockets. Coastal dune systems act as long-term repositories for heavy mineral accumulation, where wind-driven sediment transport generates cross-bedded units enriched in ilmenite, especially near slip-face bases. Heavy mineral assemblages within the studied placer deposits are dominated by ilmenite, constituting approximately 45–50% of the total heavy mineral content, depending upon locality and depositional environment. Other associated heavy minerals include garnet, sillimanite, rutile, zircon, monazite and leucoxene. The combined effects of wave sorting, longshore drift, aeolian concentration and repeated marine reworking have collectively controlled the textural maturity and economic concentration of ilmenite along the east coast (Figure 2).

METHODOLOGY

Representative bulk placer samples (10 samples from each deposits) were collected systematically from Kakinada, Bhimili, Srikurmam and Chatrapur coastal deposits using channel and grab sampling methods. Heavy mineral concentrates were separated using standard gravity concentration techniques followed by magnetic separation employing Frantz Isodynamic Magnetic Separator to obtain purified ilmenite fractions. Rare Earth Element concentrations were determined using inductively coupled plasma–mass spectrometry (ICP–MS) at the CSIR-National Geophysical Research Institute, Hyderabad. Prior to the analysis, samples were powdered in agate mills and subjected to acid digestion using HF–HNO_3–$HClO_4$ mixtures in closed Teflon vessels (Balaram et al., 1995). Calibration was performed using internationally accepted multi-element reference standards including BHVO-2, BCR-2 and AGV-2. Analytical quality control was ensured through procedural blanks, duplicate analyses and certified reference materials. Analytical precision for REE determinations was generally better than ±5%, while analytical accuracy remained within ±3% relative standard deviation. REE concentrations were normalized to CI chondrite values following McDonough and Sun (1995).

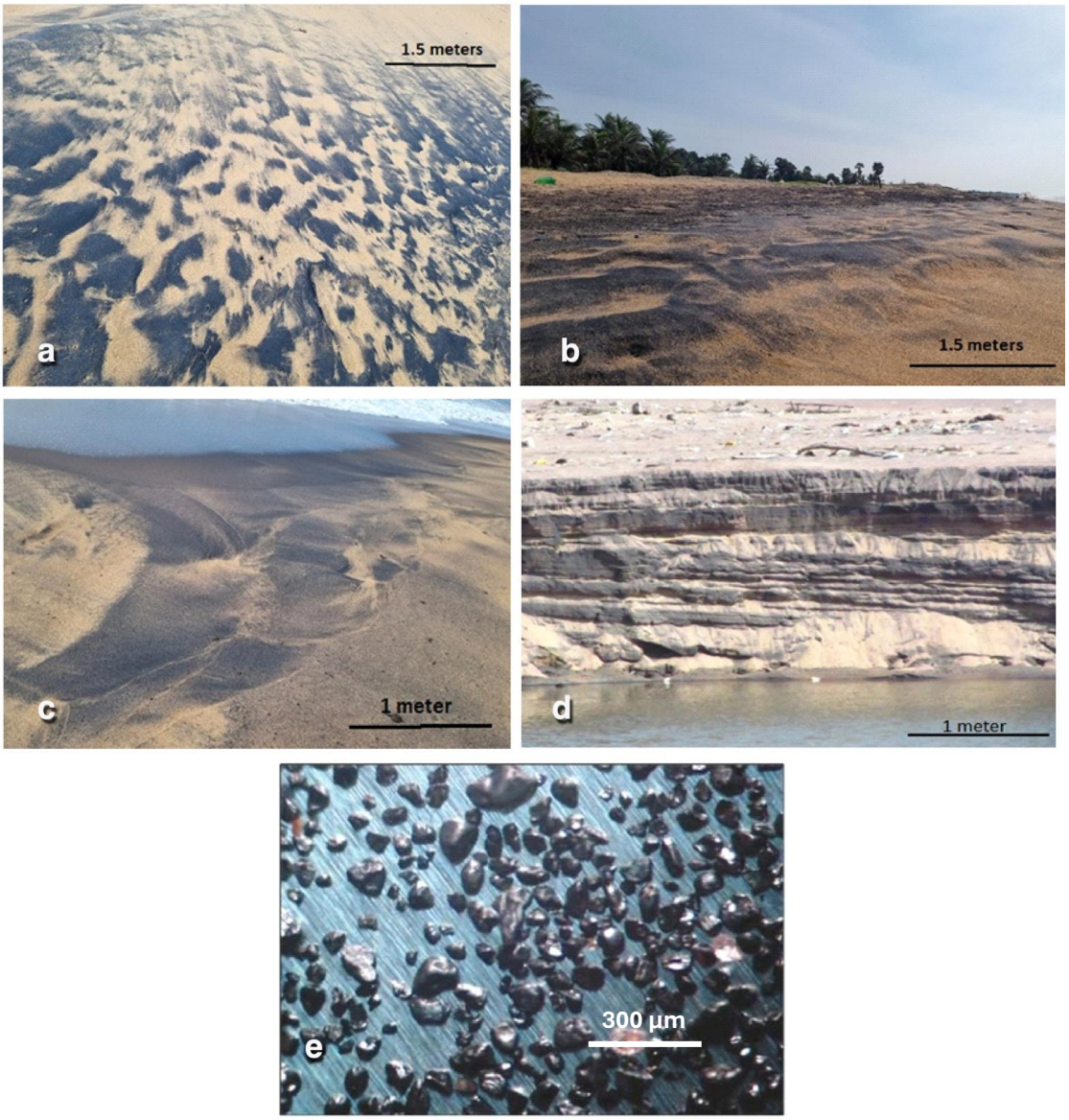


Figure 2. Photographs showing Ilmenite occurrence in beach environment. **(a)** Heavy mineral concentration with abundant ilmenite in the foreshore,**(b)** backshore, and **(c)** Dunal belt. **(d)** Density stratification of alternate heavy and light minerals in the Berm Cut. **(e)** Ilmenite grains under the Binocular microscope.

RESULTS

Major element compositions of the studied ilmenites are presented in Table 1. All deposits exhibit high TiO_2 contents ranging from 49.5 to 52 wt %, consistent with ilmenite derived from igneous parent rocks. FeO contents vary between 44 and 46 wt %, whereas SiO_2, Al_2O_3, MgO and alkali oxides occur only in minor amounts. Average REE concentrations are presented in Tables 2 and 3. Chondrite-normalized REE patterns reveal strong enrichment of light rare earth elements relative to heavy rare earth elements across all deposits (Figure 3). La/Yb_N ratios range between 9 and 27, indicating pronounced LREE fractionation. Moderate negative Eu anomalies ($Eu/Eu^* = 0.81–0.89$) are consistently observed. Middle REE enrichment is particularly pronounced in ilmenites from Bhimili and Chatrapur. A subtle positive Tb anomaly observed in certain samples, may reflect localized middle REE enrichment associated with magmatic differentiation and crystal-chemical substitution within the ilmenite lattice. Similar middle REE enrichments have been reported from ilmenites associated with evolved alkaline and granitoid systems (Kravchenko and Svisero, 1990). Chondrite-normalized REE patterns of east coast placer ilmenites shown in Figure 3.

Table 1. Average major elemental composition (wt %) in four deposits based on 10 samples from each deposit.

Oxide	Kakinada	Bhimili	Srikurmam	Chatrapur
TiO_2	50.0	50.0	49.5	52.0
FeO*	44.0	44.5	45.0	46.0
SiO_2	1.2	1.0	0.9	0.8
Al_2O_3	0.6	0.7	0.6	0.5
MgO	0.4	0.3	0.4	0.3
MnO	0.25	0.20	0.30	0.25
CaO	0.15	0.12	0.10	0.10
$Na_2O + K_2O$ (trace)	0.10	0.08	0.08	0.06
Total (approx.)	~97.7	~96.9	~96.9	~99.3

Table 2. Average REE concentrations of placer ilmenites (ppm) based on 10 samples from each deposit

Element	Kakinada	Bhimili	Srikurmam	Chatrapur
La	53.4	116.6	87.4	130.17
Ce	112.4	474.2	175	252.17
Pr	13.4	27.12	20.2	30.17
Nd	47.4	48.8	70.4	104.67
Sm	9.4	15.35	12.2	16.54
Eu	1.22	1.05	1.25	0.89
Gd	7.46	12.08	11.2	12.89
Dy	7.47	7.37	10.8	7.13
Er	3.45	3.47	6.04	3.41
Yb	3.54	3.17	6.4	3.3
Lu	0.52	0.5	1.02	0.55
Tb	1.42	1.7	1.93	1.73
Ho	1.42	1.22	2.27	1.17
Tm	0.64	0.5	0.93	0.5

Table 3. Chondrite-normalized REE concentrations (in ppm) of ilmenites from present study. Normalizing values after Mcconough and Sun (1995)

Element	Kakinada	Bhimili		Srikurmam	Chatrapur
La	225.32	492.83		368.35	549.24
Ce	183.32	773.58		285.34	411.25
Pr	145.65	294.78		219.56	327.93
Nd	103.72	106.77		154.04	229.06
Sm	61.44	100.33		79.74	108.14
Eu	21.03	18.1		21.55	15.34
Gd	37.49	60.7		56.28	64.77
Dy	29.41	29.01		42.52	28.07
Er	20.91	21.03		36.61	20.67
Yb	21.99	19.69		39.75	20.5
Lu	21.67	20.83		42.5	22.92
Tb	39.44	47.22		53.61	48.05
Ho	25.36	21.79		40.54	20.89
Tm	25.6	20.0		37.2	20.0

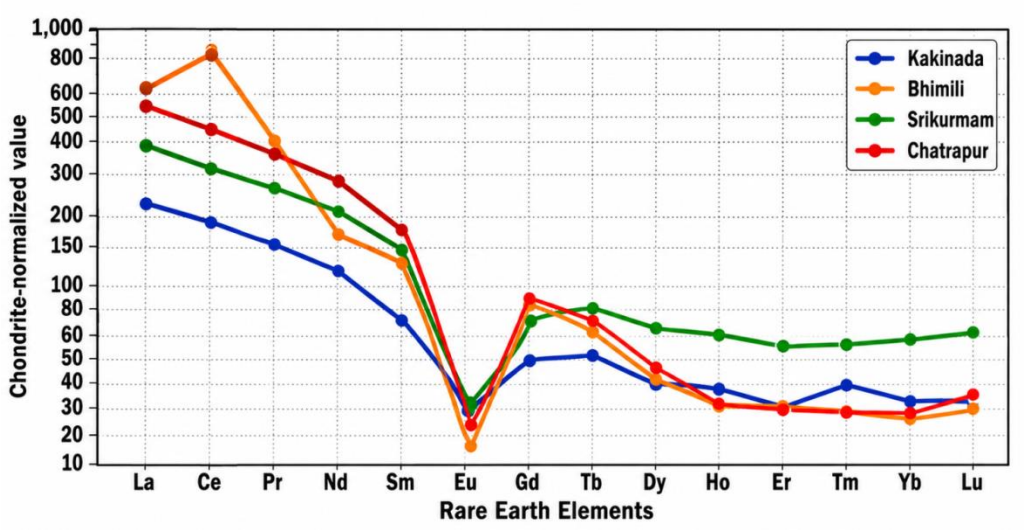


Figure 3. Chondrite-normalized REE patterns of placer ilmenites from the east coast of India**.**

DISCUSSION

REE Signatures and provenance constraints

The REE pattern clearly exhibits pronounced LREE enrichment, followed by a steep decline toward Sm–Eu, a strong negative Eu anomaly, and subsequent recovery toward Gd–Tb, with relatively flat to subdued HREE concentrations**.** This indicates that the ilmenites did not simply inherit a uniform REE signature from a single lithology. Rather, the patterns are consistent with complex or polygenetic provenance and/or mineral–melt processes affecting REE incorporation into ilmenite. The LREEs (La–Nd) are strongly enriched relative to the middle and heavy REEs. Bhimili shows the strongest LREE enrichment, particularly an exceptionally high Ce value. Chatrapur also exhibits strong LREE enrichment, with La–Nd progressively decreasing toward Sm. Similarly, Srikurmam has substantial LREE enrichment but a somewhat smoother pattern, while Kakinada has the lowest overall LREE enrichment among the four localities.

The most striking feature is the negative Eu anomaly, particularly at Chatrapur and Bhimunipatnam. The pronounced LREE enrichment suggests contribution from evolved magmatic components and/or accessory-mineral-bearing felsic to intermediate source rocks, rather than a simple REE pattern expected from an unmodified mafic source. The chondrite-normalized REE patterns of placer ilmenites from Kakinada, Bhimili, Srikurmam and Chatrapur are characterized by pronounced enrichment of light rare earth elements, depleted heavy rare earth elements and moderate negative Eu anomalies. Such patterns indicate significant magmatic fractionation and probable plagioclase-controlled differentiation processes prior to ilmenite crystallization (Bhattacharaya et al., 2012). These REE signatures are inconsistent with derivation solely from khondalite-group meta-sedimentary rocks of the Eastern Ghats Belt. Khondalites and associated metapelites generally display comparatively flatter REE profiles, stronger Eu depletion and lower abundances of Ti-bearing minerals due to sedimentary recycling and metamorphic redistribution processes (Ramakrishnan et al., 1994; Dobmeier and Raith, 2003). Furthermore, metasedimentary lithologies are typically poor sources for large-scale ilmenite enrichment.

In contrast, felsic granitoids, alkaline intrusives and mafic magmatic rocks commonly display strong LREE enrichment and moderate Eu anomalies, similar to those observed in the present study. Comparative REE plots demonstrate strong similarity between the studied placer ilmenites and published REE signatures of alkaline granitoids and evolved magmatic systems. The Chondrite Normalized REE patterns of East Coast placer ilmenites, have been compared with representative source lithologies in question using the data from various studies **(**McDonough and Sun, 1995; Pophare and Umathay, 2009). A comparison has been made between REE patterns of placer ilmenites from east coast of India with REE patterns of representative potential source lithologies from Eastern Ghats from different sources (Figure 4)

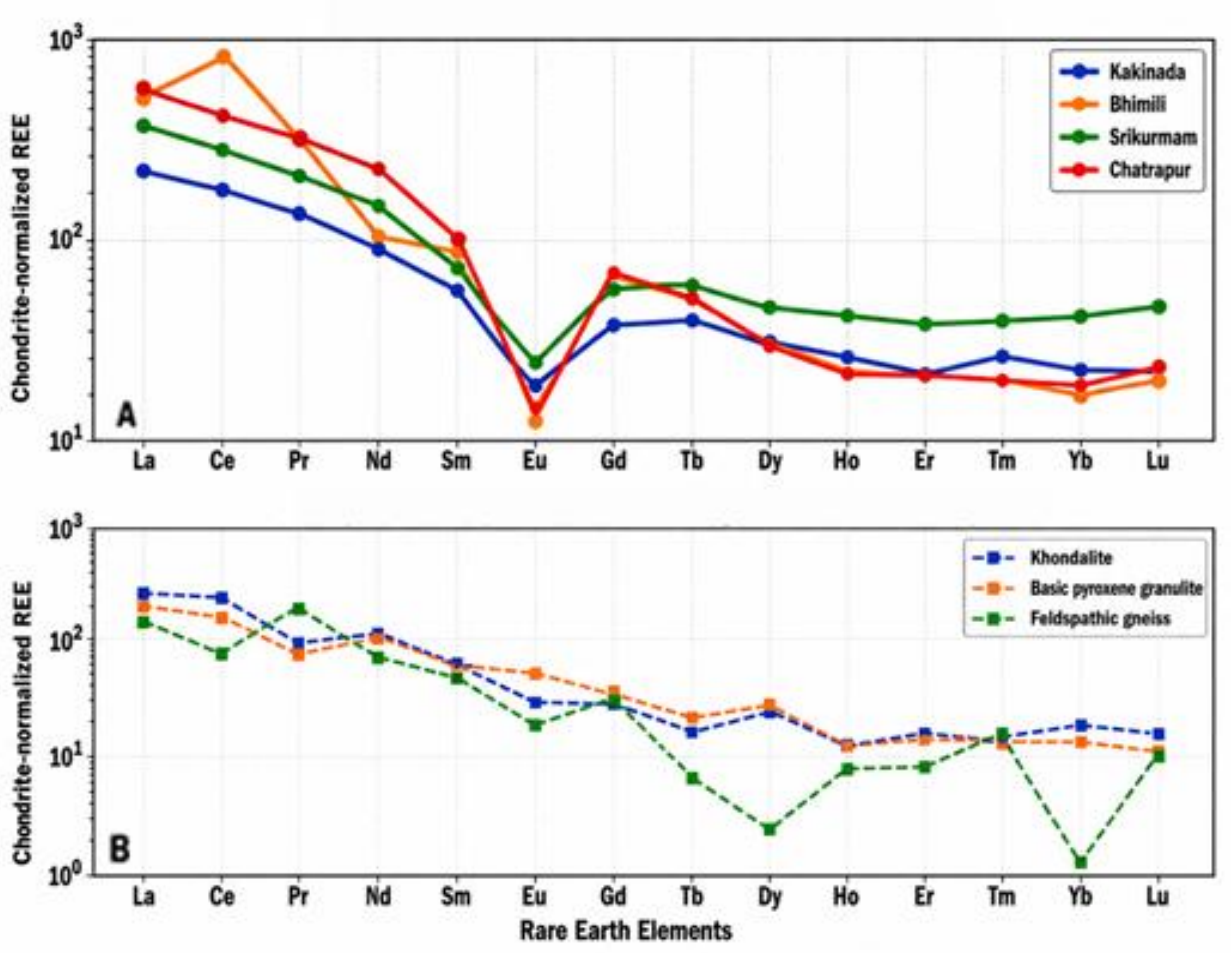


Figure 4. Comparative chondrite-normalized REE patterns of (**A)** placer ilmenites from the east coast of India, and **(B)** representative potential source lithologies from the Eastern Ghats (Source: McDonough and Sun, 1995; Pophare and Umathay, 2009)

The comparative chondrite-normalized REE patterns provide important constraints on the provenance of the East Coast placer ilmenites. Although the studied ilmenites exhibit pronounced LREE enrichment, variable HREE abundances and moderate negative Eu anomalies, these characteristics cannot be attributed exclusively to a single lithological source. The EGB terrain comprises a heterogeneous assemblage of khondalites, charnockites, pyroxene granulites, feldspathic gneisses, migmatites, granites, pegmatites and other high-grade metamorphic and magmatic lithologies, each capable of contributing distinct REE signatures to the sedimentary system (Pophare and Umathay, 2009).

The similarity between some of the studied ilmenite patterns and the REE characteristics of felsic to intermediate/mafic lithologies therefore suggests that the placer ilmenites may have received contributions from multiple lithological sources within the Eastern Ghats, rather than from khondalite-group metasedimentary rocks alone. This interpretation is consistent with previous provenance studies of the east coast heavy-mineral placers, which identify the Eastern Ghats lithological assemblage as the principal source while recognizing contributions from charnockites, granites, pegmatites and other magmatic rocks.

The studied placer ilmenites most probably represent a polygenetic provenance within the Eastern Ghats, with substantial contributions from felsic to mafic magmatic and high-grade metamorphic lithologies, rather than derivation exclusively from khondalite-group metasedimentary rocks.

The relatively high La/Yb_N ratios and muted Eu anomalies further suggest limited post-depositional alteration and preservation of primary igneous signatures during sediment transport and coastal reworking (Table 4) This inference is supported by comparable REE fingerprints documented in global placer ilmenites from Brazil, Australia and Africa, where igneous protoliths have been identified as dominant source contributors (Prates Hallal et al., 2025).

Table 4. Provenance indicating REE ratios of the east coast ilmenites

Locality	(La/Yb)	(La/Sm)	(Gd/Yb)	Eu/Eu*
Kakinada	10.25	3.67	1.70	0.85
Bhimili	25.03	4.91	3.08	0.82
Srikurmam	9.27	4.61	1.42	0.89
Chatrapur	26.78	5.08	3.16	0.81

Genetic parentage of placer ilmenites

Integration of REE geochemistry with major element data indicating high TiO_2 contents, strongly supports an igneous genetic parentage probably an alkaline composition for the studied placer ilmenites. The persistence of coherent REE patterns across geographically separated deposits suggests derivation from compositionally similar source terranes rather than localized recycling from heterogeneous metamorphic units (Darby, 1984). The moderate Eu anomalies indicate magmatic plagioclase fractionation, whereas strong LREE enrichment reflects evolved crustal magmatic processes. These observations are consistent with erosion of ancient granitoid, alkaline and basic igneous terranes incorporated subsequently into the Eastern Ghats Belt during Proterozoic tectono-thermal events. (Sengupta et al., 1999). Such igneous crustal components likely supplied ilmenite-rich detritus to the Eastern Ghats Belt over prolonged periods of denudation, transportation and reworking. Prolonged erosion of these Precambrian igneous terranes, coupled with repeated cycles of Quaternary marine transgression and regression, facilitated efficient hydraulic sorting and concentration of ilmenite along the east coast of India. The genetic linkage established in this study demonstrates the importance of integrating mineral chemistry, regional geology and REE systematics for refining provenance models of coastal placer deposits.

CONCLUSIONS

1. Placer ilmenites from the east coast of India exhibit strong LREE enrichment and moderate negative Eu anomalies.
2. Metamorphic and metasedimentary lithologies of the Eastern Ghats Belt are unlikely to represent dominant primary contributors.
3. High TiO_2 contents and REE systematics indicate derivation from alkaline igneous source rocks.
4. Provenance is linked to Archean–Mesoproterozoic igneous terranes that pre-date or formed early crustal precursors to the Eastern Ghats orogeny.
5. The studied placer ilmenites are interpreted to have a predominantly polygenetic provenance within the Eastern Ghats Belt, reflecting substantial contributions from felsic to mafic igneous and high-grade metamorphic source rocks. The integrated major-element and REE characteristics do not support derivation exclusively from khondalite-group metasedimentary rocks, but instead indicate erosion and mixing of compositionally diverse lithologies within the Eastern Ghats hinterland.
6. The study highlights the usefulness of REE geochemistry in provenance analysis, heavy mineral exploration and reconstruction of Precambrian crustal evolution. Further the REE geochemical approach has potential application in the study of offshore placer systems.

Acknowledgements

The authors acknowledge the CSIR-National Geophysical Research Institute, Hyderabad, for providing ICP–MS analytical facilities. Field and laboratory assistance from colleagues is gratefully acknowledged. The authors sincerely acknowledge Prof. Vijay Kumar Kopparapu, IIPE, Visakhapatnam, for his critical review of the manuscript and valuable suggestions, which significantly contributed to improving the interpretation of the REE data. We are thankful to the anonymous referees for their constructive criticism, which has helped us in improving the manuscript.

Author credit statement

Mokka Jagannadha Rao: Conceptualization, writing original draft, preparation of the manuscript, and coordination of the editorial review and revision process; G. Sandeep: Interpretation of the results, preparation of diagrams, and compilation and processing of field photographs and related materials; J. Venkataramana: Sample analysis, generation of analytical data, and contribution to the analytical aspects of the study. All the authors reviewed and approved the final version of the manuscript

Data availability

The datasets generated and/or analysed during the present study are available from the corresponding author or from J. Venkataramana, upon reasonable request.

Compliance with ethical standards

The authors declare that they have no conflict of interest. The authors further confirm that the manuscript complies with applicable ethical standards and copyright requirements.

References

Ali, M.A., Krishnan, S. and Banerjee, D.C., 2001. Beach and inland heavy mineral sand investigations and deposits in India – An overview. Expl. Res. for Atomic Minerals, 13, 1–21.

Balaram, V., Ramesh, S.L. and Anjaiah, K.V., 1995. Comparative study of the sample decomposition procedures in the determination of trace and rare earth elements in anorthosites and related rocks by ICP-MS. Freseniu's J. Analytic. Chem., 353, 176–182.

Bhattacharya, S., Chaudhary, A.K. and Basei, M., 2012. Original nature and source of khondalites in the Eastern Ghats Province, India. In: Mazumder, R. and Saha, D. (eds.), Palaeoproterozoic of India. Geol. Soc., London, Spl. Publ., 365, 147–158.

Darby, D.A., 1984. Trace-elements in ilmenite: A way to discriminate provenance or age in coastal sands. Geo. Soc. Am. Bull., 95, 1208–1218.

Dobmeier, C. and Raith, M.M., 2003. Crustal architecture and evolution of the Eastern Ghats Belt and adjacent regions of India. Geol. Soc. London, Spl. Publ., 206, 145–168.

Jagannadha Rao, M., Venkata Ramana, J., Venugopal, R. and Chandra Rao, M., 2005. Geochemistry and ore mineralogy of ilmenite from beach placers of the Visakhapatnam–Bhimunipatnam deposit, Andhra Pradesh. J. Geol. Soc. India, 66, 147–150.

Jagannadha Rao, M., Venkata Ramana, J., Aaron, A., Jaya Raj, Raja Rao, G. and Rajesh, P., 2016. Geochemical and ore-mineralogical characterization of beach placer ilmenite from Srikurmam deposit, Andhra Pradesh, India. J. Ind. Geophys. Union, 22(2), 171–177.

Kravchenko, S.M. and Svisero, D.P., 1990. Rare earth elements in ilmenite from alkaline rocks. Int. Geol. Rev., 32, 1035–1045.

Mahadevan, C. and Sri Ramdas, A., 1948. Black sands of the Visakhapatnam coast. Curr. Sci., 17, 150–151.

McDonough, W.F. and Sun, S.S., 1995. The composition of the Earth. Chem. Geol., 120, 223–253.

McLennan, S.M., 1989. Rare earth elements in sedimentary rocks: Influence of provenance and sedimentary processes. In: Lipin, B.R. and McKay, G.A. (eds.), Geochemistry and Mineralogy of Rare Earth Elements. Rev. Mineralogy, Mineralogical Society of America, 21, 169–200.

Pophare, A.M. and Umathay, R.M., 2009. Geochemical characterisation of lithologies from Burugubanda Graphite Deposit Area, East Godavari District, Andhra Pradesh. Gond. Geol. Mag. 24(2), 123–130.

Prates Hallal, G., Porcher, C.C., Veettil, B.K., de Almeida Espinoza, J.M. and Rolim, S.B.A., 2025. Distribution of ilmenite minerals in placer deposits along the middle coast of Southern Brazil using spaceborne and ground-based remote sensing. PLOS ONE, 20(2), e0314238. https://doi.org/10.1371/journal.pone.0314238.

Ramakrishnan, M. and Vaidyanadhan, R., 2010. Geology of India, Vol. 1., Geol. Soc. India, Bangalore, 556 pp.

Ramakrishnan, M., Chandra, R., Gopalan, K., Reddy, T.K. and Rao, A.T.R., 1994. The Eastern Ghats Belt: Lithology, Structure and Evolution. Geol. Soc. India Mem., 33, Bangalore, 253 pp.

Ravi, G.S., Gajapathi Rao, R. and Yugandhara Rao, A., 2001. Coastal heavy mineral sand deposits of Andhra Pradesh. Expl. Res. Atomic Minerals, 13, 53–85.

Sengupta, P., Dasgupta, S., Mukhopadhyay, B. and Harris, N.B.W., 1999. Geochemistry and origin of megacrystic granitoid rocks from Eastern Ghats Granulite Belt. Gond. Res., 2(1), 105–115.

Subba Rao, D.V. and Divakara Rao, V., 1999. Basic granulites of the Eastern Ghats: Petrology and tectonic implications. J. Geol. Soc. India, 54, 509–528.

Received on: 18-12-2025; Revised on: 08-09-2026; Accepted on: 10-09-2026

J. Ind. Geophys. Union, 30(6) (2026), 528-536
http://doi.org/10.71122/JIGU.30(6)2026.0051

Performance of CMIP6 climate models for temperature and precipitation over the Northwest Himalaya

Vartika Sharma[1*], Veluswamy Venkatramanan[1], Peeyush Gupta[2,3], M. S. Shekhar[2], R. Bhatla[3] and Jashandeep Singh[2]
[1]School of Interdisciplinary and Transdisciplinary Studies, Indira Gandhi National Open University, Maidan Garhi, New Delhi-110068, India
[2]Defence Geoinformatics Research Establishment, Him Parisar, Sector 37A, Chandigarh-160036, India
[3]Department of Geophysics, Institute of Science, Banaras Hindu University, Varanasi- 221005, India
*Corresponding author: vash82@yahoo.com

ABSTRACT

Accurate climate projections in the Himalayan region depend heavily on selecting global climate models that reliably capture temperature and precipitation dynamics across complex mountainous terrain. The present study evaluates the performance of two CMIP6 models namely CESM2 and BCC-CSM2-MR, previously identified as the top-performing models for temperature and precipitation, respectively over the northwest Himalaya. This region has been divided into three sub-regions viz. Jammu & Kashmir and Ladakh, Himachal Pradesh and Uttarakhand. Annual temperature and precipitation patterns have been analyzed for both the historical (1950–2014) and future (2015–2050) periods. Historical evaluations against ERA5 reanalysis data confirm that both CMIP6 models consistently capture the observed regional trends. Present findings indicate a historical warming trend across all three northwest Himalaya sub-regions. Conversely, historical precipitation showed a declining trend overall, as well as in Jammu & Kashmir and Ladakh and Himachal Pradesh, while Uttarakhand experienced an increasing trend. Future projections across three Shared Socioeconomic Pathways (SSP1-2.6, SSP2-4.5, and SSP5-8.5), show continued temperature increases across all the regions. However, future precipitation trends vary; the northwest Himalaya exhibits declining trends under SSP1-2.6 and SSP5-8.5, but a slight increase under SSP2-4.5.

Keywords: CMIP6, northwest Himalaya, Climate Models, Climate scenario, Temperature, Precipitation

INTRODUCTION

The Himalaya is one of the most climatically sensitive and topographically complex regions on Earth. Steep elevation gradients, cryospheric feedbacks and strong monsoon-western disturbance interactions, pose significant challenges for forecasting weather phenomena using coarse-resolution global climate models. For the Indian subcontinent, this massive orographic barrier acts both as thermal engine and a physical obstacle, driving the dynamics of the Indian summer monsoon and western disturbances (Rani et al., 2021; Hunt et al., 2025). The northwest Himalaya region is particularly vulnerable to hydro-meteorological extremes such as cloudbursts, flash floods and heavy snowfall, which have increased in frequency and intensity over the past century (Rao et al., 2016; Shekhar et al., 2017; Budakoti and Singh, 2023).

Understanding climate variability and projecting future climate change over any region (Bhatla et al., 2020, 2026; Gupta et al., 2019), especially over Himalaya Mountain region (Matta et al., 2025), has become a major focus of atmospheric and climate research due to its higher warming rates than the global average. However, due to the sparse observational network and highly heterogeneous terrain, climate modelling has become an essential tool for investigating past, present and future climatic conditions in this region (Momblanch et al., 2019). Global climate models, particularly those developed under the Coupled Model Intercomparison Project (CMIP), are widely used for climate change assessments (Eyring et al., 2016). Earlier studies primarily relied on CMIP3 and CMIP5 models, which provided projections of temperature, precipitation and atmospheric circulation patterns (Taylor et al., 2012). However, due to coarse spatial resolution and limited representation of complex orography, many CMIP5 models exhibited considerable biases in simulating precipitation and temperature over the Himalayan region (Palazzi et al., 2013; Meher et al., 2017). To overcome these limitations, the latest generation of models under the CMIP6 has been increasingly used in climate research (Eyring et al., 2019). CMIP6 models incorporate improved physical parameterizations, higher spatial resolution and better representation of land–atmosphere and ocean–atmosphere interactions, compared to earlier model generations (Gusain et al., 2020; Dutta et al., 2024). As a result, CMIP6 models generally show improved skill in simulating large-scale climate patterns, including the Indian summer monsoon and regional temperature distribution (Lalande et al., 2021; Srivastava et al., 2024).

Several studies have been conducted on India's drought challenge using CMIP6 models under historical and future climate scenarios (Verma et al., 2023; Bhatla et al., 2025). Verma et al. (2023) assessed historical and future droughts over India using five CMIP6 climate models and the standardized precipitation index. Their results show that Australian Community Climate and Earth System Simulator - Earth System Model Version 1.5 (ACCESS-ESM1.5) and Norwegian Earth System Model version 2 - Medium Atmosphere, Medium Ocean Resolution (NOR-ESM2-MM), best reproduce historical droughts. Future projections indicate increasing drought frequency and severity, particularly under Shared Socioeconomic Pathway 5 - 8.5 (SSP5-8.5), highlighting the need for enhanced drought

monitoring, mitigation and climate adaptation strategies. Bhatla et al., (2025) used 10 CMIP6 general circulation models (1901–2014) and applied a multi-model ensemble approach to assess drought projections under SSP2-4.5 and SSP5-8.5 for the near (2031–2060) and far (2071–2100) future. Their results identify northwest India and northcentral India as major drought hotspots, with SSP5-8.5 projecting greater drought frequency, intensity and duration due to stronger anthropogenic forcing.

Before using climate model data for future projections, it is essential to evaluate their performance against observational datasets (Gleckler et al., 2008). Several studies have performed model evaluation over the Himalayan region and the adjacent Tibetan plateau, which share similar climatic characteristics (Duan and Xiao, 2015; You et al., 2016). Comparative analyses of multiple CMIP6 models against observed temperature and precipitation datasets, indicate that most models successfully reproduce the broad spatial patterns of climate variables over the Tibetan plateau, although systematic biases such as cold bias in temperature and wet bias in precipitation still persist (Zhu and Yang, 2020). Nevertheless, the pattern correlation between simulated and observed climatology is generally high, often exceeding 0.75, suggesting that CMIP6 models provide a reasonable representation of large-scale climate features (Fan et al., 2020; Yang et al., 2021).

The present paper aims to systematically select and evaluate the performance of CMIP6 models in simulating historical and future temperature and precipitation over the northwest Himalaya region and its three sub-regions. Past and future climate projections based on the SSP2-4.5 scenario, which represents an intermediate socioeconomic development pathway characterized by moderate greenhouse gas mitigation, result in an approximate radiative forcing of 4.5 Wm^{-2} by 2100 that have been used for future climate scenario studies. In addition, two additional shared socioeconomic pathways scenarios, such as SSP1-2.6 and SSP5-8.5, have also been used for the future climate studies over the studied region.

DATA AND METHODOLOGY

Selection of CMIP6 models for temperature and precipitation studies

The primary objective of this study is to identify the best-performing CMIP6 models for simulating temperature and precipitation over the northwest Himalaya based on past literature and to carry out performance analysis of these models with European Center for Medium Range Weather Forecasting Re-Analysis (ERA5) temperature and precipitation data. Zhu and Yang (2020) evaluated the performance of 23 models from CMIP6 project in simulating historical temperature and precipitation over the Tibetan plateau from 1961 to 2014. They concluded that while models from CMIP6 shows improved accuracy in capturing spatial temperature patterns and reduced cold biases compared to CMIP5, systematic cold and wet biases still persist. The study by Li et al. (2021) evaluated the performance of 18 CMIP6 models in simulating historical and future climate over two distinct subregions of the third pole: the monsoon-dominated southeastern third pole and the westerlies-dominated upstream areas of the Amu Darya and Syr Darya. They concluded that while CMIP6 models successfully capture intra-annual variability and spatial patterns, they exhibit persistent systematic cold and wet biases, with annual temperatures underestimated and precipitation significantly overestimated, particularly in the southeastern third pole. In another study, Lalande et al. (2021) evaluated the performance of 26 CMIP6 global climate models in simulating climate over high mountain Asia during 1979-2014. Their analysis showed that although, CMIP6 models reproduce the large-scale climate variability and long-term trends reasonably well, they still exhibit systematic biases including a cold bias in temperature and an overestimation of snow cover over the Tibetan plateau.

Shahi et al. (2023) also evaluated the ability of 16 CMIP6 global climate models to simulate extreme precipitation events associated with the Indian summer monsoon and to project their future changes under the SSP5-8.5 high-emission scenario. They found that four models namely Community Earth System Model Version 2 (CESM2), Community Earth System Model Version 2 - Whole Atmosphere Community Climate Model (CESM2-WACCM), Norwegian Earth System Model version 2 - Medium Atmosphere, Medium Ocean resolution (NorESM2-MM) and Taiwan Earth System Model Version 1 (TaiESM1), perform best in reproducing the observed extreme precipitation characteristics and project a significant increase in the frequency, intensity and spatial extent of extreme rainfall events over India by 2041-2070, particularly over central India. Further, Bhuyan et al. (2024) further evaluated the performance of 47 CMIP6 climate models during the historical period (1975-2014) and used the 8 best-performing models to project future monsoon responses (June-July-August) over the Himalaya-Tibetan Highland. They concluded that, while the multi-model mean improves the representation of spatial distributions and reduces wet biases (~2 mm/day) compared to the 47-model average, systematic cold and wet biases still persist across the region. Future projections under the SSP585 scenario indicated a

significant warming trend of 0.6-0.9°C decade^{-1} and increased precipitation by the end of the 21st century.

Thus, based on the above inferences, the chosen weighted criteria for selection of top models for temperature and precipitation over the Himalayas are given in Table 1 and based on this table, the performance score of different models from CMIP6 for temperature and precipitation are included in Figure 1.

From Figure 1(a), Community Earth System Model Version 2 (CESM2) has been identified as the best model for temperature. This model developed by the National Center for Atmospheric Research, USA, is a fully coupled earth system model that integrates atmosphere, ocean, land, sea-ice and biogeochemical processes, providing improved representations of land–atmosphere interactions and climate feedback. Its atmospheric component operates at a nominal horizontal resolution of approximately 0.9° x 1.25°, while the ocean component has an approximate 1° x 1° horizontal resolution.

The model provides historical simulations (1850–2014) and future climate projections (2015–2100) under the CMIP6 framework using the shared socioeconomic pathways.

From Figure 1(b), Beijing Climate Center Climate System Model Version 2 – Medium Resolution (BCC-CSM2-MR), has been identified as the best model for precipitation. This model which is the best model found in this study for precipitation, is developed by the Beijing Climate Center, China Meteorological Administration. It is a medium-resolution coupled climate model designed to improve the simulation of atmospheric circulation, land-surface processes and the hydrological cycle, with an atmospheric horizontal resolution of approximately 1.125° x 1.125° and an ocean resolution of about 1° x 1°. The model provides historical simulations (1850–2014) and future climate projections (2015–2100) under the CMIP6 framework, using the shared socioeconomic pathways.

Study domain and methodology

The study region, showing the entire northwest Himalaya and its three sub-regions, is depicted in Figure 2. Evaluation of CESM2 model temperature data and BCC-CSM2-MR model precipitation data have been carried out with ERA5 Reanalysis data to investigate the performance of both data for the whole northwest Himalaya as well as for its three regions: J&K and Ladakh, Himachal Pradesh and Uttarakhand.

Table 1. Weighted criteria for the evaluation of the CMIP6 models.

Criteria	*weight*
mean bias	high
seasonal cycle realism	high
spatial pattern correlation	high
elevation sensitivity	medium
trend fidelity	medium
native spatial resolution	Medium
literature performance consistency	High

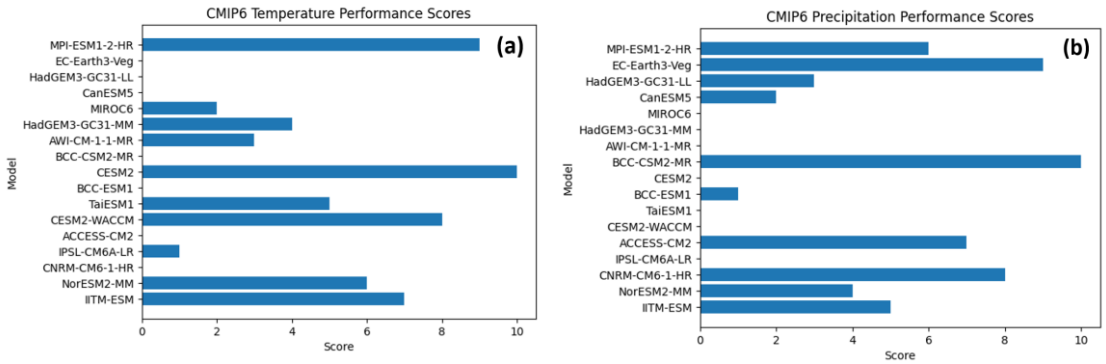


Figure 1. Performance score of different models from CMIP6 for **(a)** temperature and **(b)** precipitation.

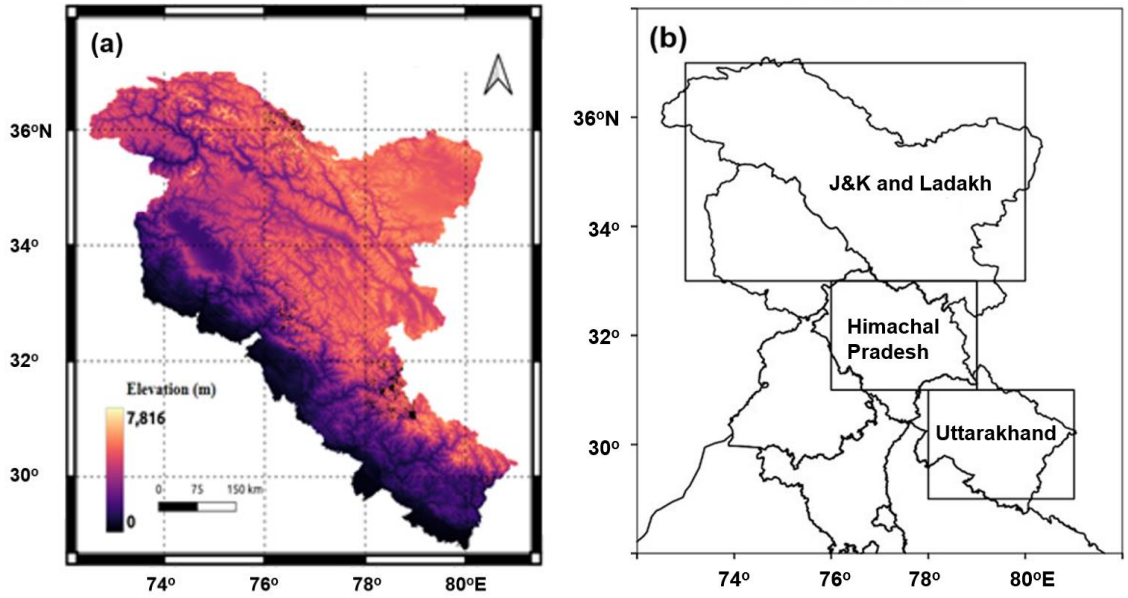


Figure 2. **(a)** Elevation map of northwest Himalaya and **(b)** Study domain of northwest Himalaya region and its three sub-regions: J&K and Ladakh, Himachal Pradesh and Uttarakhand.

CMIP6 temperature and precipitation data for northwest Himalaya and three sub-regions, available in NetCDF format, were downloaded from the Copernicus climate data store implemented by European Center for Medium Range Weather Forecasting. The temperature and precipitation data were downloaded for two CMIP6 models: CESM2 and BCC-CSM2-MR both for historical (1950-2014) and future (2015-2050) time periods. Observed data for comparison were obtained for the same historical period from the ERA5 reanalysis dataset. Future projections were selected from the three different scenarios i.e. SSP1-2.6, SSP 2-4.5 and SSP5-8.5. Raw temperature data was originally in Kelvin and has been converted to degrees celsius. Precipitation data were prepared as standard cumulative monthly precipitation totals (mm) to allow direct comparison with historical observations. To obtain a long-term analysis (1950–2050), CMIP6 historical model outputs (ending in 2014) were concatenated with CMIP6 future scenarios (starting in 2015) to produce an analytical time series. The time series of temperature and precipitation were analyzed using linear regression to quantify the rate of climatic changes and to assess the statistical significance. The total decadal trend of the climate variables was represented by the slope of the regression line. The statistical significance was strictly analysed by p-value based on f-distribution of the regression model. The trend metrics (slope and p-value) were calculated individually for the entire northwest Himalaya region and for each of the three sub-regions to differentiate local climatic changes from regional patterns. To evaluate the performance and accuracy of the CMIP6 climate models against the ERA5 observational data, several statistical error metrics were computed. These included the mean absolute error and the root mean square error. Additionally, the correlation coefficient and coefficient of determination were calculated to evaluate the goodness-of-fit and determine the proportion of variance in the historical observations accurately predicted by the CMIP6 simulations.

RESULTS AND DISCUSSION

Trends of temperature from CESM2 model

The performance study has been carried out for CESM2 historical temperature data from 1950 to 2025 (Figure 3). For northwest Himalaya as well as its three sub-regions, J&K and Ladakh, Himachal Pradesh and Uttarakhand, there is a significant increasing trend in temperature during the period from 1950 to 2025 for both CMIP6 model data and ERA5 data. It may be noted that the period from 1950 to 2014 is generally considered as the historical data and the period from 2015 onwards as the future scenario for CMIP6 project. However, in the present study, we have considered the past data as the period from 1950 to 2025 to evaluate the performance since the observations are already available for the said period. It is interesting to observe that CESM2 temperature data has a systematic positive bias over ERA5 temperature data for all the regions of northwest Himalaya during the whole period of study (1950–2025). The results show that there has been an increasing trend in CESM2 temperature data by 0.02°C year^{-1} and ERA5 temperature data by 0.008°C year^{-1} during this period for northwest Himalaya. The details of statistical analysis for temperature is depicted in Table 2, which shows that the mean absolute

error is less than the root mean square error and also the mean absolute error and root mean square error are comparatively close to each other for all the regions, including northwest Himalaya thereby confirming less error in CMIP6 model data.

Again, the correlation coefficients between CESM2 and ERA5 temperature data is high for the three sub-regions of northwest Himalaya except for the northwest Himalaya (0.48), which may be due to the inclusion of a greater area encompassing variable topography and climatology. Hence, the CESM2 model temperature data can be confidently used for past and future projection studies over the Northwest Himalaya after applying a standard systematic bias of 3° C year^{-1} to 4° C year^{-1}.

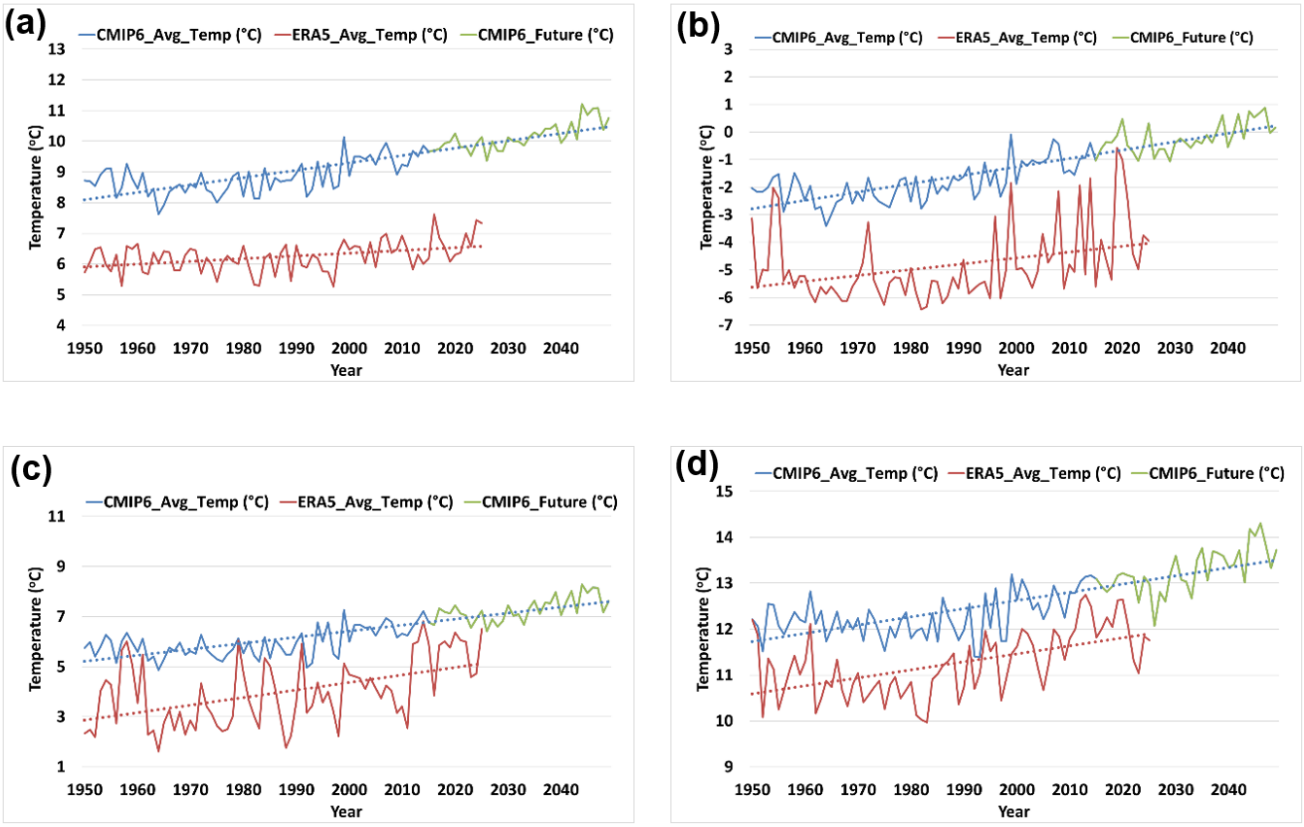


Figure 3. Trends of temperature using CESM2 model data (1950 – 2050) and ERA5 data (1950 – 2025) over **(a)** northwest Himalaya, **(b)** J&K and Ladakh, **(c)** Himachal Pradesh and **(d)** Uttarakhand.

Table 2. Statistical analysis between CESM2 model and ERA5 reanalysis temperature data

Statistical parameters	*Region*			
	northwest Himalaya	J&K and Ladakh	Himachal Pra-desh	Uttarakhand
Mean absolute error (°c)	2.73	3.18	2.10	1.13
Root mean square error (°c)	2.79	3.35	2.30	1.21
Correlation coefficients	0.48	0.64	0.78	0.78
Slope (°c year^{-1}) CESM2	0.02	0.03	0.02	0.01
Slope (°c year^{-1}) ERA5	8.91E-03	2.11E-02	3.00E-02	1.75E-02
p-value CESM2	1.56E-13	8.87E-16	4.67E-12	5.41E-09
p-value ERA5	3.02E-04	2.23E-03	7.93E-06	2.79E-07

Trends of precipitation from BCC-CSM2-MR model

Precipitation trends between BCC-CSM2-MR and ERA5 model data for the whole northwest Himalaya as well as for J&K and Ladakh, Himachal Pradesh and Uttarakhand have been shown in Figure 4. As seen from this figure, there is a decreasing trend in precipitation during the period from 1950 to 2025 for the northwest Himalaya, J&K and Ladakh and Himachal Pradesh, except Uttarakhand, where it shows an increasing trend for both CESM2 and ERA5 model precipitation data. However, all the increasing and decreasing trends in precipitation are found to be insignificant during the period from 1950 to 2025 (Table 3). The decreasing slopes for precipitation for BCC-CSM2-MR model for northwest Himalaya, J&K and Ladakh and Himachal Pradesh are 0.64 mm year^{-1}, 1.5 mm year^{-1} and 0.83 mm year^{-1} respectively. Similarly, the decreasing slopes for ERA5 model precipitation data for northwest Himalaya, J&K and Ladakh and Himachal Pradesh are 0.17 mm year^{-1}, 1.14 mm year^{-1} and 0.38 mm year^{-1} respectively. However, for Uttarakhand, an increasing trend in precipitation with slopes 2.59 mm year^{-1} and 0.63 mm year^{-1} are found for BCC-CSM2-MR and ERA5 models respectively. The statistical analysis for precipitation is depicted in Table 3. The mean absolute error for northwest Himalaya, J&K and Ladakh, Himachal Pradesh and Uttarakhand are 33.22 mm, 84.29 mm, 120.62 mm and 107.96 mm respectively, whereas the respective root mean square error values are 41.30 mm, 111.99 mm, 150.57 mm and 152.79 mm. The correlation coefficients between BCC-CSM2-MR and ERA5 precipitation data is high for northwest Himalaya, as well as its three sub-regions.

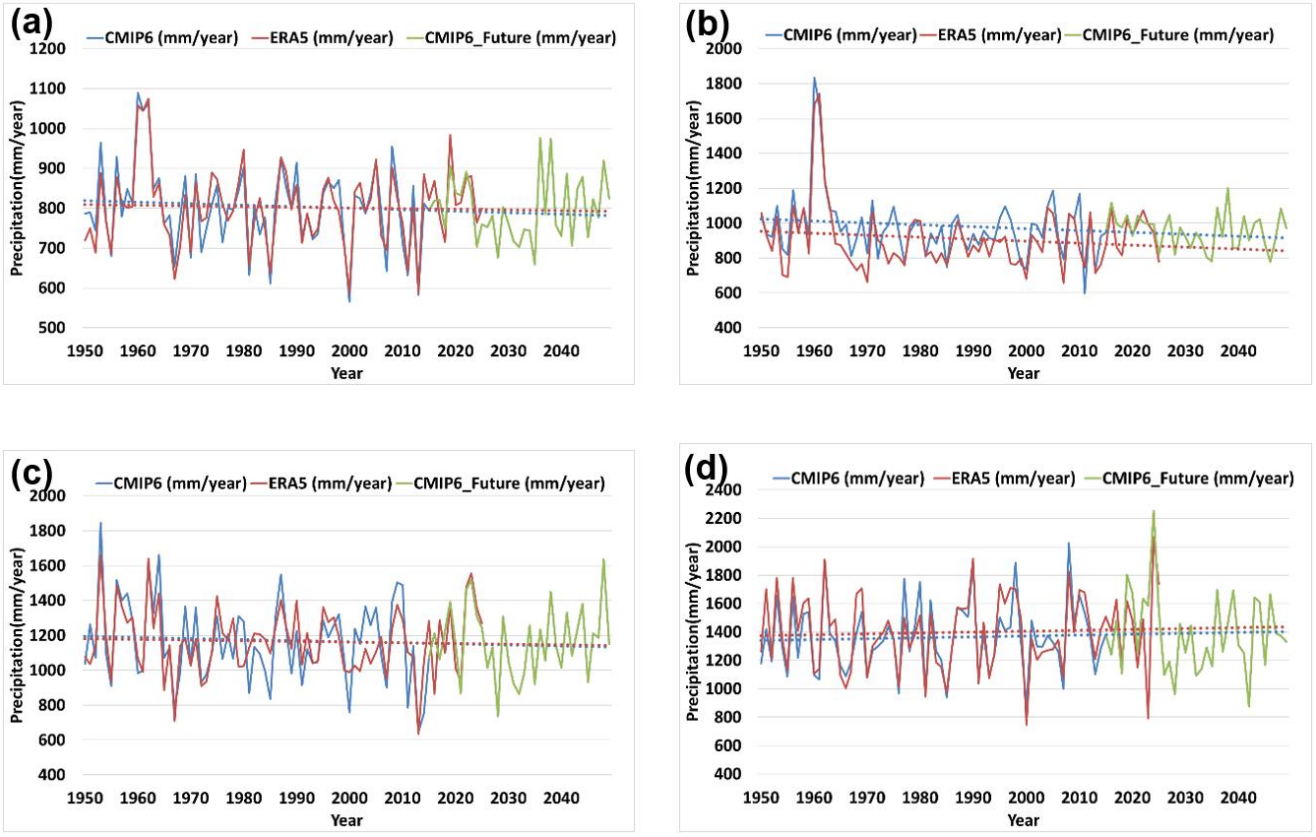


Figure 4. Trends of precipitation using BCC-CSM2-MR model data (1950 – 2050) and ERA5 data (1950 – 2025) over **(a)** northwest Himalaya, **(b)** J&K and Ladakh, **(c)** Himachal Pradesh and **(d)** Uttarakhand.

Table 3. Statistical analysis between BCC-CSM2-MR model and ERA5 reanalysis precipitation data

Statistical parameters	*Region*			
	Northwest Himalaya	J&K and Ladakh	Himachal Pradesh	Uttarakhand
Mean absolute error (mm)	33.22	84.29	120.62	107.96
Root mean square error (mm)	41.30	111.99	150.57	152.79
Correlation coefficients	0.91	0.88	0.76	0.84
Slope (mm year^{-1}) BCC-CSM2-MR	-0.64	-1.50	-0.83	2.59
Slope (mm year^{-1}) ERA5	-0.17	-1.14	-0.38	0.63
p-value BCC-CSM2-MR	0.23	0.10	0.50	0.06
p-value ERA5	0.74	0.23	0.71	0.66

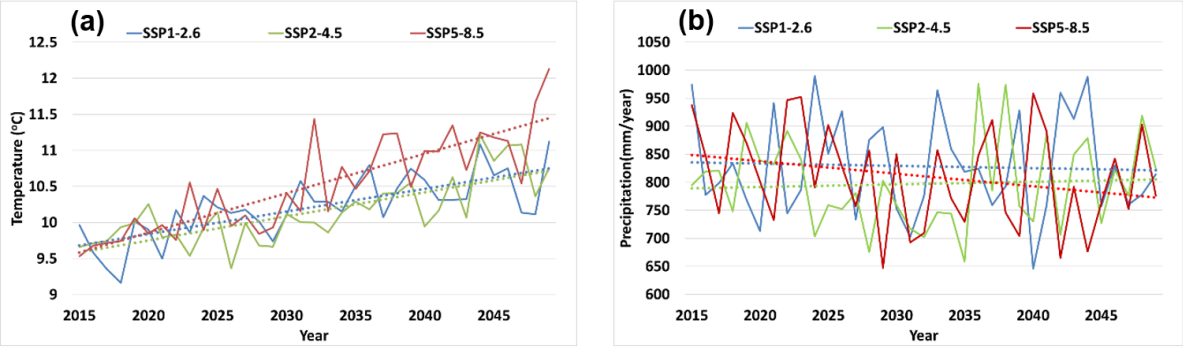


Figure 5. Future climate projection for **(a)** annual temperature and (b) precipitation over the northwest Himalaya.

Future projection for temperature and precipitation

The future projections for temperature and precipitation during the period from 2015 to 2050 for the three scenarios SSP1-2.6, SSP2-4.5 and SSP5-8.5 have been given in Figure 5. Here, the results have been presented for the northwest Himalaya region only. As seen from the figure, increasing trends are shown for all the scenarios in temperature data over this region during 2015-2050 (Figure 5a), suggesting an increase in temperature over the region in future. However, for precipitation (Figure 5b), decreasing trends are shown for the scenarios SSP1-2.6 and SSP5-8.5, where an increasing trend is seen for SSP2-4.5 over northwest Himalaya. The increasing trend for SSP2-4.5 may be due to the increase in the recent extreme precipitation events over the Indian Himalayan region contributing to more liquid precipitation in comparison to the solid precipitation in the context of moderate global warming and climate change (SSP2-4.5). However, a more detailed study needs to be carried out to investigate the physics and dynamics of the atmosphere for arriving in any conclusions for the increasing trends for SSP2-4.5.

CONCLUSIONS

Climate modelling studies over the northwest Himalayan region have evolved significantly with the development of CMIP6 datasets and high-resolution regional climate models. This study presents a ranked evaluation of CMIP6 models for temperature and precipitation in the northwest Himalayan region. The results identify CESM2 as the best temperature model and BCC-CSM2-MR as the best precipitation model. The following main conclusions are drawn from the present study:

1. Performance evaluation of CESM2 model shows increasing trends for temperature over northwest Himalaya and its three sub-regions (J&K and Ladakh, Himachal Pradesh and Uttarakhand) with systematic positive biases with respect to ERA5 Reanalysis data for the historical period 1950 to 2025.
2. BCC-CSM2-MR model precipitation data shows decreasing trends in precipitation over northwest Himalaya, J&K and Ladakh and Himachal Pradesh whereas it shows an increasing trend for Uttarakhand for the same historical period.
3. Future projections (2015-2050) of temperature from CESM2 model for three shared socioeconomic pathways scenarios: SSP1-2.6, SSP2-4.5 and SSP5-8.5, show increasing trends over the northwest Himalaya.
4. Future projections of precipitation from BCC-CSM2-MR model show an increasing trend in precipitation for

SSP2-4.5 scenario whereas decreasing trends are seen for SSP1-2.6 and SSP5-8.5.

5. Although CESM2 and BCC-CSM2-MR models provide the most reliable temperature and precipitation simulations, respectively, among the evaluated CMIP6 models, their projections should be interpreted with appropriate caution, particularly when assessing localized climate change affects over the complex terrain of the Himalayas.

Acknowledgement

The authors express their sincere gratitude to Ms. Anisha (Junior Research Fellow) for compiling the CMIP6 temperature and precipitation data for identifying the best suitable models.

Author Credit Statement

All authors contributed to the study conception and design. Vartika Sharma, Peeyush Gupta and M. S. Shekhar are credited for drafting the manuscript, data acquisition, interpretation and review. Veluswamy Venkatramanan, Rajeev Bhatla and M. S. Shekhar are credited for supervision, paper drafting and reviewing, Jashandeep Singh is credited for data acquisition, and processing. All authors read and approved the final manuscript.

Data Availability

The data used in this study are in the open source and can be downloaded from CMIP6 Project portal: https://cds.climate.copernicus.eu/datasets/projections-cmip6

Compliance with Ethical Standards

The authors declare no conflict of interest and adhere to copyright norms.

References

Bhatla R., Singh, S., Verma, S., Tyagi, P., Maurya, A. and Pant, M., 2020.The study of rainfall variability during pre and post monsoon seasons over All India and its different regions in changing climate. J. Ind. Geophys. Union, 24(3), 57-71.

Bhatla, R., Verma, A., Vishwakarma, A. and Mall R.K., 2025. India's Drought Challenge: Insights from CMIP6 Models on Historical and Future Climate Scenarios. Int. J. Climatol., 1-22. https://doi.org/10.1002/joc.70075.

Bhatla, R., Dangi, M., Verma, A. and Gupta, M., 2026. Prediction of pre-monsoon temperature of Varanasi using machine learning and deep learning techniques. J. Ind. Geophys. Union, 30(4), 263-275.

Bhuyan, D.P., Salunke, P. and Chadha, M., 2024. Climate projections for Himalaya–Tibetan Highland. Theor. Appl. Climatol., 155(2), 1055–1065.

Budakoti, S. and Singh, C., 2023. Comprehensive study of extreme rainfall events using model simulations and remotely sensed observations. Hydrol. Sci. J., 68(16), 2317–2335.

Duan, A. and Xiao, Z., 2015. Does the climate warming hiatus exist over the Tibetan Plateau? Sci. Rep., 5, 13711. https://doi.org/10.1038/srep13711.

Dutta, U., Bhowmik, M., Hazra, A., Shiu, C.-J. and Chen, J.-P., 2024. Towards better representation of Indian summer monsoon rainfall in CMIP6 models: Evaluation of MISO and MJO simulation. Theor. Appl. Climatol., 155(9), 9007–9027.

Eyring, V., Bony, S., Meehl, G.A., Senior, C.A., Stevens, B., Stouffer, R.J. and Taylor, K.E., 2016. Overview of the Coupled Model Intercomparison Project Phase 6 (CMIP6) experimental design and organization. Geosci. Model Dev., 9, 1937–1958.

Eyring, V., Cox, P.M., Flato, G.M. et al., 2019. Taking climate model evaluation to the next level. Nat. Clim. Change, 9, 102–110.

Fan, X., Miao, C., Duan, Q., Shen, C. and Wu, Y., 2020. The performance of CMIP6 versus CMIP5 in simulating temperature extremes over the global land surface. J. Geophys. Res. Atmos., 125(18), e2020JD033031. https://doi.org/10.1029/2020JD033031.

Gleckler, P.J., Taylor, K.E. and Doutriaux, C., 2008. Performance metrics for climate models. J. Geophys. Res. Atmos., 113(D6), D06104. https://doi.org/10.1029/2007JD008972.

Gupta P., Verma, S., Bhatla, R., Payra, S. and Yadava, P.K., 2019. Long term (1984-2013) winter temperature variability and cold wave analysis over Varanasi City. J. Ind. Geophys. Union, 23(4), 343-351

Gusain, A., Ghosh, S. and Karmakar, S., 2020. Added value of CMIP6 over CMIP5 models in simulating Indian summer monsoon rainfall. Atmos. Res., 232, 104680. https://doi.org/10.1016/j.atmosres.2019.104680

Hunt, K.M.R., Baudouin, J.-P., Turner, A.G., Dimri, A.P., Jeelani, G., Pooja, Chattopadhyay, R., Cannon, F., Arulalan, T., Shekhar, M.S., Sabin, T.P. and Palazzi, E., 2025. Western disturbances and climate variability: A review of recent developments. Weather and Clim. Dyn., 6(1), 43–112.

Lalande, M., Ménégoz, M., Krinner, G., Naegeli, K. and Wunderle, S., 2021. Climate change in the High Mountain Asia in CMIP6. Earth Syst. Dyn., 12(4), 1061–1098.

Li, Y., Wang, C. and Su, F., 2021. Evaluation of Climate in CMIP6 Models over Two Third Pole Subregions with Contrasting Circulation Systems. J. Clim., 1–64. https://doi.org/10.1175/JCLI-D-21-0214.1.

Matta, G., Kumar, A., Singh Tomar, D. and Kumar, R., 2025. Climate change in the Himalayan region: Susceptible impacts on environment and human settlements. Front. Environ. Sci., 13, 1550843. https://doi.org/10.3389/fenvs.2025.1550843.

Meher, J.K., Das, L., Akhter, J., Benestad, R.E. and Mezghani, A., 2017. Performance of CMIP3 and CMIP5 GCMs to simulate observed rainfall characteristics over the Western Himalayan region. J. Clim., 30(19), 7777–7799.

Momblanch, A., Holman, I. and Jain, S., 2019. Current Practice and Recommendations for Modelling Global Change Impacts on Water Resource in the Himalayas. Water, 11(6), 1303. https://doi.org/10.3390/w11061303.

Palazzi, E., von Hardenberg, J. and Provenzale, A., 2013. Precipitation in the Hindu-Kush Karakoram Himalaya: Observations and future scenarios. J. Geophys. Res. Atmos., 118(1), 85–100.

Rani, S.I.T.A., George, J.P., Rajagopal, E.N., Renshaw, R., Maycock, A., Barker, D.M. and Rajeevan, M., 2021. IMDAA: High Resolution Satellite-era Reanalysis for the Indian Monsoon Region. J. Clim., 1–78. https://doi.org/10.1175/JCLI-D-20-0412.1.

Rao, P.C., Shinde, A.S. and Jaswal, A.K., 2016. Intense precipitation causing floods over Himalayan region of northern India: A case study on role of atmospheric rivers. J. Ind. Geophys. Union, 20(2), 191–200.

Shahi, N.K., Rai, S., Verma, S. and Bhatla, R., 2023. Assessment of future changes in high-impact precipitation events for India using CMIP6 models. Theor. Appl. Climatol., 151(1–2), 843–857.

Shekhar, M.S., Narasimha Rao, N., Paul, S., Bhan, S.C., Singh, G.P. and Singh, A., 2017. Winter precipitation climatology over Western Himalaya: Altitude and range wise study. J. Ind. Geophys. Union, 21(2), 148–152.

Srivastava, A., Delworth, T.L., Dixon, K.W., Cooke, W. and Rosati, A., 2024. Evaluation of CMIP6 models in simulating the mean and variability of the Indian summer monsoon. J. Clim., 37(3), 895–915.

Taylor, K.E., Stouffer, R.J. and Meehl, G.A., 2012. An overview of CMIP5 and the experiment design. Bull. Am. Meteor. Soc., 93(4), 485–498.

Verma A., Viswakarma, A., Bist, S., Kumar, S. and Bhatla R., 2023. A Long-term drought assessment over India using CMIP6 framework: present and future perspectives. Mausam, 74 (4), 963-972.

Yang, X.L., Zhou, B.T., Xu, Y. and Han, Z.Y., 2021. CMIP6 evaluation and projection of temperature and precipitation over China. Adv. Atmos. Sci., 38(5), 817–830.

You, Q., Min, J. and Kang, S., 2016. Rapid warming in the Tibetan Plateau from observations and CMIP5 models in recent. decades. Int. J. Climatol., 36(7), 2660–2670.

Zhu, Y.-Y. and Yang, S., 2020. Evaluation of CMIP6 for historical temperature and precipitation over the Tibetan Plateau and its comparison with CMIP5. Adv. Clim. Chang. Res., 11(3), 239–251.

Received on: 17-07-2026; Revised on: 08-08-2026; Accepted on: 11-08-2026

GUIDE FOR AUTHORS

The Journal of Indian Geophysical Union (JIGU), a SCI Journal published bimonthly by the Indian Geophysical Union (JIGU), is an inter disciplinary journal from India that publishes high-quality research in earth sciences with special emphasis on the topics pertaining to the Indian subcontinent and the surrounding Indian Ocean region. The journal covers several scientific disciplines related to the Earth sciences such as solid Earth Geophysics, geology and geochemistry, apart from marine, atmosphere space and planetary sciences. J-IGU welcomes contributions under the following categories :

*Research articles, short notes and students section reporting new findings, results, etc.

*Review articles providing comprehensive overview of a significant research field.

In addition, JIGU also welcomes short communications, after communications and report on scientific activity, book reviews, news and views, etc.

The manuscript should be submitted electronically as a single word format (.doc file) including the main text, figures, tables, and any other supplementary information along with the signed "Declaration Letter". The manuscript should be submitted by email (jigul1963@ gmail.com) to the Chief Editor.

After acceptance of the manuscript the corresponding author would be required to submit all source files (text and Tables in word format) and figure in high resolution standard (*.jpg, *.tiff, *.bmp) format. These files may be submitted to JIGU as a single *.zip file along with the "Copyright Transfer Statement".

IMPORTANT INFORMATION

Ethics in publishing; J-IGU is committed to ensuring ethics in publication and takes a serious view of plagiarism including self-plagiarism in manuscripts submitted to the journal, Authors are advised to ensure ethical values by submitting only their original work and due acknowledgement to the work of others used in the manuscript. Authors must also refrain from submitting the same manuscript to more than one journal concurrently, or publish the same piece of research work in more than one journal, which is unethical and unacceptable. Editor of JIGU is committed to make every reasonable effort to investigate any allegations of plagiarism brought to his attention, as well as instances that come up during the peer review process and has full authority to retract any plagiarized publication from the journal and take appropriate action against such authors if it is proven that such a misconduct was intentional.

Similarly, Editor and Reviewers are also expected to follow ethical norms of publishing by ensuring that they don't use any unpublished information, communicated to them for editorial or review purpose, in their own research without the explicit written consent of the author. They are also expected to keep manuscript' data/ observations/ any other information related to the peer review confidential to protect the interest of the authors. Reviewers should refrain from reviewing the manuscripts in which they have conflicts of interest resulting from competitive, collaborative, or other relationships or connections with any of the authors, companies, or institutions connected to the manuscript.

Conflict of interest

All authors are requested to disclose any actual or potential conflict of interest including any financial, personal or other relationships with other people or organizations within three years of beginning the submitted nor that could inappropriately influence, or be perceived to influence, their work.

Submission declaration

Submission of a manuscript implies that the work has not been published previously and it is not under consideration for publication elsewhere, and that if accepted it will not be published elsewhere in the same or any other form, in English or in any other language, without the written consent of the publishers. It also implies that the authors have taken necessary approval from the competent authority of the institute/organization where the work was carried out.

Copyright

After acceptance of the manuscript the corresponding author would be required to sign and submit the "Copyright Transfer Statement".

MANUSCRIPT PREPARATION

The corresponding author should be identified (include E-mail address, Phone/Mobile number). Full affiliation and postal address must be given for all co-authors.

Abstract:

An abstract of not more than 300 words must be included.

Text:

The manuscript should be structured to include a front page containing the title, Author(s) name, affiliation and address of the institute, where the work was carried out, and 5-to-6 Key words. Author(s) present address, if different from the above mentioned address, may be given in the footnote. The corresponding author should be identified with an asterisk and his/her email ID should be provided. This page should be followed by the main text consisting of Abstract, Introduction, Methods/ Techniques/ Area description, Results, Discussion, Conclusions, Acknowledgements, and References. Tables and Figures with captions should be inserted at the end of main text. It should not be inserted in the body of the text.

Figures/ Illustrations:

figures should be provided in camera-ready form, suitable for reproduction (which may include reduction) without retouching. Figures in high-resolution (at least 300 dpi) standard formats (*.jpg, * tiff, *.bmp) are acceptable. Figures should be numbered according to their sequence in the text. References should be made in the text to each figure. Each figure should have a suitable caption.

Tables:

Authors should take note of the limitations set by the size and layout of the journal. Table should not exceed the printed area of the page. They should be typed on separate sheets and details about the tables should be given in the text. Heading should be brief. Large tables should be avoided and may be provided as supplementary information, if required.

Equations:

Equations should be numbered sequentially with Arabic numerals and cited in the text. Subscripts and Superscripts should be set off clearly.

Equation writing software that presents each equation as an object in MS Word will be accepted. Style and convention adopted for the equations should be uniform throughout the paper.

References:

All references to publications cited in the main text should be presented as a list of references in order following the text and all references in the list must be cited in the text. References should be arranged chronologically, in the text. The list of references should be arranged alphabetically at the end of the paper.

References should be given in the following form:

Kaila, K.L., Reddy PR., Mall D.M., Venkateswarlu, N., Krishna V.G. and Prasad, A.S.S.S.R.S., 1992, Crustal structure of the west Bengal el eon deep seismic sounding investigations. Geophys. J. Int., 1,45-66.

REVIEW PROCESS:

All manuscripts submitted to the journal are peer-reviewed. It is advisable to send the contact details of 4 potential reviewers along with the manuscript to expedite the review process. Editor has the option to select reviewers from the list or choose different reviewers. The review process usually takes about 3 months. All enquiries regarding the manuscript may be addressed to the Chief Editor.

GALLEY PROOF:

Technical editing of manuscripts is performed by the editorial board. The author is asked to check the galley proof for typographical errors and to answer queries from the editor. Authors are requested to return the corrected proof within two days of its receipt to ensure uninterrupted proceedings The editor will not accept new material in proof unless permission from the editorial board has been obtained for the addition of a "note added in proof". Authors are liable to be charged for excessive alterations to galley proof.

PUBLICATION CHARGES:

There are no page charges for publication. The corresponding author will receive a soft copy (pdf format) of his/her published article. Should the author desire to purchase reprints of his/her publication, he/she must send the duly signed Reprint Order Form (accompanies the galley proof and contains price details) along with the corrected galley proof to the Editor. The reprint charges must be paid within one month of sending the Reprint Order Form.

Any payment related to printing or purchase of reprints should be made in the form of a Demand Draft in the name of Treasurer, Indian Geophysical Union, payable at Hyderabad.

You may download the pdf file from:
http://iguonline.in/journal/instructions.php